Electronic and Optical Properties of Surface-Anchored Metal-Organic Frameworks

Zur Erlangung des akademischen Grades eines

DOKTORS DER NATURWISSENSCHAFTEN

(Dr. rer. nat.)

Fakultät für Chemie und Biowissenschaften

Karlsruher Institut für Technologie (KIT) - Universitätsbereich

genehmigte

DISSERTATION

von

M.Sc. Jianxi Liu

aus

Wuwei, P. R. China

Dekan: Prof. Dr. Peter Roesky

Referent: Prof. Dr. Christof Wöll

Korreferent: Prof. Dr. Stefan Bräse

Tag der mündlichen Prüfung: 14.07.2015

DOI: 10.5445/IR/1000049126

This thesis was carried out under the supervision of Prof. Dr. Christof Wöll at the Institute of Functional Interfaces (IFG) in Karlsruhe Institute of Technology (KIT). This thesis is submitted for Doctor of Philosophy degree at Karlsruhe Institute of Technology, and has not been submitted in any other university for any degree.

I hereby declare that the thesis is my original work and has been written by me unless stated otherwise in the body of the thesis, and I have faithfully and properly cited all sources used in the thesis. I followed the standing rules of the “Universität Karlsruhe (TH)” to ensure good scientific practice as amended time for time.

Karlsruhe, 01.06.2015

Jianxi Liu

Dedicated

To

My Loving Mother

Abstract

Crystalline, continuous and monolithic surface-anchored metal-organic framework (SURMOF) thin films were fabricated using liquid-phase epitaxial (LPE) methods. The thickness of these thin films was controlled and showed, over respective fabrication processes, a high degree of precision. The high quality nanoporous thin film materials were further used for the fabrication of electronic, optoelectronic and photonic devices.

Understanding the electric transport in SURMOFs is essential, both from a fundamental perspective and with regards to the future development of MOF based electronic devices. In this respect, a series of HKUST-1 [$Cu_3(BTC)_2$] SURMOF thin films were integrated in a mercury-drop-based tunneling junction. The transport properties of these SURMOFs were shown to be analogous to those of hybrid metal-organic molecular wires, as manifested by a very low value of the tunneling decay constant ($\beta \approx 0.006$ Å^{-1}). Together with their insulating behavior, they also seem to display a linear correlation between the thickness of the film and the measured increased resistance. Upon loading ferrocene (Fc) in pores of HKUST-1, a noticeable increase in transport current was observed. A transport model and ab-initio electronic structure calculations were used and revealed a hopping transport mechanism that relates the changes upon Fc loading to the SURMOF films.

Furthermore, HKUST-1 SURMOFs with different crystallographic growth directions were successfully produced on different self-assembled monolayers (SAMs) modified gold electrodes by means of LPE methodology. Then, cyclic voltammetry (CV) experiments were carried out to study the electrochemical behavior of these SURMOFs in an aprotic ionic liquid (IL). The method proved to be highly suitable for investigating the changes in electric conductivity of the SURMOFs upon filling their pores with a small electroactive molecule, here Fc. Additionally, cyclic voltammetry methods provided valuable insights for the determination of the film quality.

In addition to the improved electrical conductivity of MOFs, other properties such as visible light absorption and photocurrent generation were attained by choosing suitable organic ligands with specific properties. Porphyrin was used as an electron donor to fabricate SURMOFs. The well-defined stacking of the highly ordered photoelectroactive molecules on the electrodes enabled the realization of the artificial light harvester and an effective transformation into photocurrent. Monolithic, homogenous films deposited on

fluorine-doped tin oxide (FTO) substrates, which can act as electrodes, were used in a home-made photoelectrochemical cell for evaluating the photocurrent generation capacity of the material.

Furthermore, thanks to promising properties useful for optical sensor and photonic device integration, monolithic dielectric mirrors were fabricated by stacking layers of SURMOF HKUST-1 and indium tin oxide (ITO) on a modified Si-substrate. The highly porous SURMOF layers were deposited again using a versatile LPE method, while the ITO layer was sputter-deposited using magnetron sputtering. The SURMOF-based hybrid photonic band gap (PBG) materials exhibited a high optical quality (reflectivity of 80%) and were color tunable over the whole visible range by varying the layer thicknesses accordingly. The optical sensing capabilities of these PBG materials were demonstrated by investigating the chemo-responsive optical sensing upon exposure to different organic solvents.

Finally, the monolithic Prussian blue (PB) thin films were deposited on a conductive substrate through a layer-by-layer or LPE method, as well as through a spin-coating process. Even after several redox cycles, the high stability and the crystallinity as well as the high orientation remained unchanged, as confirmed by characterization of the SURMOF thin films. The reversible change from a blue colored to a transparent film also demonstrates the potential of these porous materials as components for electrochromic devices.

Zusammenfassung

Kristalline, kontinuierliche sowie monolithische Oberflächen können als Dünnfilme in Form von verankerten metallorganischen Gerüstverbindungen (SURMOF) mit Hilfe des Flüssigphasen-Epitaxie Verfahrens (LPE) hergestellt werden. Die Dicke solcher dünnen SURMOF-Filme kann gezielt mit dem LPE Verfahren eingestellt werden. Die so hergestellten nanoporösen SURMOF Filme wurden für die Herstellung von elektronischen, optoelektronischen sowie photonischen Bauelementen verwendet.

Das Verständnis des elektrischen Transports in SURMOF-Netzwerken ist äußerst wichtig, sowohl aus einer fundamentaler Sicht als auch im Hinblick auf die künftige Entwicklung MOF-basierter Anwendungen. In diesem Zusammenhang wurden eine Reihe von HKUST-1 [$Cu_3(BTC)_2$] SURMOF Filme mit Hilfe der Quecksilbertropfen-basierten Tunnelkontakt Methode untersucht. Die Transporteigenschaften dieser SURMOFs scheinen denen der hybridmetallorganischen molekularen Drähten zu ähneln; was durch einen sehr niedrigen Wert der Tunnel-Abklingkonstante aufgezeigt werden konnte ($\beta \approx 0.006$ $Å^{-1}$). Zusammen mit ihrem Isolationsverhalten konnte weiterhin auch gezeigt werden, dass sie einen konstanten, linearen Anstieg des Widerstands bei zunehmender Filmdicke besitzen. Beim Beladen mit Ferrocen (Fc) in die freien Poren von HKUST-1 wurde eine deutliche Zunahme des Transportstroms gemessen. Ein Transportmodell sowie ab-initio Elektronenstrukturrechnungen wurden verwendet, wobei ein Hopping-Transportmechanismus beschrieben werden kann.

Weiterhin konnten HKUST-1 SURMOFs mit unterschiedlich kristallographischen Wachstumsrichtungen erfolgreich auf modifizierten Goldelektroden mittels der LPE-Methode abgeschieden werden. Anschliessend wurde an den Filmen cyclische Voltametrie (CV) durchgeführt, um das elektrochemische Verhalten dieser SURMOFs in einer aprotischen ionischen Flüssigkeit (ILs) zu untersuchen. Diese Methode erwies sich als äußerst geeignet, um Veränderungen der elektrischen Leitfähigkeit der SURMOFs beim Füllen der MOF Poren z.B. mit kleinen elektroaktiven Molekülen wie Ferrocene zu ermitteln. Außer der Verbesserung der elektrischen Leitfähigkeit von MOFs, wurden unter anderem Photostrommessungen durch Auswahl geeigneter organischer Liganden durchgeführt. Hierbei wurden Porphyrin-Liganden als Elektronen-Donor-Systeme verwendet, um gezielt neuartige SURMOFs herzustellen. Durch die wohldefinierte Stapelung solcher hoch-geordneter photoelektroaktiver Porphyrin-Moleküle auf den

verschiedenen Elektroden konnte bereits erfolgreich ein erstes Photovoltaic (PV) Device dazu entwickelt werden.

Des Weiteren konnten auch erste optische Sensoren aus photonischen Halbleiter-SURMOF Strukturen entwickelt werden. Diese di-elektrischen HKUST-1/ITO Spiegel werden durch Stapeln von LPE gesprühten SURMOF (HKUST-1) Schichten und gesputterten Indiumzinnoxid (ITO) Filmen auf Si-Substrat hergestellt. Diese SURMOF basierenden Hybrid PBG Materialien zeigten eine hohe optische Qualität (Reflektionsvermögen von ca. 80%) und ihre Farbe kann durch die Wahl der Schichtdicke varriert werden. Die PBG Materialien wurden weiterhin als chemo-responsive optische Sensoren verwendet, dabei wurde die Wechselwirkung mit verschiedenen organischen Lösemitteln untersucht.

Zuletzt wurden elektroaktive sowie elektrochrome monolithische Preußisch Blau (PB) Dünnfilme auf leitfähigen TCO Substraten/Elektroden hergestellt. Für die Herstellung wurde die Layer-by-Layer Methode, das LPE Sprühverfahren sowie auch Spin-Coating eingesetzt. Selbst nach mehreren Redox-Zyklen während der electrochromen Schaltvorgängen, blieben sowohl die Kristallinität als auch die Orientierung unverändert erhalten. Die reversible Änderung von einer blauen hin zu einer transparenten Schicht weist auf die potentielle Verwendung von elektochromen und monolitischen PB-Materialien als Komponenten für zukünftige optoelektronische Bauelemente hin.

Table of Contents

1 Introduction

1.1 Metal-organic frameworks (MOFs)

Metal-organic frameworks (MOFs), also known as porous coordination polymers (PCPs), are crystalline three-dimensional (3D) networks with well-defined pores formed through the interconnection of metal ions or clusters by organic ligands (Figure 1.1).[1-5] MOFs have been classified as a relatively new class of coordination materials even though the very first reference about the coordination polymers can be dated back to 1959.[6] In the time after, the research done and reported in this area was rather limited. However since 1991s, more than 20000 MOF structures[2] have been reported and studied,[7] owing a more systematical design and construction approach.

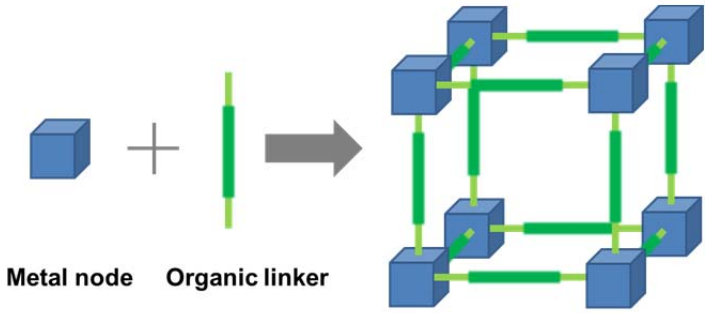

Figure 1.1 Scheme of a typical cubic topology of MOF structure by connecting the metal nodes and organic linkers.

Comparing with common porous materials such as activated carbons and zeolites, MOFs exhibit many characteristic features which also make these materials more and more attractive. These highly ordered frameworks display permanent porosity, and their pore size can be tuned from several angstroms to several nanometers.[8] Their surface area are typically ranging from 1000 to 10000 m^2 g^{-1}, and their density can be as low as 0.13 g cm^{-3}.[2] Their structures and targeted properties can be designed by careful selection of the composing metal centers and different functional linkers, integrating both inorganic and organic properties in one material. These remarkable properties have made MOFs to be largely investigated as potentially suitable host architectures for a variety of different applications, ranging from gas storage,[9, 10] separation,[11, 12] catalysis,[13, 14] sensing[15] and drug delivery,[16] to name a few.

1.1.1 Synthesis of MOFs

1.1.1.1 Methods

Multiple methods have been employed for synthesizing MOFs for the last 2 decades, such as hydrothermal and solvothermal methods,[17-19] ultrasonic methods,[20] microwave synthesis,[21] electrochemical synthesis,[22] mechanochemical synthesis.[23] Among them, the hydrothermal and solvothermal methods are the most commonly used techniques which are characterized by a slow diffusion process. The reactions take place in closed vessels containing the starting materials and solvent under controlled temperature, and occasionally pressure is applied by increasing the temperature above the boiling point of the solvent. The MOFs produced by this method have normally a good thermal stability, since the reactions carried out with conventional heating methods typically last up to several days.[24]

Exploring different synthesis methods is important for producing MOFs for all kinds of applications, because different methods can lead to different structures, particle sizes and morphologies, as well as reaction time, yields, etc.[25]

1.1.1.2 Parameters

MOFs are inorganic-organic hybrid networks made from the inorganic metal ions or clusters and the organic ligands, so their pore geometries and size, as well as functionalities can be tailored depending on the metal centers and different functional linkers used.

The designing of the metal clusters, also called as secondary building units (SBUs) is an important step in MOF synthesis, as the topologies describing the units can be common to several structures.[26] Once the synthesis of the SBUs is formed, the linking geometries are established. This can be used to predict and direct the construction of MOFs in targeting defined topological networks. The organic ligands act as a bridge between SBUs in the networks, and can also be designed for providing further properties like rigidity or other structural features. The construction of MOFs with predetermined structural topologies also results from the orientation and distribution of the chelating groups of the organic linker. Overall, the final topology of MOFs is determined by the combination of both, the inorganic nodes (as connectors) and the organic ligands (as linkers).[27]

Furthermore, the MOF synthesis offers a high degree of flexibility by varying the

inorganic and organic compositions as well as other conditions like the concentration of starting materials, pH value, solvent, temperature, pressure and the reaction time.[25] These conditions can influence the structures, yields, particle sizes and morphologies.

1.1.1.3 Post synthetic modification (PSM)

Post synthetic modification (PSM) is a method for further functionalizing or modifying a framework after its synthesis, and provides additional ways of controlling the structures and properties of MOFs.[28, 29] PSM can modify both the inorganic metal nodes and organic linkers without altering the main structure and overall stability of the frameworks. Due to the possibility of introducing different types of functional groups as well as varying the number of functional groups into the framework, PSM can be advantageous compared to a prefunctionalization approach.[28]

For instances, MOF-5 ($Zn_4O(BDC)_3$, BDC = 1,4-benzenedicarboxylate) crystals can undergo metal center exchange, to produce the Ni-based MOF-5 analogue.[30] The amino groups (-NH_2) on several MOF linkers have been shown to be accessible to further PSM reaction. IRMOF-3 (IR = Iso-reticular) constructed from Zn_4O SBUs and NH_2–BDC (2-amino-1,4-benzenedicarboxylic acid) linkers can be modified with alkyl anhydrides to generate a series of alkyl functionalized MOFs with identical framework structures.[31] Azide-modified dicarboxybenzene ligand on MOFs offers a robust platform for azide-alkyne click PSM reaction.[32]

1.1.1.4 MOF composites

MOF composites composed of MOFs and at least another constituent (including other MOFs) are hybrid materials with properties different from the individual MOF or the other materials.[1] The concept could not only extend the physical and chemical properties of MOFs, but also enhance the overall performance that is not provided by the individual components alone.

Furthermore, weak points in MOF properties such as poor chemical or mechanical stability in humid environment in water could also be overcome. For example, MOF composites have been successfully made with metal nanoparticles/nanorods, oxides, polymers, biomolecules, and so on.[33, 34] Consequently, the remarkable characteristics of the MOF composites resulting from the synergistic combination of different components make them suitable for a wide range of applications. The MOF composites possess also high degree of synthetic flexibility.

1.1.1.5 MOFs representatives

Numerous method and techniques combined with the abundance of available components and the variable process parameters have led to the production of thousands of MOF materials. Some representatives, either well characterized or widely studied because of their specific properties, are depicted in Figure 1.2.

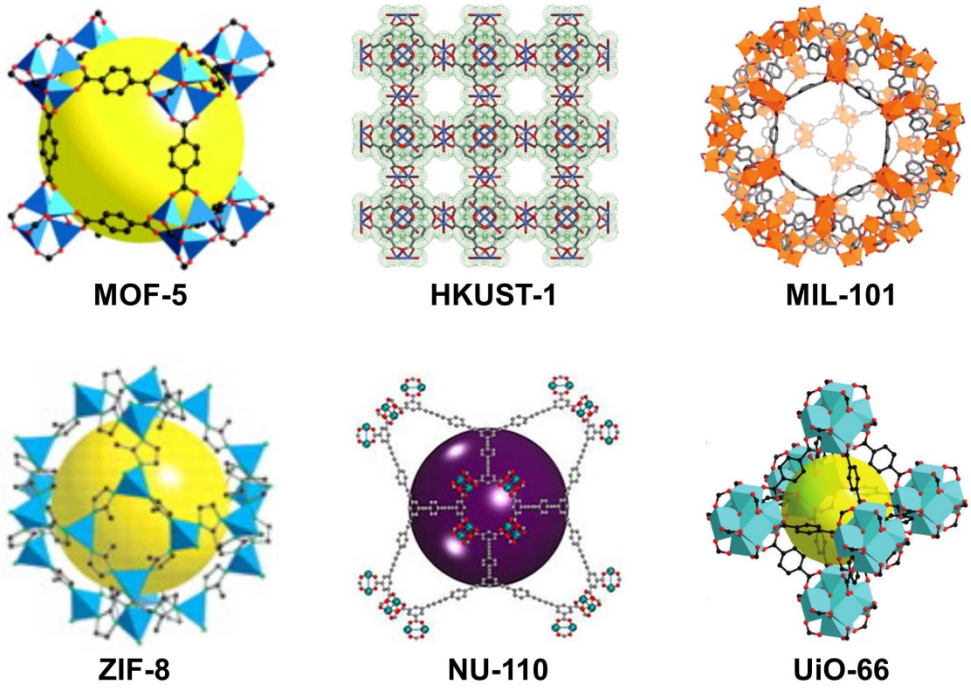

Figure 1.2 Representative MOFs. (Taken from references[14, 35-38] [27])

MOF-5 ($Zn_4O(BDC)_3$, BDC = 1,4-benzenedicarboxylate) was first synthesized and characterized in 1999 by Yaghi et al. It has a high porosity and shows remarkable gas sorption properties at low pressure.[39] Later, an isoreticular series (same framework topology) of MOF-5 structures were synthesized by designing organic linkers of different size, and thus realizing a simple design strategy for controlling the pore dimensions.[35] HKUST-1 (HKUST = Hong Kong University of Science and Technology) was firstly synthesized in 1999 by Williams et al.[36] Numerous research works have been done on this MOF because it is easily synthesized with high yields and the structure is highly stable against high temperature and further chemical modifications. In 2005, MIL-101 (MIL = Matérial Institut Lavoisier) having a high chemical stability was reported by Férey et al.[40] Then series of MIL-53 were synthesized as flexible nanoporous materials for the adsorption and in vitro drug delivery.[41] ZIFs (ZIF = zeolitic imidazolate framework),

especially ZIF-8, have attracted much attention because of their great chemical and thermal stability.[37] NU-110 (NU = Northwestern University) has the highest surface area and pore volume reported yet, and shows great hydrogen uptake property.[38] UiO-66 (UiO = Universitetet i Oslo) has also a good hydrothermal stability and can undergo a large number of functionalization by PSM.[42]

1.1.2 Properties and applications of MOFs

The physical and chemical properties arising from the metal components, organic linkers, and their combination give various MOF structures, a high porosity (greater than 50%), various pore sizes and shapes (several angstroms to several nanometers with various geometry), a high surface area (from 1000 to 10000 $m^2\ g^{-1}$), a consequent pore volume (up to 4.4 $m^3\ g^{-1}$), a significant thermal stability (typically exceeding 200 °C).[2] These specific properties have led to the development of different applications, with some of the most significant (gas storage and separation, catalysis, sensing and drug delivery) described in the following.

1.1.2.1 Gas storage and separation

One of the most widely investigated properties of MOFs is gas adsorption or capture because of the high storage capacity. Particularly, fuel gases storage such as hydrogen and methane, but also carbon dioxide capture have been receiving much attention. The hydrogen adsorption capacity of MOFs relies mainly on the surface area and pore volume,[43] but can also be optimized by the inclusion of open metal sites and lighter metals.[44] Gas separation capacity of MOFs generally depends on both the pore size and the affinity of MOFs to the targeted gases.[2]

MOF UTSA-76a has been reported to have high methane uptake capacity whit ~260 $cm^3\ cm^{-3}$, and a record high methane storage working capacity of ~200 $cm^3\ cm^{-3}$ (between 5–65 bar). The origin of such high working capacity is attributed to the active pyrimidine groups of the linkers.[45] MOF-210 has reported to have the very highest BET (Brunauer-Emmett-Teller) surface areas with 6240 $m^3\ g^{-1}$, and its carbon dioxide storage capacity is 2870 mg g^{-1}.[46]

The multivariate MOFs (MTV-MOFs) have been synthesized by a complex arrangements of several functional groups within the pores. Instead of forming separate domains during the synthesis, MTV-MOFs incorporate the different functionalities by specifically mixing

the linkers. As shown in Figure 1.3, various MTV-MOF-5 type structures have been constructed from BDC (1,4-benzenedicarboxylate acid) and its derivatives -NH_2, -Br, -$(Cl)_2$, -NO_2, -$(CH_3)_2$, -C_4H_4, -$(OC_3H_5)_2$, and -$(OC_7H_7)_2$ and contain up to eight distinct functionalities in one phase. The properties of MTV-MOFs are not simply the linear sum of its individual components. For instances, MTV-MOF-5-EHI (a member of MTV-MOF-5 series) exhibits up to a 400% better selectivity for carbon dioxide over carbon monoxide compared to its single linker MOFs materials.[47]

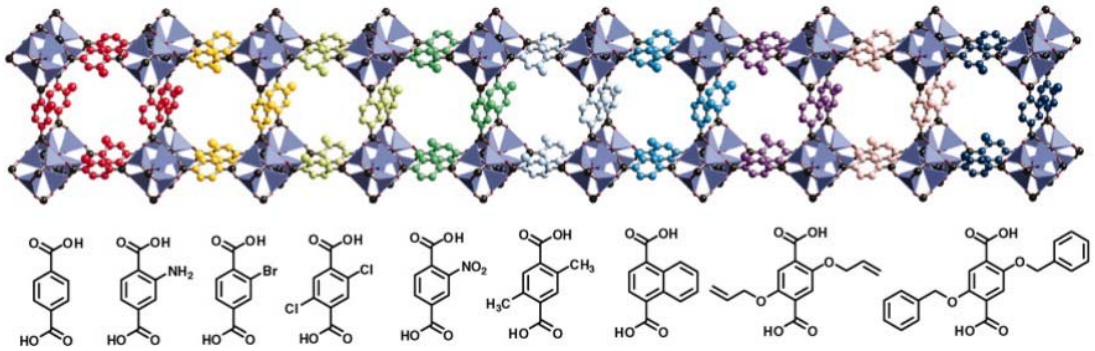

Figure 1.3 MOF materials that combine sets of different links with different functional groups (upside); molecular structures of the different linkers: from left to right, BDC (1,4-benzenedicarboxylate acid), NH_2-BDC, Br-BDC, $(Cl)_2$-BDC, NO_2-BDC, $(CH_3)_2$-BDC, C_4H_4-BDC, $(OC_3H_5)_2$-BDC, and $(OC_7H_7)_2$-BDC links (downside). (Taken from ref.[47])

1.1.2.2 Catalysis

MOFs can be turned into catalyst matrix through different approaches: either directly through synthesizing the MOFs with active building blocks, metal nodes or specifically designed complex organic linker, or directly, by having the catalyst species loaded within the pores or grafted on the organic ligand or SBU by PSM.[13, 14] Figure 1.4 presents two cases of MOF-based catalytic reactions strategies from metal nodes and from functionalized linkers, respectively.

The first example of catalysis in MOFs was reported by Fujita et al. in 1994 on the cyanosilylation of aldehydes in Cd-based MOF, $Cd(4,4'\text{-bpy})_2(NO_3)_2$ (bpy = bipyridine). The reaction of benzaldehyde and cyanotrimethylsilane successfully gives 2-(trimethylsiloxy)phenylacetonitrile with a yield of 77% and a shape selectivity of the catalysis reaction is observed.[48]

HKUST-1, $Cu_3(BTC)_2$ (BTC = 1,3,5-benzene tricarboxylate), based catalysis reaction was reported on the metal sites. By activation (removal of solvent from the pores), the open metal sites are exposed and can act as Lewis acid catalysts.[49]

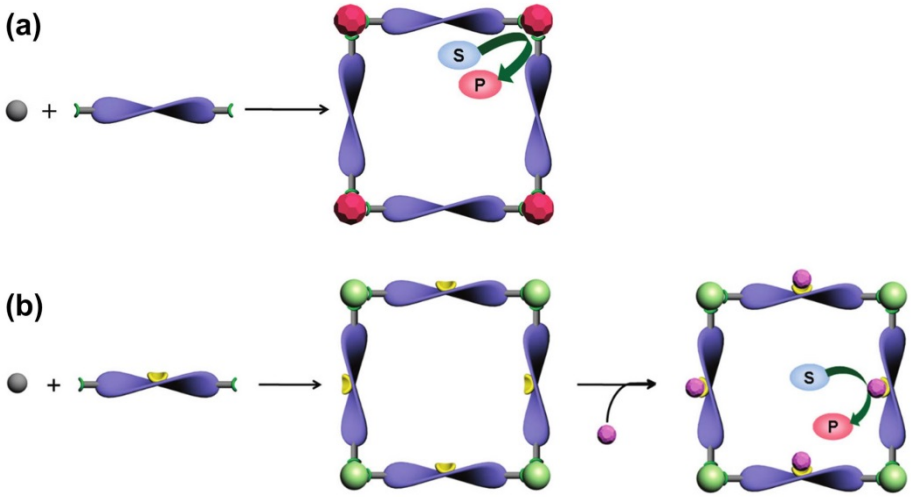

Figure 1.4 Representative strategies to construct of MOF-based catalysts; (a) a synthetic strategy for MOF-based metal node catalysts, (b) a synthetic strategy for PSM of the MOF linker to give a catalytically active center. (Taken from ref.[13])

Chiral MOFs, $LCu_2(solvent)_2$ (L is a chiral tetracarboxylate ligand derived from 1,1′-bi-2-naphthol), have been constructed and give the same structures but different open channel sizes. They provide an ideal platform for generating heterogeneous catalysts by postsynthetic grafting of the Ti(IV) complex onto the chiral dihydroxy groups. The resulting materials has proven to be highly active asymmetric catalysts for converting aromatic aldehydes into chiral secondary alcohols.[50]

By taking advantage of the porosity properties of MOFs, guest species can be loaded within the pores. The palladium loaded MOF-5 has been shown to have a high catalytic activity during the selective hydrogenation of styrene to ethyl benzene.[51]

1.1.2.3 Sensing

The highly porous structures and well-defined pores and channels in MOFs also provide an adequate matrix for accommodating analyte molecules, and at the same time, supporting specific recognition and selective sensing process.[52] Typically, monitoring changes in the electrical, photophysical, or mechanical behaviors of the MOFs material can translate into measuring a sensed signal.[15]

The most widely explored type of MOF sensor to date is based on luminescent frameworks. The luminescence based sensing has been applied to various fields and use the MOFs emission properties for the detection of small molecules, volatile organic compounds, ionic species, as well as explosives and explosive-like molecules or even temperature changes (fluorescent thermometers), and also for biosensing and imaging.[53]

For example, $[(WS_4Cu_4)I_2(dptz)_3]$ (dptz = 3,6-di-(pyridin-4-yl)-1,2,4,5-tetrazine) MOF has been synthesized and shown to have a solvatochromic behavior: a large shift in the absorption spectrum in response to a change in absorbing solvent can be observed (Figure 1.5). The material shows a negative solvatochromic effect with increasing solvent polarity (blue shift of the absorption band). [54]

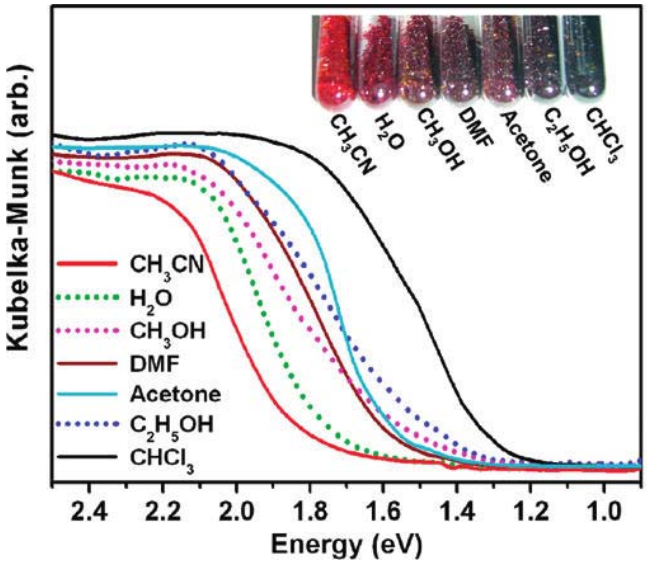

Figure 1.5 Visible spectra and photograph of MOF crystals containing solvents as condensed vapors. A negative vapochromic effect is observed for both hydroxylic and nonhydroxylic solvent vapors. (Taken from ref.[54])

1.1.2.4 Drug delivery

Owing the tunability of the structure and porosity toward enhanced drug interaction and loading, but also their biocompatibility and bioelimination features, MOFs are well suited to serve as carriers for drug delivery and imaging. They can absorb and release large amounts of therapeutics as tested with ibuprofen, nitric oxide, and procainamide.[55] Scale-down MOF particles to the nanometer range could make them nanocarriers of high efficiency.[56]

Designing longer organic linkers for MOF synthesis could provide larger pores, to offer a larger storage space and a greater number of adsorption sites in MOFs. The IRMOF-74-I to IRMOF-74-XI are a series of isoreticular series of MOF-74 structures with pore apertures ranging from 14 to 98 angstroms (the biggest pore so far), as presented in Figure 1.6. The permanent porosity and high thermal stability (up to 300 °C) make these MOFs excellent candidates for applications in gas adsorption, catalysis as well as delivery. It was found that activated IRMOF-74-IV is able to take up vitamin B12, and an oligoethylene glycol-functionalized IRMOF-74-VII and IRMOF-74-IX can let natural proteins pass through them.[8]

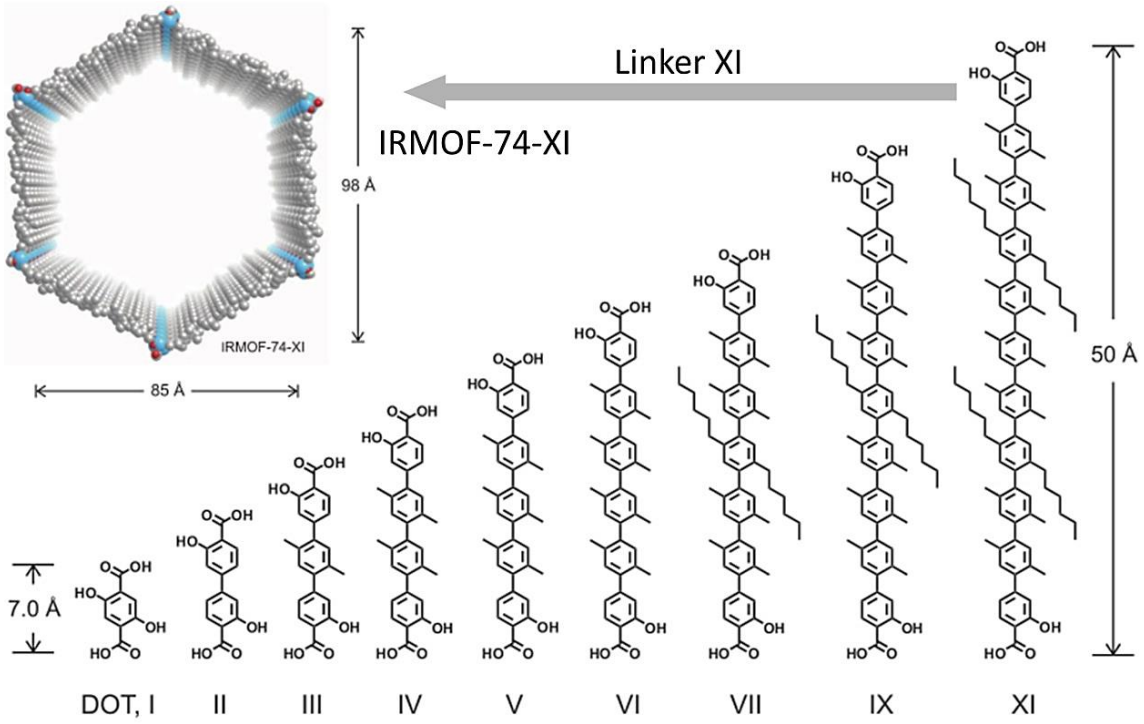

Figure 1.6 Chemical structures of the organic linkers used for synthesizing the series of IRMOF-74, and the perspective views (left top) of a single one-dimensional channel with pore aperture of 98 Å for IRMOF-74-XI (from linker XI). (Taken from ref.[8])

Flexible nanoporous MIL-53, $[M^{III}(OH)(BDC)_x]$ (M^{III} = Al, Cr, Fe, BDC = 1,4-benzenedicarboxylate), have been used as controlled delivery systems because of the breathing phenomenon of the structure. Figure 1.7 depicts the effect with the drug adsorption and delivery of Ibuprofen (*α*-*p*-isobutylphenyl-propionic acid) by MIL-53(Cr) MOFs, and the process can be controlled by changing of the temperature.[41]

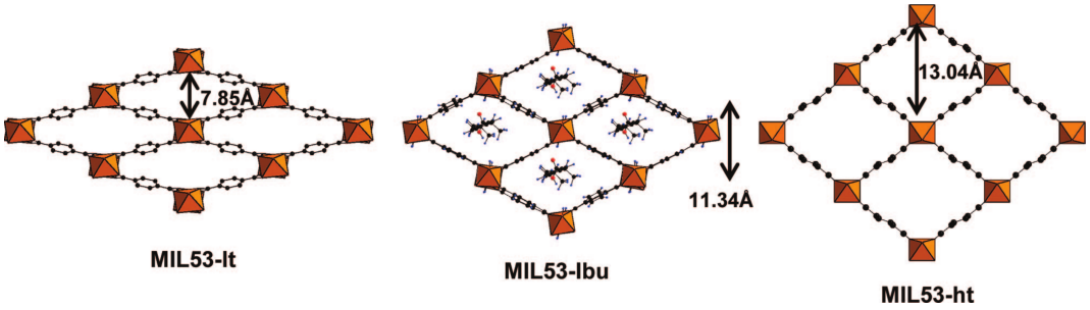

Figure 1.7 Schematic representation of the breathing effect of the MIL-53(Cr) upon dehydration-hydration; the three states are MIL53-lt (lt = low temperature), MIL53-Ibu (Ibu represents the adsorption of Ibuprofen), MIL53-ht (ht = high temperature). (Taken from ref.[41])

1.2 Preparation of MOF thin films and their device applications

Compared to the conventional solvothermal process yielding MOF powders,[57] the preparation or processing of MOF films, membranes, or composites are getting more and more critical when considering implementation in devices for sensing, electronics, energy production, or optical applications.[33, 58, 59]

Numerous methods have been developed for processing MOFs as thin films. One of the main strategies for producing MOF film is based on the MOF powder synthesis by a solvothermal method. The MOF films are prepared either during the reaction or after the synthesis by processing the MOF powder. These methods include direct solvothermal deposition,[60] solvothermal mother solution method[61] and spin-coating method.[62] There are also other distinctive methods such as gel-layer synthesis,[63] electrochemical deposition,[64] Langmuir-Blodgett (LB)[65] and Liquid phase epitaxy (LPE) method.[66] The differences between these various methods for the film preparation originate not only from the type of substrate used, but also from the properties of the depositing procedure and the related applications.[67] Some of the typical methods for preparation of MOF films as well as the characteristic MOF device application are introduced in the following.

1.2.1 Direct solvothermal deposition

The direct solvothermal deposition method provides a facile way for the fabrication of strongly adhering, homogeneous, and crystalline MOF films.[68, 69] With this method, the MOF films are deposited during solvothermal process by inserting the desired substrates

into the precursor solution. The substrates need to be functionalized prior use. The nature of the substrate surface, especially its acid/base properties, has little influence on whether or not a film can grow, or on the morphology and overall quality of the MOF films.[70]

ZIF-8 films grown on glass or silicon substrate have been prepared by a solvothermal deposition method and have been investigated as selective sensors for chemical vapors and gases.[71] Various thicknesses of ZIF-8 thin films can appear different colors as shown in Figure 1.8(a). When the ZIF-8 film is exposed to vapors of propane with various concentrations, UV-vis transmission spectra show a red shifts of the interference peaks (Figure 1.8(b)). Using the same method, the ZIF-8 based sensor has been responsive to ethanol vapor but not to water (Figure 1.8(c)).

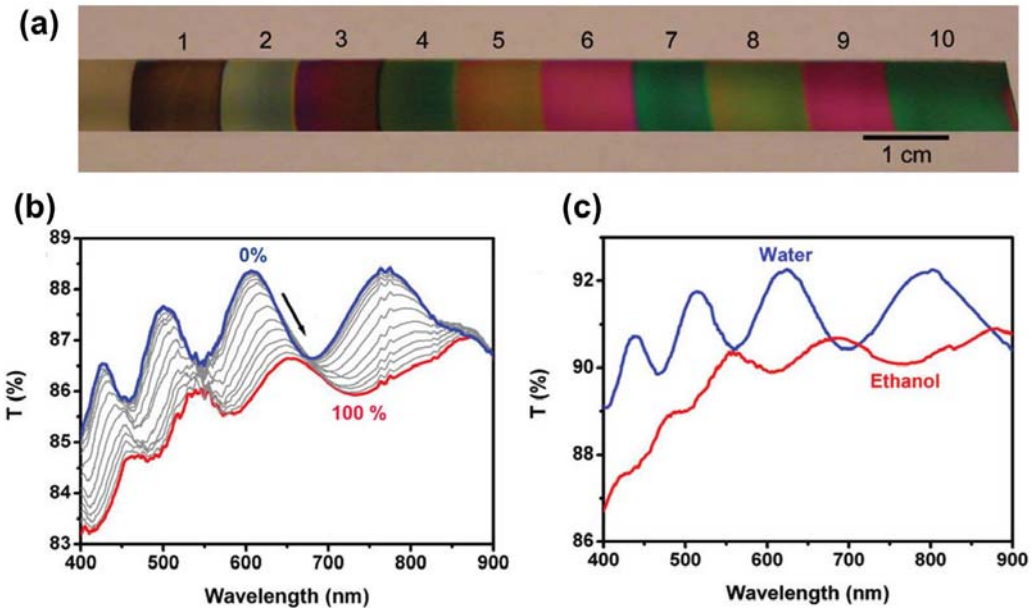

Figure 1.8 (a) Photograph of a series of ZIF-8 films grown to various thicknesses on silicon substrates; UV-vis transmission spectra of a 10 cycles ZIF-8 film on glass substrate after exposure to vapors of (b) propane at various concentrations (from 0% (blue) to 100% (red)), and (c) ethanol (red) or water (blue). (Taken from ref.[71])

A series of pyrazolate MOFs containing redox-active naphthalene diimide (NDI) linkers, Zn(NDI-X) (X = H, NHEt, and SEt), have been produced on substrates by solvothermal deposition method, as shown in Figure 1.9. These MOF thin films deposited on FTO substrates exhibit a reversible redox behavior. The fast and reversible color switching makes these MOFs adequate for implementation in electrochromic window devices.[68]

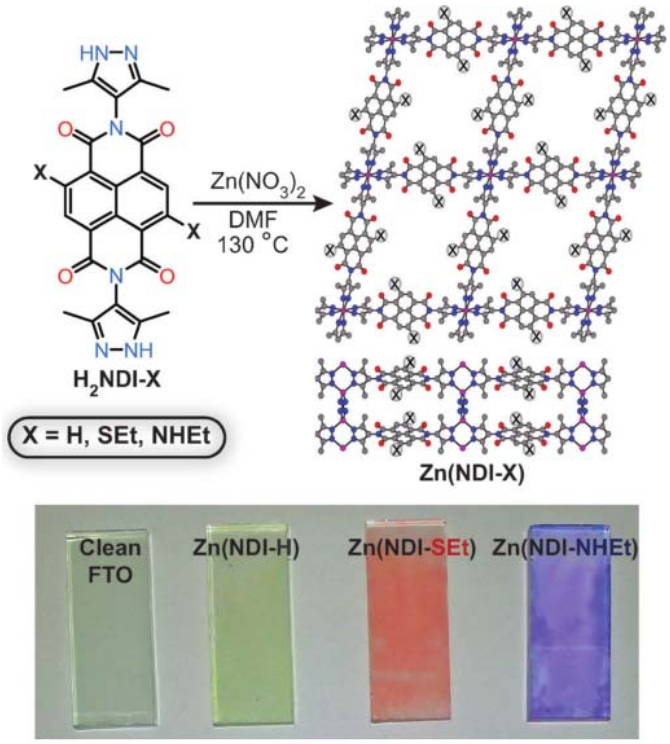

Figure 1.9 Synthesis of Zn(NDI-X) (X=H, NHEt, and SEt) MOF and the simulated structure (top); optical images of the macroscopic films of the series of Zn(NDI-X) MOF on FTO (fluorine-doped tin oxide) substrates. (Taken from ref.[68])

Furthermore, a free standing MIL-53 membrane has been formed under mild hydrothermal condition by sacrificing AAO (anodized aluminum oxide) membrane to coordinate with H_2BDC (BDC = 1,4-benzenedicarboxylate acid). The thickness of the membrane is equivalent with that of the AAO film. The free standing MIL-53 membrane has shown good mechanical strength and specific properties for gas separation. The free standing MOF membranes could have more important applications since they are not bound to any substrates.[72]

1.2.2 Solvothermal mother solution method

The solvothermal mother solution method is based on the solvothermal MOF synthesis process. First, MOF powders have to be synthesized by solvothermal method. Then, by filtering off the large crystals from the reaction mixture, the fresh mother solution is obtained. Finally, the MOF films are constructed by depositing the MOF crystals through incubating the functionalized substrates in the mother solution for different periods of time.[61, 73]

Continuous MOF-5 ($Zn_4O(BDC)_3$, BDC = 1,4-benzenedicarboxylate) thin films have been synthesized by the solvothermal mother solution method on a glassy carbon electrode (GCE) with 4-carboxyphenyl as a covalent linker. As shown in Figure 1.10, the MOF-5 thin films on GCE substrates have been used as a photoelectrochemical sensor for the detection of ascorbic acid.[74]

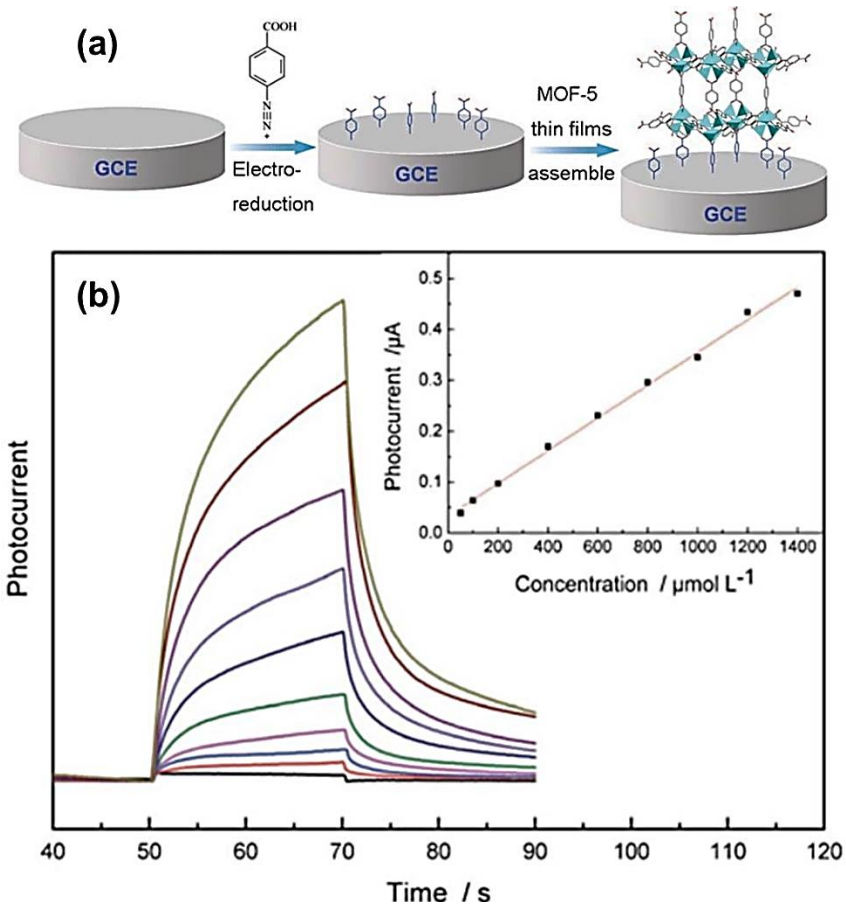

Figure 1.10 (a) Schematic illustration of the MOF-5 film fabricated on a GCE. (b) Photocurrent responses of the MOF-5 film at 0 V to a light excitation, (inset: linear curve); 0.1 M NBu_4ClO_4 in acetonitrile, with the presence of 0, 50, 100, 200, 400, 600, 800, 1000, 1200, and 1400 μmol L^{-1} ascorbic acid (from bottom to top), was used as electrolyte. (Taken from ref.[74])

1.2.3 Spin-coating method

Spin coating is widely used to produce a layer or film to a base material because it is a very fast process and extremely homogenous and thin films can be obtained. The thickness of the films can be controlled by varying the coating cycles, the substrate rotation speed

and the concentration of the deposited solid in the precursor suspensions.[75] One disadvantage of this method is that the prepared films are not strongly bound to the substrate.

A MOF film by spin-coating method results from the deposition of the MOF powder particles, synthesized by solvothermal method, onto the desired substrate from the precursor solution.[62] Many MOF thin films have been prepared by this method to be used in device applications.

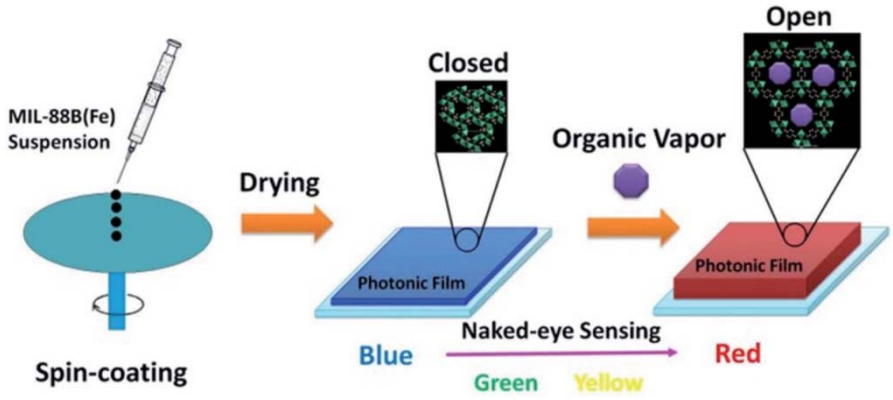

Figure 1.11 Schematic illustration of the fabrication of NH_2-MIL-88B MOF photonic films and the process for sensing organic vapors. (Taken from ref.[75])

A series of photonic MOF films of Fe-MIL-88B-NH_2, ($Fe_3O(H_2N\text{-}BDC)_3$, H_2N-BDC = 2-amino-1,4-benzenedicarboxylic) have been fabricated by spin-coating, as illustrated in Figure 1.11. The produced films show substantial optical responses to exposure to the vapors of various organic solvents. The specific response of the MOF can be observed with naked eyes.[75]

1.2.4 Gel-layer synthesis

Gel-layer method, a more recently developed approach, enables the synthesis of different oriented MOF thin films on functionalized gold surface at room temperature, as shown in Figure 1.12.[63] The first step with this method is the deposition of a poly-(ethyleneoxide) (PEO) gel layer onto a self-assembled monolayer (SAM) coated gold surface. This layer is used for storing one reactant of the MOF synthesis (e.g. by loading with the MOF metal-ion precursor). The gel layer is then immersed into a solution of the other reactant (e.g. a linker solution). This allows the linker to slowly diffuse into the gel layer. The

MOF nucleation is directed at the interface with the substrate. The gel-layer method is promising for applications of functional MOF thin films with controlled orientations.

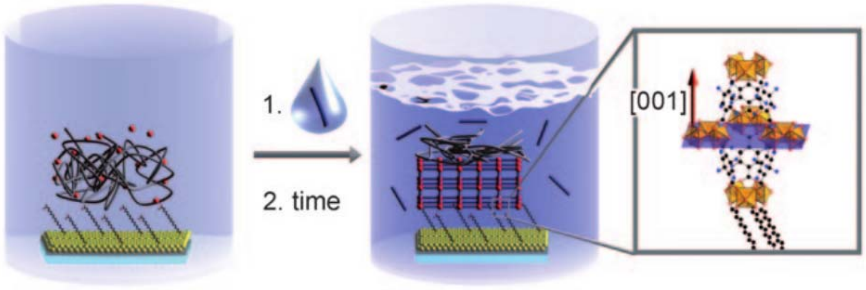

Figure 1.12 Representation of the gel-layer approach for fabrication of uniquely oriented nanoscale MOF films. A SAM functionalized Au substrate is loaded with the poly(ethylene glycol) gel layer containing metal salt (metal ions in red) and covered with a solution containing the linker molecules (blue). (Taken from ref.[63])

1.2.5 Electrochemical deposition

Electrochemical deposition is an effective and versatile method for growing uniform MOF thin films on conductive substrate surfaces.[22, 76] The electrochemical deposition of MOF film has been introduced by researchers at BASF.[64] HKUST-1 films on copper electrode were produced by applying an anodic voltage in a linker solution of BTC (1,3,5-benzene tricarboxylate).

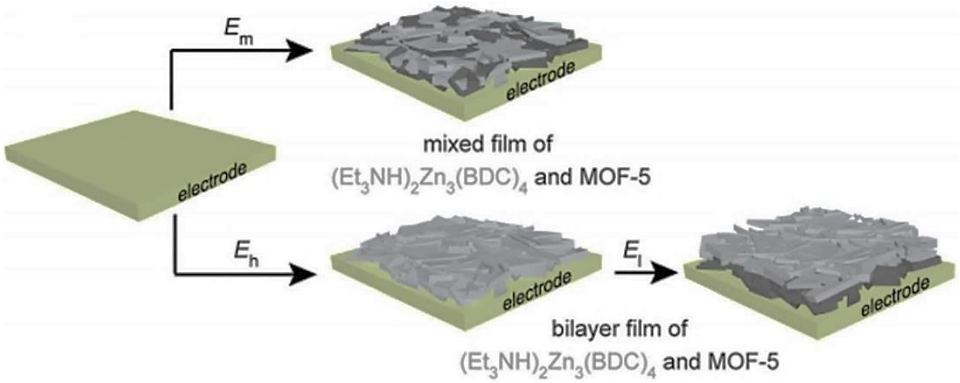

Figure 1.13 Schematic illustration of the preparation of a biphasic MOF thin films (mixed film) at cathodic potential, E_l ($E_l < E_m < E_h$). (Taken from ref.[77])

Biphasic MOF thin films, $(Et_3NH)_2Zn_3(BDC)_4$ and $(Zn_4O(BDC)_3$ (the latter is also know as MOF-5, BDC = 1,4-benzenedicarboxylate), have been formed on an electrode by

cathodic electrodeposition at room temperature (Figure 1.13). The deposited MOFs can be either the mixed film or the bilayer film of the two materials owning to the applied potential. This method for MOFs synthesis enable the direct surface functionalization of conductive substrate.[77]

Electrophoretic deposition is another well-established technique for thin films fabrication based on electrochemical techniques, especially used for depositing charged nanoparticles onto a conductive substrate.[78]

Figure 1.14 shows the scheme of the electrophoretic deposition process of MOFs film. For this method, the charged MOF particles are first synthesized. A direct current (DC) electric field is then applied on the electrode in a suspension of the charged MOF particles in a nonpolar solvent. This results in the deposition of a MOF film. The fabrication of patterned MOF film is obtained by creating patterned structures of photoresist using photolithography: the MOF films are deposited on the exposed conductive areas using the electrophoretic deposition method (Figure 1.14(b)).[78]

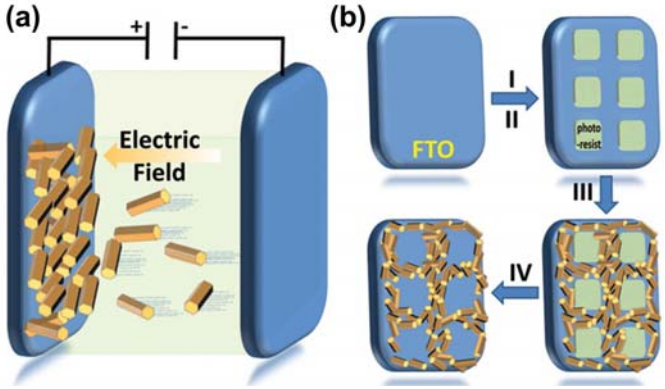

Figure 1.14 (a) Schematic illustration of the electrophoretic deposition method for MOFs film growth; the charged MOF particles are attracted to the oppositely charged electrode by applying an electric field. (b) Schematic illustration the procedures for the patterning of MOF film by electrophoretic deposition. (Taken from ref.[78])

By using the electrophoretic deposition method, several representative MOFs (such as NU-1000,[79] UiO-66,[80] HKUST-1[36] and MIL-53[81]) films have been deposited on conductive substrates, and the patterned MOF structures have also been successfully grown on electrodes. The deposited NU-1000 films thus obtained show a reversible redox behavior thanks to its pyrene based linkers.[78]

1.2.6 Langmuir-Blodgett (LB) method

The Langmuir-Blodgett (LB) method for the fabrication of MOF thin film was developed by H. Kitagawa and co-workers.[65] It is a facile bottom-up method for the deposition of a perfect and preferentially oriented MOF nanofilm on a solid surface at ambient temperature. The NAFS-1 MOF, CoTCPP-py-Cu, thin film (CoTCPP stands for 5,10,15,20-tetrakis(4-carboxyphenyl)porphyrinato-cobalt(II)) depicted in Figure 1.15, have been deposited with the individual sheets being highly ordered. The thin layers are integrated one after another by a horizontal dipping process onto the substrate with intermediate rinsing. The dipping and rinsing repetition leads to the sequential layer-by-layer growth of NAFS-1 with any desired thickness.[65]

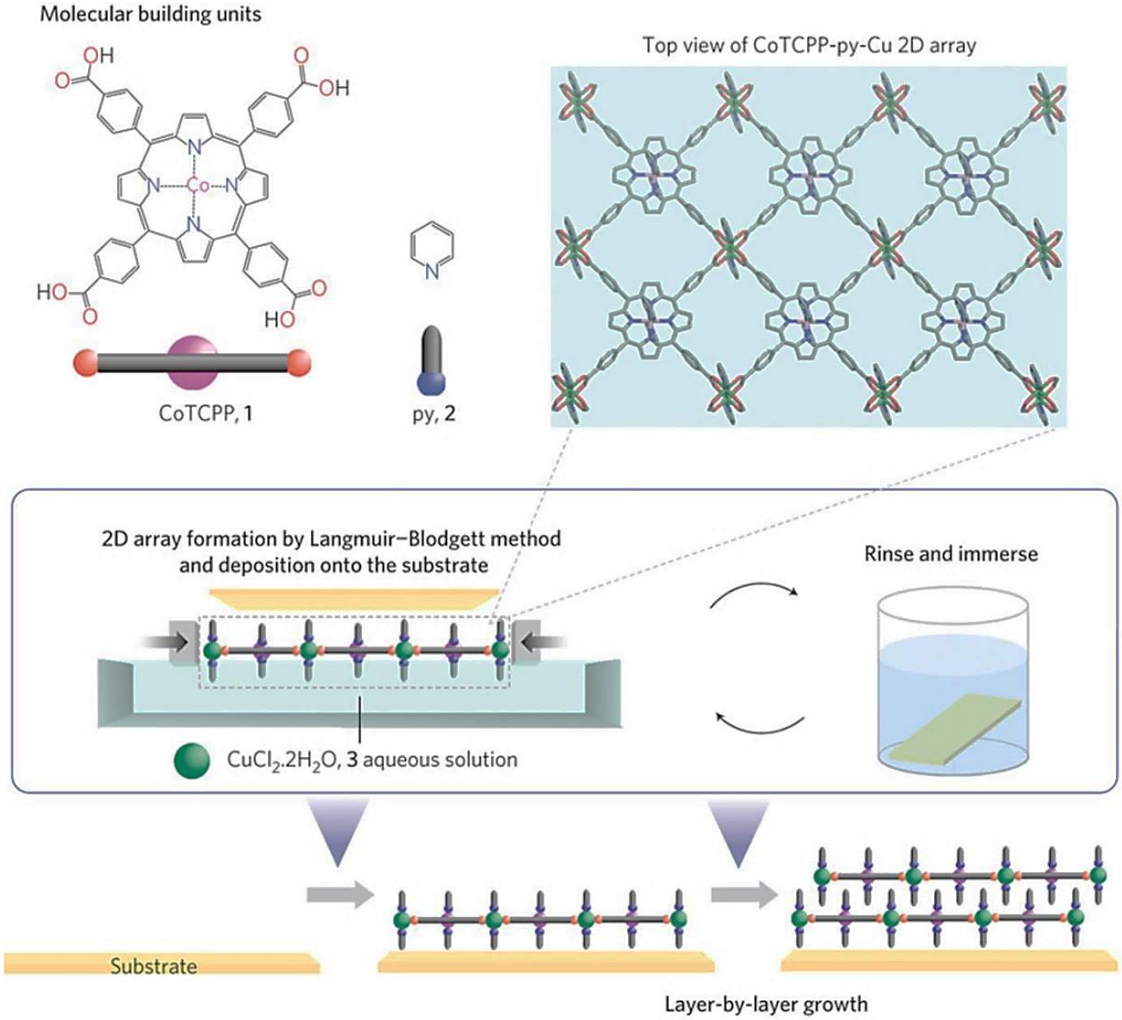

Figure 1.15 Top: molecular structure of the precursors (CoTCPP, 1; py, 2), (where TCPP = 5,10,15,20-tetrakis(4-carboxyphenyl)porphyrin, py = pyridine), and the 2D array of the CoTCPP-py-Cu (NAFS-1) MOF. Bottom: Schematic illustration of the Langmuir-Blodgett method for the fabrication of NAFS-1 MOF thin film. (Taken from ref.[65])

1.2.7 Liquid phase epitaxy (LPE) method

Liquid-phase epitaxy (LPE) method relies on the stepwise, layer-by-layer adsorption of coordinating metal ions and organic ligands from the liquid phase on well-defined substrates.[82] As schematized in Figure 1.16, a functionalized substrate is immersed according a sequential and stepwise procedure into the distinct solutions of metal precursor and organic ligand. The immersions are alternated with rinsing step with solvent to remove excess reactants.

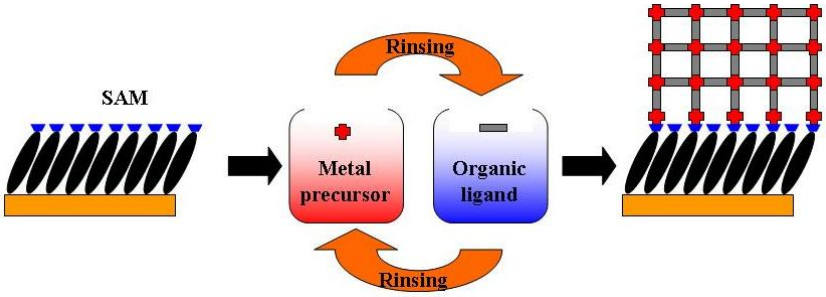

Figure 1.16 Schematic illustration of the layer-by-layer approach for the growth of MOFs thin film on SAM functionalized substrates. The method is conducted by repeating the immersion of the substrate into the distinct solutions of metal precursor and organic ligand. (Taken from ref.[83])

Shekhah *et al*.[66] have first prepared such MOF thin film on SAM coated Au surface. The produced HKUST-1 films have been shown to be highly crystalline and to have a well controlled orientation.

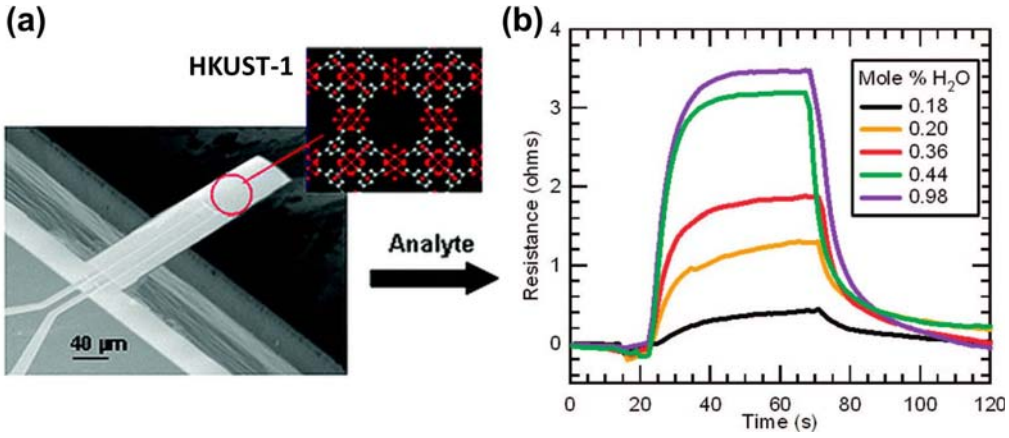

Figure 1.17 (a) HKUST-1 MOF thin film deposited on microcantilever. (b) Temporal response of the microcantilever piezoresistive sensor to different concentration of water vapor diluted in N_2, the concentration of water was increased from bottom (black line) to top (violet). (Taken from ref.[84])

In an application study, HKUST-1 thin films have deposited on a microcantilever surface by the LPE method, and the stress-induced chemical recognition has been detected for a variety of gases (Figure 1.17). It has been found that the energy of molecular adsorption within the nanoporous of HKUST-1 can be efficiently converted to mechanical energy demonstrating the system to be a highly responsive, reversible, and selective sensor.[84]

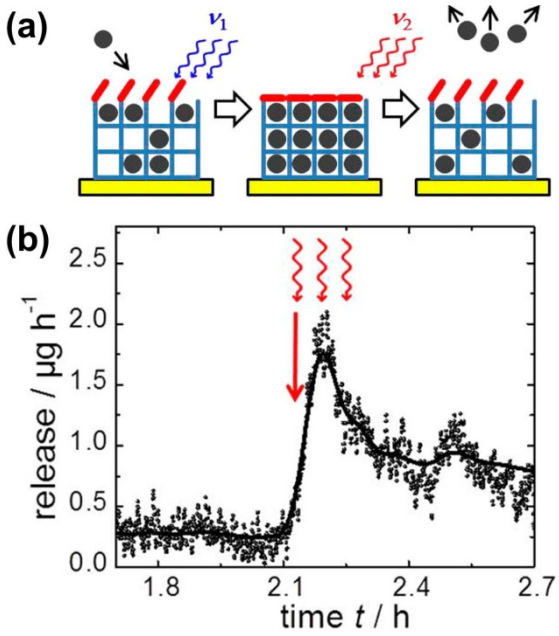

Figure 1.18 (a) Scheme of the optically triggered release of guest molecules from two-component MOF thin films. (b) Triggered release of the guest molecule (butanediol) from the photoswitchable MOF thin film determined by quartz crystal microbalance. The red arrow indicates beginning of the release by irradiating with light at 560 nm. (Taken from ref.[85])

A two-component MOF film has been synthesized on solid surfaces by LPE method. As shown in Figure 1.18, the bottom layer, $Cu_2(BPDC)_2(BiPy)$ MOF (BPDC = biphenyl-4,40-dicarboxylic acid; BiPy = 4,40-bipyridine) can be grown on substrate to serve as a reservoir, and another layer, $Cu_2(AB\text{-}BPDC)_2(BiPy)$ MOF (AB-BPDC = 2-azobenzene 4,40-biphenyldicarboxylic acid), can be grown atop to serve as a valve which can be, at wish, opened or closed. This "MOF-on-MOF" system permits an optically triggered release of guest molecules. By irradiating at a specific wavelength, the photoswitchable linkers of the outer layer are switched between a *trans* or *cis* conformation state. This either obstructs or clears the outer layer pores and the loaded guest molecules can be released through this optically controlled process.[85]

1.3 Surface-anchored metal-organic frameworks (SURMOFs)

Surface-anchored metal-organic frameworks, SURMOFs, refer to these homogenous and perfectly oriented MOF thin films prepared by the stepwise LPE method.[67, 82] The SURMOF thickness is normally in the nanometer range (but can also be in micrometer range with a larger number of deposition cycles), and their growth orientation can be controlled by suitably functionalizing the substrate surface.

Self-assembled monolayers (SAMs) are the most favored choice for the surface functionalization in SURMOFs preparation processes because of their long-range two-dimensional (2D) order, various accessible functional end groups, practical processing, and the available methods for selective surface patterning (e.g. by microcontact printing or photolithography).

Different LPE based techniques have been developed to achieve homogeneous SURMOF thin films provide a true control over their thickness and growth direction. Up to now, four types of the distinctive LPE methods have been described. Those includes the dipping method,[66] the spraying method,[86] the pump method,[87] and the quartz crystal microbalance (QCM) method.[88, 89]

1.3.1 Dipping method

As mentioned in the previous section (section 1.2.7), the first LPE deposited MOF thin film has been HKUST-1 material and has been obtained by the dipping method.[66] For this method, four different containers are usually required for: (I) a metal source solution, (II) a rinsing solution after metal solution application, (III) an organic ligand solution, and (IV) a rising solution after ligand exposure. A functionalized substrate is immersed into each container sequentially (from I to IV). The incubation time in metal precursor and organic ligand solutions can span several to tens of minutes, and each rinsing step less than ten seconds, so each deposition cycle requires approximately 0.5–1.5 hours. The final film thickness is well controlled by the number of cycle repetition applied. The prepared SURMOFs are usually highly crystalline and have a well controlled orientation and film thickness. However, the process is rather labor intensive and time consuming.

Recently, an automatization of dipping method using a robotic system has been developed.[90] The system is an automated and computer controlled robot which performs the dipping process and has proven reliable for SURMOF production.

1.3.2 Spraying method

The spraying method is more recent LPE method based on a layer-by-layer fabrication process, and is applied for the production of monolithic, oriented, and crystalline SURMOF films on solid substrates.[86] There are also four steps for each deposition cycle. First, the metal solution is sprayed on the substrate (step 1), then the rinsing solvent is applied (step 2), followed by the ligand solution (step 3) and again the rinsing solvent (step 4). The number of spraying cycles determines the final thickness of the constructed SURMOF thin film.

The spraying method allows SURMOFs to be grown as a faster pace than with the dipping process, and the thickness of SURMOF films obtained can easily reach the micrometer range. The spraying process is also completely automated by computer control, as depicted in Figure 1.19. This high-throughput technique allows preparing SURMOF films with a thickness of 1 µm within a few hours only.

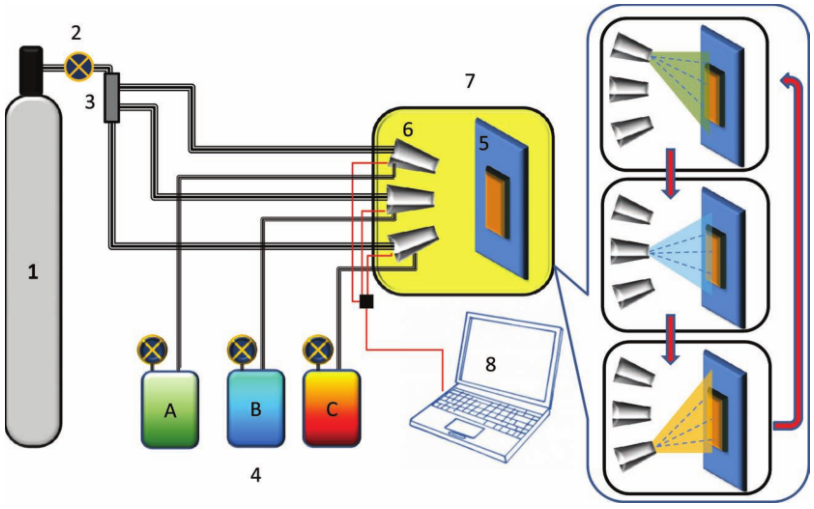

Figure 1.19 Scheme of the spraying method for SURMOF fabrication; (1) Gas supply, (2) gas flow controller, (3) three-way valve gas distributor, (4) solutions storage containers (A, B, C represent the different solution), (5) sample holder and the sample, (6) dosing valves, (7) spray chamber, (8) PC. (Taken from ref.[86])

1.3.3 Pump method

The pump method is also a program controlled system with extra functionalities to control the temperature in the range of -20–100 °C (20–100 °C when using ethanol as a solvent).[87] The pump method for SURMOF fabrication is schematized in Figure 1.20.

For this method, the solution of metal precursor, rinsing solvent, organic ligand, and again rinsing are sequentially pumped into the sample cell. The SURMOF fabrication results by repeating the immersion cycles. Long incubation times are also required for the pump method; this method is then normally used to prepare comparatively thinner SURMOF films (less than 100 nm).

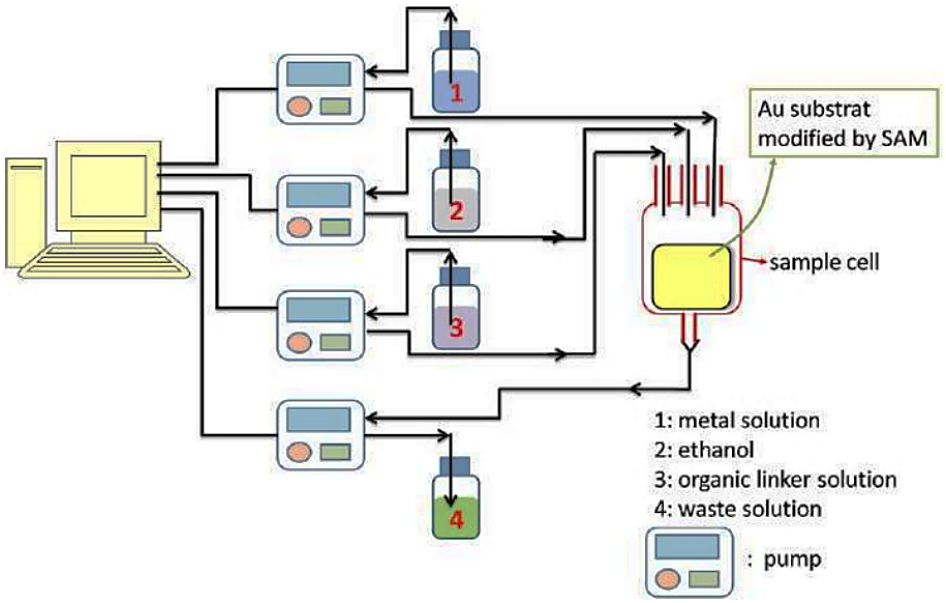

Figure 1.20 Scheme of the pump method for SURMOF fabrication. The solutions are sequentially pumped into the substrate containing cell. The solutions are a metal precursor and an organic ligand solutions and a rinsing solvent (e.g. ethanol) for intermediate rinsing. The fabrication is done by repeating these immersion cycles. (Taken from ref.[87])

1.3.4 Quartz crystal microbalance (QCM) method

Quartz crystal microbalance (QCM) is an extremely sensitive mass variation detector (with ng sensitivity) and has been used to analyze mass changes or thickness of thin films on rigid surfaces under vacuum, gaseous, or liquid environment.[91] QCM system based method for the preparation of SURMOF film is an automated real-time deposition process monitoring based on the layer-by-layer growth.[89] The technique with the film deposition on the quartz sensor (growth on a surface in terms of adsorption) monitors the changes of the resonance frequency of the sensor, allowing any fabrication processes, adsorption or desorption (through rinsing) to be directly observed.

A scheme of an *in-situ* SURMOF thin film preparation inside a QCM cell is presented in Figure 1.21. The solutions (metal precursor source, rinsing solvent, and organic ligand

solution) are sequentially flushed through the cell to grow the SURMOF. The fabrication is achieved by repeating these cycles. One advantage with this method is that the prepared SURMOF thin films on quartz crystal sensors can be directly used for further monitoring of phenomena such as occurring in adsorption/desorption and diffusion application.

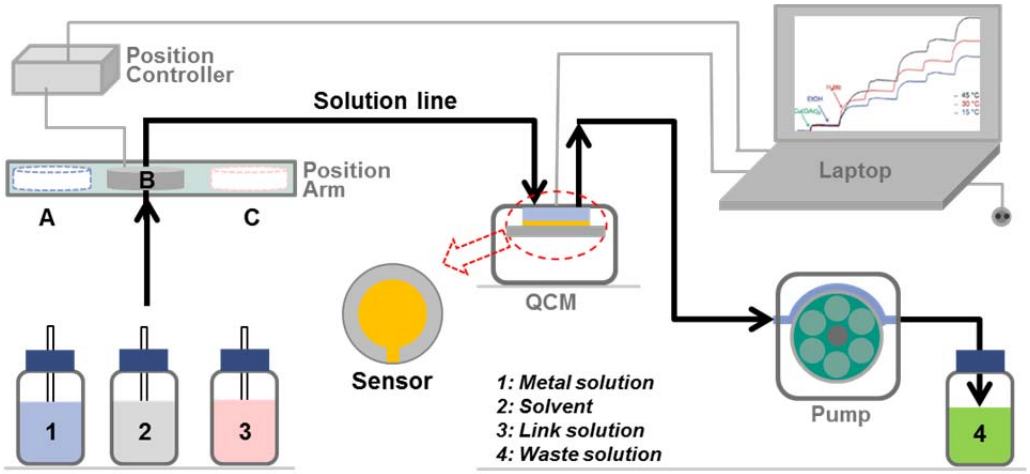

Figure 1.21 Scheme of *in-situ* SURMOFs preparation inside the cell of a quartz crystal microbalance (QCM). The solutions are sequentially flown through the cell for the SURMOF growth. The applied solutions are a metal precursor source, an organic ligand solution, and a solvent for intermediate rinsing.

1.4 Motivation

For developing MOFs implementing devices, a method that provides robust anchoring of MOF thin films on substrate with a high quality and a low defect density is required.[58, 89] The sequential stepwise LPE deposition method has been confirmed to form compact SURMOF thin films with well-defined and oriented crystals.[67] It is thus a promising technique to produce various SURMOF and/or SURMOF-based hybrid materials with a series of different thickness, whereby their dielectric, optical, and mechanical properties, with the film used as coatings, offer a sound basis for future industrial applications and device developments.

MOFs based electronic devices have attracted gradually more attentions,[59, 92-94] especially in the area of batteries,[95, 96] fuel cells[97] and capacitors.[98] In the latter case, MOFs act either as an active electronic component by being involved in the charge transport, or as a porous scaffolds matrix with a structure supporting role. So far, the electrical conductivity

of MOFs has only received little attention. Investigating the electronic conductivity of the MOF thin films becomes then critical for the application of these materials in the area of electronic devices. The tenability of the electrical conductivity of SURMOFs can be potentially used for the development of advanced electronic devices and sensor.

The mercury-drop-based tunneling junction has been shown to be a very efficient method, to study the electric transport properties of SAMs[99] or organic chains doped with metal centers assembled on a conductive substrate,[100] This is due to several advantages when considering the deposition of metallic top electrode on thin films or surface anchored molecular wires. The deposition of metallic top electrodes on SURMOF scaffolds may also produce defect or introduce the penetrating metallic element during the deposition process. In this regard, the mercury-drop method was selected and used in the present work to investigate the electric transport properties of SURMOF thin films.

To improve the electrical conductivity and to exploit MOFs as factual components of electronic devices, one effective strategy is to take advantage of the high porous quality of the SURMOFs and to load electroactive guest molecules into the nm-size pores of the framework.[101, 102] In this thesis, the Fc (ferrocene) molecules were used to be loaded in high quality SURMOF thin films. The effect of the guest loading on the electrical properties was then investigated by the mercury-drop method. Furthermore, by means of electrochemical studies, the conductivity of thicker SURMOF thin films with the effect of Fc loading were also studied.

In terms of availability of suitable electroactive organic ligands,[103, 104] the other strategy for developing novel electronic, optical and photoactive microporous materials with MOFs is through processing MOFs into compact and defect free MOF thin films.[105] Porphyrin, a well-studied photoelectroactive molecule, allowed an effective way for fabrication of MOF thin films by stacking of the high ordered ligands in the MOF-frameworks on electrodes. The artificial light harvester and photocurrent generation was realized through these porphyrin-based MOF thin films.

Furthermore, hybrid nanostructured materials, comprising of organic/metalorganic thin films and inorganic metal oxide materials, are inherently multi-functional, and are promising for a wide range of new applications.[59, 106, 107] Along with the properties of monolithic, high crystalline and greatly oriented SURMOF thin films, the hybrid organic/inorganic materials were confirmed to be promising for optical sensor and photonic device applications.

To summarize, the main objectives of this thesis are: (i) the preparation of high quality SURMOF thin films with well controlled orientation on well-defined substrates, (ii) the investigation of the electrical, optical, as well as photoelectrical properties of these SURMOF thin films; (iii) and by taking advantage of these properties, the fabrication of SURMOFs based devices, and evaluation of their performance.

2 Methods and General Experimental Information

2.1 Characterization methods and instrumental information

In the first section of this chapter, the techniques which were used for the characterization of produced thin films and coatings are introduced, with a theoretical background. Information about the instrumentation, as well as specific measurement processes are also described. The relevant techniques include X-Ray Diffraction (XRD), Ultraviolet-Visible (UV-Vis) spectroscopy, Fourier Transform Infrared (FTIR) spectroscopy, Raman spectroscopy, Spectroscopic Ellipsometry (SE), Scanning Electron Microscopy (SEM), Atomic Force Microscopy (AFM), Time-of-Flight Secondary Ion Mass Spectrometry (ToF-SIMS), mercury-drop-based tunneling junction, Cyclic Voltammetry (CV), and Pulsed Amperometric Detection (PAD).

2.1.1 X-ray diffraction (XRD)

X-ray diffraction (XRD) is the most commonly used method to elucidate the structures of materials, to confirm or determine the crystal structures and orientation, but also to measure the size, shape and internal strain/stress of small crystalline regions, and measuring the average layer distances. So it is also a routinely used method for MOFs and/or SURMOFs.

2.1.1.1 Theoretical background

X-rays are electromagnetic radiation with wavelengths in the range 0.1-10 Å, which were discovered in 1895 by the German physicist Wilhelm Conrad Röntgen (Nobel Prize for physics in 1901) and were so named because their nature was unknown at the time. Since the X-ray wavelengths have the same order of magnitude as the interatomic distances in condensed phases, X-rays are frequently used to study the internal (crystalline) structure of materials.[108]

When a crystal is hit with monochromatic X-rays at certain incident angles, the beam is scattered by the electrons of the atoms without change in wavelength, and intense reflected X-rays are produced when the wavelengths of the scattered X-rays interfere constructively. When the constructive interference occurs, the diffracted X-rays will leave the crystal at an angle equal to that of the incident beam. The phenomenon is called X-ray diffraction.[109]

2.1.1.2 The application of Bragg's law

A schematic representation of X-ray scattering from a crystalline material is shown in Figure 2.1. With respect to the equidistant hkl lattice-planes and the interplanar distance d_{hkl} of the material, an X-ray photon with wavelength λ and incident on the crystal at an angle (θ) reflects at atom z from the surface of a substance. This photo will travel a lesser distance than another, from the same packet, which reflects from farther plane of atoms (atom B in the figure) inside the crystal. Constructive interference will then be observed for the X-rays that are reflected from the lattice planes at the specular angle, if the path length difference between X-rays scattered from different hkl-planes is an integer (n) times the wavelength (λ). The general relation between the waves of the incident X-rays, angle of incidence and spacing between the crystal lattice planes of atoms is known as Bragg's Law,[109] and is expressed in eq. (2−1):

$$n\lambda = 2d \sin\theta \qquad (2-1)$$

This expression explains how the cleavage faces of a crystal reflect X-rays according to the angle of incidence and the X-ray wave interference.

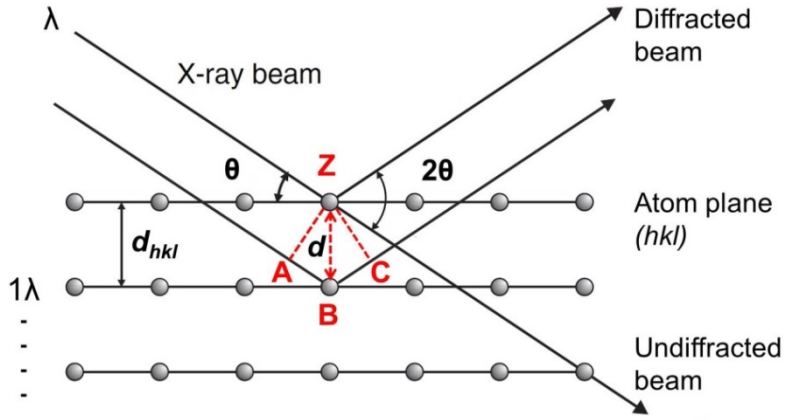

Figure 2.1 Schematic representation of X-ray scattering from a crystalline material, and the reflection geometry and trigonometry used for deriving the Bragg's Law. The lower beam (2) must travel the extra distance (AB + BC) to continue traveling parallel and adjacent to the top beam (1). (Adapted from ref.[110])

Bragg's Law may also be interpreted graphically in a practical way using reflection geometry and trigonometry, as shown in Figure 2.1. With the incident angle equal to the reflecting angle, the necessary conditions to make the phases of the beams coincide are that incident X-rays have to be in phase and parallel at the point where of incidence. The

beam strikes first at atom z of the top layer. It penetrates deeper to a lower layer and is scattered by atom B. If the two reflected beams travel farther adjacent and parallel, they will have path length difference equating AB + BC. This additional distance must be an integral (n) multiple of the wavelength (λ) for the phases of the two beams to be identical (shown as eq. (2−2)); if not in phase the produced ray will be feint:

$$n\lambda = AB + BC \tag{2−2}$$

Recognizing d (same with d_{hkl}) as the hypotenuse of the right triangle ABZ, simple trigonometry relates d and θ to the distance (AB + BC). The distance AB being opposite to θ one gets:

$$AB = d \sin\theta \tag{2−3}$$

Because AB = BC eq. (2−2) becomes,

$$n\lambda = 2AB \tag{2−4}$$

Substituting eq. (2−3) in eq. (2−4), eq. (2−1) was gotten, which is the final expression of Bragg's law.

Bragg's law identifies the angles of the incident radiation relative to the lattice planes for which diffraction peaks occurs, and the condition for constructive interference of the X-rays scattered from a defined set of parallel lattice planes.

2.1.1.3 X-ray diffractometer

Most diffractometers used in material science are based on the reflection geometry. In this case, the source and detector are on the same side of the sample and the scattered X-rays are reflected onto the detector. This is known as the Bragg-Brentano type geometry as shown in Figure 2.2.

The main components of diffractometer are the X-ray tube, the incident-beam optics, the sample holder, the receiving-side optics, and the detector. The source is typically an X-Ray tube. The incident-beam optics control the beams output by the X-ray source, and manipulate it into a monochromatic, narrow, and parallel form focused on to the sample. The sample holder keeps the specimen fixed in the right position during the experiment. The receiving-side optics retrieves the diffracted X-rays from the sample, which includes the anti-scatter slit and detector slits and a monochromators for focusing of the beam onto the detector. The detector transforms the diffracted X-rays to electronic signals.

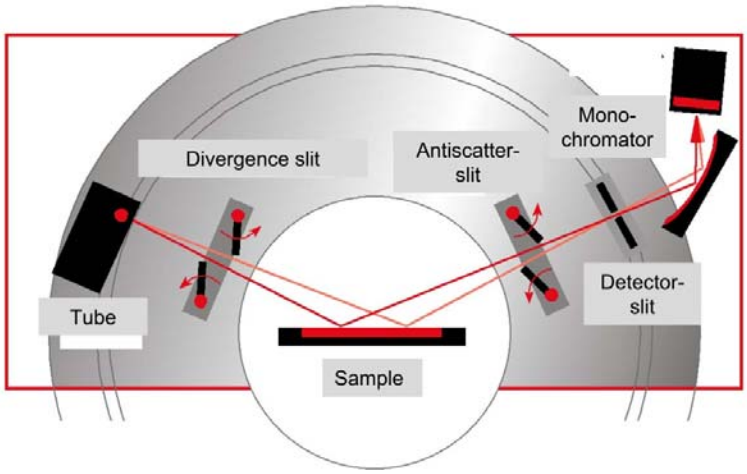

Figure 2.2 The scheme of typical Bragg-Brentano type geometry for X-ray diffractometer, mainly including X-ray tube, Incident-beam optics (divergence slit), Sample holder, receiving-side optics (antiscatter slit, detector slit and monochromator) and detector. (Taken from ref.[111])

2.1.1.4 The diffraction patterns

Diffraction occurs when incident X-rays are scattered by a periodic array of atoms in crystal materials, producing constructive interference at specific angles. The resulting diffraction pattern of a crystal, comprising both the peak positions and signal intensities (Figure 2.3), provides structure information about the lattice parameters of the sample. The size, shape, and orientation of the unit cell can be known by the diffraction pattern analysis.[109]

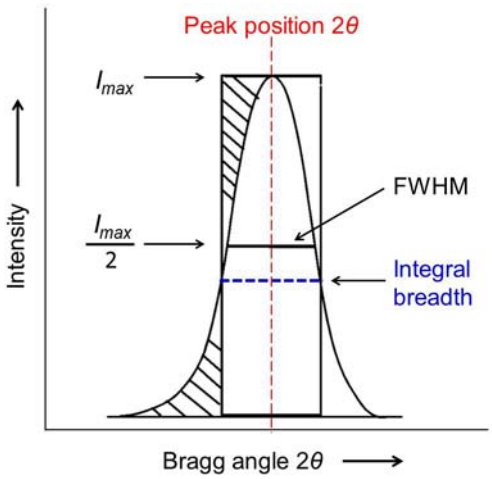

Figure 2.3 Information content of a XRD pattern: peak position, intensity and profile (peak shape, FWHM, integral breadth). (Adapted from ref.[112])

The unit cell parameters of crystalline materials are determined from the angular positions of the Bragg reflections. In large, perfect crystals, there is always a ‘‘deeper’’ lattice plane for which a path length distance of 0.5 λ is valid. As shown in Figure 2.1, if only two rows of atoms were involved for scattering of the X-rays, the signal intensity from constructive to destructive interference would be a sine-squared function of θ. However, with more atoms rows involved, the constructive interference peaks become very sharp with mostly destructive interference and low reflectivity in between. This sharpening of the peaks as the number of rows increases is very similar to the sharpening of the diffraction peaks from a diffraction grating as the number of slits increases.[110]

There are two different ways of characterizing the width of a reflection peak. The conventional FWHM (full width at half maximum) describes the width of the diffraction peak (in radians) at half height between the background and peak maximum. The integral breadth, *B(2θ)*, has to be applied if crystallite size should be precisely analyzed, and can be interpreted as the width of a rectangle having the same area and height of the peak (Figure 2.3).[111]

If a sample had large, strain-free and perfect crystallites, the diffraction peaks of the XRD pattern would be extremely narrow. However, real crystals exhibit structural imperfections which cause nonhomogeneous strain distribution. As a consequence, the diffraction lines can broaden. This can also result from instrumental factors and other material properties, such as size of crystalline domains, shape of the crystalline domains and size distribution. Figure 2.4 shows the effect of the lattice strain on a diffraction peak position and width. Uniform strain causes the shifting of the peak position, while the non-uniform strain causes broadening of diffraction peaks.

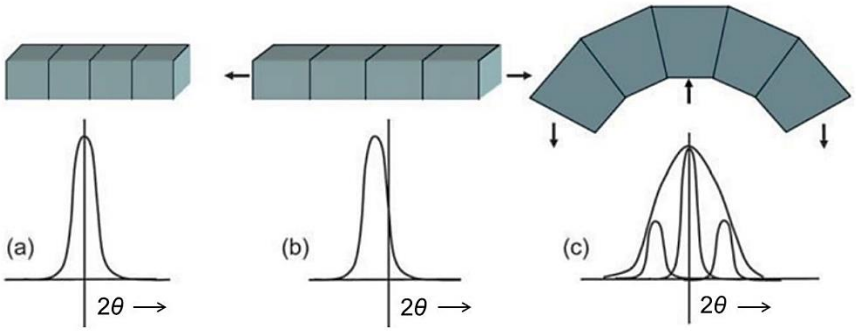

Figure 2.4 Effect of lattice strain on diffraction peak position and width: (a) no strain, (b) uniform strain (peak moves), (c) non-uniform strain (peak broadens). (Taken from ref.[112])

2.1.1.5 Thin films XRD measurement

For powder XRD measurements, the sample is piled to produce a random orientation distribution of crystallites, so that there is always population for which the orientation permits diffraction. In this process, all the diffraction peaks will possible be measured. However, when a sample is "thin film", the two-dimensionally formed by the sample surface, leads to more difficult measurements because of the different characteristics of the thin film and the additional mechanical constraints.[113]

The thin-film samples have normally a large anisotropy either along the out-of-plane (parallel along the stacking, referring to the thickness) direction or along the in-plane direction (within surface plane). So the properties and characteristics along two directions are anisotropic and become more interesting.[114] For example, when a thin film has a strong preferred orientation, only one set of specific lattice planes can be detected, especially for the SURMOFs prepared by LPE method in this thesis.

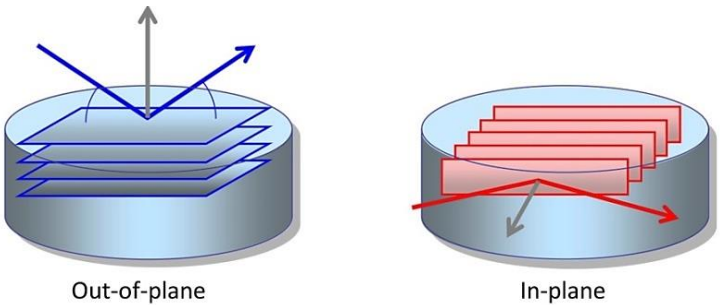

Figure 2.5 Schematic illustration of (a) out-of-plane and (b) in-plane XRD scan mode for thin film measurement. (Taken from ref.[114])

With the improvements in measurement technology and instrumentation, it is possible to investigate lattice planes of thin film that are both parallel and perpendicular to the sample surface. Figure 2.5 shows the schematic illustration of geometries for the out-of-plane and in-plane scan mode of XRD measurement. By using both of the scan modes, the characteristics of the thin film, including crystal structure, crystallinity, crystalline phase as well as distortion/relaxation, can be investigated in detail.

2.1.1.6 Instrumental information

For this study, XRD measurements were carried out on two diffractometers, for out-of-plane and in-plane experiments respectively, to investigate the structures of SURMOFs films as well as other coordination network compounds.

Out-of-plane XRD was carried out on a Bruker D8 Advance in θ–θ geometry equipped with a Si-strip detector (PSD Lynxeye©) using Cu $K\alpha_{1,2}$ radiation (λ = 0.15419 nm). On the tube side a variable divergence slit set to V12 (variable slit opening with 12 mm sample spot size) and on the receiving side a 2.5° Soller slit was used.

In-plane XRD was carried out on a Bruker D8 Discover in θ-2θ geometry equipped with a quarter Eulerian cradle, tilt-stage, 2.3° Soller-slits on both sides, a Göbel-mirror, and a PSD Lynxeye®, utilizing also the Cu $K\alpha_{1,2}$ radiation (λ = 0.15419 nm).

2.1.2 Ultraviolet-visible (UV-Vis) spectroscopy

Ultraviolet-visible (UV-Vis) spectroscopy is usually used to determine the concentration, according to Lambert-Beer law, of a solute absorber, such as transition metal ions, highly conjugated organic compounds, and biological macromolecules. The wavelengths of UV-Vis absorption bands can also be correlated with electronic transitions of matters, which are valuable in determining the functional groups (Chromophores) within a molecule.

2.1.2.1 Theoretical background

UV-Vis refers to the absorption or the reflectance spectroscopy in the UV-Vis spectral region, which is conventionally divided into three sub-domains termed low UV (185–400 nm), visible (400–700 nm) and near infrared (700–1100 nm). The UV-Vis spectra of the analyte represent the interaction between the radiation in UV region and matter, and measure the absorbance, transmittance, or reflection (for thin films) as a function of wavelength. The UV-Vis spectra show only a few broad absorbance bands because of the limited electronic transitions of the atoms.[115]

In the UV–Vis region of the electromagnetic spectrum, molecules undergo electronic transitions.[116] Organic compounds represent the majority of the materials studied in the UV–vis range. The observed electronic transitions in an organic compounds involve electrons engaged in σ or π or non-bonding n (atoms with lone pairs, such as O, N, S, Cl, etc.) electron orbitals, as shown in Figure 2.6. The more excitable the electrons of a sample are (e.g. lower energy gap between the bonding and the antibonding), the longer the wavelength of light it can absorb is.

$\sigma \rightarrow \sigma^*$ transition: an electron in a bonding σ orbital is excited to the corresponding antibonding orbital. Specifically, the saturated hydrocarbons contain this type of bonding

in the near UV region. And the absorption maxima of this transition are not seen in typical UV–vis spectra.

n → σ* transition: saturated compounds containing n electrons (non-bonding electrons) are capable to be excited to the σ antibonding orbital. These transitions usually need less energy than σ → σ* transitions, which can be excited by wavelengths of 150–250 nm.

π → π* transition: an electron in a bonding π orbital is excited to the corresponding antibonding orbital. These transitions need an unsaturated group in the molecule to provide the π electrons, and can be excited by the region 200–700 nm.

n → π* transition: an n electron (non-bonding electrons) is excited to an antibonding π* orbital. This transition is usually observed in molecules containing a hetero-atom carrying lone electron pairs as part of an unsaturated system.

Numerous inorganic compounds contains electrons engaged in d orbitals which are responsible for transitions of weak absorption located in the visible region (**d → d transition**), and are generally responsible for the color of the materials. Furthermore, the electrons transfer between two metal sites differing only in their oxidation state is named intervalence charge transfer (**anion → anion transition**). The intense blue color of Prussian Blue results from intervalence charge transfer, which is associated with the energy of the transfer of electrons from Fe(II) to Fe(III).[117, 118]

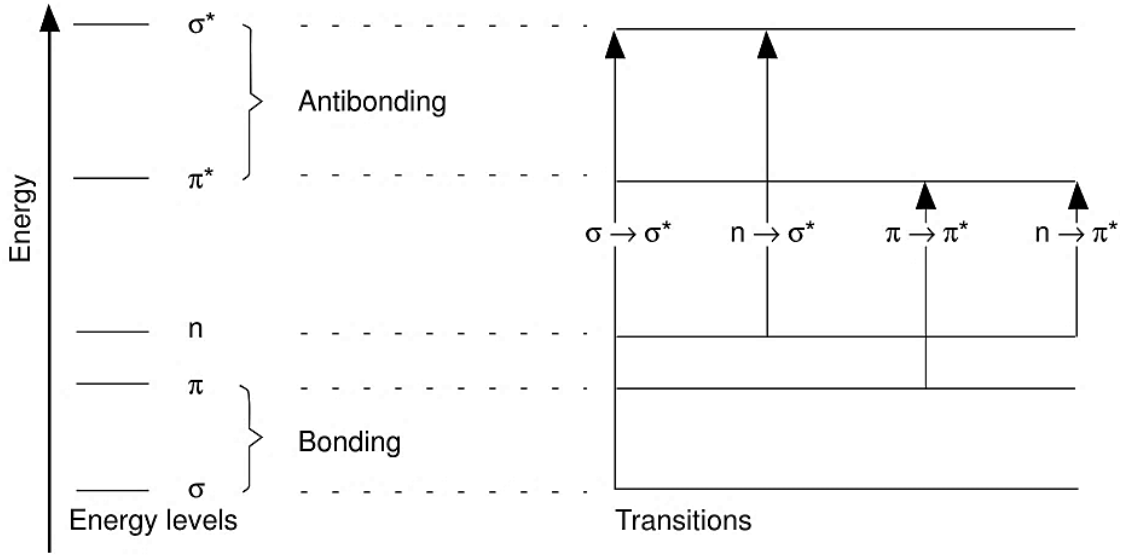

Figure 2.6 Electron transitions of organic compounds in UV-Vis spectroscopy. (Taken from ref.[119])

2.1.2.2 Instrumental information

UV-VIS absorption and angle dependent reflectance measurements were performed on a Cary 5000 UV-VIS-NIR Spectrometer (Agilent Technologies, USA). UV-VIS absorption measurements were done in transmission mode. The angle dependent reflectance measurements were carried out with a computer controlled Agilent UMA® specular reflectance accessory, which is specially designed for absolute reflectance (%R) measurements at variable angles of incidence. (Results relating to this technique are presented in Chapter 4).

In-situ spectral reflectometry was performed by using a spectrometer (NanoCalc 2000) equipped with a combined halogen and deuterium light source (DH-2000 FHS, Mikropack). Four optical fibers are equipped in one wire, where fiber 1 and 2 led to the lamp and illuminated beam (2 mm diameter spots) onto the sample surface. Additionally, this equipment was also used for the time dependent chemo-responsive optical sensing under Glove-box conditions, where the sorption/detection reflectometry studies were performed by exposing with organic vapours (Results relating to this technique are presented in Chapter 4).

2.1.3 Fourier transform infrared (FTIR) spectroscopy

Infrared (IR) spectroscopy is a reliable and powerful technique widely used for the identification and structural analysis, based on the vibrations of chemical bonds of the atoms, in both organic and inorganic chemistry. The samples for IR characterization can be solid, liquid, gas, as well as the interfacial species.[120]

2.1.3.1 Theoretical background

Analytical infrared studies are based on the absorption (or reflection) of the electromagnetic radiation with a wavelength between 1 and 25 μm. This spectral range is sub-divided into three smaller areas, the near-infrared (near-IR, 1–2.5 μm), the mid-infrared (mid-IR, 2.5–50 μm) and the far-infrared (far-IR, beyond 25 μm). However, because the near-IR is poor in specific absorption bands and the far-IR requires the use of specialized optics and sources, these spectral ranges are not used as widely as the mid-IR region which provides more information on the structures of compounds.[116]

Due to the many advantages of Fourier transform infrared (FTIR) spectroscopy, such as multiplex (information from all wavelengths is collected simultaneously) and throughput

(interferometer throughput is determined only by the diameter of the collimated beam coming from the source), almost every spectrometer used today in mid-infrared spectroscopy is of the Fourier-transform type.[120]

Infrared absorption by molecules results from the transitions between quantized vibrational energy states. Molecular vibrations can range from the simple coupled motion of the two atoms of a diatomic molecule to the much more complex combination of each atom motion in a large polyfunctional molecule. Vibrations can involve either a change in bond length (stretching) or bond angle (bending).

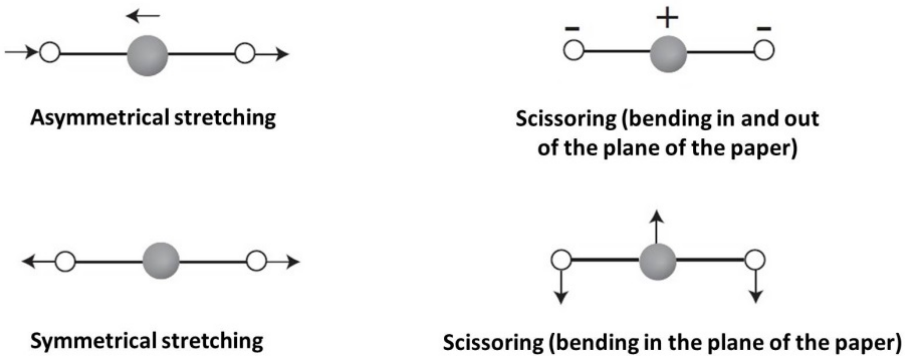

Figure 2.7 Stretching and bending vibrational modes for the linear CO_2 molecule. (Taken from ref.[121])

For molecules with N number of atoms in them, linear molecules have 3N–5 degrees of vibrational modes (CO_2 is shown as an example in Figure 2.7), whereas nonlinear molecules have 3N–6 degrees of vibrational modes (H_2O is shown as an example in Figure 2.8). In order for a vibrational mode in a molecule to be "IR active", it must be associated with changes in the dipole.[116]

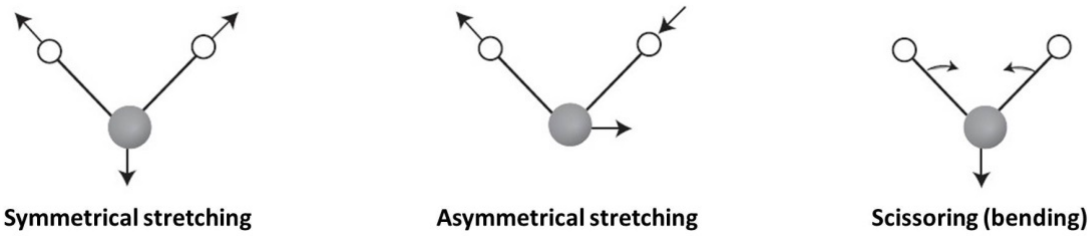

Figure 2.8 Stretching and bending vibrational modes for nonlinear H_2O molecule. (Taken from ref.[121])

An organic compound with the formula CH_2X_2, where X can represents any other atom, has nine different vibrational modes. Figure 2.9 presents six of these modes involving only the -CH_2- group: symmetric and antisymmetric stretching, scissoring, rocking, wagging and twisting. The -CH_2- group has 6 vibrational modes because it is attached to two X, unlike H_2O molecule which only has 3 modes.[121]

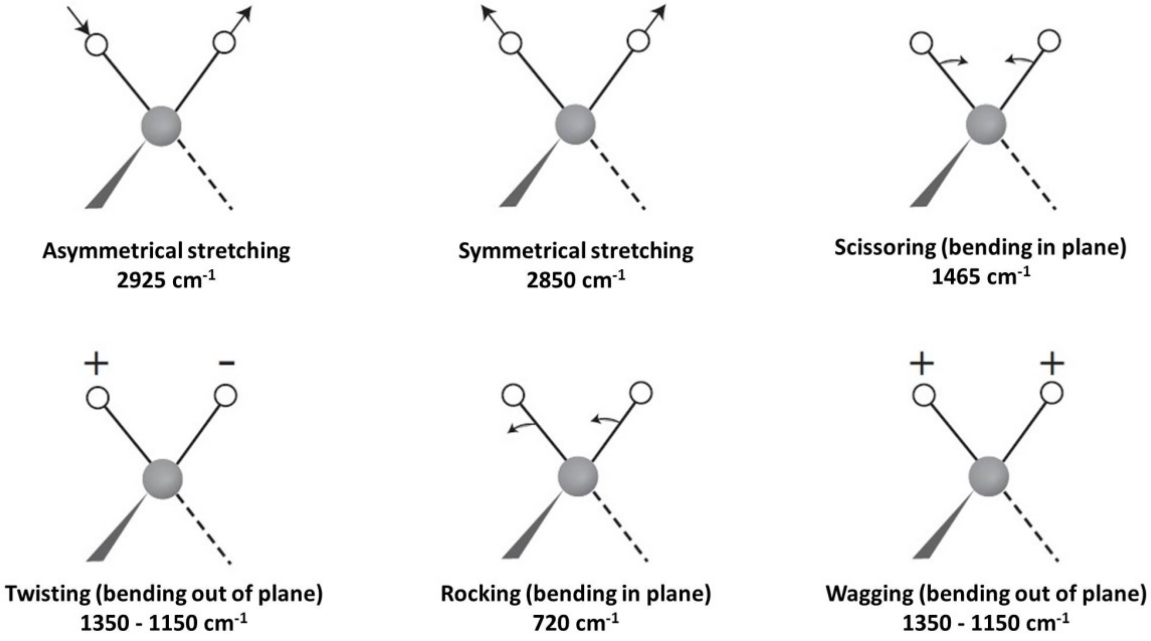

Figure 2.9 Stretching and bending vibrational modes for methylene bridges; in this case, the 3N–6 rule does not apply since the -CH_2- group presents only a portion of a molecule. (Taken from ref.[121])

In FTIR, an IR polychromatic beam is shone through a Michelson interferometer and a sample, to detector measuring how much of that beam is absorbed by the sample. The Michelson interferometer is the essential component, and consists of perpendicular mirrors with a beam splitter between them, as shown in Figure 2.10. One mirror of the interferometer is moved, while the other one is fixed (Stationary Mirror), to generate wave interference. All wavelengths are passing through the interferometer and to the sample compartment. The light is then refocused on to the detector. The absorption spectrum as a function of wavenumber (cm^{-1}) is obtained by the Fourier transform of the interferogram, which is itself a function of the mirror displacement (cm).[120] With this design, a reference spectrum needs to be recorded first. The absorption spectrum of the sample actually results from subtracting the reference spectrum from the produced sample spectrum.

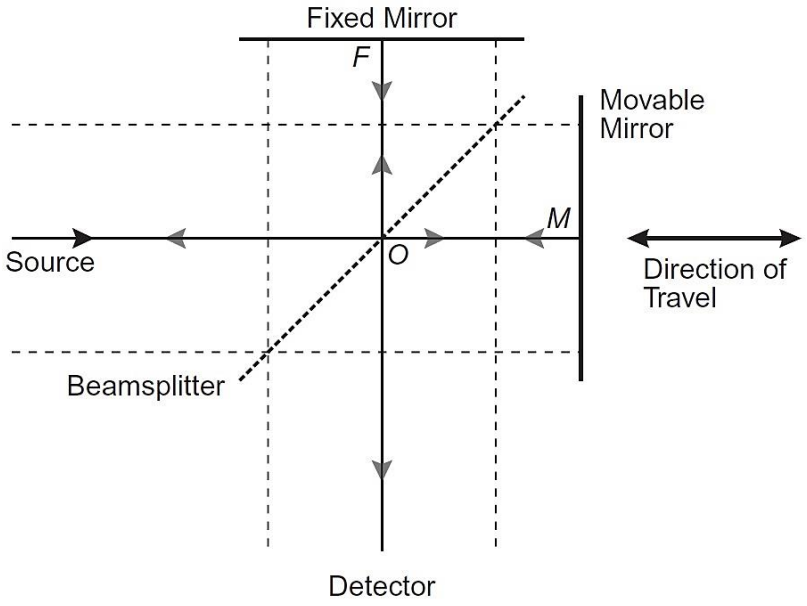

Figure 2.10 Schematic diagram of a Michelson interferometer configured for FTIR. The median ray is presented by the solid line, and the extremes of the collimated beam are presented by the dashed line. (Taken from ref.[120])

2.1.3.2 Infrared reflection absorption spectroscopy (IRRAS)

Infrared reflection absorption spectroscopy (IRRAS) is a powerful surface specific spectroscopic method for the investigation of absorbed monolayers, thin films, and coatings placed on a highly reflective surface. In an IRRAS experiment, the sample is investigated in reflection geometry under grazing incidence (typically 80°). The sensitivity of this method can be significantly enhanced by employing the polarization modulation technique (PM).[122]

2.1.3.2.1 Polarization and grazing incidence

A linearly polarized light can be defined by the sum of two orthogonal components, the *s*- and *p*-polarized light, as shown in Figure 2.11(a). The *p*-polarized light is parallel to the plane of incidence, while the *s*-polarized light is perpendicular to the plane of incidence (parallel to the surface).[123]

Figure 2.11(b) presents phase shift of the *s*- and *p*-polarized radiations as the function of incident angle (θ) at a clean metal surface. It can be seen that the *s*-polarized light undergoes a uniform phase shift of 180° for all angles of incidence (from 0 to 90°), resulting in a nearly total cancellation of the amplitude at the surface (destructive

interference) and giving a vanishing electric field at the surface. There is then no consequent electric field parallel to the surface. However, the phase shift of *p*-polarized light is strongly dependent on the angle of incidence and reaches 90° at higher degree, which results in amplitude addition (constructive interference). Thus it is necessary to perform IRRAS experiments at a high angle of incidence (close to grazing incidence), due to the fact that the large electric field is established to interact with the dipole moment of the vibrations perpendicular to surface at this incidence.[123]

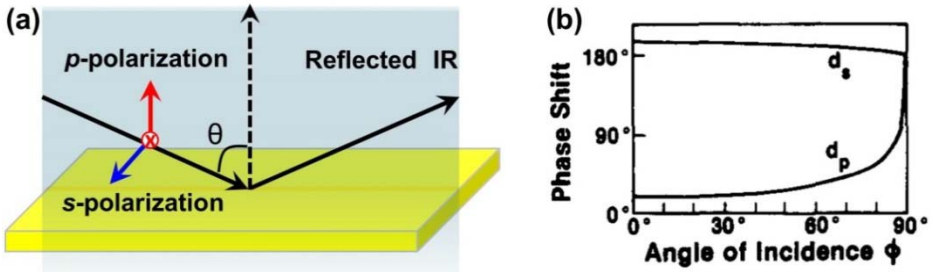

Figure 2.11 (a) Scheme of the incident IR beam (at the angle of θ) reflected by the metallic surface (yellow), the incidence plane (perpendicular light blue plane) is defined by the incident and the reflected light path, and the *p* (red) and *s* (blue) component of the polarized IR radiation; (b) phase shift of the *s* (d_s) and *p* (d_p) component radiations versus angle of incidence θ at a clean metal surface. (Adapted from ref.[123])

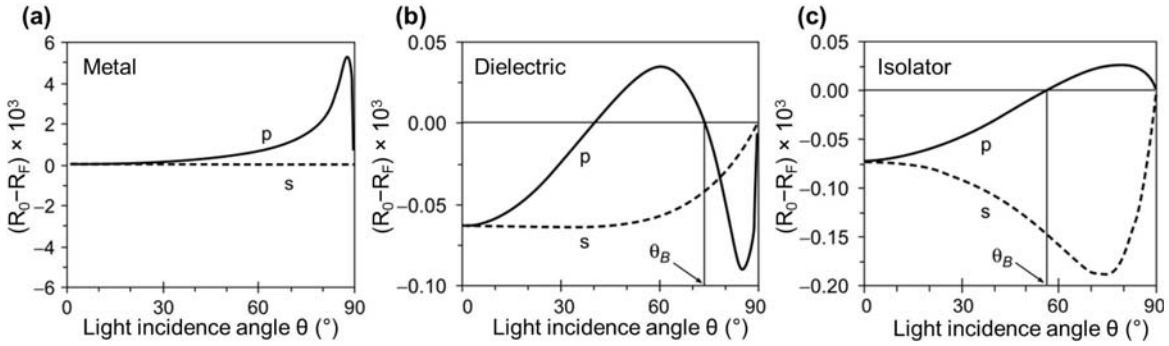

Figure 2.12 Calculated reflectivity differences between the clean substrate (R_0) and the adsorbate-covered substrate (R_F) for different substrate materials as a function of the light incidence angle for p-polarized radiation (solid lines) and s-polarized radiation (broken lines) at 3000 cm^{-1}. (Taken from ref.[122])

Figure 2.12 presents the calculated reflectivity differences (R_0–R_F) for various substrate materials (R_0) after being covered with adsorbate (R_F) and as a function of the light incidence angle for *p*- and *s*-polarized radiation. It can be seen that the adsorbate on

metallic surface interact with the *p*-polarized fraction of light, and the intensity reaches the maximum at large angles of incidence (88°) for the *p*-polarized light, but not with the *s*-polarized one.[122]

2.1.3.2.2 Surface selection rule

As mentioned previously, only the *p*-component radiation interacts with the surface of sample (Figure 2.12(a)). Consequently, only the active vibrations, having a component of the dynamic dipole polarized along the normal to the sample/substrate interface, can be detected by IRRAS. These results give the so-called "surface selection rule", which is used to study the molecular orientation of thin films or monolayers deposited on metal or dielectric substrates.[120]

Figure 2.13 illustrates the situation with electric fields of the incident IR light with both perpendicular (red) and parallel (blue) components, and the transition dipole moment (TDM) of molecules and the mirrors charges on metallic surface. Only vibrations with a dipole moment perpendicular to the surface are excited, because the surface electric field is enhanced by the electric field resulted from the induced mirror charges in the metallic substrate surface. The displacement of the dipole moment depends on the absorbed molecules perpendicular or parallel to substrate surface.

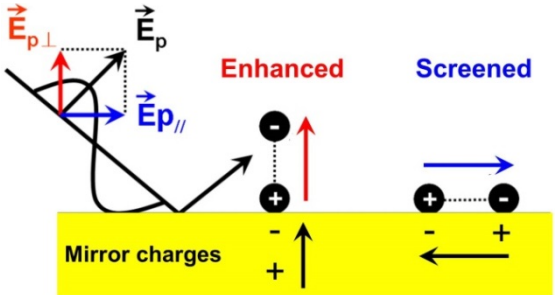

Figure 2.13 Schematic drawing of IR surface selection rule on metallic surface.

2.1.3.3 Instrumental information and conditions relating this work

The IRRA spectra were acquired using the infrared spectrometer Bruker VERTEX 80. The absorption band positions are given in wave numbers ν in cm^{-1}, with a resolution of 2 cm^{-1}. All the IRRA spectra were recorded in grazing incidence reflection mode at an angle of incidence amounting to 80° relative to the surface normal using liquid nitrogen cooled mercury cadmium telluride (MCT) narrow band detectors. Perdeuterated hexadecanethiol SAMs on Au/Si were used for background measurements.

2.1.4 Raman spectroscopy

Raman spectroscopy is a form of vibrational spectroscopy, and is complementary to IR absorption spectroscopy. As mentioned in the previous section, the vibrational states of a molecule can be probed through infrared spectroscopy, because the vibrational transitions typically require an amount of energy that corresponds to the infrared region of the spectrum. However, molecules which have no net dipole moment (such as N_2 and O_2) are not observable in the IR spectra, and functional groups with symmetric bonds (such as -S–S-, -C–S-, -C=C-) give weak responses in the IR spectra.[124]

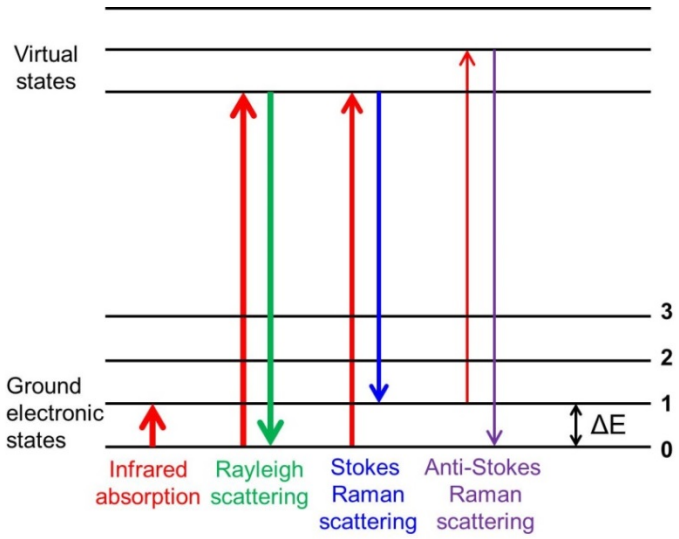

Figure 2.14 Energy-level diagram showing the different vibration states involved in Raman signal, ΔE = absorbance. The line thickness is roughly proportional to the signal strength from the different transitions.

Raman spectroscopy involves shining a monochromatic light source (i.e. laser) on a sample and analyzing the scattered light. When light is scattered from a molecule, the majority of the scattered light is of the same frequency as the excitation source (incoming light); this is known as Rayleigh or elastic scattering, as shown in Figure 2.14. However, a small fraction of light (approximately 10^{-5} % of the incident light intensity) is scattered with a shift in energy (or wavelength) due to interactions between the incident light and the vibrational energy levels of the molecules in the sample. The resulting inelastically scattered light can be of either lower (Stokes) or higher (anti-Stokes) energy than the incoming light.[125]

Plotting the intensity of this "shifted" light versus frequency results in a Raman spectrum of the sample. Generally, Raman spectra are plotted relative to the laser frequency used such that the Rayleigh band lies at 0 cm^{-1}. On this scale, the band positions will lie at frequencies that correspond to the energy levels of different functional group vibrations due to an interaction of light with the molecule.

The excitation wavelength used in Raman spectroscopy can range from the near infrared to the ultraviolet. However, the choice of the wavelength should be done carefully, because the wavelength could possibly destroy the sample by absorption or induce resonance and fluorescence if it is not chosen well. For materials that show fluorescence, it is vital to choose a longer wavelength that will minimize this effect, otherwise the weak Raman interaction will be swamped because the high intensity of fluorescence could make the detector overload. Whereas shorter wavelength lasers (higher energy) can be useful for penetrating certain samples where fluorescence is not a problem.[125]

In this thesis, the Raman spectra were recorded with a Bruker Senterra Raman microscope (Bruker Optics, Ettlingen, Germany) using a green laser at 532 nm for excitation. The 2D Raman-Map characterization was performed on the same instrument. The analysis of the data was done with the Bruker evaluation software OPUS 7.2.

2.1.5 Spectroscopic ellipsometry (SE)

Ellipsometry is a very sensitive optical technique that uses polarized light to probe the thickness and dielectric properties of a thin film sample. Upon analyzing the change of polarization of the light reflected off a sample, ellipsometry can yield information about layers that are thinner than the wavelength of the probing light itself.[126]

Spectroscopic ellipsometry (SE) refers to ellipsometric measurements that are carried out at various wavelengths of the incident beam, which covers the visible range (VIS) and parts of both the ultraviolet (UV) and the near infrared (NIR) range of the electromagnetic spectrum. SE can provide information about not only single layers, but also thick layers, complex materials and multilayer systems. Due to its great versatility, SE is an established technique for thin film analyses, as well as the quality controls in industrial fabrication.

A schematic of an ellipsometry measurement is shown in Figure 2.15. The incident light is a linear polarized light with both *p*- and *s*-components, which is produced by a polarizer. The light undergoes amplitude and phase changes for both *p*- and *s*-components upon

passing through the material, and becomes elliptically polarized. A rotating polarizer after the sample measures these changes. The detector converts light to electric signals yielding the measurement of the reflected polarization.

Ellipsometry measures the complex reflectance ratio (ρ, a complex quantity), which is commonly written as:

$$\rho = \tan(\Psi)e^{j\Delta} \tag{2−5}$$

where $\tan(\Psi)$ is the amplitude ratio upon reflection, and Δ is the phase shift (difference).

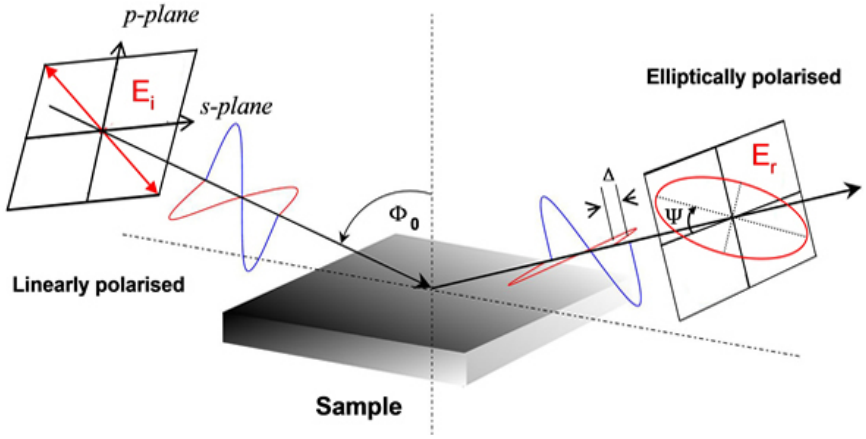

Figure 2.15 Schematic of an ellipsometry measurement in which linearly polarized incident light (left) changes to elliptically polarized light (right) after oblique reflection off of the sample. Modeling the change in polarization provides thin film parameters such as thickness and optical constants. (Taken from ref.[127])

The thin film characterization using SE generally requires the modeling of the sample, because the characteristic optical parameters cannot be extracted directly from the measured Ψ and Δ. The constructed model describing the sample is used to calculate the predicted response from Fresnel's equations integrating the material thickness and optical parameters. The modeled data are tested with match function against the experimental measurements to extract the desired parameters. In the case of multilayer samples, the model considers the thickness and optical constants parameters of all distinct layers, thus each layer has to be modeled individually.[128]

In this thesis, SE analyses were performed on a multiple wavelength ellipsometer (M-44, J. A. Woollam Co., Lincoln, USA). An arc lamp with a high pressure Xe discharge point

source was used. Modeling, fitting, and regression analyses of the ellipsometric data were performed using the software provided by the manufacturer (WVASE^{TM}). For the photo band gap simulations, the program WINCPC for Woollam M-44 ellipsometer was used.

2.1.6 Scanning electron microscopy (SEM)

The scanning electron microscope (SEM) is a type electron microscope with broad applications in the study of solid materials. The SEM is mainly used to image at high-resolution the shapes of objects (morphology), but can also be used to show the spatial variations in chemical compositions (density). SEM is then usefull to investigate the morphology, the structure, and the orientation of crystals in thin film materials.[129]

SEM uses a focused beam of high-energy electrons to interact with atoms in the sample and generate various signals at the surface of sample. These signals include secondary electrons (SE), backscattered electrons (BSE), diffracted backscattered electrons (EBSD), photons (here characteristic X-rays), visible light and heat.[129] Though rarely a single machine would be equipped with all necessary detectors, various information about the sample can be obtained by collecting and analyzing these signals:

(i) Secondary electrons and backscattered electrons are commonly used for imaging: the morphology and topography of samples are acquired from SE, and the composition contrasts in multiphase samples (i.e. for rapid phase discrimination) are acquired from BSE;

(ii) Diffracted backscattered electrons are used to determine crystal structures and orientations of minerals;

(iii) Characteristic X-rays are used for elemental analysis, referring to energy-dispersive X-ray spectroscopy (EDS).

Figure 2.16 shows a scheme of a SEM setup. The SEM column and sample chamber are under vacuum. This allow the electrons to travel freely from the electron beam source to the sample and then to the detectors. An incident electron beam (energy is ranging from 0.1 keV to 40 keV) is generated from an electron gun above the sample chamber by thermal emission, with a heated tungsten filament, or with a field emission cathode. The electrons are focused to a spot about 0.4 to 5 nm in diameter by a series of electromagnetic lenses in column. Scanning coils near the end of the column direct and position the focused beam onto the targeted sample surface.[129]

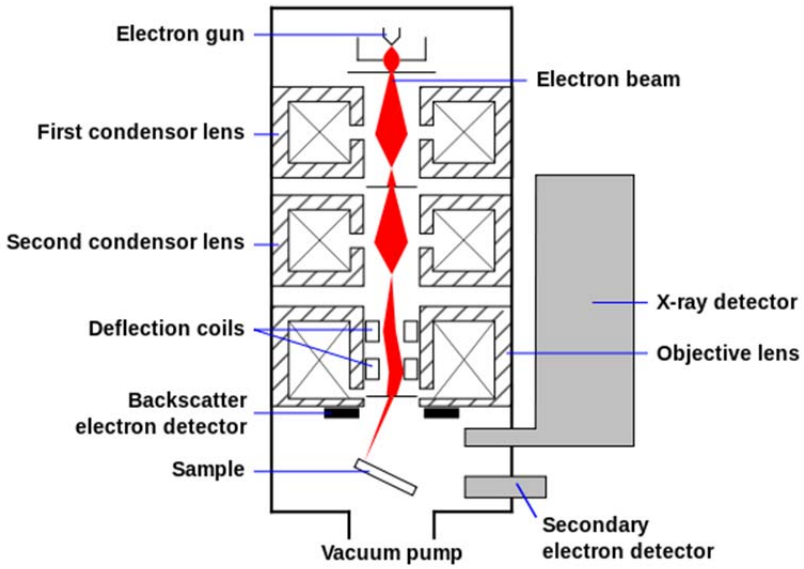

Figure 2.16 Scheme of a SEM. (Taken from ref.[130])

To create an SEM image, the incident electron beam is scanned in a raster pattern across the sample surface by deflecting it in the *x* and *y* axes. The emitted electrons are detected for each position in the scanned area by an electron detector. The intensity of the recorded electron signal is converted to monochromatic visual signal with varied brightness. SEM micrographs have a large depth of field rendering the characteristic 3D appearance of the surface structure of the sample.[129]

Magnification in a SEM can be controlled over a range of up to 6 orders of magnitude from about 10 to 500,000 times, and the resolution can be lower than 1 nanometer, due to the very narrow electron beam. Specimens can be observed in high vacuum, in low vacuum, in dry conditions (in environmental SEM), and in a wide range of temperatures.

In this thesis, SEM measurements were performed on a HR-SEM (Gemini®-Series, Zeiss, Germany) operated at 3.5-5 kV to check the morphology and cross-section of the samples.

2.1.7 Atomic force microscopy (AFM)

Atomic force microscopy (AFM), also known as scanning force microscopy (SMF), is a type of scanning probe microscopy (SPM), which works by scanning a very sharp probe along the sample surface to form images. AFM was developed to image surface structures with an extremely high resolution (down to the nanometer scale) and to measure the forces interacting between the probe and the sample surface.

Basically, in a standard AFM in oscillation mode, the tip of a cantilever (made of Si or Si_3N_4) is brought into proximity of a sample surface with two piezoelectric elements generating the relative movement between the cantilever and the sample, as shown in Figure 2.17. While the sharp tip of the cantilever moves over the sample, the cantilever itself bends according to the surface interaction. The deflection is detected by a laser beam which is reflected from the backside of cantilever onto a set of position sensitive photodiodes. By setting the constant tip-sample distance or oscillating amplitude in a feedback principle as it scans over the surface, the surface morphology can be reconstructed from the signal applied to the piezoelectric elements. Generally, the imaging modes of AFM are in contact modes and tapping mode (the cantilever is vibrated or oscillated at a given frequency) depending on the application.[131]

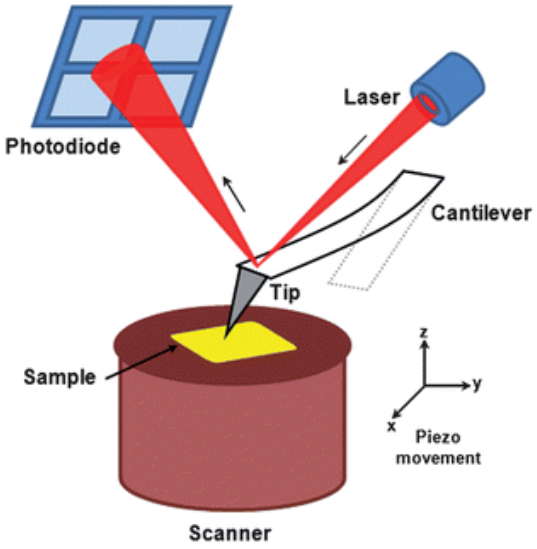

Figure 2.17 Scheme of an AFM. (Taken from ref.[132])

Comparing to other high resolution microscopy (such as SEM and TEM), AFM has several great advantages. One is that AFM can image almost any type of surface, including conductor, insulator as well as biological samples. It is also simple to operate in most environments, such as under atmospheric (or other gases), vacuum conditions or liquid immersion (aqueous solutions as well as other solvents) of the sample. AFM can provide a 3D surface profile with a resolution at a sub-Angstrom along the z direction (height resolution) and down to1 nm on X-Y directions (lateral resolution).

In this thesis, Tapping-mode AFM was used to measure the morphology and thickness of the SURMOF films on a Multimode AFM (Bruker, Germany) with a "*J*" scanner. (Results

are shown in Chapter 3.1). Contact-mode AFM measurements were performed with a Bruker dimension instrument equipped with a liquid cell. In this case ethanol was used as the liquid for liquid condition measurement (Results are shown in Chapter 4.1).

2.1.8 Time-of-flight secondary ion mass spectrometry (ToF-SIMS)

Time-of-flight secondary ion mass spectrometry (ToF-SIMS) is a highly sensitive surface analytical technique to provide elemental, chemical state, and molecular information (based on mass). Generally, three operational modes are available (surface spectroscopy and imaging, depth profiling) using ToF-SIMS. Samples can be of various natures and varied forms such as metals, semiconductors, insulators, organic or inorganic, as a solid or compacted powder.[133]

Figure 2.18 presents a schematic diagram of the ToF-SIMS instrument. It uses a pulsed and focused ion beam to dislodged chemical species from the very outermost surface (1-2 nm) of the sample (on the Target). Secondary ions, known as particles, generated farther from the impact site tend to be molecular compounds, typically fragments of much larger organic macromolecules. These particles are then accelerated into a "flight tube". The particle velocity is thus dependent on the charge of mass. This allows the mass to be determined by measuring the exact time at which the particle reaches the detector (i.e. time-of-flight).[134]

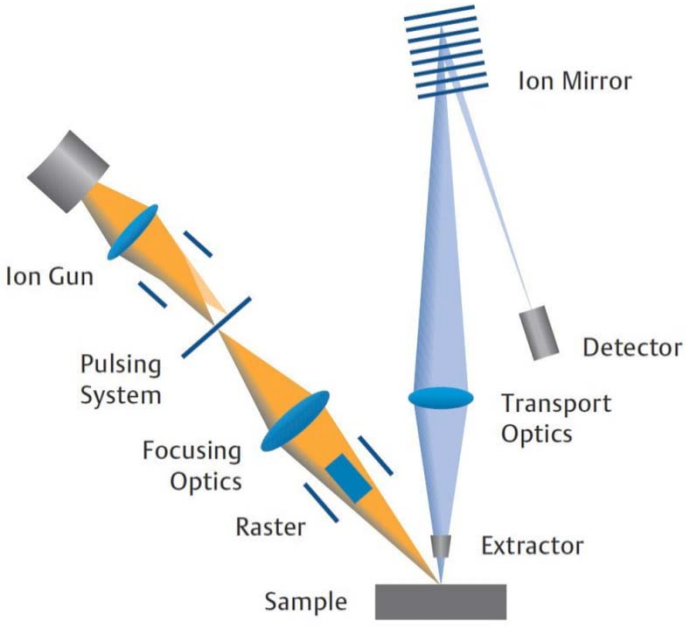

Figure 2.18 Schematic diagram of the ToF-SIMS instrument. (Taken from ION-TOF GmbH[135])

Surface imaging provided by ToF-SIMS is the spatial distribution of different species to yield surface reactivity maps. And depth distribution information is obtained by combining TOF-SIMS measurements with ion milling (sputtering) to characterize a thin film structure. The high mass resolution and high mass range makes this system adequate for both elemental and molecular surface analysis.

In this thesis, ToF-SIMS was performed on a TOF.SIMS5 instrument (ION-TOF GmbH, Münster, Germany). This spectrometer is equipped with a Bi cluster primary ion source and a reflection type time-of-flight analyzer.

2.1.9 Mercury-drop-based tunneling junction

The mercury-drop (Hg-drop) method, introduced by Rampi and Whitesides, is usually used to study electric transport properties of SAMs on a conductive substrate.[136-140] A schematic diagram of the mercury drop setup is given in Figure 2.19 (a). The passivated mercury drop is extruded from an appropriately modified Hamilton syringe and gently positioned on top of the sample, and the process for approaching of the Hg-drop to sample surface is shown in Figure 2.19 (b). Then current-voltage (I-V) curves are measured to investigate the electrical properties of the samples.

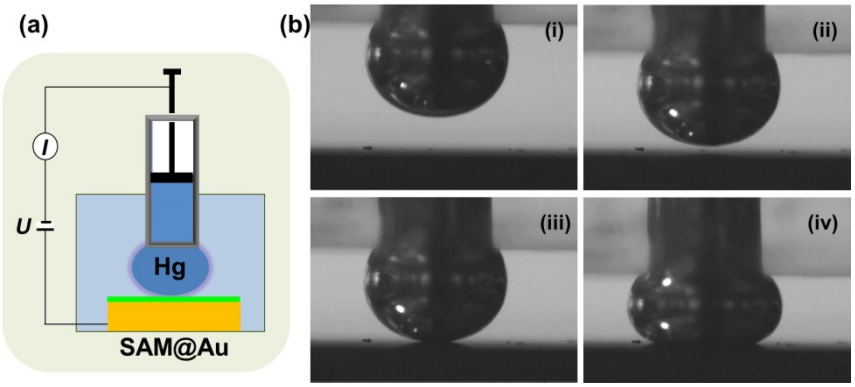

Figure 2.19 (a) Schematic diagram of the mercury-drop junction setup. (b) Images of the Hg-drop; the process, from (i) to (iv), shows how is the Hg-drop getting contact with sample surface with the final contact area is about 600 μm in diameter.

This Hg-drop method provides several advantages compared to the application of solid metallic electrodes to investigate the electrical properties of surface anchored molecular wires or thin films. Firstly, this method is compatible with a wide range of organic structures that might otherwise be damaged by the deposition of the metals electrodes atop.

Secondly, the assembly of the Hg-based junction is rather simple and does not require sophisticated and expensive equipment for electrodes evaporation. Finally, the Hg-drop surface is free of structural features and gently adapts to the topography of the film to be investigated. All these characteristics are advantageous for the study of the SURMOFs.

In this thesis, the electrical properties of SURMOF thin films were measured by using a mercury-drop setup built by the team of Prof. Zharnikov,[99] as shown in Figure 2.20. A mercury drop (around 600 μm in diameter) is extruded from a gastight Hamilton syringe, whose plunger metallic core is connected to a Keithley 2635A source meter through a tungsten wire. The drop of Hg was first passivated with hexadecanethiol ($C_{16}H_{33}$-SH, HDT) to avoid amalgamation and short circuit. It was then gently contacted to the bottom electrode in a cell filled with HDT in hexadecane. A CMOS camera with a Macro lens (The Imaging Source DMK22AUC03 1/3 in. Micron with MR 8/O) was used to observe the deposition of Hg-drop. From the sideway view of the junction, the diameter of Hg-drop was measured and hence the contact area value calculated. The SAMs or SURMOF thin film samples were used as bottom electrodes, which were connected with the source meter by means of a metal clip and a suitable cable connector.

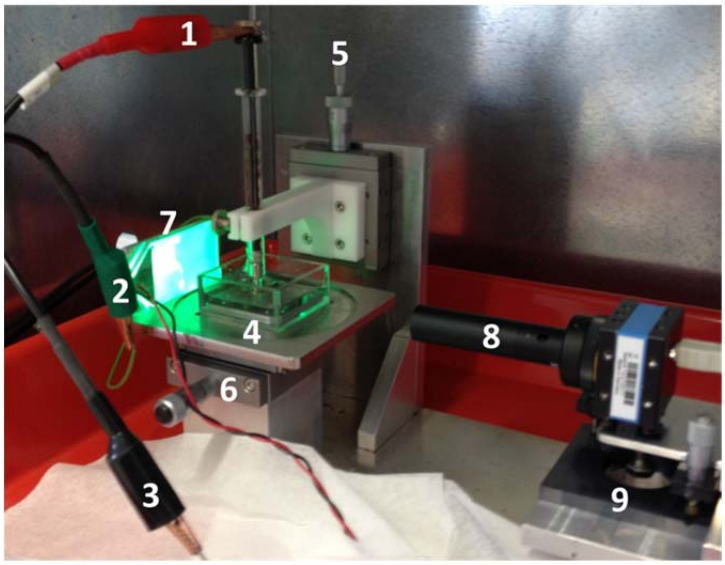

Figure 2.20 The mercury-drop junction setup; the numbers represent as follows: 1. Top electrode connected with the Hamilton syringe (Hg-drop electrode), 2. Bottom electrode connected with the sample inside the spectroscopic cell, 3. The ground electrode, 4. A spectroscopic cell to contain the sample in solution, 5. The screw for Z-direction differential drive of mercury-drop, 6. The sample stage for X-Y direction drives, 7. LED backlight, 8. Camera, 9. The state for X, Y and Z direction drives of camera.

2.1.10 Electrochemical methods

Electrochemistry is the branch of physical chemistry concerned with the interrelation of electrical and chemical effects. A part of this research area includes the study of electric energy production by chemical reactions, or the chemical reaction caused by the passage of an electric current. There are various extremely important electrochemical processes, encompassing different phenomena (e.g., electrophoresis and corrosion), devices (electro analytical sensors, electrochromic displays, batteries, and fuel cells), and technologies (the electroplating of metals).[141]

An electrochemical experiment always involves a reduction-oxidation (redox) process which takes place at the interface of an electrode, and involves the electron transfer to or from a molecule or ion changing its oxidation state. Current flows through the electrodes as a result of the electrons movement. An electrolyte is a phase in which charge is carried by ions.

The typical three-electrode system consists of a working electrode, a counter electrode and a reference electrode. Working electrode is the electrode on which the reaction of interest is occurring. It can consist of materials ranging from inert metals (such as gold, silver or platinum) to inert carbon and film electrodes. Counter electrode is used to provide a circuit over which the electrical current is expected to flow. It is often made of an electrochemically inert material, such as gold, platinum, or carbon. The reference electrode is the electrode which has a stable and well-known electrode potential. By using the reference electrode, the current between the working and the counter electrode, and the voltage between the reference and the working electrode can be monitored. It can be, for example, a saturated calomel electrode (SCE), a silver/silver chloride (Ag/AgCl) electrode, or a normal hydrogen electrode (NHE). A pseudo-reference electrode (or quasi-reference electrode) is also used (such as Pt) if the common reference electrodes are not applicable.

There are many electrochemical techniques possible depending on the specific experimental requirements. Voltammetry is basically referred to a technique where the potential of the working electrode is controlled and the resulting current flow is measured. The most general applications are cyclic voltammetry (CV) and pulsed amperometric detection (PAD). For CV method, the working electrode potential is linearly scanned over time in either the negative or positive direction; after the set potential is reached, the potential is ramped in the opposite direction to return to the initial potential. This cycle of ramped potential application can be repeated as many times as desired. For the PAD

method, a working potential is applied for a short time, followed by higher or lower potentials that are used to trigger the reversible switching of the potentials.[141]

In this thesis, electrochemical analysis was performed on a workstation (Palm Instruments, Netherlands) from a home-made electrochemical cell as a three-electrode system with a pseudo-reference electrode (Pt).

2.2 Materials, general experiments

2.2.1 Materials

2.2.1.1 Chemicals

Copper acetate monohydrate (Cu), 1,3,5-benzenetricarboxylic acid (BTC), benzene-1,4-dicarboxylic acid (BDC, 98%), 1,4-diazabicyclo[2.2.2]octane (Dabco, 99%), ferrocene (Fc), Prussian Blue (PB), 16-mercaptohexadecanoic acid (MHDA, 97%), hexadecane (HD), and hexadecanethiol (HDT), acetate acid, dichloromethane (99.8%) were obtained from Sigma-Aldrich (Germany) and used without further purification.

5,15-diphenyl-10,20-di(4-carboxyphenyl)porphyrin (free base porphyrin), and Pd(II) 5,15-diphenyl-10,20-di(4-carboxyphenyl)porphyrin (Pd porphyrin) were purchased from Livchem Logistics GmbH (Germany) and used without further purification.

The iodine/triiodine solution (I^-/I_3^-, 50 μM, Iodolyte AN-50) was purchased from SOLARONIX (Switzerland).

Ethanol (99.99%) was purchased from VWR (Germany).

Ionic liquid 1-Butyl-3-methylimidazolium bis(trifluoromethylsulfonyl)imide (99.5%) was purchased from IOLITEC (Germany).

Platinum wires were purchased from Advent Research Materials Ltd (UK).

2.2.1.2 Substrates

The silicon substrates with a [100] orientation: (i) single-face polished single crystal silicon wafers were obtained from Silicon Sense (US) for general use; (ii) double-faces polished silicon wafer (thickness: 525 ± 20 μm; specific resistivity: 8−12 Ω/cm) were purchased from Silchem Handelsgesellschaft GmbH (Germany). They were treated by O_2 plasma (Diener Plasma, by using 50 sccm pure O_2) for 30–40 min to remove impurities as well as to increase the number of -OH functional groups before use.

The gold substrates were obtained from Georg Albert PVD (Silz, Germany). They were prepared by thermal evaporation of 100 nm of gold (99.99% purity) onto polished single crystal silicon (100) wafers (Silicon Sense) using a 5 nm titanium adhesion layer. The evaporated films were polycrystalline, with grains having predominantly a [111] orientation. The as-deposited Au substrates were kept in Ar filled containers until use.

The fluorine doped tin oxide (FTO) coated glasses and Pt coated FTO substrates (used for counter electrode) were purchased from SOLARONIX (Switzerland). In order to clean the surface and generate -OH groups on it, the FTO glass was washed in acetone and ethanol separately for 10 min and in an ultrasonic bath. Then plasma treatment under O_2 was applied for 30–40 min before use.

The indium tin oxide (ITO, 10% SnO_2 and 90% In_2O_3) substrate was purchased from Kurt J. Lesker (UK). It was treated by O_2 plasma (Diener Plasma, by using 50 sccm pure O_2) for 30 min to remove impurities as well as to increase the number of -OH functional groups before use. The QCM sensors were purchased from LOT-ORIEL (UK).

2.2.2 Preparation of SAMs

2.2.2.1 MHDA (16-mecaptohexadecanoic acid) SAM

Gold substrates were immersed into an ethanolic solution of MHDA (20 µM, in 90% ethanol and 10% acetic acid) for 72 hours at room temperature while kept in the dark. Thereafter, the substrates were rinsed with ethanol and dried under a N_2 stream to obtain MHDA SAM. The SAMs were prepared shortly before use. A schematic representation is shown in Figure 2.21.

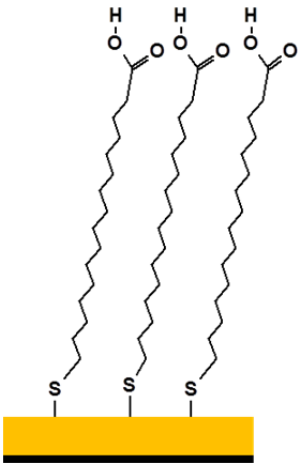

Figure 2.21 Schematic representation of the MHDA SAM on gold.

2.2.2.2 CMMT (9-carboxy-10-(mercaptomethyl) triptycene) SAM

Gold substrates were immersed into an ethanolic solution (20 µM) of CMMT for 72 hours at room temperature in the dark. Thereafter, the substrates were rinsed with ethanol and dried with an N_2 stream to obtain CMMT SAM. The SAMs were prepared shortly before use. A schematic representation is shown in Figure 2.22.

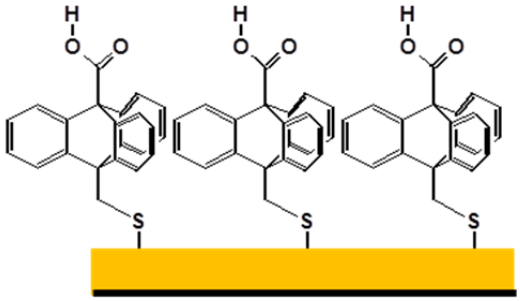

Figure 2.22 Schematic representation of the CMMT SAM on gold.

2.2.2.3 TPMTA (4'-carboxyterphenyl-4-methanethiol) SAM

Gold substrates were immersed into an ethanolic solution (20 µM, in 90% ethanol and 10% acetic acid) of TPMTA for 72 hours at room temperature and in the dark. Thereafter, the substrates were rinsed with ethanol and dried with an N_2 stream to obtain the TPMTA SAM. The SAMs were prepared shortly before use. A schematic representation is shown in Figure 2.23.

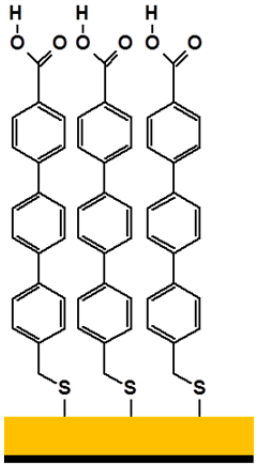

Figure 2.23 Schematic representation of the TPMTA SAM on gold.

2.2.3 Production of SURMOFs

2.2.3.1 HKUST-1 grown on SAMs (CMMT, MHDA and TPMTA) modified Au substrates

The liquid phase epitaxy (LPE) grown HKUST-1 SURMOFs with different thickness were prepared on SAMs (CMMT, MHDA and TPMTA) modified Au substrates by the spraying method according to the procedure reported in the literature.[86] Copper acetate (1 mM in ethanol) and 1,3,5-benzenetricarboxylic acid (BTC, 0.1 mM in ethanol) were alternately sprayed on the target SAMs (CMMT, MHDA and TPMTA) for 15 and 20 s, respectively. After the spraying of each component, the coordination of reactant was allowed for another 25 s before the target was abundantly rinsed with ethanol to remove any unselectively bound material. The alternatively spraying of the metal and linker solutions (i.e. a cycle) was then repeated 5, 7, 10, 15 and 20 times to produce HKUST-1 SURMOFs samples of specific thickness.

2.2.3.2 HKUST-1 grown on Silicon or ITO substrates

The liquid phase epitaxy (LPE) grown HKUST-1 SURMOFs with different thickness were prepared on Silicon and ITO substrates by the spraying method described previously. Copper acetate (1 mM in ethanol) and 1,3,5-benzenetricarboxylic acid (BTC, 0.1 mM in ethanol) were alternately sprayed on the targeted Silicon or ITO substrates for 20 and 30 s, respectively. After the spraying of each component, 25 s was allowed for further coordination of the reactant before the target was abundantly rinsed with ethanol to remove any unselectively bound material. The spraying of the metal and linker solutions was then repeated 20, 26, 34, and 40 cycles to get HKUST-1 SURMOFs samples, each with a different thickness.

2.2.3.3 Porphyrin-based SURMOF 2 grown on FTO substrate

A concentration of 20 μM 5,15-diphenyl-10,20-di(4-carboxyphenyl)porphyrin (free base porphyrin) or Pd(II) 5,15-diphenyl-10,20-di(4-carboxyphenyl)porphyrin (Pd porphyrin) in ethanol (spray time: 25 s, waiting time: 35 s) and a concentration of 1 mM zinc acetate in ethanol (spray time: 15 s, waiting time: 35 s) were sequentially deposited onto the substrates in a layer-by-layer fashion. In between, pure ethanol was used for rinsing to remove unreacted or byproducts species from the surface (rinsing time: 5 s). The thickness of the sample was controlled by the number of deposition cycles. All the samples were prepared at room temperature.

2.3 Theoretical analysis

Theoretical calculations were contributed by Prof. Fabian Pauly and Mr. Andreas Irmler from University of Konstanz.

In order to gain insight into the electronic structure of HKUST-1, density functional theory (DFT) calculations were done with the program package TURBOMOLE.[142] The def-TZVP basis set and the B3-LYP hybrid functional with empirical dispersion corrections was used.[143, 144] It has been shown that this exchange-correlation functional leads to a good description of the fragments of the HKUST-1 MOF.[145]

In order to understand the charge transport mechanism in SURMOFs and to explain the shallow dependence of conductance on length, one-dimensional (1D) toy model was established to describe the transition from tunneling to hopping conduction.[146] The SURMOF is modeled by a 1D chain. The chain sites correspond to the Cu_2 centers, and the coupling of adjacent sites (only nearest neighbor couplings are considered) is *via* the benzene moiety of the trimesic acid linker. It takes dephasing into account by connecting each chain site to an external, phase-randomizing reservoir.

3 Electronic Properties of SURMOFs and Their Applications

3.1 Electric transport properties of HKUST-1 and the effect of Fc loading

3.1.1 Background

MOFs have been considered as possible components of electronic devices,[58, 59, 93, 94] with either an active electronic role (being involved in the charge transport) or a mere supplementary role (as porous scaffolds), in fuel cells,[97] batteries[95, 96] and capacitors.[98] Although the foreseen potential of MOFs for electronic applications is very promising, the investigation of their fundamental transport properties is still in its incipiency.

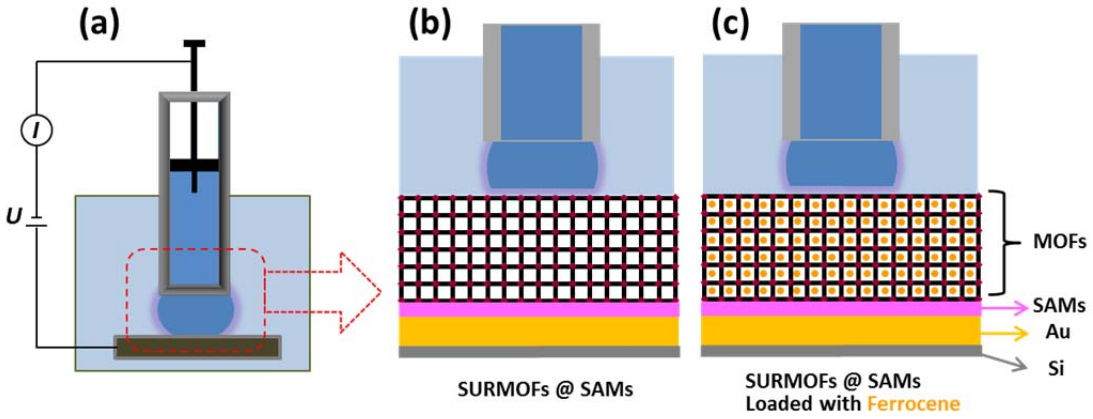

Figure 3.1 (a) Scheme of the Hg-based tunneling junction for the study on electric transport properties, (b-c) the zoomed in part from (a) for the case of pristine and Fc loaded HKUST-1 SURMOFs.

As mentioned in Chapter 2.1.9, the mercury-drop-based (Hg-based) tunneling junction method is an advantageous technique for characterizing the thin film conductivity thanks to the gentle contact of the metal electrode on the sample. Here the SURMOF HKUST-1 ($Cu_3(BTC)_2$) thin films are chosen and integrated in a Hg-based tunneling junction for electric transport properties characterization, as shown in Figure 3.1. The liquid Hg drop worked as the top electrode and SURMOF grafted gold films as bottom electrode in which the charge transport properties are investigated. Further, guest molecules mediated electric transport properties of the HKUST-1 SURMOFs are also studied by loading Fc (ferrocene) into the pores of HKUST-1.

3.1.2 Preparation of HKUST-1 SURMOFs and Fc loading

The HKUST-1 SURMOFs were prepared onto Au surface functionalized with CMMT SAMs (CMMT = [9-carboxy-10-(mercaptomethyl) triptycene], the details about the SAM preparation are described in the Chapter 2.2) by using the well-established LPE spraying method (Chapter 2.3). As already mentioned (Chapter 1.2.7), the advantage of the sequential step-by-step method is the preparation of films of adjustable thickness through varying the number of spraying cycles. For this study, 5, 7 and 10 spray cycles were applied to prepare different thickness of HKUST-1 SURMOFs, and the produced thickness was measured by means of AFM as described below.

One of the characteristics of MOFs and SURMOFs is their porosity, hence their ability to act as host for small molecules. In the context of electronic applications, it has been demonstrated that certain guests can modulate and increase the conductivity of the hosting framework.[101, 102, 147] For example, the electrical transport properties of HKUST-1 films can be enhanced by inserting electroactive species and small molecules, such as iodine[147] or TCNQ[102] into the framework's cavities. The loading leads to a huge increase of the conductivity in comparison to the undoped films (about 2 orders of magnitude after iodine loading[147] and six orders of magnitude after TCNQ[102]). In both cases, the increase in electrical conductivity has been explained through the strong interaction between the MOFs and the guest molecules.

Ferrocene molecules have also been used for electroactive guest loading. For instance, electrical transport properties of oriented HKUST-1 thin films have been studied on the basis of cyclic voltammetry experiments.[101] It was also found that the conductivity of HKUST-1 is improved after Fc loading. The explanation is that Fc molecules act as redox mediators, and the Fc molecules immobilized in the pores of the framework trigger a charge hopping transport mechanism.

In this part, HKUST-1 SURMOF thin films with different thickness were used for Fc loading. The loading was conducted according to the literature.[101] Firstly, the activation of SURMOFs, to remove residual solvent molecules trapped inside the pores for achieving efficient loading, is required. The pristine HKUST-1 SURMOF thin films were placed in a small vessel and heated to 60 °C in air for 20 minutes for solvent evaporation. Thereafter the samples were exposed immediately to a vapor of Fc at room temperature for 72 hours for the loading.

3.1.3 Characterization of the pristine and Fc-loaded HKUST-1 SURMOFs

3.1.3.1 XRD of the HKUST-1 before and after Fc loading

All the films of HKUST-1 SURMOF were characterized by out-of-plane XRD after preparation. For XRD measurement, scans were set from 5° to 20° (*2θ*) with a step width of 0.024° and 16.4 seconds per step. In order to compare the measured intensity for different spray cycles, the same sample was used for each XRD measurement. In all cases, the obtained SURMOF films exhibited the expected high orientation along [111] with high quality (Figure 3.2, black line), as shown by the presence of the characteristic (111), (222) and (333) peaks (with *2θ* of 5.84°, 11.67° and 17.54°, respectively).

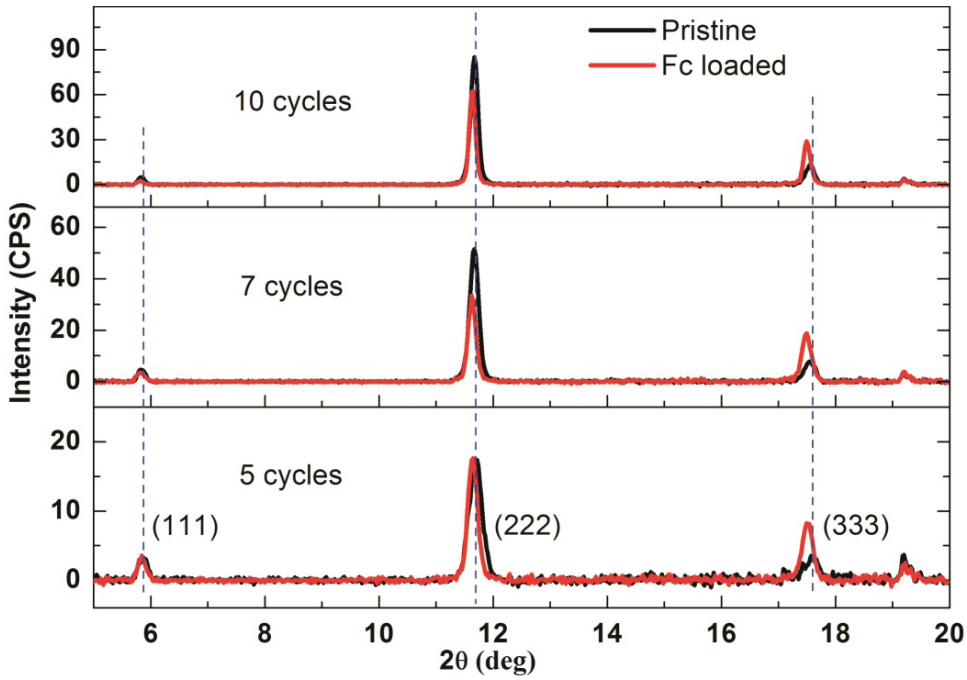

Figure 3.2 Out-of-plane XRD data of HKUST-1 SURMOFs, pristine (black) and Fc-loaded (red). From top to bottom: 10, 7, and 5 spraying cycles.

XRD results of the ferrocene loaded HKUST-1 SURMOFs are also presented in Figure 3.2 (red). After loading with Fc, a decrease in the intensity of the (222) peak and an increase in the intensity of the (333) peak occurred, as shown in Figure 3.2. The changes in the relative intensities of the (222) and (333) peaks can be attributed to the changes in structure form factor associated with incorporation of Fc molecules in the pores of HKUST-1, since the Fc which loaded in the pores of HKUST-1 has also strong scatter of X-rays.[109]

It is also clearly shows that the intensity of the recorded XRD patterns increases with the number of the spray cycles applied, which can be correlated with the size of the coherent scattering domains. The SURMOF thickness is actually increased by increasing the spraying cycles from 5 to 10, suggesting that the vertical dimensions of the ordered domains are noticeably larger.[86]

Not only the information about the MOF structures can be provided by XRD pattern, but also more details such as the coherent scattering domain size, the lattice constant, as well as stress and strain in crystals, can be obtained. The analysis of these parameters from the HKUST-1 SURMOFs before and after Fc loading are presented below and compared with AFM results.

3.1.3.2 IRRAS of the HKUST-1 before and after Fc loading

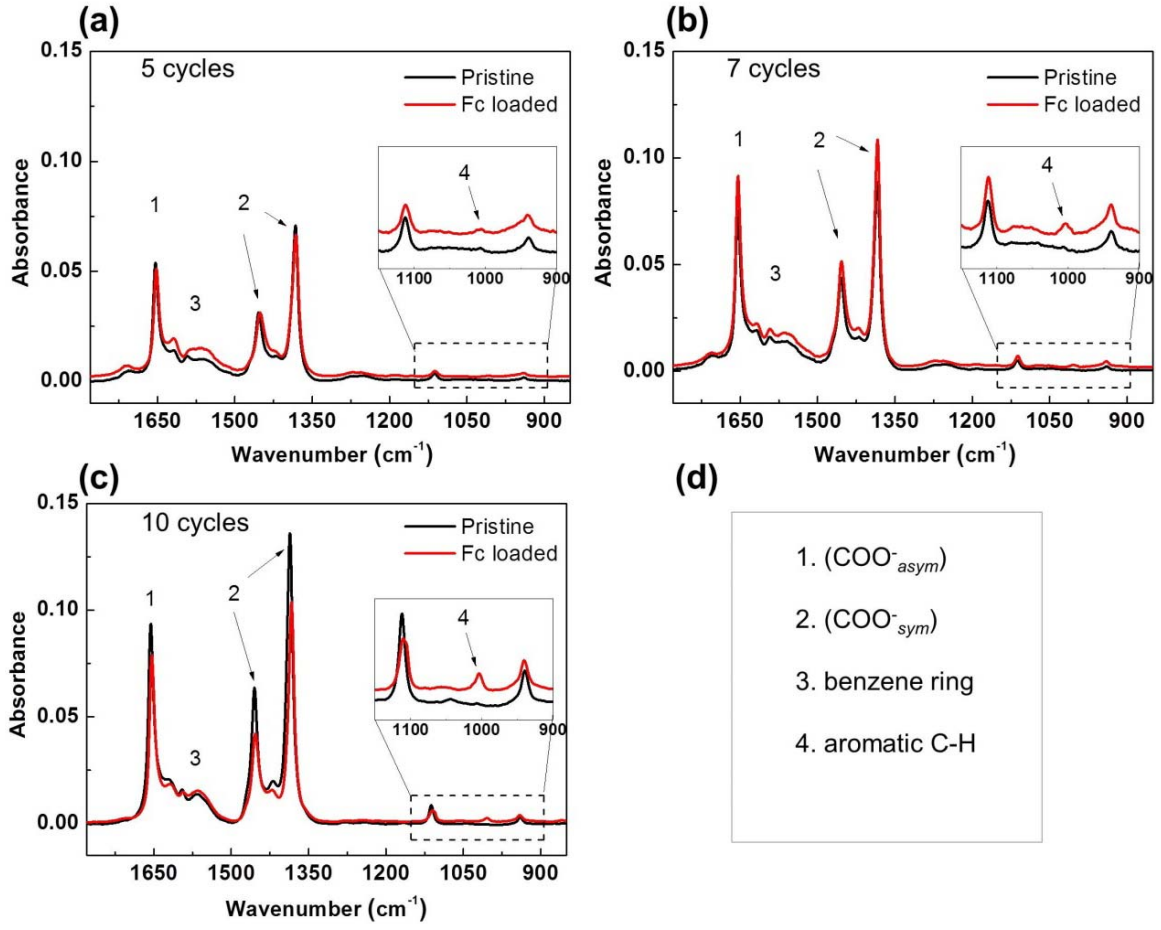

Figure 3.3 IRRAS of HKUST-1 SURMOFs with different spray cycles before and after Fc loading: (a) 5 cycles, (b) 7 cycles, (c) 10 cycles; the attribution of different features from HKUST-1 are presented in (d).

The IRRAS of all the HKUST-1 SURMOF thin films with different spray cycles (representing different thickness which was confirmed by AFM, as described below) were checked before and after Fc loading (Figure 3.3).

Figure 3.3(a-c) shows the IRRAS of HKUST-1 SURMOF thin films with different spray cycles before and after Fc loading. It can be clearly seen from the spectra that the intensity of IRRAS increases with the number of the spraying cycles applied. That means the more spray cycles are applied the thicker the SURMOFs are grown; this results in the contribution to the IRRAS intensity. But the band positions as well as the relative intensity of the different features are rather identical and correspond to the same HKUST-1 SURMOF structures.

The characteristic absorption bands of the pristine HKUST-1 SURMOF thin films are attributed as following: the band at 1656 cm^{-1} is attributed to COO_{asym}; 1619, 1595 and 1564 cm^{-1} attributed to benzene ring; 1455 and 1386 cm^{-1} attributed to COO_{sym}; 1112 and 940 cm^{-1} attributed to aromatic C-H. After loading with ferrocene (red curves) a new absorption band at 1004 cm^{-1} was observed, and originated the C-H in-plane bending of the ferrocene ring.

3.1.3.3 Characterization of film thicknesses by AFM before and after Fc loading

A tapping-mode AFM measurement was performed to measure the thickness of the HKUST-1 SURMOF thin films. The applied cantilever is a NSC18 (Mikromasch HQ), and the scan rate was 0.4 Hz at a 70 × 70 μm scan size under ambient laboratory conditions (21-24 °C).

In order to have an internal reference for the height measurement, a small area of the SURMOF samples was removed by chemical etching (immersion into nitric acid 0.2 mM for about 2 s, then immediately rinsed with ethanol and dried under N_2 stream), leaving the gold surface underneath exposed.

Figure 3.4 depicts the AFM topographic images of the produced depth (left) of HKUST-1 SURMOF thin films with different spraying cycles and the corresponding cross-section analysis (right). The difference in height between this area and the area with the SURMOF has been used to measure the sample thickness, as shown in Figure 3.4(a-c), resulting in the thickness of HKUST-1 SURMOFs of 45.6 ± 6.4 nm, 58.3 ± 6.3 nm, and 71.6 ± 9.9 nm for the 5, 7, and 10 spraying cycles, respectively.

The same procedures were followed to measure the thickness of the ferrocene loaded

samples. Film thicknesses of 46.2 ± 5.7 nm, 58.6 ± 7.0 nm, and 72.2 ± 4.0 nm were found from the same 5, 7, and 10 spraying cycles, respectively, of the sample loaded with ferrocene (Figure 3.4(d-f)). As expected, no difference in the SURMOF thickness is observable before and after ferrocene loading.

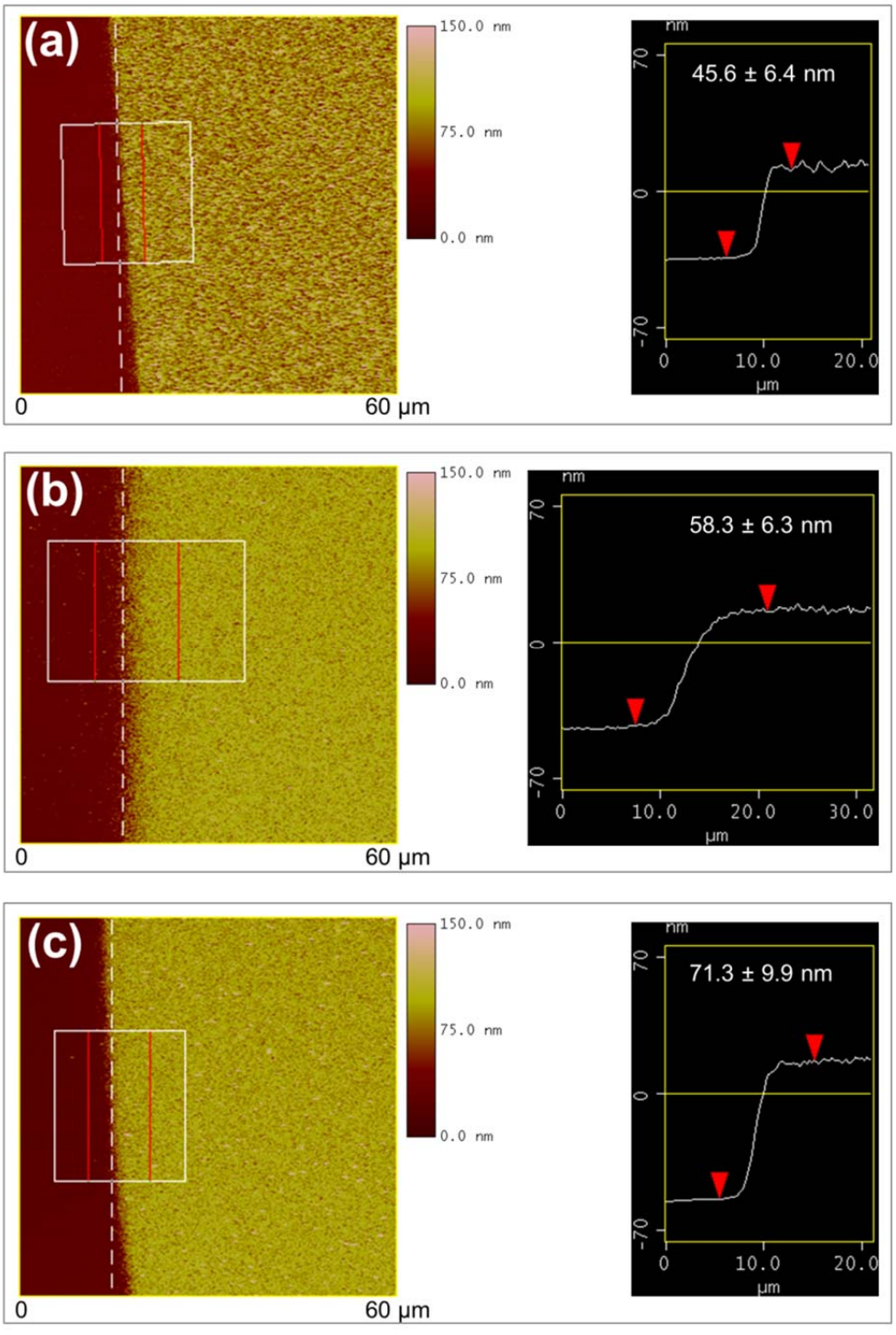

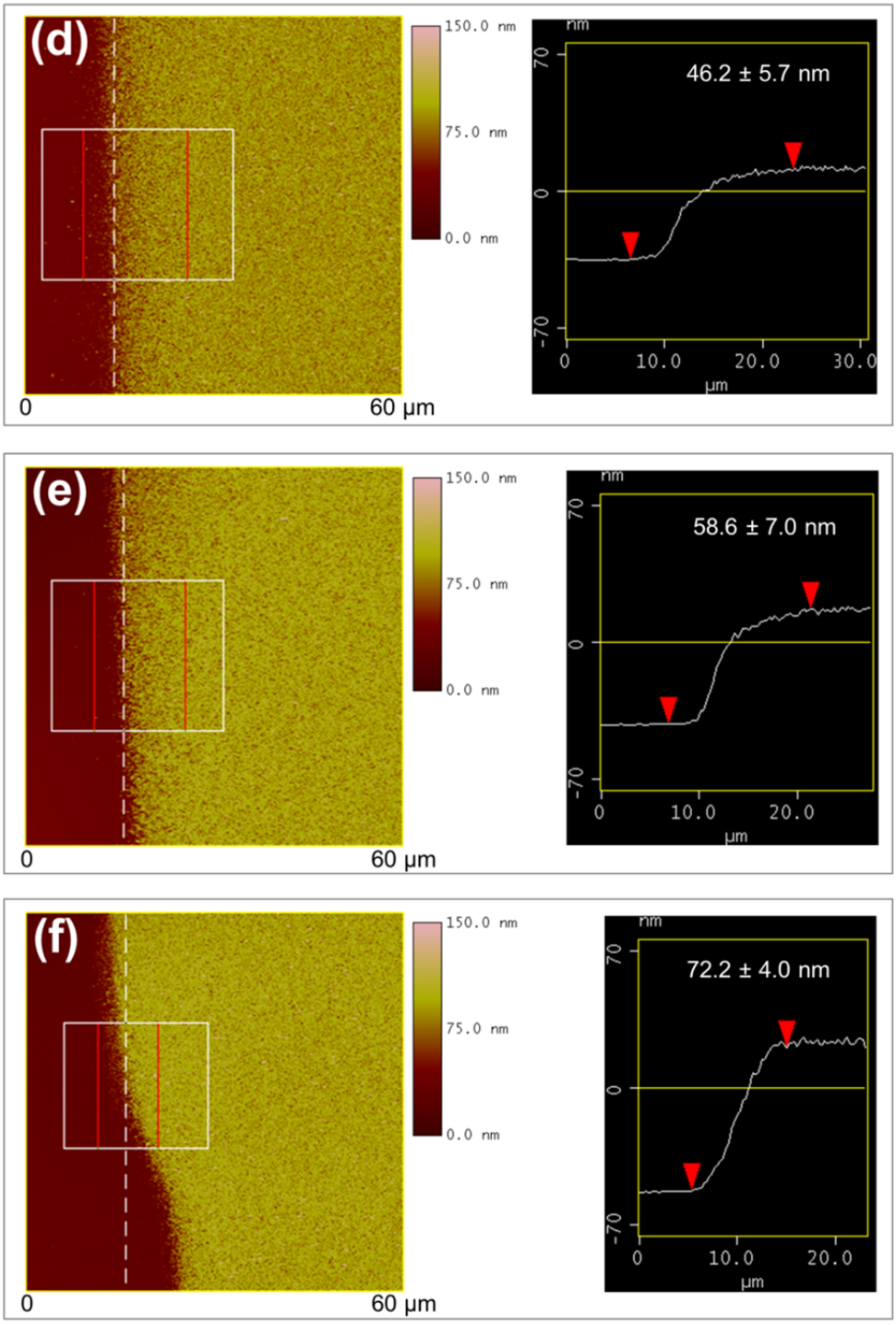

Figure 3.4 AFM topographic images (left) and cross-section analysis (right) of HKUST-1 SURMOFs with different spraying cycles. (a-c) 5, 7, and 10 spraying cycles of the pristine HKUST-1 SURMOFs; (d-f) Fc loaded HKUST-1 SURMOFs for the same samples of 5, 7, and 10 spraying cycles. An average thickness value is analyzed within the white frame (left). The thicknesses are determined by the number of spraying cycles, and the error of thickness is given by roughness average (Ra) of the AFM cross-section analysis. The removal of these HKUST-1 SURMOFs was achieved by chemical etching.

The Scherrer equation (equation (3−1)) relates the domain size of crystallites to the broadening of measured XRD peak in a diffraction pattern, which is named after Paul Scherrer.[148] It is used to calculate the domain size of crystals, and determine the coherent scattering domain size of SURMOF thin films in this case.

After a background correction, the peak position was calibrated using the position of the substrate Au(111) diffraction peak at 38.2°, which was measured additionally after sample measurement. The analysis of the data was done with the Bruker evaluation software DIFFRACT.EVA 3.0. With this software, the coherent scattering domain size of crystallites or thin film of crystallites were calculated on the basis of the Scherrer equation by using the integral breadth of the out-of-plane (222) XRD reflexes (in Figure 3.2), since this resulted in the best resolution.

$$L_{vol} = \frac{K\lambda}{B(2\theta)\cos\theta} \tag{3−1}$$

Where L_{vol} is the domain Size, θ is the diffraction angle, K is the Scherrer constant (0.89), λ is 0.15406 nm (Cu Kα_1), and $B(2\theta)$ is the integral breadth.

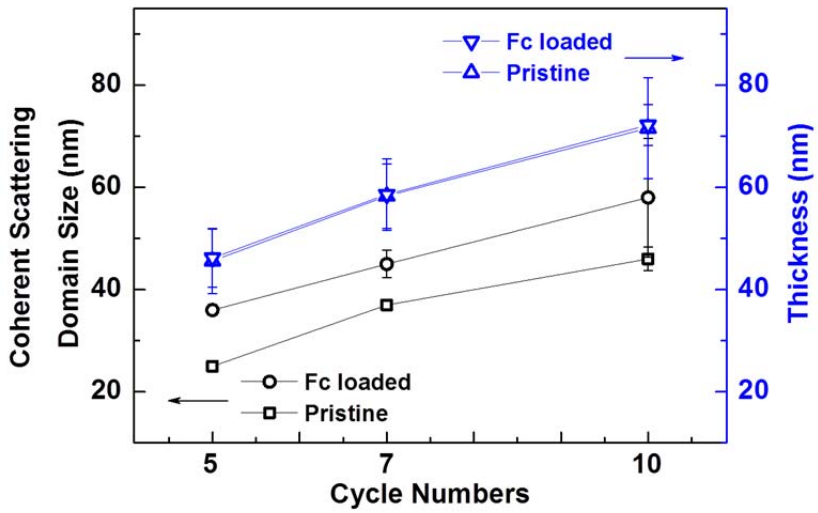

Figure 3.5 Calculated coherent scattering domain size perpendicular to substrate surface of the HKUST-1 SURMOFs for different numbers of deposition cycles before (black squares) and after (black circles) loading with ferrocene. The error bars, where not visible, are smaller than the symbols. The thickness of these HKUST-1 SURMOFs before (blue up-triangle) and after (blue down-triangle) loading with ferrocene, as determined by AFM cross-section analysis. The error bar is determined from the averaged roughness (Ra).

Since the instrumental contribution to the line broadening was considered, but no stress/strain contributions were added, the calculated coherent scattering domain size represents a lower limit. The described procedure for domain size analysis was carried out for both the pristine and Fc loaded HKUST-1 SURMOF samples. As shown in Figure 3.5, the calculated domain sizes after Fc loading appears dramatically increased for each of the spraying cycle samples. And it can also be clearly seen that the estimated film thickness (referring to the domain size) of SURMOFs is indeed lower than those measured by AFM.

However the Scherrer equation is not applicable to all kinds of crystallites, but only to those grains smaller than about 0.1 to 0.2 μm. Most importantly, not only the domain size contributes to the width of a diffraction peak, but also factors like instrumental effects, inhomogeneous strain, as well as imperfection of crystal lattice can broaden the measured diffraction peak.

These results indicate that not the physical thicknesses of these SURMOF thin films are different before and after the Fc loading, but rather the calculated domain sizes of Fc loaded HKUST-1 SURMOFs appear much larger than in the respective pristine samples. Comparing the precise lattice constants with the effect of Fc loading is thus necessary, and the results are shown in the following section.

3.1.3.4 Determination of the lattice constants for the pristine and Fc loaded HKUST-1 SURMOFs

The precise lattice constants were determined by applying the interpolation method of Taylor and Sinclair equation (3−2).[109] In this equation, α_{hkl} is unknown and is determined by equation (3−3) adapting to cubic crystal system, and the layer distance d is determined by the Bragg equation (3−4). After background correction, the Cu $K_{\alpha 2}$ contribution was stripped, and the peak position was calibrated using the Au(111) standard diffraction peak at 38.2°. Then the peak positions (i.e. the diffraction angles) were determined by the Bruker evaluation software DIFFRACT.EVA 3.0.

$$a_{hkl} = S(0.5\frac{\cos^2\theta}{\sin\theta} + \frac{\cos^2\theta}{\theta}) + a_0 \tag{3−2}$$

$$\frac{1}{d^2} = \frac{h^2 + k^2 + l^2}{a_{hkl}{}^2} \tag{3−3}$$

$$\lambda = 2d\sin\theta \tag{3−4}$$

Where α_{hkl} is the lattice constant, h,k,l is the set of Miller indices, S is the slope, θ is the diffraction angle, α_0 is the precise lattice constant, d is the layer distance, and λ is 0.15406 nm (Cu $K\alpha_1$).

As discussed in the previous section, the observed peak shift in the XRD patterns (Figure 3.2 and Figure 3.6 (a)) indicates a lattice expansion. That means the ordering of the (111) planes of the HKUST-1 SURMOFs is increased after Fc loading. This occurs as a consequence of the allocation of ferrocene molecules inside the pores.

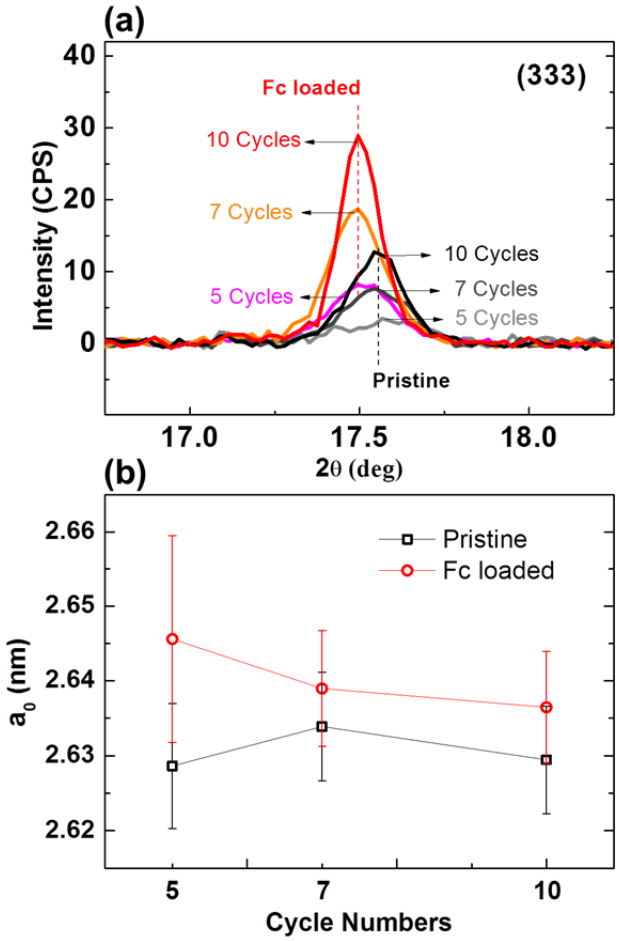

Figure 3.6 (a) Zoom in on the (333) Bragg peak of the XRD pattern to monitor the shift to lower 2θ values after the Fc loading; (b) calculated lattice constant a_0 of the cubic HKUST-1 SURMOFs for different number of deposition cycles before (black squares) and after (red circles) loading with ferrocene. The error bar is estimated to be 2 standard deviations.

However, as presented in Figure 3.6 (b), the calculated lattice constants by Taylor and Sinclair equation showed no significant change for the pristine and Fc loaded HKUST-1

SURMOFs. So the determination of the lattice constants showed that the loading with ferrocene is not responsible for an expansion of the framework, but rather for an increased ordering of the coherent scattering domains.

3.1.3.5 Stability of the HKUST-1 SURMOFs in the experimental condition

Since the electric transport properties of these HKUST-1 SURMOFs were measured by a mercury-drop method in 1 mM hexadecanethiol ($C_{16}H_{33}$-SH, HDT) solution in hexadecane (Details of the method are described in Chapter 2.1.9, and results are presented in the next section), it is necessary and important to investigate the stability of the SURMOF thin film under these experimental conditions during the electrical properties measurement.

The stability of the HKUST-1 SURMOF over time in hexadecane (with 1 mM HDT) was checked by immersion the sample for different periods of time (up to 20 hours), and the out-of-plane XRD measurement was applied to check the stability of the SURMOF structures. It can be seen from Figure 3.7 that the intensity of XRD peaks of the measured HKUST-1 SURMOF sample does not change during the 20 h immersion in the HDT solution. The positions as well as the relative intensities of the peaks show also no change. The results proved that the HKUST-1 SURMOF thin film is stable under the given experimental condition.

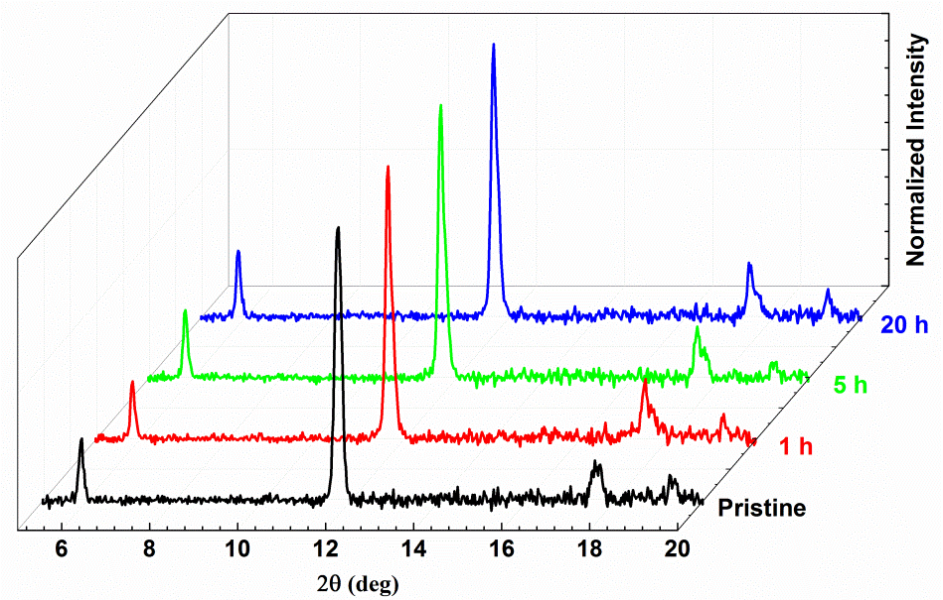

Figure 3.7 Out-of-plane XRD data of a 10 spraying cycles HKUST-1 SURMOF thin film sample before and after immersion in HDT solution in hexadecane after various amounts of time (from 1 to 20 h).

3.1.4 Assembling the mercury-drop-based tunneling junction

The electric transport properties of the pristine and guest molecules loaded HKUST-1 SURMOFs with various thicknesses were measured on the Hg-drop setup. (*Setup built by the team of Prof. Zharnikov from University of Heidelberg*. Details about the setup are described in Chapter 2.1.9).

The tunneling junction was assembled as reported in the literature.[99] The top electrode is a drop of mercury which is normally passivated with HDT ($C_{16}H_{33}$-SH) to avoid amalgamation and short circuit.[136, 139, 149] The bottom electrodes are the SAMs modified gold substrate, the series of HKUST-1 SURMOF thin films with [111] orientation with respect to the gold surface, and the same SURMOF thin films after ferrocene loading. The measurements were conducted in a cell filled with HDT in hexadecane. A scheme of the mercury-drop-based tunneling junction (Hg/HDT//HKUST-1/CMMT/Au) for investigation of HKUST-1 SURMOF thin films grown on CMMT SAM is shown in Figure 3.8.

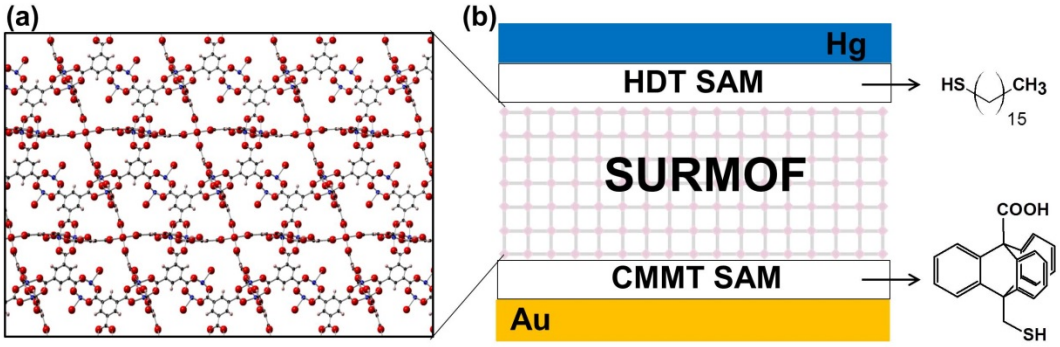

Figure 3.8 Scheme of the Hg-based tunneling junction for investigation of HKUST-1 SURMOF thin films grown on CMMT SAM. (a) Crystal structure of the HKUST-1 SURMOF grown on gold surface with [111] orientation. Oxygen, carbon, and copper atoms are coded in red, blue, and black color, respectively. (b) Schematic illustration of the contact area between the two electrodes: Hg as top electrode is passivated with a SAM of HDT, while the SURMOF thin film grown on a CMMT modified Au substrate serves as bottom electrode. The molecular formula of HDT and CMMT are presented on the right side.

Right before the measurements, the Hg-drop was prepared according to the standard protocol by immersion in 10 mM HDT solution in hexadecane for 10-15 min. The HDT passivated Hg-drop was then gently positioned on bottom electrode (the SAMs and

HKUST-1 SURMOF samples). 1 mM HDT solution in hexadecane was used to increase the stability of the drop and avoid amalgamation.[137] The whole setup was placed on a vibration isolation table and put inside a home-built Faraday cage to reduce vibrations and electrical noise, respectively.

To get the statistical and reliable results from the Hg-drop method, 3 different samples, and 5 different positions for each sample, were used for each of the tunneling junction system. For each position, 4-6 *I-V* (current-voltage) curves were recorded. All the recorded *I-V* curves were used, unless they displayed conductance values resembling a metal-metal contact that would reveal a rupture or amalgamation of the Hg-drop. In the plots, the average extracted from all the recorded curves was plotted. Data points were collected using a voltage ramp with a step size of 49 mV (between 0.01 V and 0.5 V) and a time interval of at least 5 s between individual steps.

3.1.4.1 Measuring the current flowing through the built junctions

The reliability of the set-up has to be checked before investigating the SURMOF thin films. Since the studies on electric transport properties of SAMs have shown to be a very efficient by using the Hg-drop method.[99, 136-138, 149-151] CMMT SAM on Au substrate as the bottom electrode was measured for checking the system as well as comparing with other junctions.

The current flowing through the Hg/HDT//CMMT/Au junction was measured by sweeping the bias voltage (*V*) in the negative (-0.5 V to -0.01 V) and positive range (0.01 V to 0.5 V). The contact area of the extruded Hg drop was observed with an optical microscope after depositing on top of the electrode, which has to be evaluated to calculate the current density *J* under the applied voltage *V*. Figure 3.9(a) shows the semilog plot of the current density *J* under the applied voltage *V*. The green line in the plot is the *J-V* curve of the CMMT SAM on Au electrode, and the marked blue star represents the current density at a bias voltage of 0.5 V for a nitrile-substituted phenylthiol (NC-OPE1) SAM for the sake of comparison, which is taken from reference.[99] It can be seen that the measured current density of CMMT SAMs is in good agreement with those reported for NC-OPE1 SAMs of comparable thickness, which confirmed a well grafted SAM layer.

Thereafter the HKUST-1 SURMOF thin films were assembled in the junctions (Hg/HDT//HKUST-1/CMMT/Au) at the same conditions. The semilog plot of the current density *J vs V* for different thicknesses of HKUST-1 SURMOFs is shown in Figure

3.9(b-d) as black squared line. As it can be clearly seen, the values of *J* for all the HKUST-1 SURMOF films are by far lower (by at least two orders of magnitude) than those of the CMMT SAM. This result confirms that the prepared SURMOF films (between the Hg and Au electrodes by a distance of up to about 70 nm) are compact, of high quality, and with no major defects that would otherwise cause short circuits.[101] Additionally, the measured low conductance, reflecting the poor intrinsic conductivity of HKUST-1, is in agreement with the reported value for non-oriented HKUST-1 films (around 10^{-6} S·m^{-1}).[102] The current density is decreasing with increasing film thickness (from 5 spraying cycles to 7 and 10 spraying cycles).

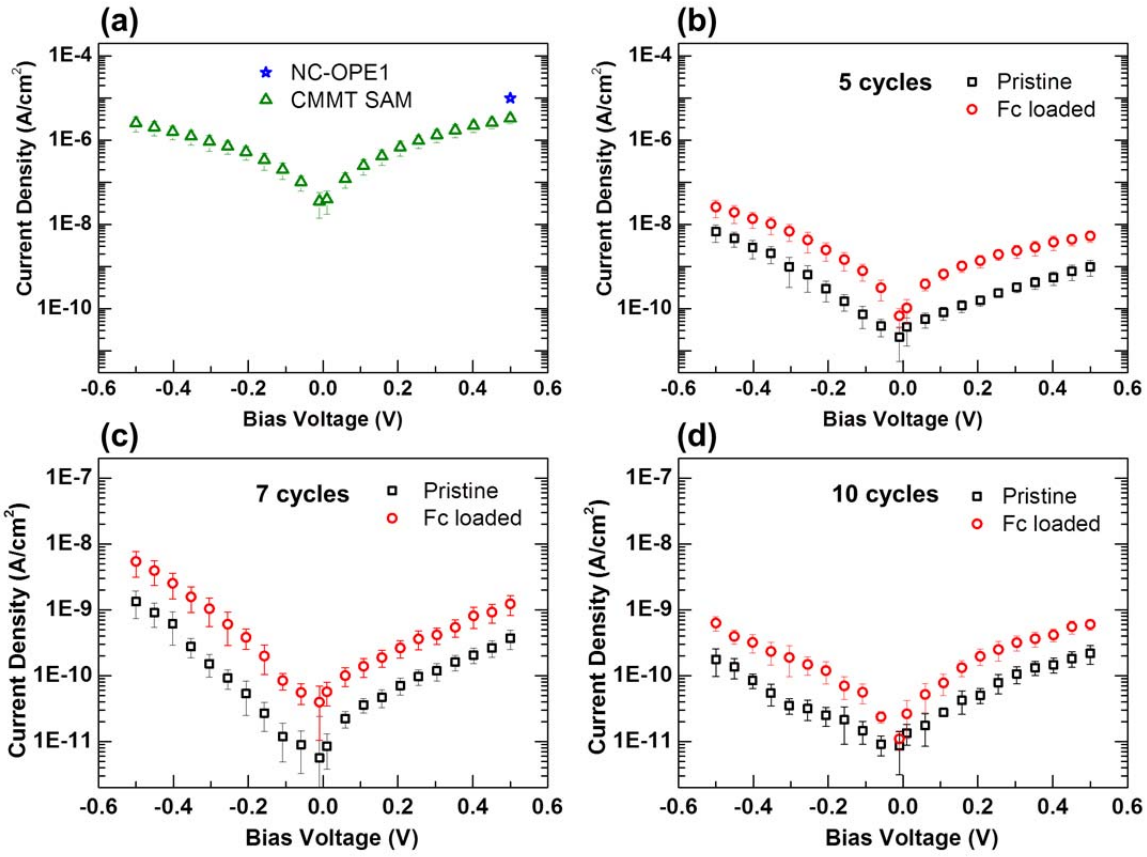

Figure 3.9 The current density changes depend on the applied voltage: (a) *Log(J) vs V* plot of CMMT SAM on Au substrate as green empty triangles. The blue star represents the current density at a bias voltage of 0.5 V for a nitrile-substituted phenylthiol (NC-OPE1) SAM,[99] which has a comparable thickness to the CMMT SAM and is given for comparison; (b-d) *Log(J) vs V* plot of HKUST-1 SURMOF prepared by 5 (b), 7 (c) and 10 (d) spraying cycles, before (black squares) and after (red circles) the loading with ferrocene.

In order to study the conductivities of these HKUST-1 SURMOFs with the effect of Fc loading, the Hg/HDT//Fc-HKUST-1/CMMT/Au junctions were built under the same condition as described above. The current flowing through the junctions of Fc loaded HKUST-1 SURMOFs were measured for the same thicknesses (5, 7 and 10 spraying cycles) as in the case of the pristine HKUST-1 SURMOFs. As it can be seen in Figure 3.9(b-d) red colored plots, the *J* values are always larger for the Fc-loaded HKUST-1 SURMOFs than for the corresponding pristine HKUST-1 SURMOFs. It was found that the loading with ferrocene results in an increase of the current density. Analyzing the values at the highest bias voltage (0.5 V), the current densities of the ferrocene loaded HKUST-1 SURMOF thin films are increased by a factor of 5.4, 3.3, and 2.8 for the samples obtained with 5, 7, and 10 spraying cycles, respectively.

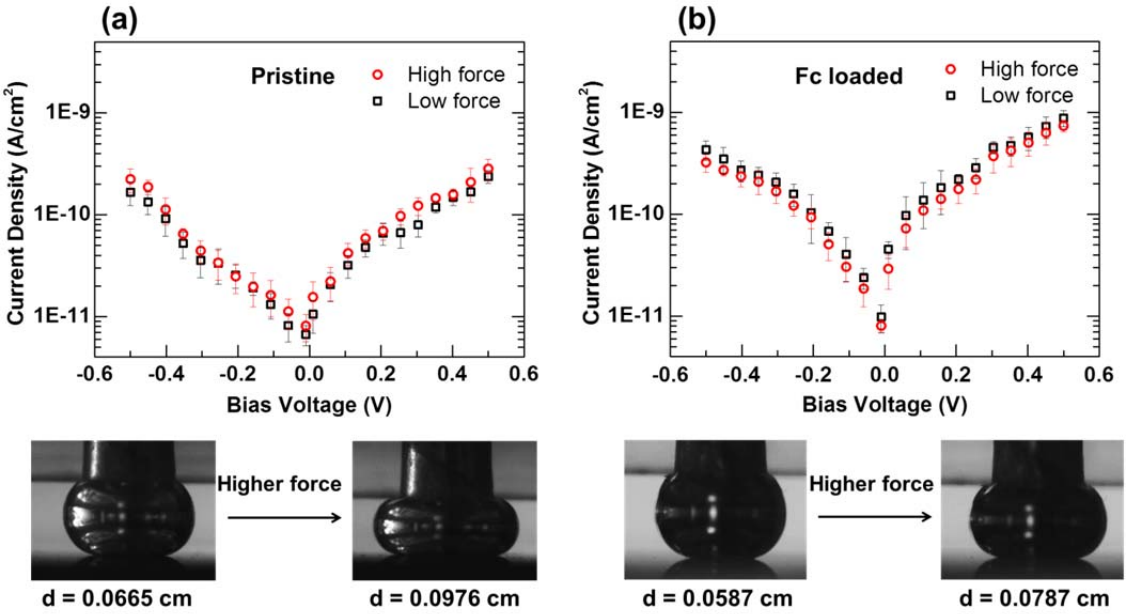

Figure 3.10 The current density *vs* voltage depends on applied forces during the electric conductivity measurement, as seen here on a 10 deposition cycle HKUST-1 SURMOF film: (a) *Log(J) vs V* plot with small (black squares) and high (red circles) applied force on the pristine sample, and (b) the corresponding Fc loaded sample. At the bottom of each plot, the microscope images of the Hg drop extruded from the gastight Hamilton syringe are shown.

Furthermore, a specific characteristic of the Hg-drop method is the possibility to tune the force applied on the bottom electrode to investigate the role of pressure on the conductance. Taking advantage of the property, the current density as a function of the

bias voltage between the mercury drop and HKUST-1 SURMOFs have been tested by varying the pressure applied through the drop on the SURMOF (Figure 3.10). At the bottom of each plot, the microscope images of the Hg drop extruded from the gastight Hamilton syringe showed the shape of Hg. As it can be seen, the diameter of the drop increases as well as the area touched by the mercury by applying a higher force. No significant changes in the value of the current could be measured, thus suggesting that the prepared HKUST-1 films are robust. This exemplifies the very favorable mechanical properties of monolithic SURMOF thin films already demonstrated by indentation experiments.[152]

3.1.4.2 Analyzing of the electric transport properties of the HKUST-1 SURMOFs before and after ferrocene loading

Insight into the charge transport mechanism within the MOFs could be obtained by taking advantage of the deployed setup combined with the possibility to adjust SURMOFs film thickness. Correlation between the measured current density J at a fixed voltage (or the measured conductance G per area A, where $G \cdot V/A = J$) with the thickness of the probed film were investigated. As shown in Figure 3.11, an overview over the transport data (from Figure 3.9) is presented, where the values of the current densities for the HKUST-1 SURMOFs are plotted against the film thicknesses at the bias voltage of 0.5 V before (black squares) and after (red circles) loading with ferrocene.

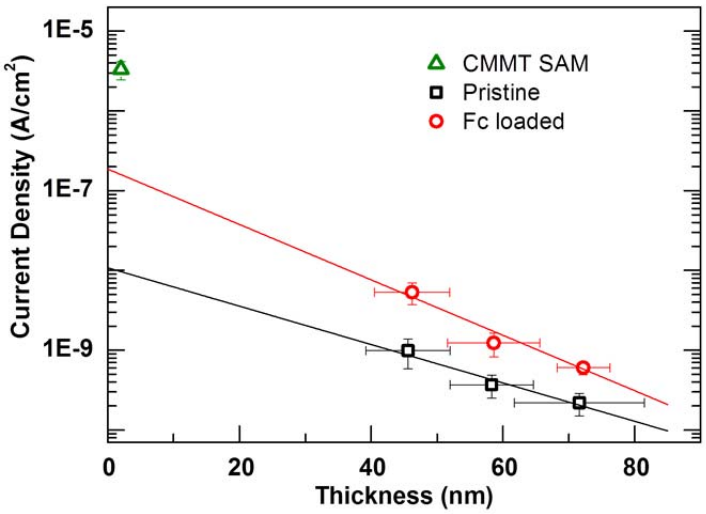

Figure 3.11 Logarithm of current density at 0.5 V depends on thickness of HKUST-1 SURMOF thin films, pristine (black empty squares) and after Fc loading (red empty circles). The green triangle marks the current density for the CMMT SAM.

It can be seen that the values of the current density increased noticeably upon loading the Fc for all three investigated HKUST-1 SURMOFs, and that the increase of conductance for the thinnest sample is larger (5.4 times) than for the thickest one (2.8 times). Moreover, there is a progressive decrease in the current density with increasing film thickness for both pristine and Fc-loaded samples. This result confirms that a thicker film results in a lower electrical conductivity, since increasing gap between the electrodes rises the resistance. The data are in agreement with the theoretical model presented below (vide infra the theoretical analysis).

Indeed, analogously to what is generally done for SAM based junctions (metal-molecule-metal junctions) by the Hg-drop method, the slope β of a linear fit of the semilog plot of J at a specific voltage value as a function of film thickness could be extracted from the experimental data (Figure 3.12(a)).[99, 100, 138-140, 150] The slope is also called "tunneling decay constant" or "attenuation factor". These terms will be used for reasons of compatibility with the literature, even if that charge transport in the SURMOF layers may be due to hopping as discussed further below.

As the β value is estimated from *ln(J)* as a function of thicknesses for a specific voltage, it is important to analyze the dependence of β on the variation of applied voltages. As presented in Figure 3.12(b), the β values at various bias voltages are rather similar. Since no significant variation was observed, β at 0.5 V as specific value for V was chosen for comparison. This is in analogy to what is reported in the literature for SAMs in Hg-based tunneling junctions.[99]

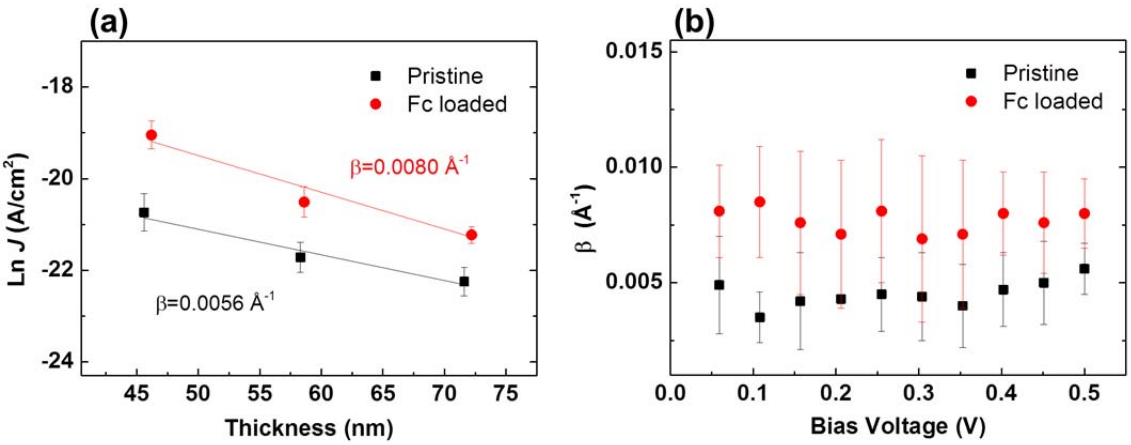

Figure 3.12 (a) Plot of *ln(J) vs* thicknesses of HKUST SURMOFs. From the slope of the linear fit the value of the decay factor β has been extracted. (b) Plot of β *vs* applied bias voltage in the range of 0.06 to 0.5 V.

With respect to those of SAMs[99, 136-139, 149, 150] consisting of short, purely organic molecular wires, the obtained attenuation factor β of the pristine HKUST-1 (*ca* 0.006 Å^{-1}) is extremely low, but it is consistent values found for "longer" organic molecular wires[139] or metal-organic molecular wires of a length up to 40 nm.[100] In these latter systems, low-lying energy states have been provided by incorporating easily oxidizable metal centers in the organic backbone; those appears involved in a multistep charge hopping mechanism to yield a linear increase of the resistance with the length (or conductance *vs* inverse length).[100] However, for the Fc loaded SURMOF samples, a similar dependence of the current density values on the film thickness as for the pristine samples was observed, as presented in Figure 3.12(a). It can be seen that the evaluated β value of the Fc loaded HKUST-1 is slightly increased (*ca* 0.008 Å^{-1}). The β values at various bias voltages are quite similar for both the pristine and Fc loaded HKUST-1 SURMOFs Figure 3.12(b), and appears, within the error bars, to barely change.

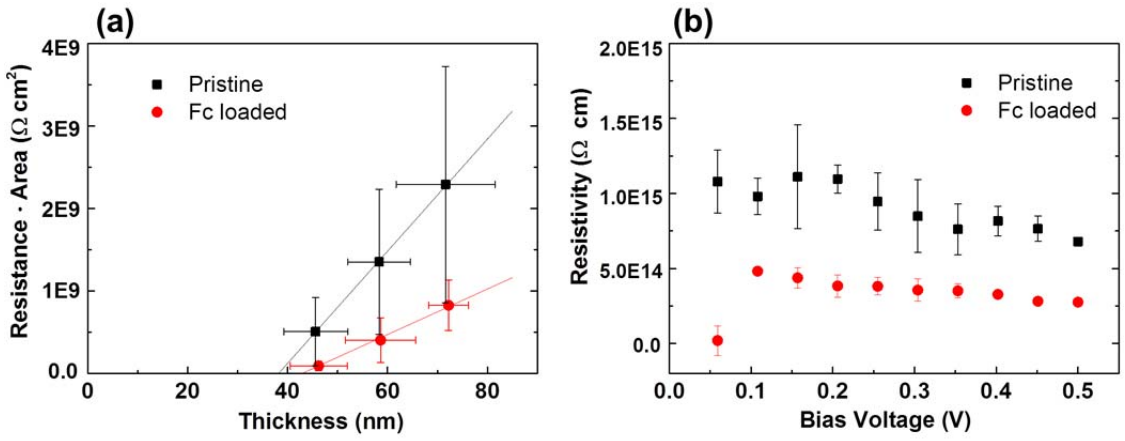

Figure 3.13 (a) Plot of the resistance times area ($R{\cdot}A$) as a function of film thickness (L) of HKUST-1 SURMOFs, pristine (black squares) and after Fc loading (red circles). The data is obtained as V/J at V=0.5 V (where $R{\cdot}A = V/J$). Straight lines show fits according to $R{\cdot}A=R_c{\cdot}A+\rho{\cdot}L$, from which the resistivity ρ can be extracted. (b) Plot of ρ *vs* applied bias voltage in the range of 0.06 to 0.5 V.

As mentioned previously, the conductance G per area A is related to J by $G{\cdot}V/A=J$, so the resistance (R) can be defined in $R = V/A{\cdot}J$. Since a linear relation $R{\cdot}A=R_c{\cdot}A+\rho{\cdot}L$ (where R_c is the contact resistance, ρ is the resistivity, and L is the film thickness) can be used to estimate the resistivity (ρ), the resistance times area ($R{\cdot}A$) *vs* film thickness (L) of HKUST-1 SURMOFs at 0.5 V can be plotted as in Figure 3.13 (a). A high resistivity ρ of $6.8{\cdot}10^{12}$ Ω·m was obtained for the pristine HKUST-1 SURMOFs from the linear fit. For

this assembled junction, R is the resistance of the whole Hg/HDT//HKUST-1/CMMT/Au system. It consists of the resistance of the SURMOF film $\rho \cdot L/A$ of thickness L and any other resistances in series with the system that are summarized with the contact resistance R_c. This contact resistance will contains for instance contributions from transport through the HDT and CMMT layers combined in the junction, as described in the schematic illustration of Figure 3.8. Since only the thickness of the SURMOF films has been varied for this system, R_c in other parts of the system may arise from hopping, tunneling or mixt phenomena. The results are compatible with the linear ohmic increase as expected for a charge hopping mechanism.

For the Fc loaded SURMOFs as shown in the Figure 3.13(a) red plot, the data is again compatible with a linear increase of the resistance with the film thickness. However, the resistivity ρ of $2.8 \cdot 10^{12}$ $\Omega \cdot$m is lower than that of the pristine sample by a factor of around 2.5. The results also support the charge hopping mechanism as leading conduction mechanism for the Fc-loaded HKUST-1 SURMOFs. Figure 3.13 (b) presents the behavior of ρ for different bias voltages V, which shows a comparatively stable resistivity for both pristine and Fc loaded HKUST SURMOFs.

The linear, algebraic increase of resistance of the HKUST-1 SURMOFs with film thickness (Figure 3.11) is generally not compatible with the exponential increase of the resistance with the sample thickness which is expected for coherent tunneling. Attempts to fit the data with the exponential decay law $G=G_c \cdot \exp(-\beta \cdot L)$ yield β values as low as 0.006 $Å^{-1}$ for pristine HKUST-1 SURMOFs (Figure 3.12(a)). This corresponds to an effective tunneling barrier φ of 0.034 meV, if $\beta=2(2m_e\varphi)^{1/2}/\hbar$ (with the electron mass m_e) is use.[153] Such a vanishingly small tunneling barrier would imply a good conduction due to molecular states being in resonance with the Fermi level of the Hg/HDT//HKUST-1/CMMT/Au system, an assumption which is not valid here. Thus coherent tunneling does not adequately describe the data. Considering the reported insulating behavior[101, 102] together with the measured high resistivity, an off-resonant hopping transport in the HKUST-1 films has been concluded. Nevertheless, a slight increase (0.008 $Å^{-1}$) of the β values for the Fc loaded HKUST-1 SURMOFs was observed. The slightly larger beta value for the Fc loaded samples led to a decrease of the conductance ratio with the increase of film thickness. The better conductivity measured after the Fc loading suggests that the ferrocene had an effect on the electronic properties of HKUST-1. This appears in agreement with the proposed theoretical model, where an increase towards the Fc loaded case is proposed (see below the theoretical analysis).

3.1.6 Theoretical analysis of charge transport mechanism

Theoretical calculations were contributed by Prof. Fabian Pauly and Mr. Andreas Irmler from University of Konstanz. The detailed analyses are presented in ref;[154] here only a short description and discussion is given.

3.1.6.1 Electronic structure analysis

To gain insight into the electronic structure of HKUST-1, density functional theory (DFT) calculations were performed. For a fragment with six Cu_2 centers, the frontier orbitals were either localized on one (or maximally two) of these centers or on the organic linker. Therefore a minimal unit with two Cu_2 centers connected by an organic linker was studied. For the linkage of the Cu_2 centers in the MOF, four oxygen pairs are connected to each of the metallic nodes. In this situation, there are low-lying unoccupied states at energies of around -5.1 eV. For this reason each Cu_2 center was saturated with two ethanol molecules. In the experiments, they are available due to the ethanol solutions used in the synthesis. They are strongly bound with a binding energy of around 2 eV per ethanol. The chosen geometry and frontier orbitals are presented in Figures 3.14 and Figure 3.15.

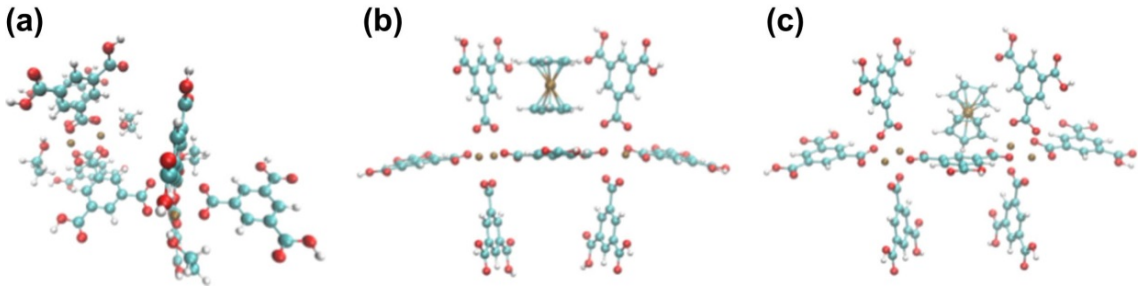

Figure 3.14 DFT calculations on MOF structure: (a) Investigated fragment with two Cu_2 centers connected by the organic linker. Each Cu_2 is saturated with two ethanol molecules. (b,c) Two possible configurations of ferrocene inside the MOF.

To determine the influence of Fc on the electronic structure of the MOF, one Fc molecule was added inside the pore. The Fc approaches the border of the pore in the geometry optimization process when added to the middle. Different configurations of the Fc relative to the MOF were studied. The geometry shown in Figure 3.14(b) seems to be the most favorable position, where the carbon rings of the Fc are parallel to those of the benzene-based linkers through π-π stacking interactions, leading to occupied states within the band gap of the MOF in terms of the electronic structure.

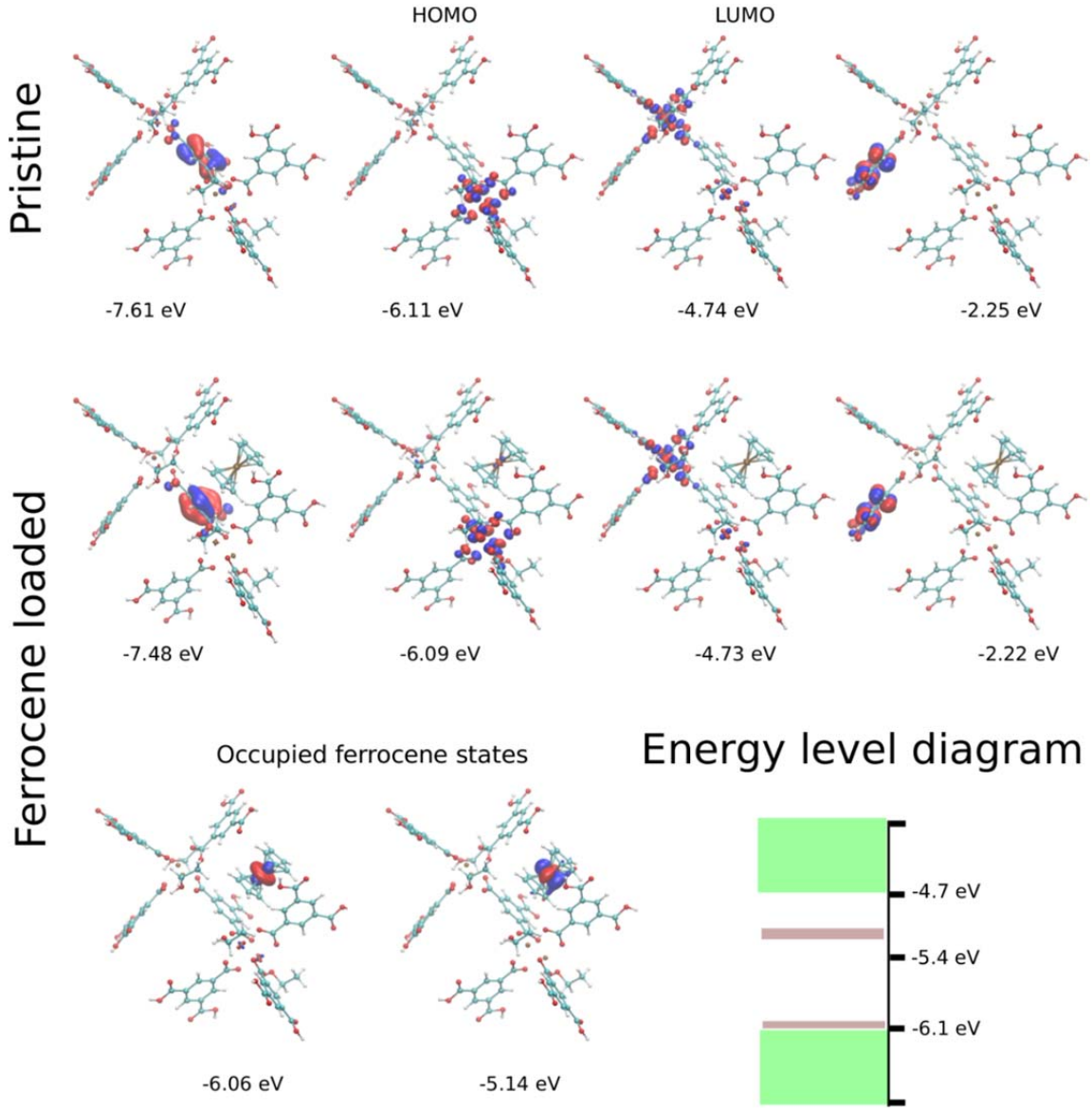

Figure 3.15 Upper row: frontier orbitals of the pristine MOF. In the middle: frontier orbitals of the Fc loaded MOF. Bottom row: the two highest occupied orbitals of Fc loaded MOF, which are both centered on the ferrocene. The alignment of these two states with respect to the MOF states is indicated in brown in the energy level diagram.

In all of the studied systems of the ferrocene loaded MOF, the electronic structure showed only small changes of the MOF states due to the presence of the ferrocene. The main differences are localized and occupied ferrocene states inside the HOMO-LUMO gap of the MOF. No indications for delocalized molecular orbitals inside or near to the HOMO-LUMO gap were found. The selected frontier orbitals are shown in Figure 3.15.

3.1.6.2 Charge transport mechanism analysis

In order to understand the charge transport mechanism in the SURMOF and to explain the shallow dependence of conductance on length, a 1D toy model that describes the transition from tunneling to hopping conduction was studied,[146] as shown in Figure 3.16. The SURMOF is modeled by a 1D chain. The model takes dephasing into account by connecting each chain site to an external, phase-randomizing reservoir. Assuming off-resonant transport, a transition from a fast, exponentially decaying conductance to an inverse ohmic length dependence was observed, which is consistent with the measured results shown Figure 3.13(a). Over a certain interval of wire lengths, this latter ohmic regime can be well approximated by an exponential law with a low β. The low β observed for these insulating, several ten nm thick SURMOF films have been explained as being due to ohmic, incoherent hopping of charge carriers.

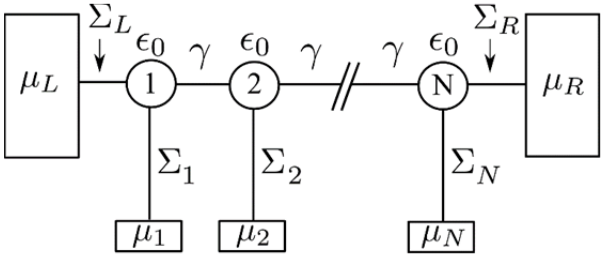

Figure 3.16 The MOF film is described through a 1D chain with N sites of onsite energy ε_0. Nearest neighbors are coupled through γ. The coupling to the leads is symmetric in the calculation, so left and right self-energies $\Sigma_L=\Sigma_R=-i\Gamma/2$ are equal. The other self-energies $\Sigma_1=\Sigma_2=\ldots=\Sigma_N=-i\eta_D/2$ describe the dephasing. Chemical potentials μ_L and μ_R are fixed by the applied bias voltage, while μ_1 to μ_N are determined by a condition of current conservation in the chain.

The major factors leading to the low intrinsic conductivity of HKUST-1 are the insulating behavior of the organic linkers and the bad electronic coupling of Cu_2 metallic nodes, related to the *meta* configuration of the benzene-derived bridges. Upon loading with ferrocene, the electronic and vibrational structures as well as the electron-vibrational couplings is modified, as evidently observed from the changes in the crystal structure (Figure 3.2). The enhanced effective electronic coupling and dephasing strength between and at the Cu_2 centers, leading to the improved transport properties, may stem from a partial lifting of the destructive electron interference that suppresses the conduction for *meta* couplings.[155-157] An enhanced electron-vibration scattering due to the fluctuating

interactions of the ferrocene molecules on top of the trimesic acid bridges can induce a decoherence that reduces the destructive interference. In addition, a changed charge rearrangement at the interfaces due to the ferrocene-related states may modify the charge injection barrier.

3.1.7 Conclusion

In conclusion, HKUST-1 SURMOF thin films were prepared on CMMT SAM modified Au substrates along the [111] orientation and then loaded with ferrocene molecules as small organic electroactive guest entities. The Fc loading was confirmed by IRRAS and out-of-plane XRD. Interestingly, the out-of-plane XRD measurements showed an enhanced ordering of the layer sequences of the (111) planes of the HKUST-1 SURMOFs through the incorporation of ferrocene. However, the lattice constant had no significant change before and after the ferrocene loading.

By assembling a mercury-based tunneling junction with the prepared various thickness HKUST-1 SURMOF thin films, either with the pristine ones or the Fc loaded ones, the charge transport properties of these films were investigated. It was found that the conductance of the SURMOF films decreased by increasing the film thickness. However, the low value of the attenuation factor ($\beta \approx 0.006$ Å^{-1}) indicates the extremely shallow dependence of the measured current density on film thickness, and has been understood in terms of a linear, ohmic increase of resistance with length in the incoherent charge hopping regime. For the effect of Fc loading inside the pores of HKUST-1 SURMOFs, the conductance was tuned to be higher than the corresponding pristine ones at identical same thickness. So the decrease in overall resistance with Fc loading and its weaker increase with film thickness indicate a reduction in the charge injection barrier and an improved electronic coupling between metal nodes. Theoretical analysis by DFT calculations was applied to help understanding the charge transport mechanism.

Part of the results in this section has been published in ACS Appl. Mat. Interfaces by Jianxi Liu et al.(2015) as ref.[154]

3.2 Electrochemical studies on HKUST-1 and the Fc mediated conductivity

3.2.1 Background

As described in previous section, series of SURMOF thin films were prepared by the stepwise LPE spraying method, which has proven to be an ideal method for the preparation of highly orientated robust SURMOF thin films with adjustable thickness.[67] Aiming for the further application of MOFs in devices, the preparation and characterization of the rather large areas covered by the MOF films are required.

However, the most widely used techniques for MOF thin film characterization, such as XRD and IRRAS, provide information only on the long-range crystalline order of MOF and the chemical compositions, respectively.[3, 158] Nevertheless, discrete pin-holes/defects which would unpredictably alter the properties of MOF thin film devices are not specifically observable. The Hg-drop method is not available for evaluating the lower conductivity or conductivity of the thicker MOF films, because the low intrinsic conductivity of most the MOFs reaches limit of the technique.

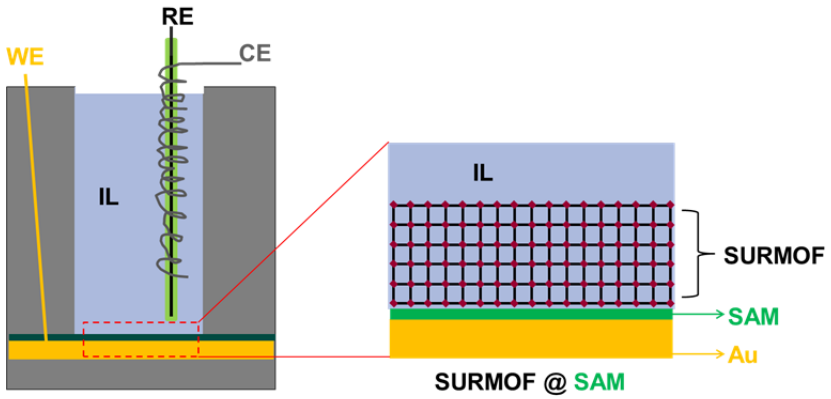

Figure 3.17 Scheme of the home-made electrochemical cell with the three electrodes set-up. The body of the cell is in PTFE. WE=working electrode (the area is 0.3 cm^2); RE=reference electrode (platinum wire inserted in a lugging capillary); CE=counter electrode (platinum wire wrapped around the lugging capillary containing the RE). The volume of the ionic liquid solution is around 1.5 ml.

Techniques of electrochemistry, such as cyclic voltammetry (CV), are available to evaluate the conductivity of thin films deposited on electrode and to gain insight into the pin-holes/defects evaluation in the range of a cm^2 large area (this is relatively large

compared to other methods such as AFM[88, 159] and Hg-method[136, 139, 150]). MOFs thin films grown, with a well-defined crystallographic orientation and controlled thickness, on a conductive substrate can be directly used as working electrodes and provide great experimental advantages.

In this part, CV was used to study the electrochemical properties of HKUST-1 SURMOFs that were used as working electrodes in a home-made cell, as depicted Figure 3.17. An aprotic ionic liquid (IL) [BMIM] [NTf_2]), (1-butyl-3-methylimidazolinium bis(trifluoronethylsulfonyl)imide), was used as solvent and supporting electrolyte. The electroactive ferrocene was used as redox probe. In order to study the electrical properties of the SURMOFs with the effect of guest loading, the ferrocene molecules were loaded into the nanopores of HKUST-1 SURMOFs. Meanwhile, the presence of pin-holes/defects could be evaluated from CV measurements which offer a swift method for observing the conductive quality of SURMOF thin films.

3.2.2 Preparation of HKUST-1 SURMOFs on SAMs and Fc loading

The possibility to control the crystallographic growth direction for SURMOFs is particularly appealing. This obtained varying the chemical functionality of the active ending groups present on the SAM template surface as well as their surface density.[160] HKUST-1 SUMOFs have been prepared on CMMT and TPMTA (4'-carboxyterphenyl-4-methanethiol) SAMs modified gold electrodes (named as SAM1/MOF and SAM2/MOF, respectively) by means of the LPE spraying method (Chapter 2.2.3). The loading of Fc was conducted from the vapor phase for both SAM1/MOF and SAM2/MOF using the same conditions as described in Chapter 3.1.

3.2.3 Out-of-plane XRD characterization

Out-of-plane XRD has been performed to check the crystallinity for both the pristine and Fc loaded HKUST-1 SURMOFs. The XRD pattern in Figure 3.18 (black plot) shows a good crystallographic orientation for SAM1/MOF with the two peaks at 2θ=11.80° and 2θ=17.70° corresponding to the main diffraction peaks (222) and (333), but a less pronounced orientation for SAM2/MOF (Figure 3.19, black plot) was observed. After loading with ferrocene, in the case of SAM1/MOF-Fc (in red), the XRD pattern showed that the (222) peak was substantial decreased and (333) was slightly increased comparing to the unloaded samples (Figure 3.18). The change in the relative intensities of the (222)

and (333) after Fc loading can be interpreted as coming from the strong scattering of the loaded iron from the ferrocene, and because the structure form factor is changed after loading. The changes were also observed from the XRD pattern of SAM2/MOF after Fc loading, in which the relative intensities of the (002) and (004) reflexes appeared differently (Figure 3.19).

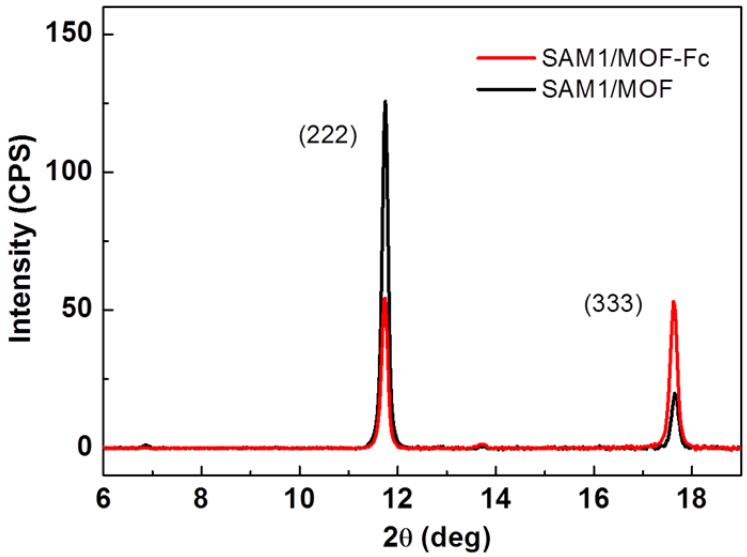

Figure 3.18 Out-of-plane XRD of the pristine (SAM1/MOF, black) and Fc-loaded (SAM1/MOF-Fc, red) HKUST-1 SURMOF grown on CMMT SAM. The relative intensities of the (222) and (333) reflexes are changed after loading.

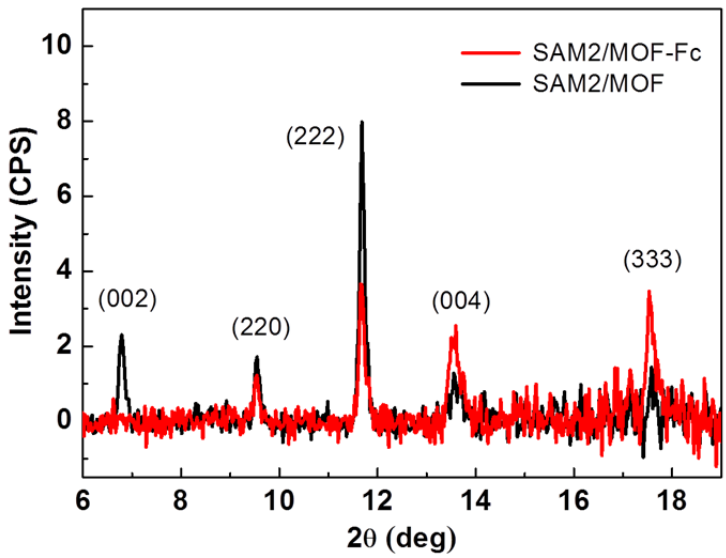

Figure 3.19 Out-of-plane XRD of the pristine (SAM2/MOF, black) and Fc-loaded (SAM2/MOF-Fc, red) HKUST-1 SURMOF grown on TPMTA SAM. The relative intensities of the (002) and (004) reflexes are changed by the loading.

3.2.4 IRRAS characterization

The IRRAS spectra for both SAM1/MOF (in Figure 3.20) and SAM2/MOF (in Figure 3.21) showed the characteristic absorption bands of HKUST-1: 1656 cm^{-1} (COO_{-asym}); 1620, 1596 and 1566 cm^{-1} (benzene ring); 1455 and 1386 cm^{-1} (COO_{-sym}); and 1112 and 940 cm^{-1} (aromatic C-H).

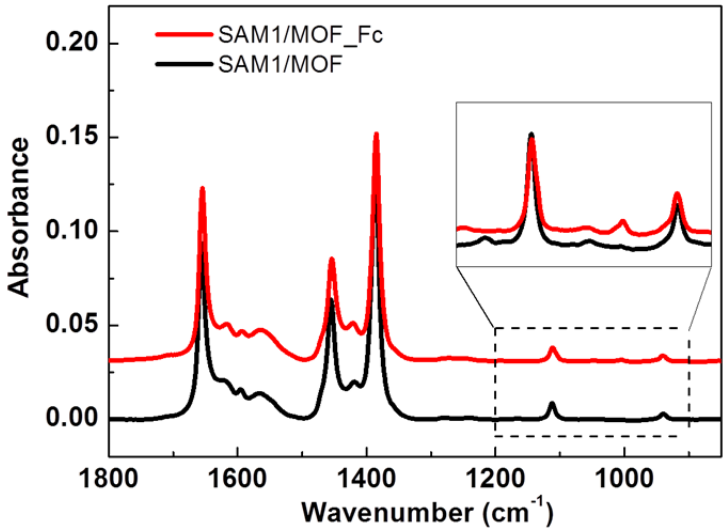

Figure 3.20 IRRA spectra of HKUST-1 SURMOFs grown on CMMT SAM before (SAM1/MOF, black curve) and after (SAM1/MOF-Fc, red curve) Fc loading. The inset shows the aromatic C-H stretching coming from the ferrocene ring.

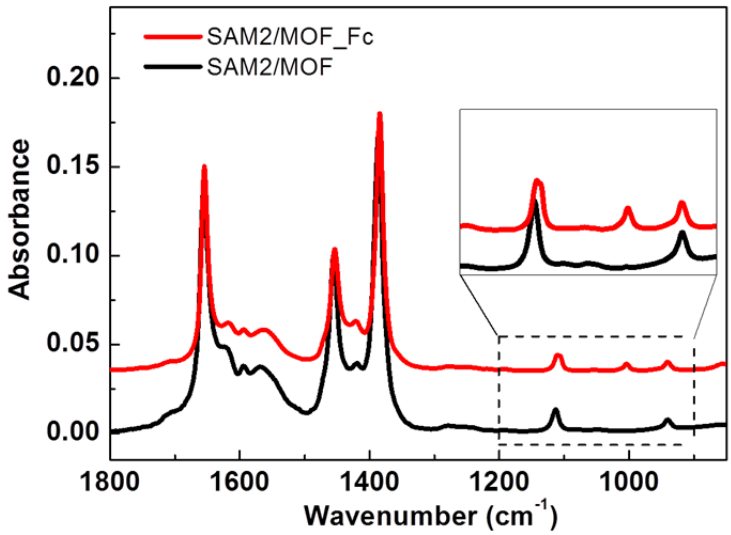

Figure 3.21 IRRAs of HKUST-1 SURMOFs grown on TPMTA SAM before (SAM2/MOF, black curve) and after (SAM2/MOF-Fc, red curve) Fc loading. The inset shows the aromatic C-H stretching coming from the ferrocene ring.

After loading with ferrocene, a new absorption band at 1004 cm^{-1}, attributed to the C-H in-plane bending of the ferrocene ring appeared for HKUST-1 SURMOFs grown on both SAM1 (CMMT) and SAM2 (TPMTA). In addition, the broad band around 1109 cm^{-1} (insets in Figure 3.20 and Figure 3.21) is the sum of the band at 1107 cm^{-1} (asymmetric ferrocene ring breathing) and that at 1112 cm^{-1} (in plane C-H stretching of the pristine HKUST-1).

3.2.5 AFM morphology and scratching characterization

AFM morphology and scratching characterization were contributed by Prof. Carmen Ocal and Mr. Markos Paradinas from Autonomous University of Barcelona (UAB, Spain).

The morphology and thickness of the HKUST-1 SURMOF thin films were measured by AFM in contact mode under low humidity conditions (<5 % RH, obtained by a continuous N_2 flux) using a commercial head and electronics from Nanotec. In order to determine the thicknesses of the SURMOF thin films, AFM scratching method was employing[161] by removing the grown MOF material from the surface until reaching the Au surface of the substrate with a Si tip on medium stiffness cantilevers (k=2.8 N/m, Nanosensors). The imaging force was set to below 10 nN, while a force in the range of 400-700 nN was applied to scratch sample.

Before the scratching procedure, a large scan size was used firstly, for imaging the morphology of the SURMOFs and choosing the area for scratch, by using either a dynamic non-contact mode or a low force contact mode to avoid film damage. Then, the scan size was reduced to a smaller region that was repeatedly imaged at a higher load (typically 400-500 nN). The applied scratching forces are high enough to eliminate the SURMOF but in a moderate manner (under load control) to avoid undesired removal of the gold film. During this process, an unstable topographic signal indicates the start of MOF materials removal. Lateral force signals were continuously recorded to detect structural differences within the SURMOF as well as to determine the instant when the underlying Au surface is reached to stop the process.

3.2.5.1 AFM morphology of Au surface

Since the SAMs (CMMT and TPMTA) used for SURMOFs preparation would not affect the morphology of Au surface, the underneath Au substrate was firstly characterized as a reference for identifying the moment when the AFM tip reaches the substrate layer during

the scratching. As it can be seen in Figure 3.22, the Au surface of the substrate consists of a homogeneous distribution of small grains which provide the smooth surface (roughness of 1.8 nm).

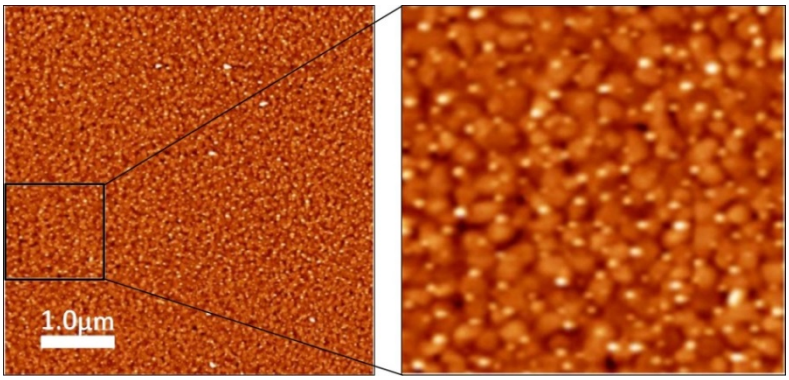

Figure 3.22 Topographic AFM images of Au surface (100 nm Au on Si) taken as a reference for the scratching experiments. The image at the right panel corresponds to the area marked in the large image (5 µm × 5 µm). The surface roughness calculated is RMS=1.8 nm.

3.2.5.2 AFM scratching of HKUST-1 grown on CMMT (SAM1/MOF-Fc)

As mentioned in Chapter 3.1, the thickness of SURMOFs would not change by Fc loading, so the AFM scratching experiments were done only on Fc loaded HKUST-1 SURMOF samples.

Figure 3.23(a) shows the morphology of HKUST-1 SURMOF grown on CMMT SAM (SAM1/MOF-Fc). The crystallites exhibit a flat top surface with a clear triangular shape indicating a predominant [111] orientation in agreement with the XRD data (Figure 3.18). The scratching process was performed in the smaller area as seen in the middle of Figure 3.23(c). The image presented in Figure 3.23(b) shows the morphology of the scanned sample, which were taken during the scratching experiment. The same gold grains were circled in both images used as a reference when reaching the substrate; the dashed lines in each image indicate the material removal front. A continuous and rather homogeneous MOF layer was found (regions below the dash line Figure 3.23(b) underlying the top crystallites but before reaching the Au substrate. The results elucidated that the crystallites were not positioned directly on the SAMs but rather on top of a continuous and homogeneous layer of HKUST-1. After the scratching experiment, the scanned area was set to the original size (same as Figure 3.23(a)) for imaging the topographic changes and

measuring the thickness. Figure 3.23(d) shows the depth profile of the SAM1/MOF-Fc. The average vertical dimension of the crystallites is ~20 nm on top, and the underlying homogeneous MOF film exhibits a thickness of ~70 ± 5 nm.

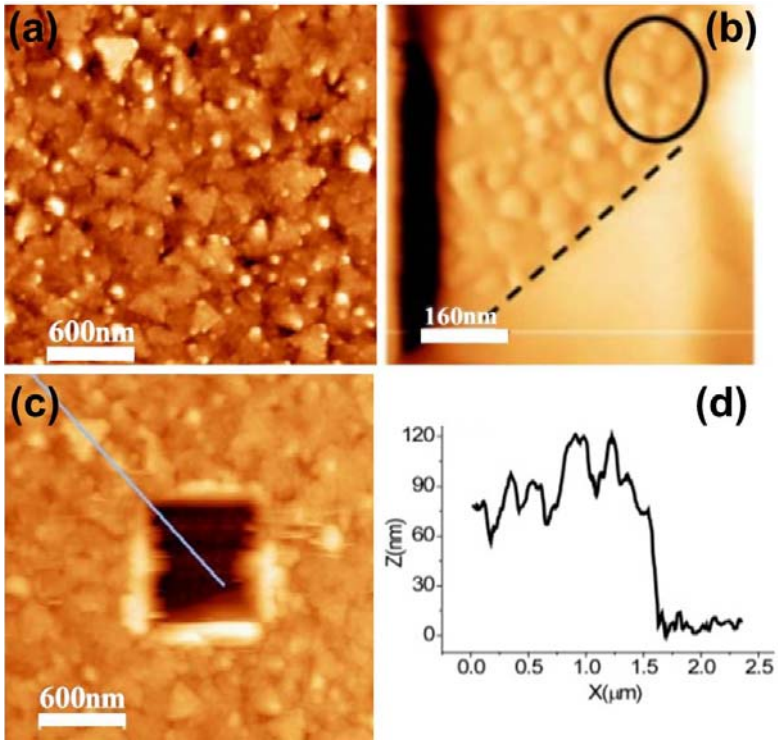

Fig. 3.23 Topographic AFM images of SAM1/MOF-Fc before (a) and after (c) removal of the MOF material from sample (square in the middle). (b) Selected images taken during the scratching (~500 nN load). Ellipse marked areas are Au surface. Dashed lines indicate the removal front (for details see text). (d) Depth profile of the HKUST-1 SURMOF after scratching along the line in (c).

3.2.5.3 AFM scratching of HKUST-1 grown on TPMTA (SAM2/MOF-Fc)

AFM morphology and scratching procedures were performed on the HKUST-1 SURMOF thin film grown on TPMTA SAM with identical conditions as previously used. Figure 3.24(a-b) present the surface morphology scans of the ferrocene loaded HKUST-1 (SAM2/MOF-Fc). The circled crystallites in Figure 3.24(a) show some presenting a flat triangular surface (red circles) and others a squared base pyramids shape (blue circles) likely corresponding to mixed [111] and [001] orientations, respectively. This observation is in accordance with the XRD measurements (Figure 3.19). These crystallites lay on top of a rather flat and homogeneous layer of SURMOF.

Figure 3.24(c) presents a topographic AFM image of the SAM2/MOF-Fc after a scratch

experiment. Part of the removed MOF accumulated at the borders of the scratched region and contributed to the jumping lines in the image. The depth profile shown in Figure 3.24(d) follows the white line in Figure 3.24(c), and was used to determine the film thickness. It can be seen that the average vertical dimension of the crystallites on top is ~35 nm, and the underlying homogeneous MOF film exhibits a thickness of ~75 ± 5 nm.

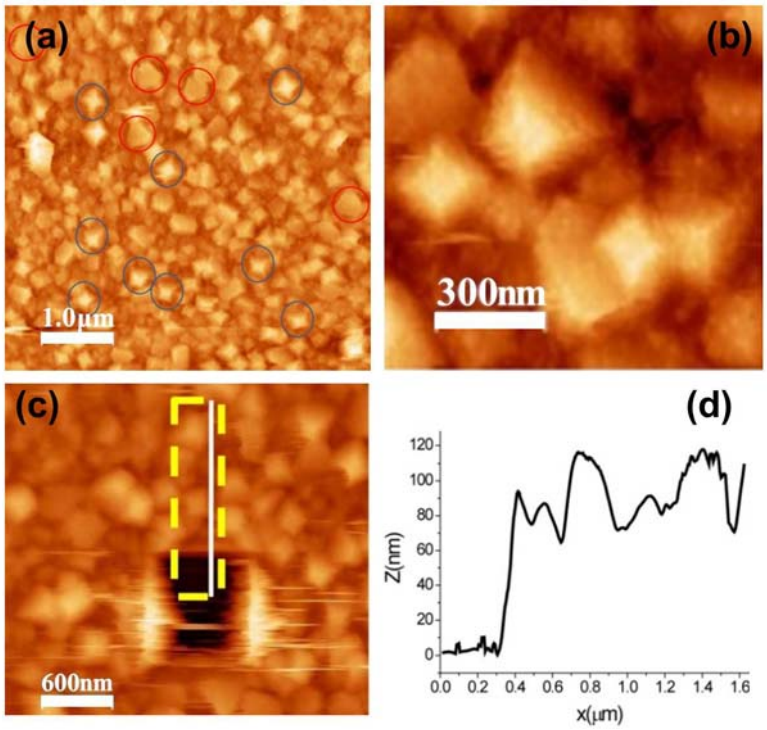

Figure 3.24 Topographic AFM image of the SAM2/MOF-Fc before (a-b) and after (c) removal of the MOF material from sample (square in the middle); (d) depth profile of the HKUST-1 SURMOF after scratching experiment along the white line seen in (c).

3.2.6 CV study on HKUST-1 SURMOFs grown on different SAMs

The cyclic voltammetry (CV) experiments were carried out in a home-made electrochemical cell (Figure 3.17) using a standard three electrode setup. The reference electrode and counter electrode were made of platinum wires (diameter 0.25 mm). The SAMs and HKUST-1 SURMOFs coated gold substrates with and without Fc loading were used as working electrodes (area 0.3 cm^2); they have been classified and named as following:

(i) CMMT series: SAM1, SAM1/MOF, SAM1/MOF-Fc;
(ii) TPMTA series: SAM2, SAM2/MOF, SAM2/MOF-Fc.

Carrying out CV experiments using these oriented and crystalline SURMOFs grown on metal substrates as working electrode is still challenging and the solvent and supporting electrolyte are to be chosen carefully since MOFs are water sensitive and could react with the applied solutions during the measurement. As liquid supporting electrolyte, the aprotic ionic liquid [BMIM] [NTf_2] meets all requirements, because the ionic components do not interfere with the coordination bonds in the HKUST-1 SURMOF and preserve it from losing its crystalline structure.[101] Moreover, as several other known ILs,[162] the used [BMIM][NTf_2] is a good supporting electrolyte also because of its electrochemical inertness (*i.e*. its wide potential window, larger than the one of the electroactive species under study) and its high conductivity (being completely ionic). Ferrocene has been used as the redox probe, and was dissolved in IL by adding a small amount of ethanol for solubility reasons (5mM, in 4/96 EtOH/[BMIM][NTf_2]).

The CV measurements were conducted in IL (5 mM Fc, 4% ethanol) at the potential window from -0.35 to +0.55 V *vs* Pt, while the scan rate was varied (20 mV/s, 50 mV/s, 100 mV/s). After the CV measurements, the samples were routinely checked by XRD, and showed no observable loss of the crystalline structure.

3.2.6.1 CV measurement of HKUST-1 grown on SAM1 (CMMT)

CV of CMMT SAM was performed at first before measuring the HKUST-1 grown on this SAM (**SAM1/MOF**). When the SAM1 was used as working electrodes, a reversible diffusion and limited Nernstian process was observed (Figure 3.25, top).

The anodic peak, corresponding to the formation of ferrocenium by oxidation of ferrocene, appears at 0.190 V at the scan rate of 20 mV/s. The cathodic peak, corresponding to the formation of ferrocene by reduction of ferrocenium, appears at 0.124 V. The exact separation (ΔE) of the oxidation and reduction peaks (66 mV) is very close to the theoretical value of 59 mV, which is determined according to the Nernst equation. By increasing the scan rate from 20 mV/s to 100 mV/s, the current density was increased accordingly but no shift in the anodic or cathodic peaks (no change in ΔE) was observed. Figure 3.25 (bottom part) shows the plot of the anodic peak current density as a function of square root of the scan rate with a linear trend observable for SAM1, in analogy to SAM MHDA behavior under similar conditions.[161] It was found that CMMT SAM would not block the electrode for CV measurement.

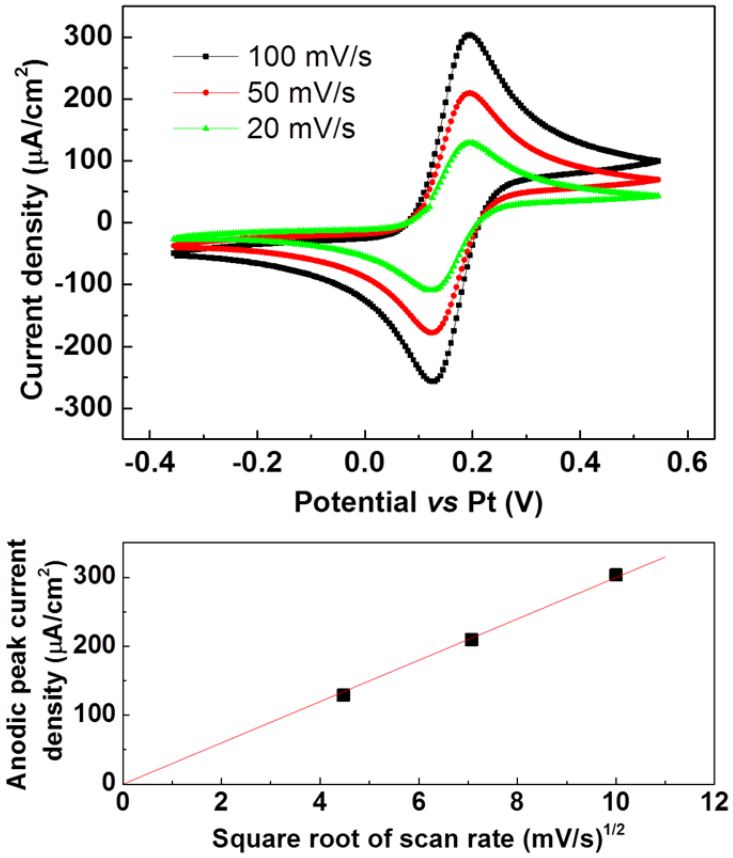

Figure 3.25 Top: CV of CMMT SAM in the presence of 5 mM Fc in [BMIM] [NTf_2] with 4% ethanol. Bottom: linear dependence of the anodic peak current density with the square root of the scan rates shown by the linear fit (red line).

Then CV of HKUST-1 SURMOF grown on CMMT modified Au electrode was carried out by applying the SAM1/MOF as working electrode, as shown in Figure 3.26. Under the same experimental conditions as for SAM1, a very low current was measured (1.3 μA/cm^2 at 0.55V) at the scan rate of 20 mV/s. The extremely low current is an indication of the insulating behavior of HKUST-1, which has the effect of blocking the electrode for CV measurement. The absence of pin-holes or defects can be concluded for the HKUST-1 SURMOF; otherwise, the diffused Fc would show redox peaks.[163] However, after the HKUST-1 was loaded with ferrocene molecules (SAM1/MOF-Fc), the CV showed a (quasi)linear increase in the measured current density. A highest current density value of 40 μA/cm^2 was observed at 0.55 V at a scan rate of 20 mV/s. By increasing the scan rate from 20 mV/s to 100 mV/s, an essentially identical current density *vs* potential was observed (in Figure 3.27), and indicates an ohmic behavior of the Fc loaded HKUST-1 SURMOFs. Also no pin- holes or defects were introduced by the loading of Fc.

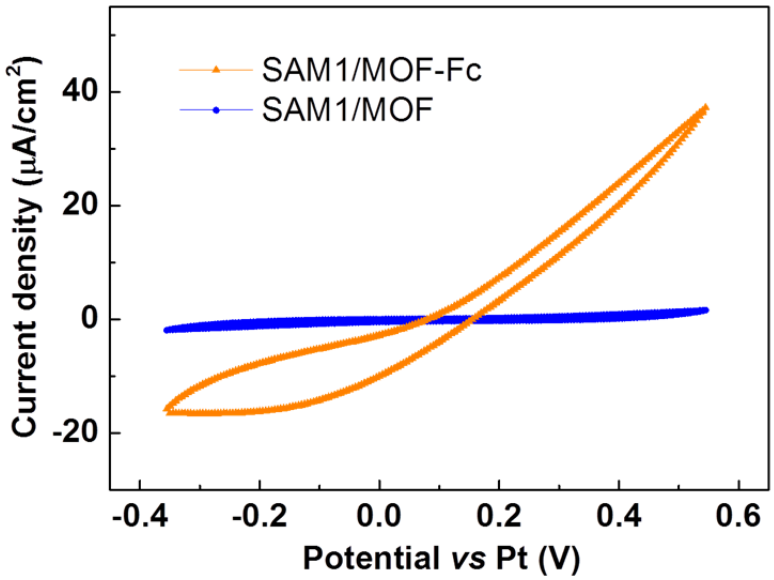

Figure 3.26 CV of pristine (blue) and Fc loaded (orange) HKUST-1 SURMOF grown on CMMT SAM (SAM1/MOF and SAM1/MOF-Fc) at the scan rate 20 mV/s.

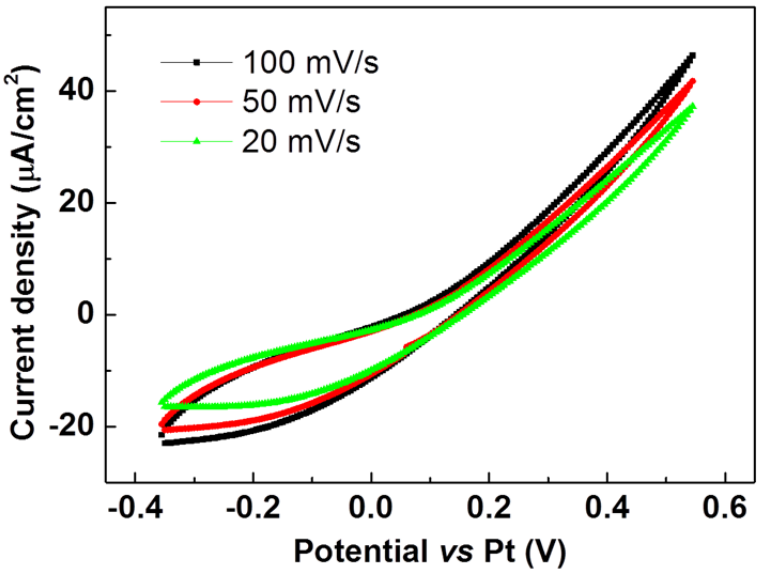

Figure 3.27 CV of SAM1/MOF-Fc at different scan rates.

3.2.6.2 CV measurement of HKUST-1 grown on SAM2 (TPMTA)

The CV of TPMTA SAM was also performed first before measuring the HKUST-1 SURMOF grown on TPMTA (SAM2/MOF), as shown in Figure 3.28 (top). When SAM2 was used as working electrode, a reversible diffusion limited Nernstian process was

observed. The anodic peak appeared at 0.200 V, while the cathodic one appeared at 0.103 V. The exact separation (ΔE) of the oxidation and reduction peaks (97 mV) was not well defined but still relatively close to the theoretical value of 59 mV.

By increasing the scan rate from 20 to 100 mV/s, no shift in the anodic or cathodic peaks (no change in ΔE) was observed, as shown in Figure 3.28 (bottom). The plot of the current density *vs* the square root of scan rate also displays a linear trend for SAM2. Compared to SAM1 (CMMT), the SAM2 (TPMTA) has a comparatively larger ΔE, but the positions of the voltage peak do not vary as a function of the scan rate; this also refers a reversible redox behavior. The SAM2 might have a slight interference on the electrode but have, before all, no blocking effect during CV measurement.

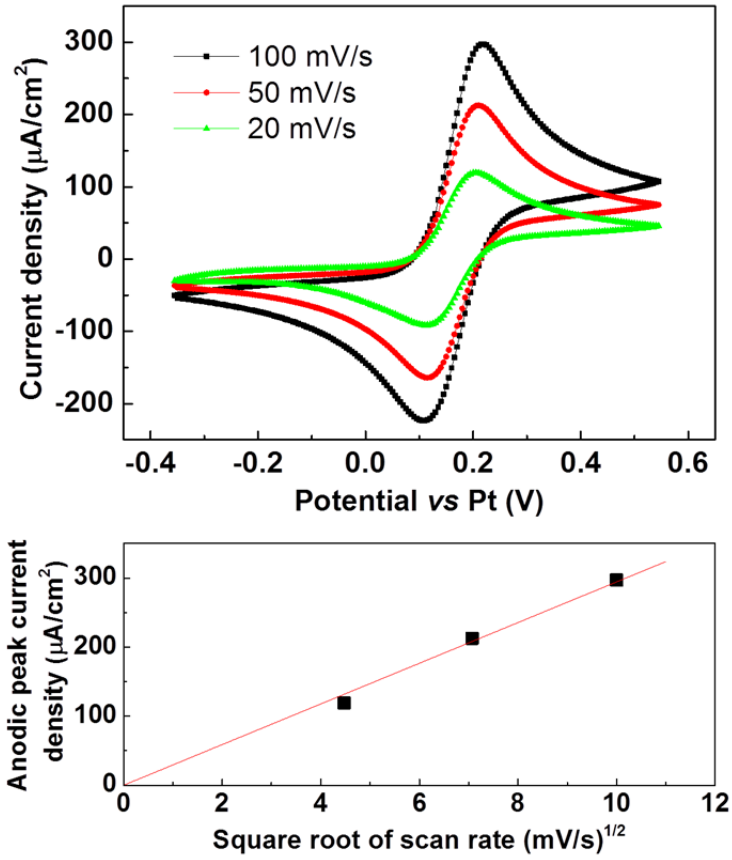

Figure 3.28 Top: Cyclic voltammetry of TPMTA SAM in the presence of 5 mM Fc in [BMIM] [NTf_2] in a 4% of ethanol. Bottom: linear dependence of the anodic current density peak with the square root of the scan rate.

Thereafter, the CV of HKUST-1 SURMOF grown on TPMTA (SAM2/MOF) was measured, as shown in Figure 3.29. When SAM2/MOF was used as working electrode

under the same experimental conditions as for SAM2, the very low current was observed. The results are consistent with SURMOF HKUST-1 grown on CMMT SAM, showing the insulating behavior of pristine HKUST-1. After loading with Fc, the CV of HKUST-1 showed an ohmic behavior. The experiment consists in following the formation of the reversible Fc/Fc^+ redox couple, which occurs only if the ferrocene come into contact with the working electrode.[163]

Interestingly, the CV of SURMOF HKUST-1 for either SAM1 (Figure 3.26) or SAM2 (Figure 3.29) taken in the range between -0.35 V and +0.55 V showed almost no current and no evidence of the reversible oxidation of ferrocene to ferrocenium. The result points to the absence of not only any major defect or pin-hole through which an enhanced diffusion should take place, but also more minor defects, causing the so called microelectrode effect.[164, 165] The latter can instead be observed when the film is mechanically scratched.[166]

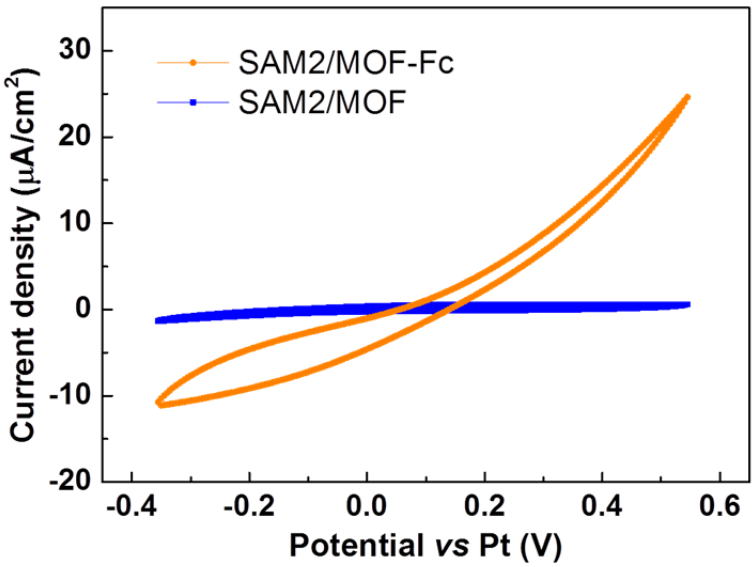

Figure 3.29 CV of the pristine (black) and Fc loaded (red) HKUST-1 SURMOF grown on TPMTA (SAM2) at the scan rate of 20 mV/s.

3.2.6.3 Conductivity evaluation

As shown in Figure 3.26 and Figure 3.29, the (quasi)linear plots of current density as a function of voltage are composed of two regions, each with a different slope. In the cathodic range (-0.35V – 0.14V), which corresponds to the formation of ferrocene through the reduction of ferrocenium cation, the linearity of the current density as a function of voltage is not clear, with the lower slope corresponding to a resistance of 236 kΩ for

SAM1/MOF-Fc, and 224 kΩ for SAM2/MOF-Fc. However, in the anodic range (0.14V – 0.55V), which corresponds to the formation of ferrocenium cation through the oxidation of ferrocene, the current density as a function of voltage dependence is linear with the slope of the CV recorded at a scan rate of 20 mV/s. The resistances corresponding to the slopes are then 45.5 kΩ for SAM1/MOF-Fc, and 63 kΩ for SAM2/MOF-Fc.

As analyzed previously by AFM scratching experiments, the average vertical dimension of the crystallites is ~20 nm and ~35 nm for SAM1/MOF-Fc and SAM2/MOF-Fc, respectively, whereas the underlying HKUST-1 films exhibit a thickness of ~70 ± 5 nm for SAM1/MOF-Fc and ~75 ± 5 nm for SAM2/MOF-Fc. By using the thickness of the homogeneous SURMOF layer as determined by AFM and the electrochemical cell area, the room temperature conductivity values (σ) of the Fc loaded HKUST-1 SURMOFs grown on both SAMs were calculated. For SAM1/MOF-Fc, the conductivity of $\sigma_a = (5.1 \pm 0.3) \times 10^{-10}$ S cm^{-1} and in $\sigma_c = (9.9 \pm 0.2) \times 10^{-11}$ S cm^{-1} at the anodic and cathodic ranges were obtained, respectively. This corresponds to conductivity values for SAM2/MOF-Fc of $\sigma_a = (4.0 \pm 0.3) \times 10^{-10}$ S cm^{-1} and $\sigma_c = (1.1 \pm 0.1) \times 10^{-10}$ S cm^{-1}. The calculated resistance and conductance of these SURMOF thin films are presented in Table 3.1. Nevertheless, these conductivity values are a lower limit because only the homogenous and continuous HKUST-1 layers were considered in the calculations.

Table 3.1 Cathodic and anodic conductivity of the HKUST-1 SURMOFs.

	Cathodic range -0.35 V – 0.14 V		Anodic range: 0.14V – 0.55 V	
	R /kΩ	σ_c /S cm^{-1}	R /kΩ	σ_a /S cm^{-1}
SAM1/MOF-Fc (CMMT)	236	$(9.9\pm0.2) \times 10^{-11}$	45.5	$(5.1\pm0.3) \times 10^{-10}$
SAM2/MOF-Fc (TPMTA)	224	$(1.1\pm0.1) \times 10^{-10}$	63.0	$(4.0\pm0.3) \times 10^{-10}$

Indeed, if contributions from the on top grown crystallites (mean vertical size ~20 nm and ~35 nm for SAM1/MOF-Fc and SAM2/MOF-Fc, respectively) are considered, an upper value of conductivity $\sigma_a = 6.6 \times 10^{-10}$ S cm^{-1} (SAM1/MOF-Fc) and $\sigma_a = 5.8 \times 10^{-10}$ S cm^{-1} (SAM2/MOF-Fc) are obtained, respectively. These values are in good agreement with the electric conductivity values measured for the SAM1/MOF-Fc films upon their integration in a Hg-based tunneling junction.[167]

3.2.7 Conclusion

It was demonstrated that the LPE method is a suitable process to produce crystalline and defect-free films of HKUST-1 on different SAMs (CMMT and TPMTA) and that the film quality was independent of the crystallographic orientation of the film. Cyclic voltammetry method was used to study the electrochemical behavior of these HKUST-1 SURMOFs and showed that the SURMOFs act as an insulating barrier for the redox of an electroactive molecule dissolved in the supporting electrolyte solution. It was also proved that by loading the HKUST-1 framework with Fc, its insulating behavior was switched into a conductive one, with the characteristics of an ohmic resistor.

3.3 Photoelectrochemical properties of porphyrin based SURMOF thin films

3.3.1 Background

To improve the electrical conductivity of MOFs, two strategies have been followed so far. One consists in the loading of electroactive guest molecules into the nanopores of the framework,[101, 102] the other in the utilization of redox active organic linkers.[104, 168] The idea of choosing suitable organic ligands with special properties is promising not only for enhancing the electric property, but also for easily fabricating new functional MOF materials which should expand the application of MOFs as device components.

In plants, porphyrins (like chlorophyll) play a central role in the natural photosynthesis process: they transform, rather effectively, solar energy into chemical energy. Inspired by nature, the porphyrin derivatives have been used as light harvester in dye sensitized solar cells (DSSCs), and manages also, to a certain extent, an efficient conversion of solar energy into electric energy.[169, 170] The production of the highly ordered array of porphyrins, as in nature, could possibly improve the efficiency in device applications where the MOF structure offers the possibility of integrating this photoactive moieties as organic linkers.

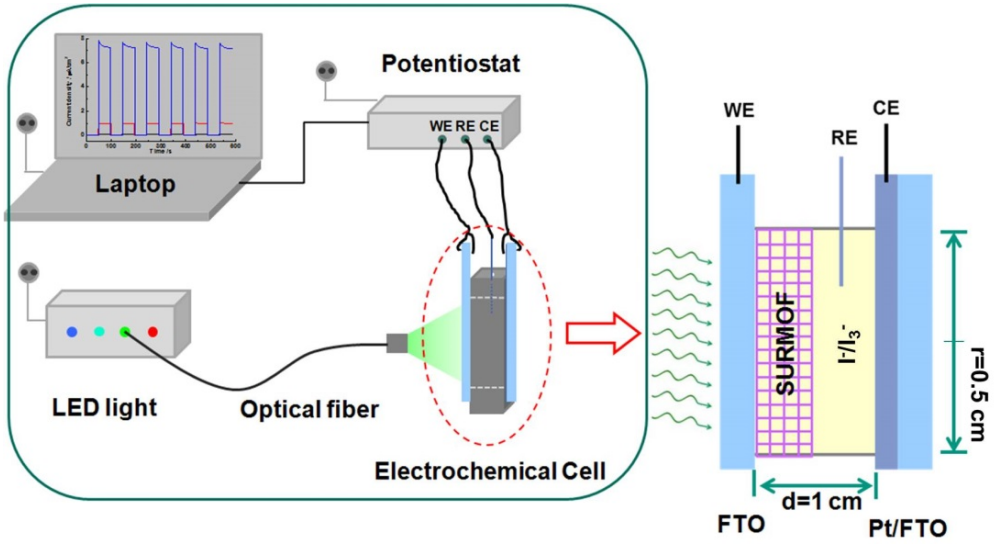

Figure 3.30 Schematic drawing of the photoelectrochemical setup equipped with three-electrode cell and LED light system for the photocurrent measurement. The distance between the two electrodes is 1 cm and the active area is 0.79 cm^2.

In this part, porphyrin-based SURMOFs were prepared on transparent and conductive FTO (fluorine doped tin oxide) substrates by LPE spraying method, named "porphyrin SURMOF 2" (SURMOF 2 = 2D surface-anchored metal-organic frameworks). As shown in Figure 3.30, these monolithic, homogenous films deposited on FTO substrates acting as electrodes were applied directly in a home-made photoelectrochemical cell for photocurrent generation studies with a typical three-electrode system.

3.3.2 Preparation of the porphyrin-based SURMOF thin films

Two kinds of porphyrin ligands were used to produce the SURMOFs in the present work; one is a free base porphyrin, and the other is Pd porphyrin (molecular structures are presented in Figure 3.32(d)). The Porphyrin-based SURMOFs were fabricated using the LPE spraying method (Chapter 2.2.3). Figure 3.31 shows the SEM morphology and cross-section analysis of the 30 spraying cycles samples. It can be seen that the films are homogeneous with a thickness of about 300 nm for both free base porphyrin Zn-SURMOF 2 and Pd porphyrin Zn-SURMOF 2. The thickness of about 10 nm per deposition cycle was estimated from the SEM cross-section images.

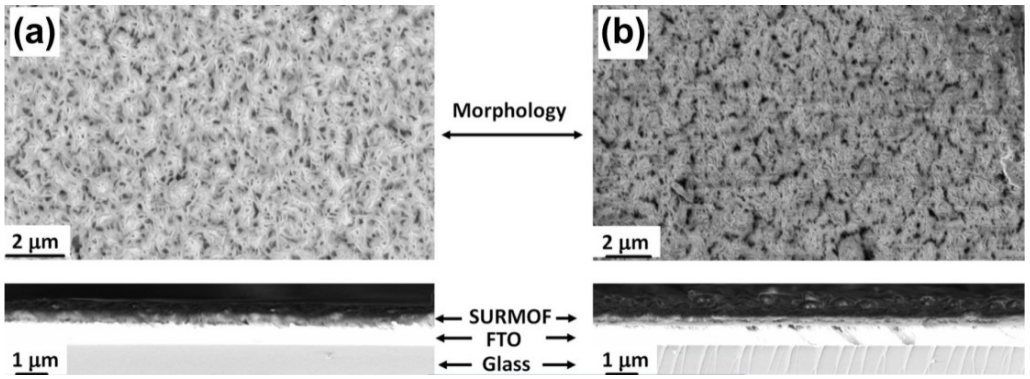

Figure 3.31 Top view and cross-section SEM images of (a) free base porphyrin Zn-SURMOF 2 and (b) Pd porphyrin Zn-SURMOF 2 grown on FTO substrates. For both samples, the thickness of 300 nm has been obtained in 30 spraying cycle.

3.3.3 XRD characterization

"SURMOF 2", comprising the so called paddle-wheel units, is a MOF structure typically stacked between copper or zinc paddle-wheel and dicarboxylic acid ligands to yield an overall P4 symmetry.[171], The proposed structures of free base porphyrin Zn-SURMOF 2 and Pd porphyrin Zn-SURMOF 2 are presented in Figure 3.32. The porphrin structures are

lying within the planes perpendicular to substrate surfaces in remarkable orders, and 1D nanometer sized channels are produced from the MOF structure parallel to the substrate surfaces.

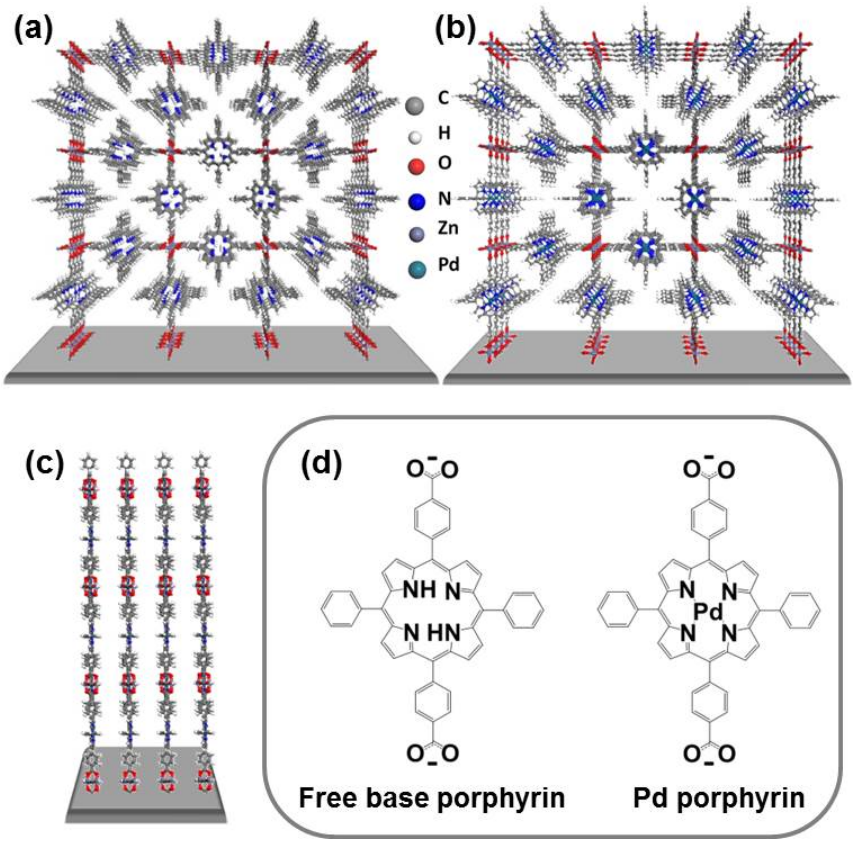

Figure 3.32 Proposed structures of (a) free base porphyrin Zn-SURMOF 2, (b) Pd porphyrin Zn-SURMOF 2 with parallel 1D channels, and (c) layers perpendicular to substrates with a layer distance about 0.6 nm; (d) molecular structures of the free base porphyrin and Pd porphyrin ligands.

Out-of-plane XRD patterns (Figure 3.33) of the free base porphyrin Zn-SURMOF 2 (black curve) and Pd porphyrin Zn-SURMOF 2 (red curve) were measured. The data were acquired over a 2θ range of 2–20°. The sharp and intense peaks with preferred orientation [001] reveal the presence of a highly oriented, well-ordered crystalline SURMOF, which are in accordance with the proposed crystal structure as presented in Figure 3.32. The lattice parameter a (perpendicular to the substrate) was determined from the observed diffraction peaks (001) at $2\theta = 3.7°$ with a d value of 2.4 nm. The d value fits well with the calculated unit cell parameter and gives the value $a = 2.4$ nm for free base Zn-porphyrin using UFF4 MOF.[172-174]

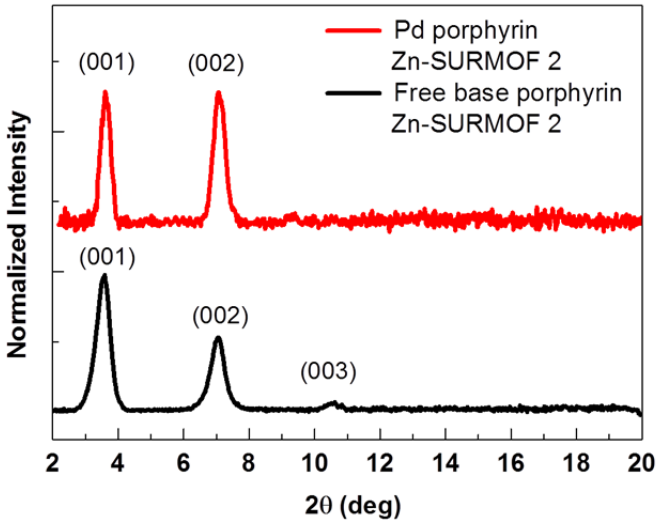

Figure 3.33 Out-of-plane XRD of the free base porphyrin Zn-SURMOF 2 (black) and Pd porphyrin Zn-SURMOF 2 (red) films grown on FTO substrates.

3.3.4 Photoelectrochemical measurements

In natural systems, these light-harvesting molecules are typically stacked to yield extended columns through which the absorbed sunlight energy is transported in the form of excitons. Charge separation, i.e. the dissociation of the exciton to yield an electron (*e*) and a hole (*h*) is achieved at a target chlorophyll pigment center.[175] Here, the assembled regular arrays of photoactive molecules, porphyrin-based SURMOFs, were assembled into photoelectrochemical cell for the photocurrent generation measurement.

The photocurrent measurements were carried out on an electrochemical workstation, and a home-made photoelectrochemical cell using three-electrode system was applied, as shown in Figure 3.30. 50 μM iodine/triiodine solution (I^-/I_3^- in acetonitrile) was used as redox components. Amperometric detection method was used to monitor the current, and the applied bias voltage was controlled at 0.06 V *vs* Pt wire electrode (as reference electrode). The free base porphyrin Zn-SURMOF 2 and Pd porphyrin Zn-SURMOF 2 thin films produced on FTO glasses were used as the working electrode, a Pt coated FTO substrate as counter electrode, and a Pt wire as the reference electrode.

Measurements were taken under illumination from fiber coupled LEDs system (Prizmatix). The illumination wavelength at 365, 400, 455, 530 and 640 nm were chosen for shining the porphyrin-based SURMOF samples during photocurrent generation measurement. The

output power was measured using Ophir Nova II power meter with PD-300-UV sensor. The output power was 112 mW for LED 365 nm, 65 mW for LED 400 nm, 135 mW for LED 455 nm, 55 mW for LED 530 nm and 102 mW for LED 640 nm. The area of light irradiation was 0.79 cm^2. All experiments were carried out at room temperature.

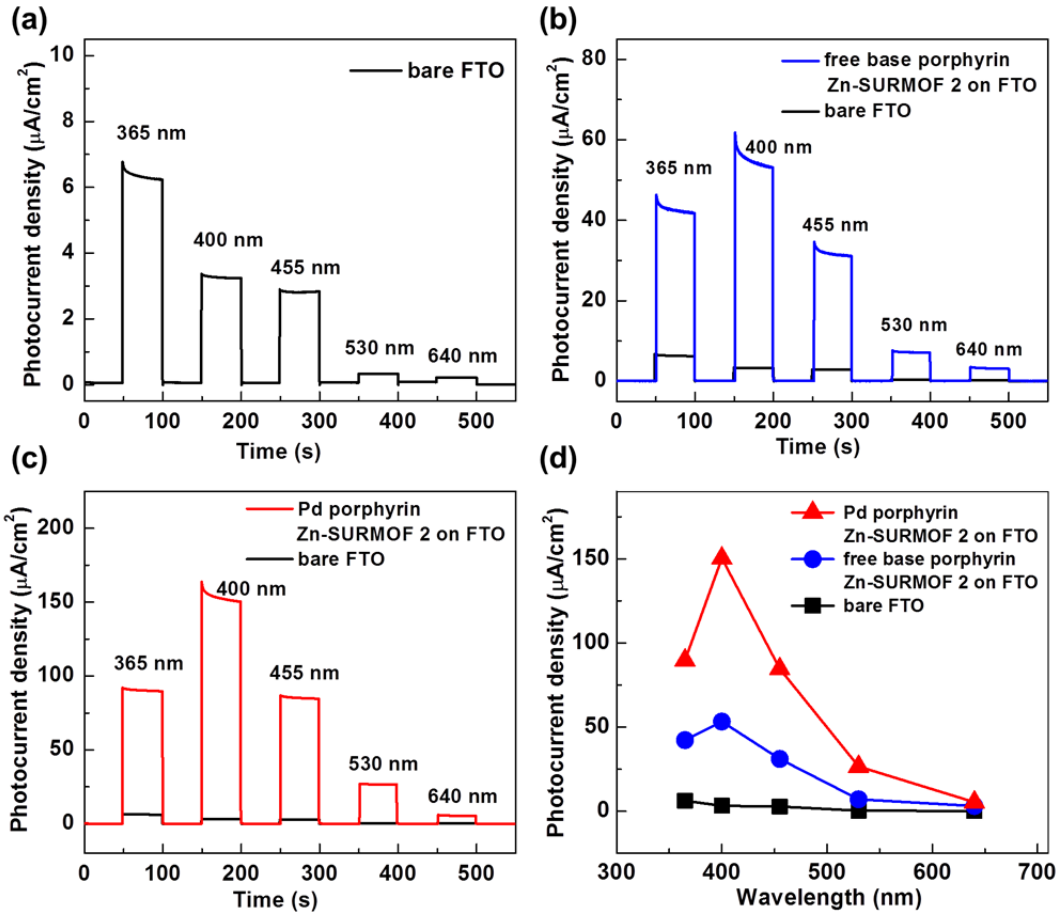

Figure 3.34 Photocurrent action data of (a) bare FTO substrate, (b) free base porphyrin Zn-SURMOF 2 on FTO substrate (in blue) and bare FTO (in black, for comparison), (c) Pd porphyrin Zn-SURMOF 2 on FTO substrate (in red) and bare FTO (in black), and (d) photocurrent generation of bare FTO substrate and porphyrin-based SURMOFs at various illuminating wavelengths of 365 nm, 400 nm, 455 nm, 530 nm and 640 nm.

First, an on-off photocurrent action of the FTO substrate and porphyrin-based SURMOF films (both films with a thickness of about 300 nm) at various illuminating wavelengths (365 nm, 400 nm, 455 nm, 530 nm and 640 nm) were measured, as illustrated in Figure 3.34(a-c). The photocurrent depending on illuminating wavelengths is summed up in Figure 3.34(d). It can be seen that the generated photocurrent from FTO substrate is very low comparing to the porphyrin-based SURMOFs, and decreases with increasing the

illuminating wavelengths. This means there is no critical influence on the photocurrent from the bare FTO substrate. For photocurrent generation from free base porphyrin Zn-SURMOF 2 and Pd porphyrin Zn-SURMOF 2, both thin films exhibited a quick photocurrent response with the light switched on and off. The generated and strongest photocurrent (the maximum) was observed at 400 nm, and follows the absorption of the pure porphyrin chromophores.

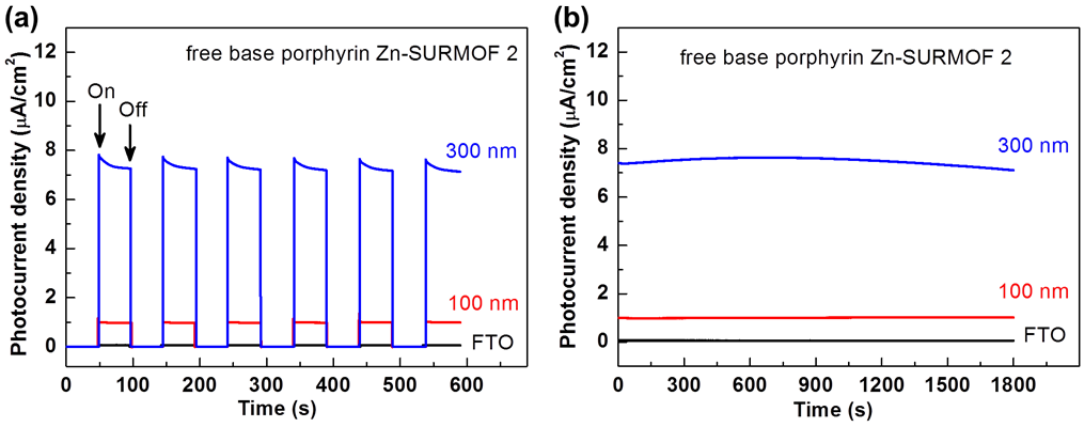

Figure 3.35 On-off photocurrent response (a) and photocurrent durability with 1800 s (b) under illumination at 530 nm of free base porphyrin Zn-SURMOF 2/FTO with different deposition thickness 300 nm (blue), 100 nm (red) and FTO (black). The arrow in (a) indicate the light "on" and "off" with the irradiation time about 50 s. The applied external voltage is 0.06 V vs Pt wire.

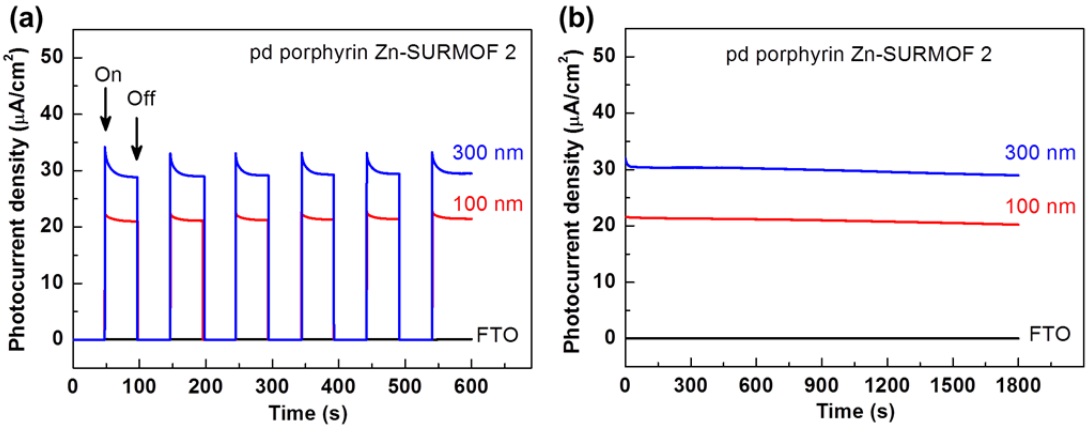

Figure 3.36 On-off photocurrent response (a) and photocurrent durability with 1800 s (b) under illumination at 530 nm of Pd porphyrin Zn-SURMOF 2/FTO with different deposition thickness 300 nm (blue), 100 nm (red) and FTO (black). The arrow in (a) indicate the light "on" and "off" with the irradiation time about 50 s. The applied external voltage is 0.06 V vs Pt wire.

Then, the on-off photocurrent response and photocurrent durability measurement of the free base porphyrin Zn-SURMOF 2/FTO and Pd porphyrin Zn-SURMOF 2/FTO under illumination at 530 nm (in the visible light region) were performed (Figure 3.35 and Figure 3.36). For both cases, the different thicknesses of the MOF films were evaluated, referring to 300 nm (blue) and 100 nm (red) in the figures. It can be seen that the generated photocurrent increases as the increase of film thickness for both free base and Pd porphyrin based SURMOFs. In the 30 min duration, both samples showed a stable generation of photocurrent. The metalloporphyrin based MOF (Pd porphyrin Zn-SURMOF 2) had however a higher photocurrent comparing to the free base porphyrin Zn-SURMOF 2 of same thickness.

3.3.6 Conclusion

The highly oriented porphyrin-based SURMOF films, free base porphyrin Zn-SURMOF 2 and Pd porphyrin Zn-SURMOF 2, were prepared on the transparent and conductive FTO substrates using a LPE spraying method. The XRD data showed that these crystalline thin films grew only along the [001] orientation. By assembling these porphyrin-based SURMOF films on a home-made photoelectrochemical cell, photocurrent generation was performed at various illuminating wavelengths, and the maximum photocurrent was observed at 400 nm for both free base and Pd porphyrin Zn-SURMOF 2. The porphyrin-based MOFs also showed remarkable photocurrent generation efficiency in the visible light region through Pd porphyrin Zn-SURMOF 2 exhibited an enhanced photocurrent generation compared to the free base porphyrin Zn-SURMOF 2.

This section is based on a publication in Angew. Chem. Int. Ed. by Jinxuan Liu et al.(2015) as ref.[176]

4 Optical Properties of SURMOFs and Their Device Applications

4.1 SURMOF-based Bragg reflectors and their optical sensing properties

4.1.1 Background

Photonic band gap (PBG) materials, also known as photonic crystals, are periodic dielectric or metallo-dielectric materials conceived to control the propagation of photons within a defined frequency range.[177, 178] Bragg stacks (BS) are one-dimensional photonic crystals fabricated by alternately stacking transparent layers with different refractive index (RI),[179, 180] as schematized in Figure 4.1. Such PBG materials consist typically of two different metal oxides,[181] but other materials such as polymers[180] have also been successfully employed. One of the particularly interesting classes of materials for the fabrication of such PBG materials is metal-organic frameworks.

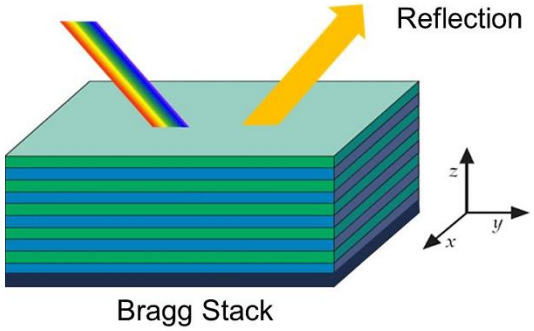

Figure 4.1 Scheme of the Bragg stack reflector. The structure is formed from the multiple thin layers stacked together at z-direction on a substrate. The "rainbow" represents incoming visible light, and the orange arrow represents the reflected light. Only specific frequency range of light is reflected in such a BS system.

MOFs, being highly porous crystallized materials, are drawing further attention in the area of optical and photonic device applications because of their versatile syntheses and produced properties (low density, high surface area and pore volume, high thermal stability, amongst others).[2, 3] The refractive index of MOFs can be tailored to be exceptionally low.[182] This makes these materials ideally suited as components for PBG materials. In previous works, polycrystalline MOF-based PBG materials have been

fabricated by spin-coating of ZIF-8 MOF-nanoparticles on TiO_2 porous layers. Upon loading with different alcohols, the optical properties of the yielding multilayered Bragg stacks change.[183] Nevertheless, a higher optical performance, necessary for a device application, requires the MOFs to be homogenous. This is not the case with the reported process, which, in a way, is by "piling up" MOF nanoparticles.

SURMOFs prepared by LPE spraying method have proven to be rather homogenous thin films with high crystallinity and a well controlled thickness by adjusting the number of spraying cycles. These monolithic SURMOF thin films exhibit low defect densities[101] as well as an excellent mechanical stability.[152]

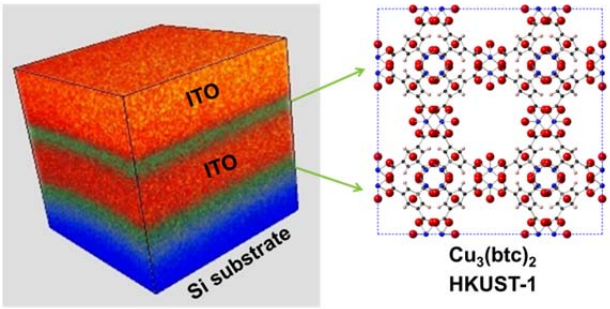

Figure 4.2 Scheme of the SURMOF-based PBG materials (2 bilayer system of ITO/HKUST-1).

In this part, SURMOF HKUST-1 and ITO thin films were applied in a multilayered PBG system (the Bragg reflector), as shown in Figure 4.2. The homogenous and highly oriented HKUST-1 SURMOFs were prepared on silicon substrate by the LPE spraying method, while the intermediate ITO (indium tin oxide) layers were deposited by magnetron sputtering, in the multilayered Bragg reflectors. These PBG materials were color tunable over the whole visible range, depending on the thickness of the corresponding layers, and displayed very high optical performance. The optical sensing capabilities employing the chemo-responsive optical signal were characterized by exposing the Bragg reflectors to various organic solvent. Such SURMOF-based PBG materials provide a basis for the future development of photonic and color-coded chemical sensing devices.

4.1.2 Fabrication of the monolithic SURMOF-based Bragg stack

The SURMOF-based Bragg stack is a monolithic, multilayered hybrid stacks obtained by alternately depositing SURMOF (HKUST-1) and ITO (indium tin oxide) layers on a

modified Si substrate. First, HKUST-1 SURMOF layer was deposited by using LPE spraying method (as described previously) with thicknesses ranging from 80 to 135 nm on the Si substrate. Subsequently, an ITO (indium tin oxide) layer was deposited using magnetron sputtering to thicknesses ranging from 62 to 100 nm. The multilayered hybrid stacks were fabricated by repeating the two processes.

The magnetron sputtering method is a kind of physical vapor deposition (PVD) technique. A thin film of ITO was sputtered through a top down approach from an ITO sputter substrate (the source, SnO_2/In_2O_3=1/9, Kurt J Lesker, UK) in a sputtering chamber. The ITO films were deposited using a r.f. (radio frequency) sputtering setup with a 3″ION' X planar magnetron source (TFC, Grafenberg, DE) mounted on a standard double-cross recipient equipped with a pre-sputter shutter and a sample positioner allowing for various working distances (150–200 mm) between the magnetron and the substrate. The base pressure was below 5×10^{-6} mbar to achieve a sufficient purity. The gas inlet was equipped with an MKS mass-flow control system (MKS Instruments Deutschland GmbH, Germany) providing a constant operating pressure of 2.5×10^{-3} mbar of 80 vol.% Ar and 20 vol.% O_2 for reactive sputtering. The r.f. sputtering power was 66 W (PFG 300 power supply, Hüttinger, Germany) leading to deposition rates of about 66 nm/h.

Before producing the SURMOF-based Bragg stack, the silicon substrates (thickness: 525 ± 20 μm; specific resistivity: 8−12 Ω/cm; from Silchem Handelsgesellschaft GmbH DE) with a [100] orientation were treated by O_2 plasma (Diener Plasma; gas flow: 50 sccm, pure O_2) for 30−40 min to remove impurities as well as to increase the number of OH functional groups and the hydrophilicity. Various thicknesses of the HKUST-1 SURMOF layers were then deposited on pretreated/modified Si substrates using the LPE spraying method (experimental details are presented in Chapter 2.2.3). The desired thickness of the individual HKUST-1 SURMOF layers were adjusted by changing the number of distinct LPE spraying cycles; e.g., 20 spraying cycles for HKUST-1 SURMOFs resulted in a total thickness of 80 nm, 26 spraying cycles in 96 nm, 34 spraying cycles in 115 nm, and 40 spraying cycles in 135 nm, as presented in Figure 4.3.

Then various thicknesses of the ITO thin films were deposited on the freshly prepared HKUST-1 SURMOF layers. The corresponding thickness of sputtered ITO layers depending on the sputtering time for each bilayer system is also presented in Figure 4.3. Thereafter, the next layers of HKUST-1 SURMOF were deposited on the freshly sputtered ITO layers. Due to the presence of OH-groups freed through the O_2 plasma treatment of

the Si substrate or freshly deposited ITO layers, the growth of subsequent HKUST-1 SURMOF layers was achieved using the same LPE method. This process (SURMOF deposition by LPE method conditions, and ITO deposition by magnetron sputtering method) was repeated until the desired number of Bragg stack (HKUST-1/ITO bilayer) was obtained.

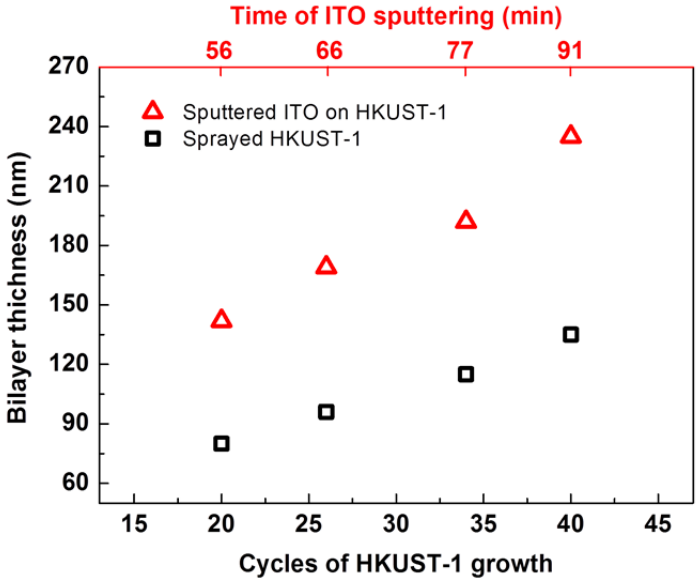

Figure 4.3 Thicknesses of the sprayed HKUST-1 SURMOF layers as a function of the number of LPE spraying cycles, and the corresponding thicknesses of sputtered ITO layer as a function of the sputtering time for each of these bilayer systems, e.g. HKUST-1/ITO (80 nm/62 nm; 96 nm/73 nm; 115 nm/85 nm and 135 nm/100 nm).

Control over the respective fabrication processes allowed tuning the thickness of the multilayered stacks with a high degree of precision. In the present study, four different types of multilayered stacks were fabricated on Si substrate with each stack comprising 5 bilayer. The SURMOF-based Bragg stacks (multilayered HKUST-1/ITO systems) were produced maintaining thicknesses of 80 nm/62 nm, 96 nm/73 nm, 115 nm/85 nm and 135 nm/100 nm, respectively.

4.1.3 Characterization of the SURMOF-based Bragg stack

4.1.3.1 XRD of the multilayered Bragg stack

XRD patterns were measured for these multilayered SURMOF-based Bragg stacks after preparation to check their crystallinity and compactness. The XRD patterns obtained for

the various thicknesses (80, 96, 115 and 135 nm) of HKUST-1 SURMOF thin films deposited on ITO layers are presented in Figure 4.4(a). The XRD patterns of Si substrate and sputtered ITO thin film on Si were measured for comparison and peak position calibration in Figure 4.4(b).

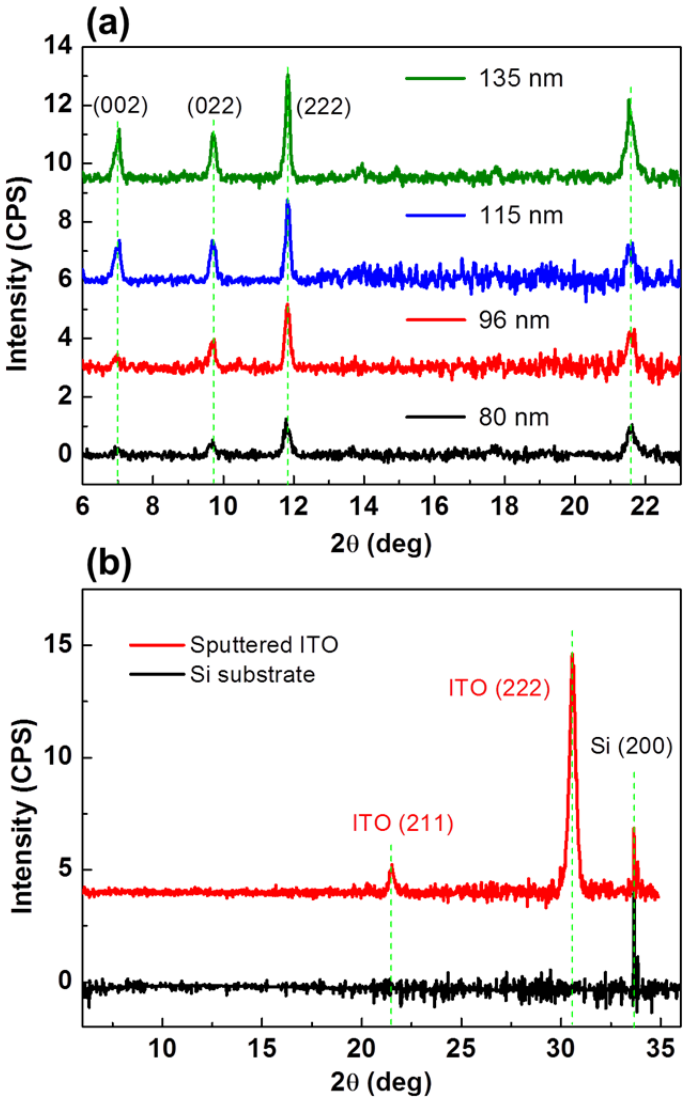

Figure 4.4 Out-of-plane XRD analysis of (a) various thicknesses of the fifth layers of the HKUST-1 SURMOFs deposited on the freshly sputtered ITO layers in the multilayered HKUST-1/ITO systems, and (b) Si substrate and the sputtered ITO thin films on Si substrate.

The prepared samples with various thicknesses of HKUST-1 SURMOFs were grown with mixed orientation. The diffraction peaks with 2θ of around 17.4°, 34.2°, and 53.9° attributed to the (002), (220), and (222) peaks of HKUST-1, respectively; and the peak at

around 21.5° was attributed to sputtered ITO thin film.[184] The results indicate the presence of crystalline SURMOF thin films. The intensity of HKUST-1 SURMOFs increased with increasing film thickness. This shows that the epitaxial growth HKUST-1 retains a similar orientation for crystallites.

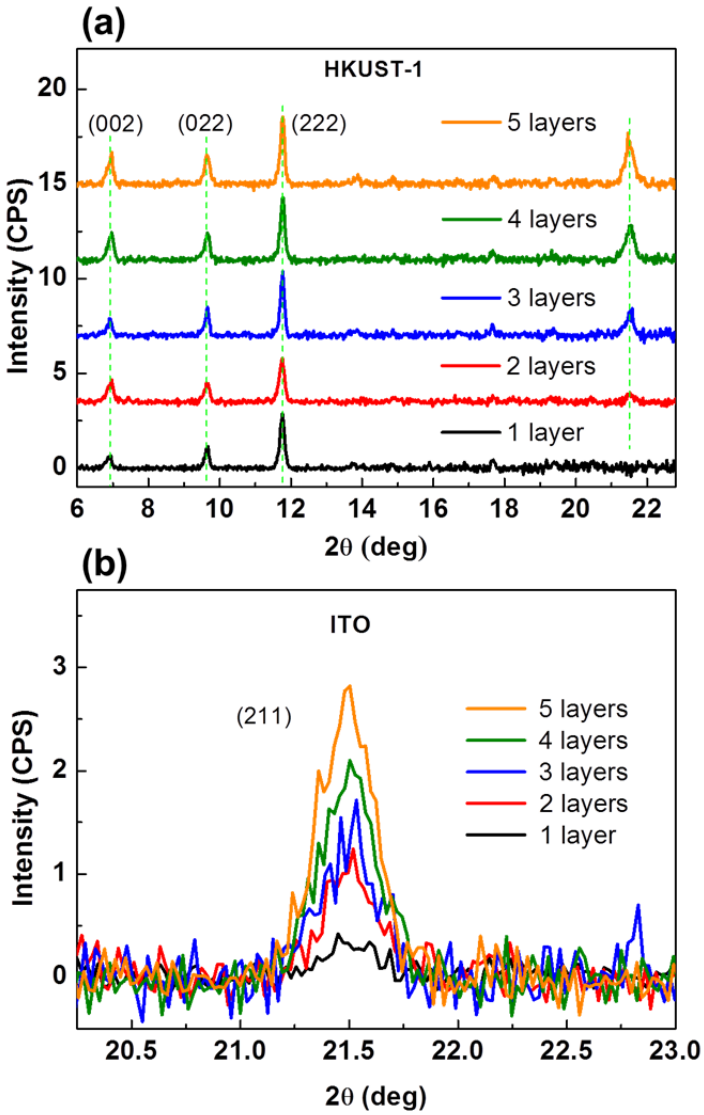

Figure 4.5 Out-of-plane XRD patterns of the different layers of (a) HKUST-1 and (b) ITO thin film for a multilayered SURMOF-based Bragg stacks.

Figure 4.5 shows the XRD patterns of various layers of HKUST-1 and ITO thin film for the multilayered ITO/HKUST-1 system. The first layer of the Bragg stacks was a HKUST-1 thin film grown on Si substrate, so the peak of ITO (211) is not observed on the first layer (1 layer) XRD pattern in Figure 4.5(a). The first ITO layer was sputtered on top of the freshly deposited HKUST-1 SURMOF. After the preparation of the first bilayer (one

ITO layer on top of the HKUST-1 SURMOF layer), another layer of HKUST-1 SURMOF was deposited on top of the sputtered ITO. A new peak (at around 21.5°) attributed to ITO (211) was then observed on the second layer of HKUST-1 SURMOF (2 layers). The intensity of HKUST-1 refraction index increased gradually with the numbers of the bilayer, because all of the deposited HKUST-1 layers contribute to the intensity of XRD patterns. The intensity of ITO (211) peaks were also observed to increase. The XRD patterns of the different layers HKUST-1 SURMOFs showed a similar crystalline orientation on both the Si and ITO surfaces. As shown in Figure 4.5(b), the XRD peak intensity of the sputtered ITO layers also increased with the number of ITO layers.

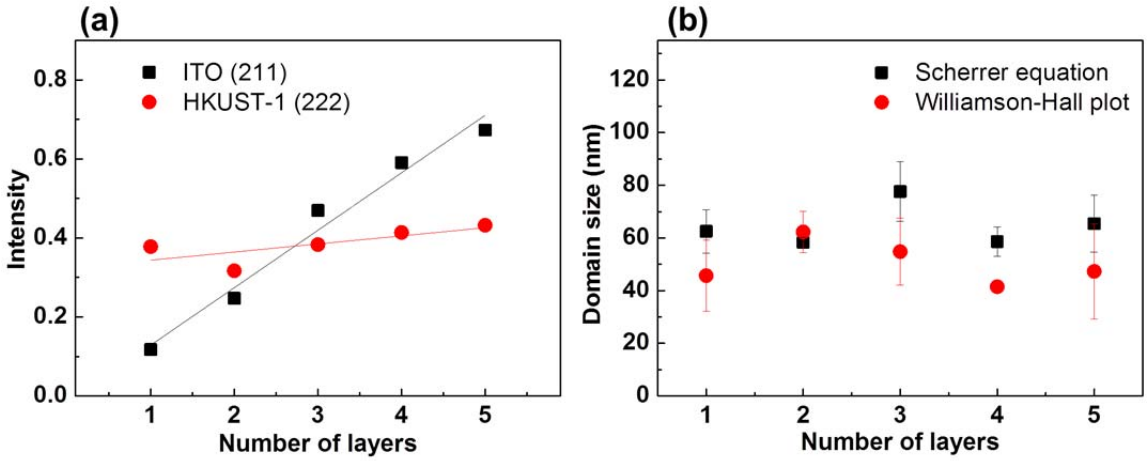

Figure 4.6 (a) comparing the peak intensity (net area) of various layers of HKUST-1 (222) and ITO (211), which were taken from Figure 4.5. The lines are corresponding to the respective linear fit. (b) Domain size L_{vol} of the various layers of HKUST-1 thin films calculated by the Scherrer equation and Williamson-Hall plot.

Further analysis of the XRD peak intensities (net area) of various layers of HKUST-1 (222) and ITO (211) are presented in Figure 4.6(a). It can be seen that the intensities increase with the number of layers. The rate of intensity change between ITO and HKUST-1 is about 7.09; this value has a good consistency with the rate of density for these two materials where ITO/HKUST-1 equals to 7.24.

As mentioned in Chapter 2.2.1 about the XRD method, not only the coherent scattering domain size but also the inhomogeneous strain can broaden the diffraction peak. Scherrer equation and Williamson-Hall plot analysis were used to evaluate the coherent scattering domain size of the various layers of HKUST-1 SURMOF. With the Scherrer equation

(equation (3-1)), introduced in Chapter 3.1.3, the domain size was calculated with an average of all refractive peaks, but without considering stress/strain. Williamson-Hall plot is a method used for determining the coherent scattering domain size and stress/strain of crystals according to (4−1).[185]

$$(B-b)\cos\theta = \frac{K\lambda}{L_{vol}} + 4\varepsilon_0 \sin\theta \qquad (4-1)$$

Where B is the integral breadth, b is the instrumental width, θ is the diffraction angle, K is the Scherrer constant (0.89), λ is 0.15406 nm (Cu Kα_1), L_{vol} is the domain Size, and ε_0 is the lattice constant mismatch (the stress/strain).

As presented in Figure 4.6(b), the coherent scattering domain size of HKUST-1 SURMOF thin films calculated by both the methods shows a quite similar value of approximately 58 nm for all the different layers (from 1 to 5 bilayer). Since the instrumental contribution to the line broadening was considered, and no stress/strain contributions were added, the calculated domain size by Scherrer equation represents a lower limit. However, for the domain size of HKUST-1 SURMOFs analyzed by Williamson-Hall plot, all of the (002), (220) and (222) reflections were considered.[186] The consistent and lesser scattering values confirmed the homogeneity of the HKUST-1 SURMOF thin films in the hybrid PBG materials.

4.1.3.2 HR-SEM cross-section analysis of the multilayered Bragg stack

Figure 4.7 shows the cross-sectional SEM images of the various multilayered Bragg stacks. The homogenous stacking of the distinct material layers can be seen in both, the 3 bilayer and 5 bilayer samples. The ITO layers showed a better resolution comparing with HKUST-1 SURMOF layers because of its higher conductivity and density.

In this case, focused ion beam (FIB) cutting method was used to reprocess the multilayered Bragg stack samples for the cross-section analysis. The FIB-cutting analysis was done by using a dual beam focused ion beam microscope (Zeiss AURIGA 60) equipped with a Ga^+ ion gun and a high resolution field emission SEM (FESEM). For milling of the samples, an acceleration voltage of 30 kV (beam current of 20 nA) was applied. The final milling step was done at 30 kV and 600 pA. FESEM imaging was performed at 5 kV, using an In-Lens detector.

As presented in Figure 4.8, the HR-SEM cross-section analysis of a 5 bilayer (HKUST-1/ITO = 135 nm/100 nm) SURMOF-based Bragg stack for the samples prepared by both mechanical break-apart and FIB-cutting.

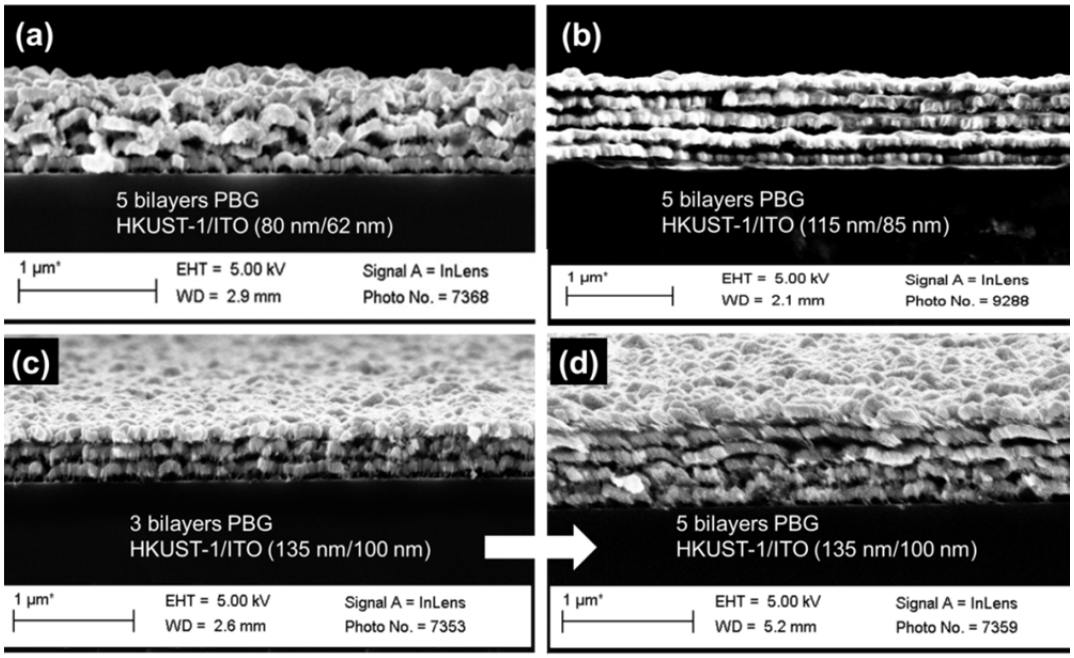

Figure 4.7 HR-SEM cross-sections of the multilayered SURMOF-based Bragg stacks. (a) 5 bilayer HKUST-1/ITO (80 nm/62 nm); (b) 5 bilayer HKUST-1/ITO (115 nm/85 nm); (c-d) 3 and 5 bilayer HKUST-1/ITO (135 nm/100 nm).

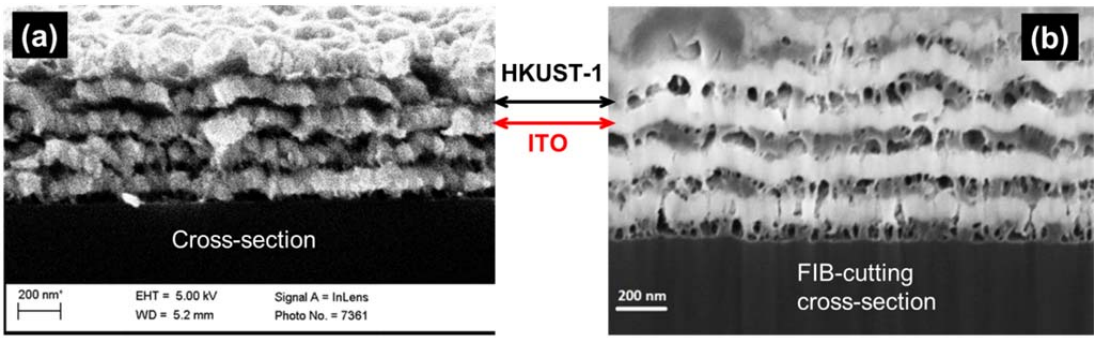

Figure 4.8 HR-SEM cross-section analysis of a 5 bilayer (HKUST-1/ITO = 135 nm/100 nm) SURMOF-based Bragg stack for the samples prepared by both mechanical break-apart (a) and FIB-cutting (b). The FIB-cutting may lead to a partially evaporation of the HKUST-1 layers, therefore the observed macro-porous structures is an artefact due to the FIB-cutting process.

During FIB-cutting, parts of materials from HKUST-1 layer were lost by thermal evaporation, and led to the observed macro-porous morphology as seen in Figure 4.8(b). Comparing the two cross-section images revealed the FIB-cutting being more cross-section analysis advantageous as it provided clearer images with more defined layer thickness and a better contrast between the different materials.

4.1.3.3 ToF-SIMS analysis of the multilayered Bragg stack

ToF-SIMS measurements were performed on the SURMOF-based Bragg stacks for a thorough investigation of the multilayered PBG systems. During the measurement, ultra-high vacuum (UHV) base pressure kept lower than 5×10^{-9} mbar. For high mass resolution, the source was operated in the "high current bunched" mode providing short Bi_3^+ primary ion pulses (the length of 1.1 to 1.3 ns allowed for high mass resolution) at 25 keV and a lateral resolution of approximately 4 μm. Spectra were calibrated from the omnipresent C^+, CH^+, CH_2^+, CH_3+, Si^+, Cu^+ and $^{113}In^+$ corresponding peaks.

For the depth profiling, a dual beam analysis was performed. The primary ion source was performed with the same conditions as mentioned above. An oxygen sputter gun was used to erode the sample. The obtained 5-dimensional data sets (x and y positions, sputter ion dose density, m/z, and count rate) are presented as x/y-area integrated ion intensities over ion dose density or as 3D rendering. Due to different sputter rates of the layers no linear depth scale is provided.

Figure 4.9 shows a 3D reconstruction of a 2 bilayer HKUST-1/ITO (135 nm/100 nm) PBG Bragg stack based on specific ion signals from ToF-SIMS depth profiling. For this analysis a 500×500 μm^2 region was continuously analyzed using the Bi_3^+ ion source, while a concentric area of 800×800 μm^2 was eroded with a 2 keV oxygen sputter beam up to a final dose density of 6.3×10^{17} cm^{-2} ions. In the ToF-SIMS images in Figure 4.9 the HKUST-1 layers are depicted as Cu with ^{65}Cu and Cu_2 signals characterizing the MOF layers, and with In_3O^+ together with other In_xO_y species characterizing the ITO layers. SIMS depth profiling confirmed a homogeneous and continuous layer system.

Figure 4.10 shows an intensity profile of $In_3O_2^+$, Cu^+, and Si^+ from a 5 bilayer HKUST-1/ITO (135 nm/100 nm) system. For this analysis a 100×100 μm^2 region was continuously analyzed using the Bi_3^+ ion source (64×64 pixel), while a concentrical area of 250×250 μm^2 was eroded with a 1 keV oxygen sputter beam up to a final dose density of 2.3×10^{18} cm^{-2} ions. ^{63}Cu, as shown in Figure 4.10, as well as ^{65}Cu and Cu_2 signals

characterize the MOF layers. In_3O_2, together with other In_xO_y species characterize the ITO layers in negative polarity Secondary Ion Mass Spectra. As seen from this graph both layers can be clearly distinguished and exhibit a regular depth distribution.

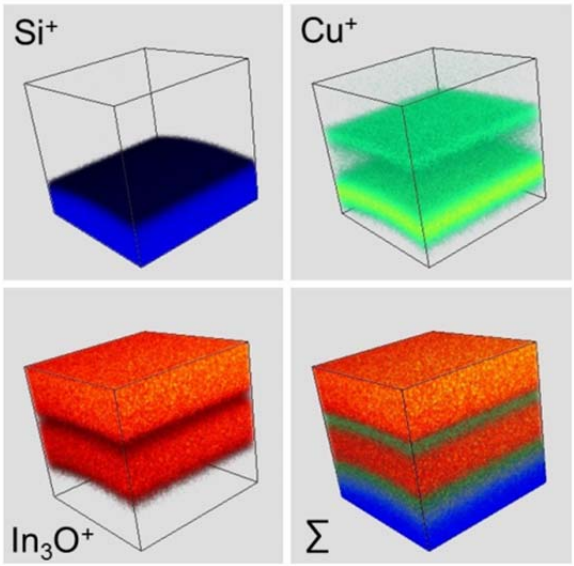

Figure 4.9 3D reconstruction of a 2 bilayer HKUST-1/ITO stack deposited on silicon substrate using ToF-SIMS depth profile data. Top left, blue: Si^+; top right, green: Cu^+; lower left, orange: In_3O^+; lower right: combined overlay.

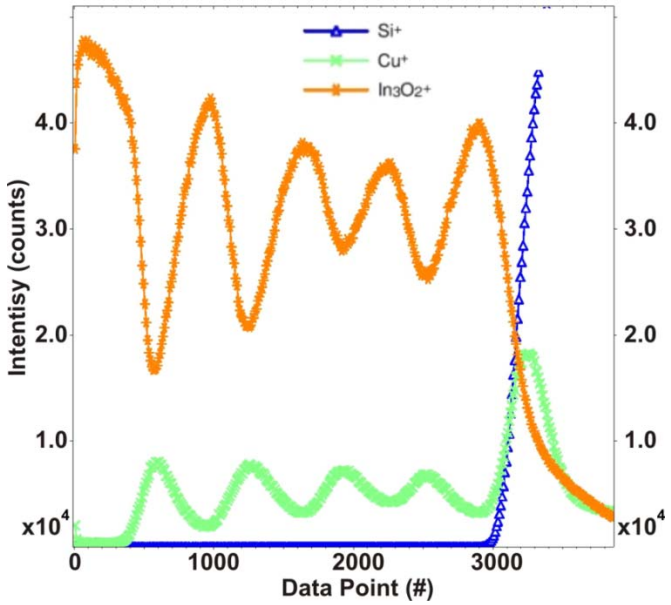

Figure 4.10 ToF-SIMS depth profile of a 5 bilayer HKUST-1/ITO stack performed with oxygen (1 keV) erosion. Orange: $In_3O_2^+$, green Cu^+, blue Si^+.

Although the ITO layers were thinner than the MOF layers, the plotting of secondary ion count rates over the applied sputter ion dose provided a nearly symmetrical profile for all 10 layers due to the different erosion rates of the materials this until the silicon substrate was finally reached. As shown in Figure 4.10, rising and falling flanks for the $In_3O_2^+$ signals are nearly symmetrical without any strong tailings towards the deeper layers. In case of the multiatomic fragment $In_3O_2^-$, no forward implantation artifacts emerged. In case of Cu, a slight forward implantation tendency was observed at the tailings on the trailing sides of the profile plots. Due to a partial doping of individual copper atoms into the substrate material (Si), the lowest MOF layer exhibited an anomalous signal.

4.1.4 Optical properties of the SURMOF/ITO hybrid PBG material

The solvent-free HKUST-1 has a reported refractive index (n) of n = 1.39 (at 200 °C)[182] at a wavelength of 750 nm. Such a low RI is in a good agreement with the static dielectric constant (n ≈ 1.30) predicted by Seifert and co-workers.[187] By exposing the activated or dry HKUST-1 thin films to moisture or ethanol (EtOH) atmosphere, its refractive index increases to n = 1.55−1.6.[182]

The spectroscopic ellipsometry measurements of the freshly produced the ITO and the HKUST-1 SURMOF thin film were performed in a wavelength range of 410–750 nm with a fixed incidence angle of 75° aligned on silicon substrates, as shown in Figure 4.11.

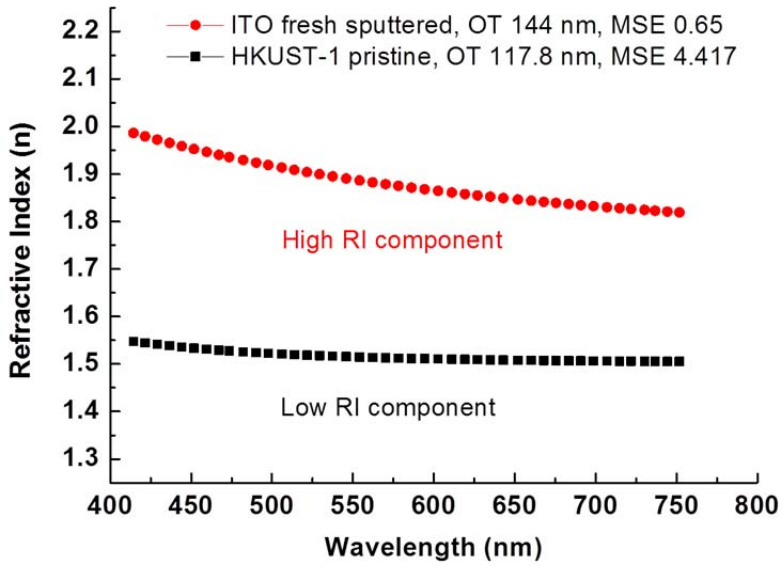

Figure 4.11 Spectroscopic ellipsometry data of the ITO and the HKUST-1 SURMOF thin film measured at ambient conditions; the ITO and HKUST-1 SURMOF indicate the high RI and low RI component in the multilayered PBG materials.

The freshly prepared ITO and HKUST-1 SURMOF thin films show the high refractive index of ITO (n ≈ 2.0) and the low refractive index of HKUST-1 (n ≈ 1.5). The optical thickness of the employed HKUST-1 SURMOF and ITO thin films are equal to the product of the geometric thickness and the refractive index of the employed layers. The RI value of the pristine (freshly prepared) HKUST-1 SURMOF was consistent with the reported water or ethanol loaded HKUST-1 thin film.[182] The multilayered Bragg stacks, comprised with the high RI component of ITO and the low RI component of HKUST-1 SURMOF, were produced by stacking the two components with various thicknesses independently. The optical properties of these hybrid PBG materials are presented in following.

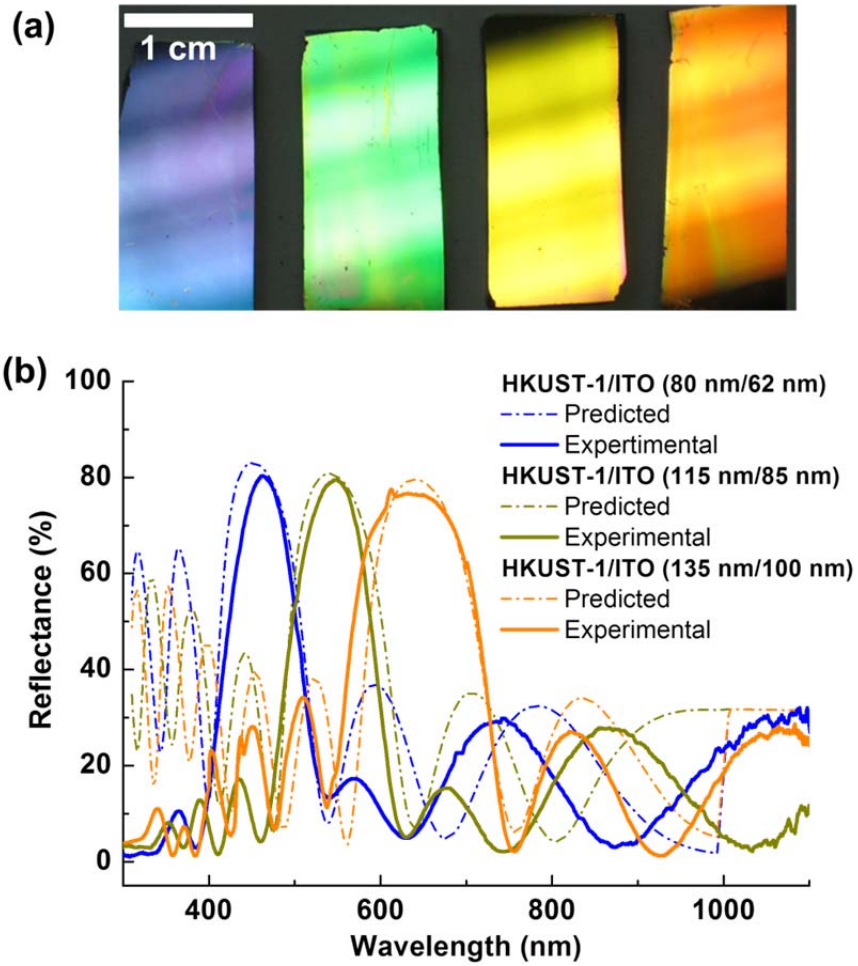

Figure 4.12 (a) Photographs of the four different SURMOF-based PBG materials (stripes are an artefact caused by the light source), the different colors correspond to the various Bragg stack reflectors consisting of HKUST-1/ITO layers ranging from 80 to 135 nm and from 62 to 100 nm, respectively, and (b) the calculated/predicted and experimentally determined reflectance of the 5 bilayer PBG materials.

Four different types of SURMOF-based PBG materials were produced and 5 bilayer were stacked for each type. As shown in Figure 4.12(a), the color of blue, green, yellow and orange from the images corresponds to various bilayer (HKUST-1/ITO) systems having the thickness of 80 nm/62 nm; 96 nm/73 nm; 115 nm/85 nm and 135 nm/100 nm respectively. Figure 4.12(b) presents the reflectance measurement of the hybrid PBG materials with a 5 bilayer stack. A comparison of the experimental optical reflectivity data with the simulated reflectivity plots revealed the exceptional optical quality of the SURMOF-based hybrid PBG. In all cases, the predicted and measured reflectivity match very well. Furthermore, the reflectivity maximum reached about 80%, exceeding the value reported for the system based on ZIF-8/TiO_2 and ZIF-8/Pt.[183]

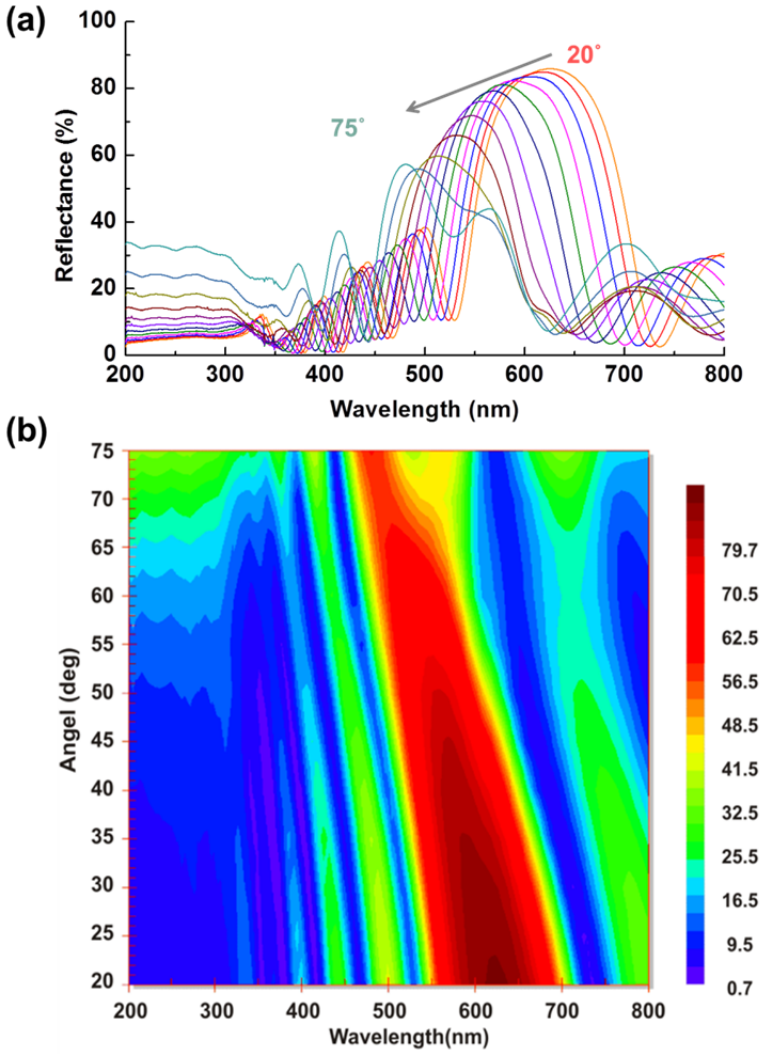

Figure 4.13 (a) Angular dependence reflectance of the 5 bilayer HKUST-1/ITO (135 nm/100 nm) hybrid PBG (orange) and (b) the corresponding contour plot, the spectra were recorded from 20° to 75° incidence with 5° increment.

The angular dependence reflectance was measured with an incidence ranging from 25° to 75° (with 5° increment). The specular reflectance of each samples was measured with a spectral bandwidth from 200 to 800 nm (size 2.5 × 2.5 cm). The data collection, evaluation and graphical analysis were carried out on the software (Cary WinUV®) provided by Agilent. Figure 4.13(a) shows an angular dependence reflectance of a 5 bilayer hybrid PBG material (HKUST-1/ITO = 135 nm/100 nm, orange colored) at variable angles of incidence. By starting with a high reflectance above 80% at around 635 nm and at 20° incidence, the PBG showed an angle dependent decrease of the maximum reflectance. The blue shift of the PBG to smaller values was observed by lowering the angle of incidence stepwise with a 5° increment during the angular reflectance measurements.

The contour plot of the angular dependence reflectance is presented in Figure 4.13(b), which showed the reflectance changes corresponding to incidence angles in a 2D image. The highest reflectance (in red color) is shifted to lower wavelength by increasing the incidence angle. Furthermore, the corresponding 3D plot of the 5 bilayer PBG material is shown in Figure 4.14. The 3D plot represents the reflectance of the stack corresponding to the wavelength and incidence angles of the beam. The iridescence can be simply demonstrated by tilting the macroscopic samples at different angles.

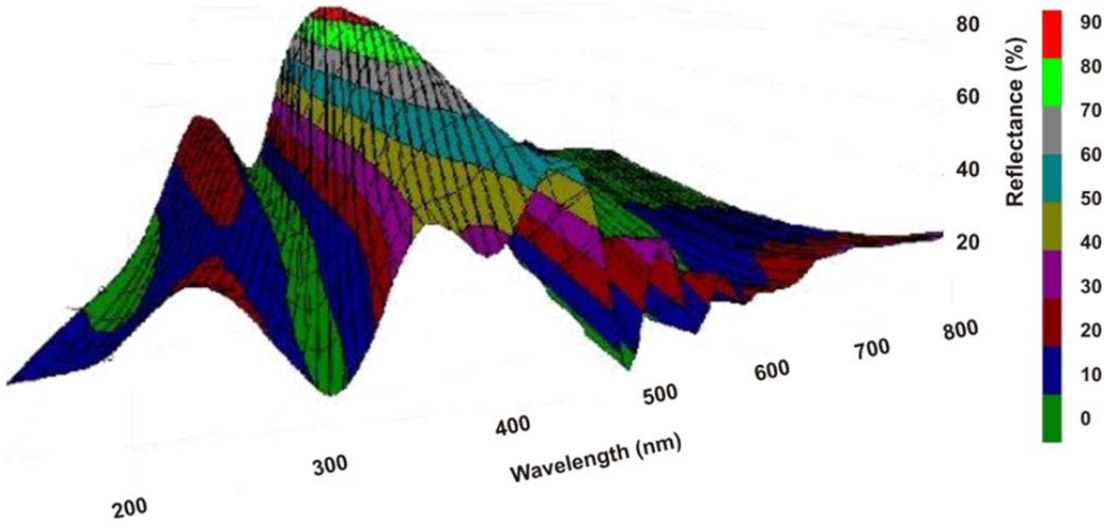

Figure 4.14 3D plot of the 5 bilayer HKUST-1/ITO (135 nm/100 nm) hybrid PBG material (orange), angular dependence reflectance was recorded from 20° to 75° incidence with 5° increment.

As shown in Figure 4.15 and Figure 4.16, the angular dependence reflectance values of the other two 5 bilayer hybrid PBG materials were also presented at variable angles of incidence: the yellow colored Bragg reflector (HKUST-1/ITO = 115 nm/85 nm) (Figure 4.15(a)) and the blue colored Bragg reflector (HKUST-1/ITO = 80 nm/62 nm) (Figure 4.16 (a)). The angle-dependent decrease of the reflectance maximum as well as the blue shift to smaller values of the PBG were also detected in these SURMOF-based PBG materials by lowering the angle of incidence stepwise with a 5° increment. The corresponding contour plots of the angular dependence reflectance on the yellow and blue colored hybrid PBG materials are presented in Figure 4.15(b) and Figure 4.16(b).

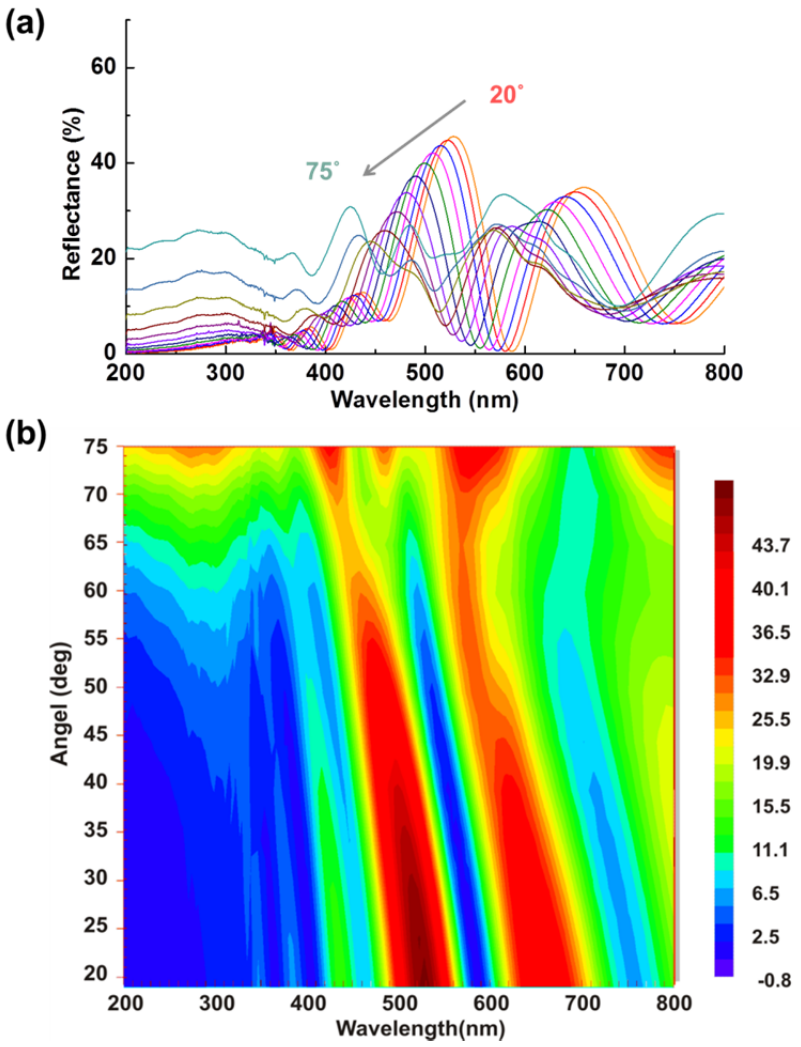

Figure 4.15 (a) Angular dependence reflectance of the 5 bilayer HKUST-1/ITO (115 nm/85 nm) hybrid PBG material (yellow) and (b) the corresponding contour plot, the spectra were recorded from 20° to 75° incidence with 5° increment.

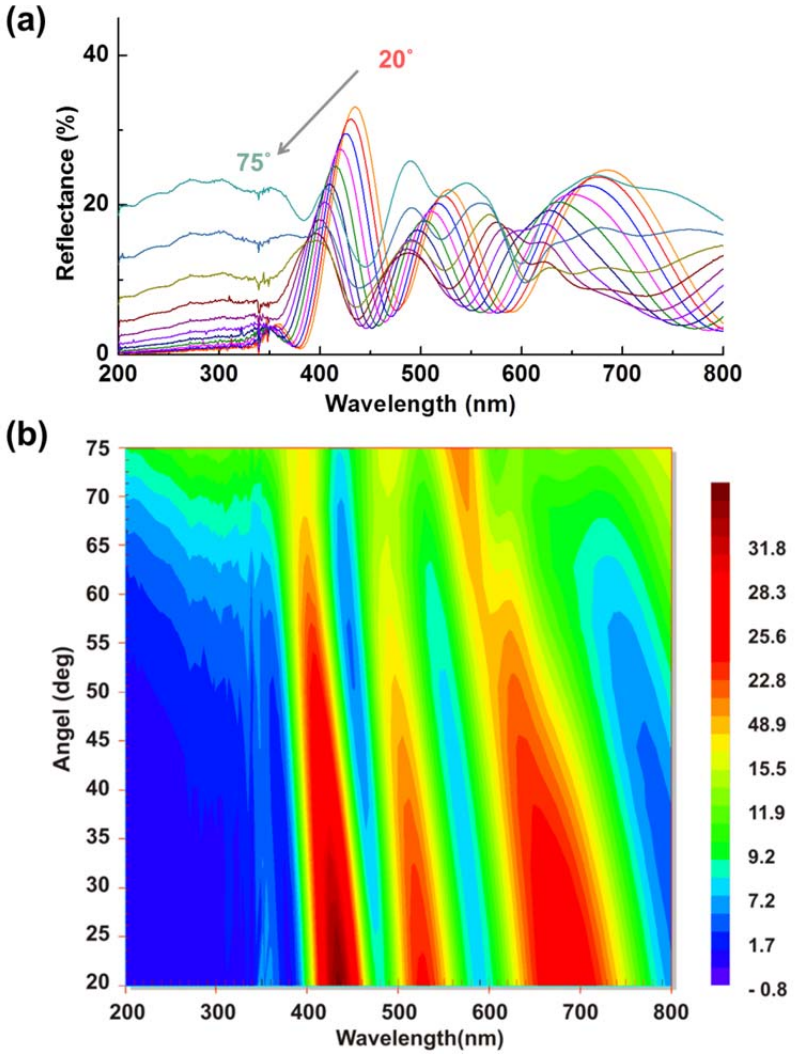

Figure 4.16 (a) Angular dependence reflectance of the 5 bilayer HKUST-1/ITO (80 nm/62 nm) hybrid PBG material (blue), and (b) the corresponding contour plot, the spectra were recorded from 20° to 75° incidence with 5° increment.

With the advantageous flexibility for chemical functionalization, post synthesis, as well as the MOFs capacity for loading other functional guests, the SURMOF-based devices provides an adequate system for optical or light induced switching[85] or for charge transport properties.[101] In the present study, such multilayered SURMOF-based Bragg stacks provided the basis for the fabrication of photonic, color-coded hybrid PBG materials, which could act further as chemical sensing devices. In the next part, the porous nature of the HKUST-1 SURMOFs integrated inside the multilayered PBG systems was exploited and modulated for adjusting the optical constant. These properties could be directly used for optical sensing.

4.1.5 Chemo-responsive optical sensing of the SURMOF/ITO hybrid PBG

Having a thermal stability typically exceeding 200 °C and other advantageous mechanical,[39] dielectric,[188] or optical[182] properties, MOF coatings provide the base functions for numerous applications. Loading the pores with appropriate guest molecules can modulate their electrical and optical properties,[85, 102] which is particularly interesting for optical sensing.[71] The significant change in refractive index resulting from loading guest molecules in the nanopores of HKUST-1[182] allows a direct the realization of a sensor, and at the same time, the sorption behavior of the MOF material can be quantitatively and accurately determined.

Activation and drying of the SURMOF/ITO multilayered PBG material led to a pronounced change in their PBG behavior, including a significant reduction of scattered light at the blue edge of the PBG as shown in Figure 4.16. This is consistent with the removal of excess water/solvent molecules from the HKUST-1 crystal structure. The dry or activated process resulted then in an improved optical quality of the PBG material, by increasing the fringe visibility and generating sharp PBG edges.

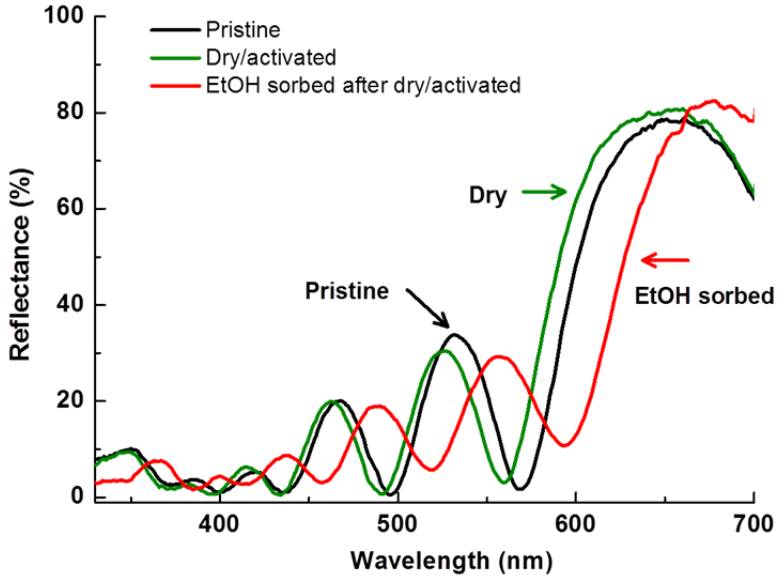

Figure 4.16 PBG blue edge changes after heating at ≈200 °C for 1−2 h for the effect of dry or activation and EtOH loading on the multilayered PBG material.

As shown in Figure 4.17, a reflectance measurement was performed on a 5 bilayer HKUST-1/ITO (135 nm/100 nm) stack for a direct optical sensing of ethanol (EtOH) and tested the reliability of the system as an optical device.

Prior to the measurements, the reflectance spectra were normalized to a reference (here from a clean Si substrate) under *in situ* conditions (in a glovebox under N_2 atmosphere). Figure 4.17 presents the process of the reversible EtOH sensing behavior. The SURMOF/ITO stack was firstly activated (dried) to remove the residual solvent (EtOH in this case) filling the pores of the SURMOFs, and reached the state refer to DRY. Thereafter, the nanopores were filled with the analyte organic solvent (here EtOH), which induce the PBG reflectance to reached a minimum. The system was then in a state referred to WET. After removing the EtOH excess from the PBG materials to leave sorbed only molecules in the pores, the reflectance increased again (system state referred to as SORBED). Finally, with another complete activation, the PBG was brought back to the DRY state with the reflectance shifted to its initial position.

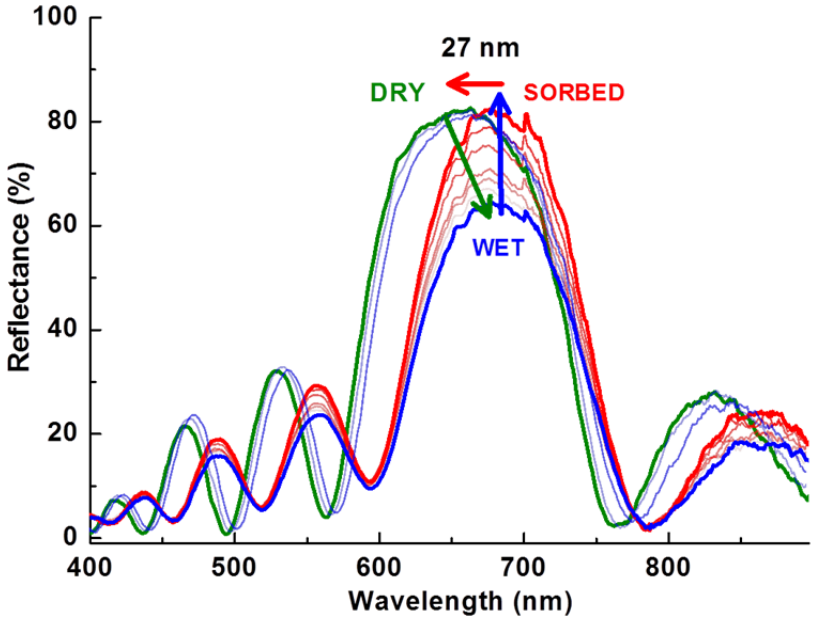

Figure 4.17 Optical sensing of ethanol on the 5 bilayer HKUST-1/ITO (135 nm/100 nm) PBG material. The state of DRY represents the activated PBG stacks (drying out the solvent from the pores of SURMOF), WET represents wetting of the PBG stacks with analyte (means ethanol in this case), and SORBED represents sorbing the ethanol in the PBG materials without excess ethanol left on surface. This process (DRY-WET-SORBED) is fully reproducible and cycleable.

As presented in Figure 4.17, when the dry or activated sample was immersed in EtOH, a pronounced redshift, as well as a reduction of the maximum reflectance by around 20%, was observed. This process was fully reversible and reproducible. The system slowly

recovered (within a few seconds, depending on the boiling point of the organic solvent) when the sample dries out. The optical sensing of other for other lower refractive index solvents was also studied and the corresponding PBG maxima measured for the DRY and WET states are given in Table 4.1

Table 4.1 Optical sensing experiments demonstrate a significant red shift of the PBG by immersing the 5 bilayer HKUST-1/ITO (135 nm/100 nm) stacks into different organic solvents (with different RI*) at 20 °C and λ=660 nm.

Immersion Solvent / RI*	PBG Start Max.	PBG (red) shift
EtOH / 1.360	658 nm	685 (27 nm)
i-PrOH /1.381	658 nm	689 (31 nm)
THF / 1.407	657 nm	681 (24 nm)
Cyclohexan / 1.424	658 nm	684 (26 nm)
Toluene / 1.487	657 nm	695 (38 nm)

Significant red shifts of 20 to 40 nm, depending of the respective organic solvent were observed. By filling the SURMOF pores with lower refractive index solvent, the reflectivity maxima were also decreased by an intensity of around 20%. The sorption behavior allowed a pronounced sensitivity for chemo-responsive optical sensing. The reflectance measurements were done in a confined setup (controlled atmosphere using a glovebox) to ascertain the absence of any environmental interference, but the optical sensing could also be realized less stringent conditions.

Furthermore, the prediction of the reflectance for the empty (solvent free) as well as the sprayed (solvent-loaded) multilayered HKUST-1/ITO (115 nm/85 nm) PBG system were performed using the proprietary software of ellipsometer. From this simulation, a lowering of reflectance of around 10% and a red shift of around 20 nm was predicted, as shown in Figure 4.18(a). The loss of reflection is arising from additional or in excess absorbed water or solvent molecules in the pores of SURMOF, as well as from an increase of the RI of the porous SURMOF constituent and the solvent layer on the Bragg stack. Figure 4.18(b) presents the simulation of the PBG shift modeling the excess ethanol as increasing the optical thickness by 10−20 nm for the multilayered Bragg stack when immersed in the solvent. The calculated significant change of the optical thickness of the PBG must significate an increase of the RI. The drying or activation process could lead to a change in the polycrystalline structure of the HKUST-1 MOF or of the sputtered ITO layer. The

compact SURMOF or ITO thin film within the PBG systems resulted in a smaller amount of defect-scattering. The further optimization of the annealing procedure is expected to lead to a further improvement of the BS optical quality.

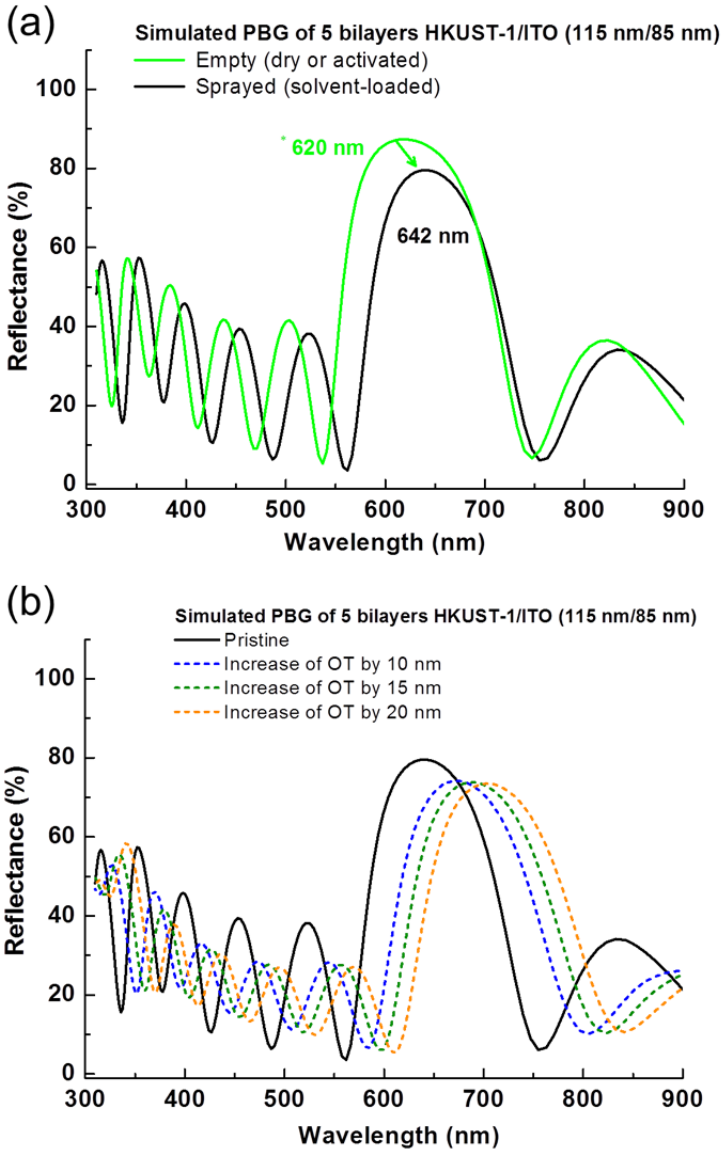

Figure 4.18 Simulation of 5 bilayer HKUST-1/ITO (115 nm/85 nm) PBG system for the (a) empty (dry or activated HKUST-1, k=0) and sprayed (solvent-loaded HKUST-1), and (b) PBG shift of the simulated increase of the optical thickness (OT) (e.g. 10, 15 and 20 nm) overlaid with EtOH as the filling organic solvent.

However, the rather rigid lattice of HKUST-1 did not expand substantially upon loading with small guest molecules.[189, 190] This is in contrast to most organic polymers for which loading with organic molecules leads to a swelling and geometric changes, as seen with

the swelling of thin polymer film by toluene vapor.[191] To confirm the absence of pronounced geometrical changes of the SURMOF-base hybrid PBG materials, *in situ* AFM on film thickness was performed upon loading guest molecules. This is a substantial advantage with SURMOFs since the built-up of mechanical stress within the Bragg stack heterostructures during the loading is avoided. As seen with the *in situ* AFM measurements of Figure 4.19, the thickness of the 5 bilayer Bragg stack remained unchanged upon immersion into EtOH from 987 nm (Air) to 985 nm (in EtOH).

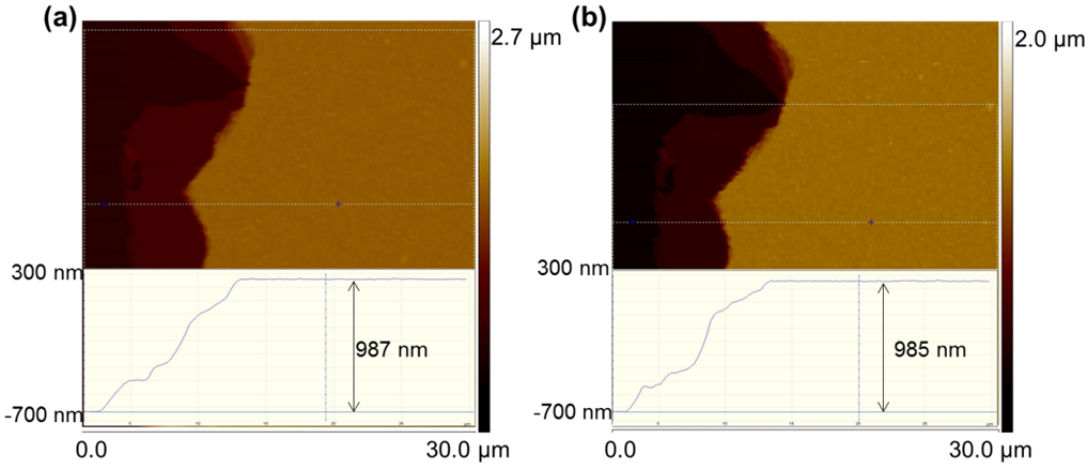

Figure 4.19 Thicknesses of a 5 bilayer PBG materials for the effect of guest molecule (solvent) loading by *in situ* AFM measurement. The thickness of the BS is 987 nm in air (a) and 985 nm in EtOH (b).

The sorption and desorption studies can be described in a dynamic way. The modulation and shifting of the PBG (activated/dried and solvent filled HKUST-1) are consistent with the prediction/simulation. The differences between the experimental and calculated reflectance spectra were explained by the existing variation of thicknesses along the various sputtered ITO and LPE sprayed HKUST-1 films. Additional effects, like the surface and eventually interface roughness losses due to scattering and reflections, can be considered.

4.1.6 Conclusion

The combination of a LPE spraying process (yielding high quality SURMOF films) with an ITO sputtering process allowed the successful fabrication of high quality optical devices on a square centimeter scale. In these hybrid systems, the SURMOF HKUST-1 acted as the low RI material while the sputtered ITO was the high RI material. By

controlling the thicknesses of the produced HKUST-1 and ITO layers, the obtained SURMOF-based hybrid PBG material was color-tunable over the whole visible range. The monolithic multilayered (HKUST-1/ITO) Bragg stacks mounted on a Si substrate showed an outstanding optical quality with low scattering losses as manifested by a reflectance of around 80% at the maximum PBG wavelength.

The SURMOF-based hybrid PBG materials provided a tunable platform with promising application as chemo-responsive optical sensing devices. The optical properties of the PBG materials showed pronounced changes during loading or unloading. Those changes were specific to the guest molecules probed. The reflection band shifts (≈20−40 nm depending on the organic molecule) were not only easily quantified by simple colorimetric methods but also directly observable by the naked eye. The process was further proved by *in situ* AFM investigations to originate from a RI modification as virtually, the thickness of the sample remained constant during the sorption/desorption process.

Part of the results in this section has been published in Chem. Mater. by Jianxi Liu et al.(2015) as ref.[192]

4.2 Prussian blue films and their electrochromic switching behavior

4.2.1 Background

Metal-organic complexes[193, 194] and coordination network compounds (CNC)[195, 196] have been extensively used in optoelectronic devices, like display/window application or organic light emitting diodes (OLEDs). Prussian Blue (PB, $Fe_4^{III}[Fe^{II}(CN)_6]_3$), a particularly interesting CNC example, has been extensively investigated for its optical, magnetic and electrical and dielectric properties.[197-199]

PB crystallizes in a simple cubic structure with cyanide ligands (C≡N) coordinating Fe^{2+} (low spin) and Fe^{3+} (high spin) ions in an alternating and highly ordered cubic unit cell.[196] A PB-type structure is shown in Figure 4.20.[200] These electron transfer properties as well as the electric conductivity and redox properties of PB are of huge interest for the fabrication of CNC based functional materials. The epitaxial preparation of monolithic films of PB enables determining the orientation dependent properties of such molecular magnetic materials. However, monolithic PB thin films produced on transparent conductive oxides (TCO), such as indium tin oxide (ITO) and fluorine doped tin oxide (FTO), electrodes have not been reported, and only the electrodeposition of epitaxial PB thin films on Au substrates (110)[201] has been reported so far.

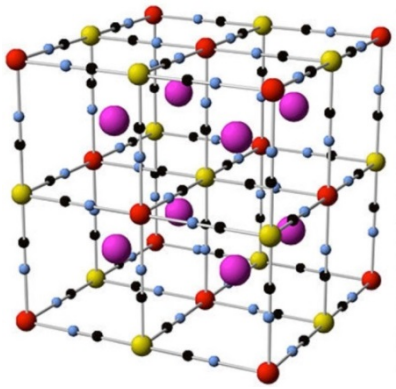

Figure 4.20 Representation of a cubic PB-type structure (Fe^{II}, Fe^{III}, C and N are coded in yellow, red, black and blue; interstitial open sites are in purple). (Taken from ref.[200])

In this part, thin films of crystalline and highly oriented Prussian Blue were fabricated on conductive substrate by the means of layer-by-layer or LPE spraying method, as well as through spin-coating process. The monolithic PB thin films were coated not only on gold

substrates but also on TCO substrates, and were then used without any further modification in an electrochemical cell to emulate as a device. The blue color of PB arises from a broad absorption band at around 700 nm, while the reduced state of this material, Prussian white (PW), is transparent. This redox process was shown to be reversible during electrochromic (EC) switching cycles, with the crystallinity as well as the high orientation remaining intact.

4.2.2 Preparation of PB thin films on the functionalized conductive substrate

PB thin films were prepared on MHDA SAM functionalized Au substrate as described in Chapter 2.2.2, and hydroxylated ITO or Si substrates by means of layer-by-layer spraying and spin-coating methods. A PB solution was prepared as following: PB powder was dissolved in H_2O/EtOH (1/9, v/v) mixture to a concentration of 1% (wt%), and an ultrasonic bath was used for 20 min to help dissolving the PB before preparing of the sample. The conductive substrates (ITO and Au) and semiconductor (Si) substrate pretreated to support PB thin films. Surface functionalization or modification of these substrates is the key to increase the quality of the films. ITO and Si substrates were pretreated by either O_2 plasma or UV-Ozone irradiation for 20-30 min to remove any organic impurities and produce hydroxylate groups on the substrate surface.

For the layer-by-layer spraying method, the functional substrates were placed on the sample holder and subsequently sprayed with above mentioned PB solution for 15 s, with 20 s waiting time between the spraying steps. The number of spraying cycles determines the final thickness of the deposited PB film. After 50 cycles, blue colored films were obtained. For the spin-coating method, a few drops (50-100 μL) of the solution were dropped onto the functional substrates at room temperature and spun at 4000 rpm for 30 s for each layer preparation.

4.2.3 Characterization of the PB thin films

4.2.3.1 XRD patterns of the prepared PB thin films

All of the prepared PB thin films were characterized by XRD. As shown in Figure 4.21, the PB thin films were grown on the Au, ITO, and Si substrates with a [00l] orientation, as proven by the presence of the characteristic (002), (004) and (006) Bragg peaks (with 2θ of around 17.4°, 34.2° and 53.9°, respectively). The XRD pattern of powder PB is presented in Figure 4.21(a) for comparison.

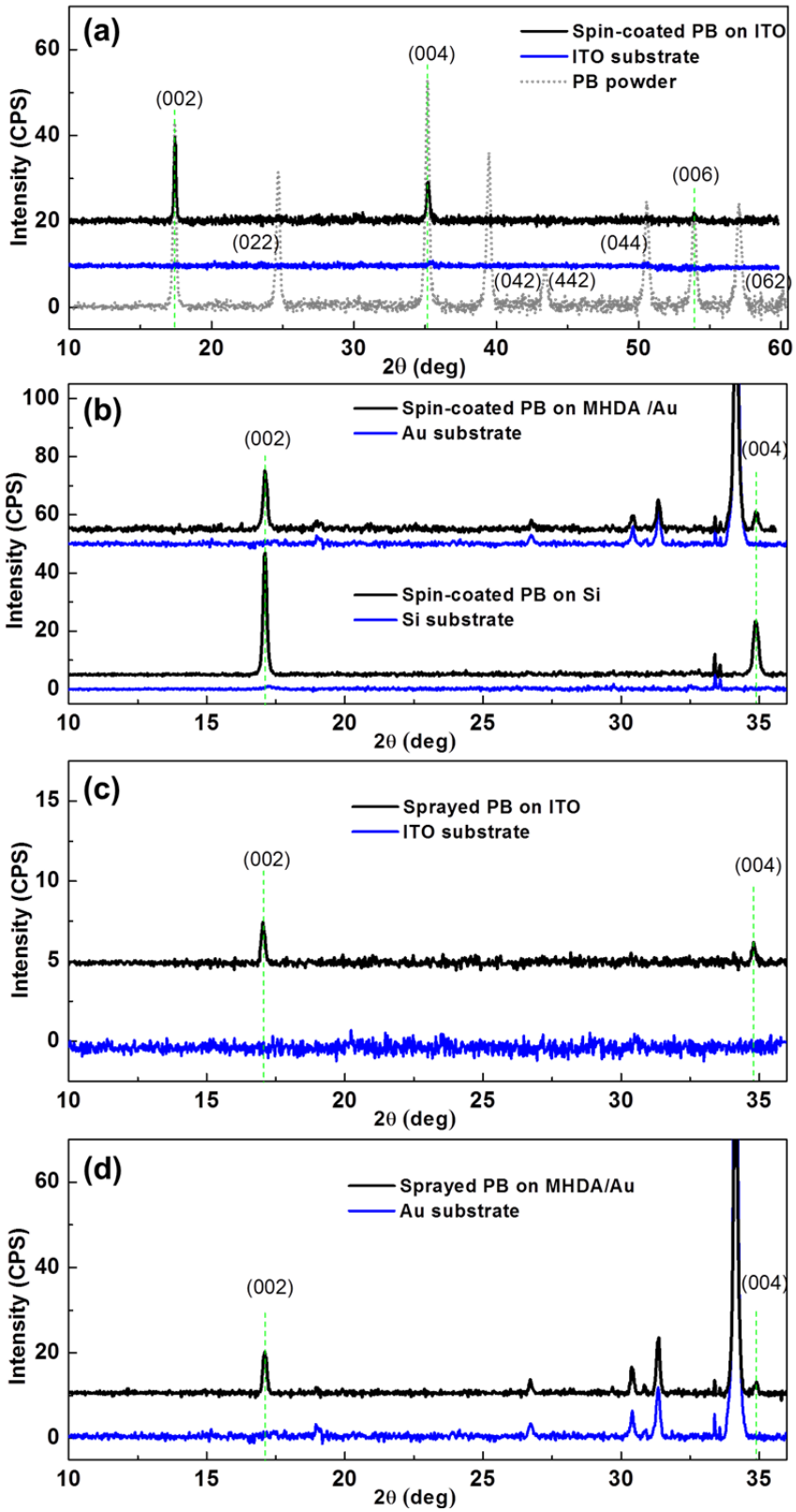

Figure 4.21 XRD of spin-coated PB thin film (black) deposited on (a) hydroxylated ITO substrate (blue) and the PB powder (grey), and (b) MHDA modified Au as well as Si substrates; XRD of layer-by-layer sprayed PB thin film (black) deposited on (c) ITO and (d) MHDA modified Au substrates.

The orientation of the produced PB thin films was also independent of the used preparation methods. The results confirmed the successfully production of crystalline and highly oriented Prussian Blue thin films on the various substrates, with no polycrystallinity as seen in PB powder XRD pattern.

4.2.3.2 HR-SEM cross-section analysis of the prepared PB thin films

To check the continuity, compactness, and homogeneity, as well as to estimate the physical thickness of the PB thin films prepared on the substrates, HR-SEM cross-sectional measurements were performed.

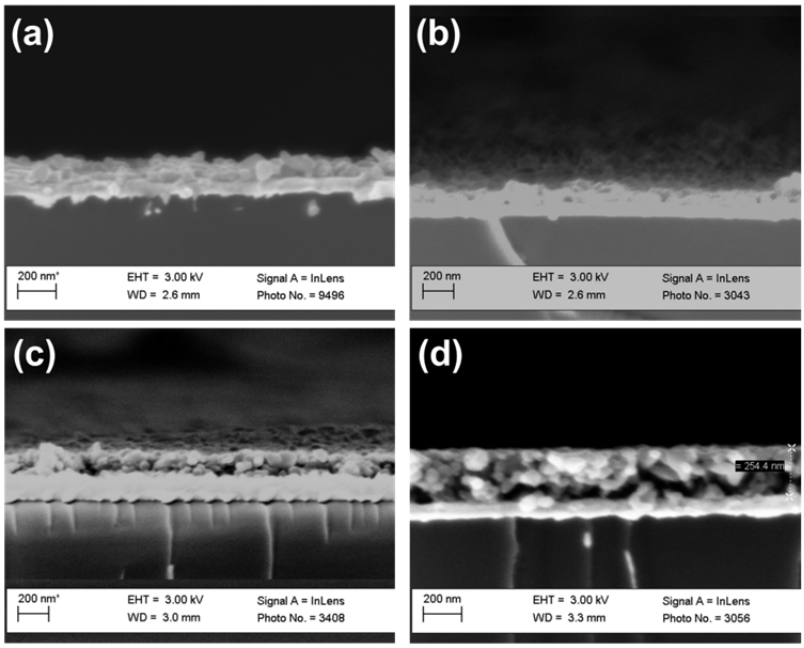

Figure 4.22 HR-SEM images of (a) 50 cycles of the sprayed PB thin films on MHDA modified Au substrate, and (b-d) 1, 3 and 5 layers of spin-coated PB thin film on MHDA modified Au substrate.

As presented in Figure 4.22, the thickness of sprayed PB thin film on MHDA modified Au substrate (50 cycles) is approximately 100 nm (Figure 4.22(a)), while the thickness of the various layers spin-coated PB thin films on MHDA modified Au substrates are about 50 nm (for the 1 layer PB), 150 nm (for the 3 layers PB) and 250 nm (for the 5 layers PB) (Figure 4.22(b-d)). The observed morphology and thickness did not show any change after the electrochemical redox switching process. The monolithic PB thin films prepared on transparent and conductive ITO substrates were directly used for electrochromic switching investigation.

4.2.4 Electrochromic switching of the PB thin films

With regard to electrical applications, the broader class of CNC also possesses a number of interesting properties. Usually, the conductivity of a CNC material is expected to be larger than that of a porous MOF material on account of the closer molecule-molecule contacts. As a result of this closer packing, CNC materials exhibit a number of advantages with regard to electrical applications,[58] and particularly with regard to electrochemistry.[69]

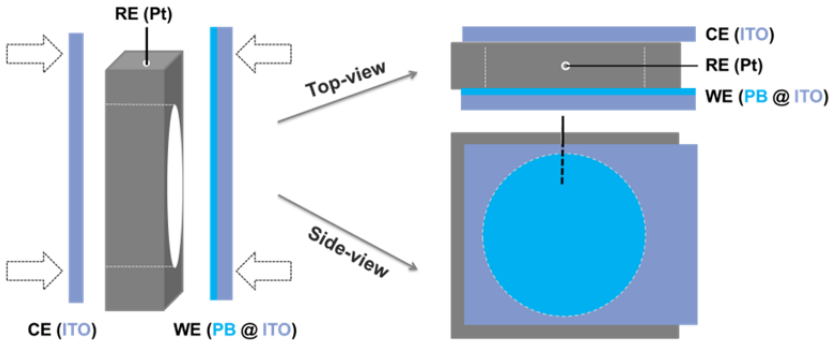

Figure 4.23 A schematic representation of a home-made electrochemical cell for electrochromic experiments. The cell is made of a PTEF core with cylindrical chamber. The two opposing and circular windows are both covered by either the counter electrode (CE) or the working electrode (WE) with silicone O-rings ensuring tight junction. A platinum wire inserted through a pinhole on the top works as reference electrode (RE). The window positioning and the optical features of the facing electrodes allow the light to pass through and the cell to be used in UV-Vis spectroscopy experiments.

For the electrochromic switching of the monolithic PB thin film, a standard three-electrode setup was used in this system and allowed the electrochemical investigation. Combining electrochemistry with UV-Vis spectroscopy, in-situ EC-UV-Vis measurements were conducted in a home-made cell, as presented in Figure 4.23. The cell chamber within the chemically inert body had two aligned windows, which are bracketed by the transparent working electrode (WE) and counter electrodes (CE) so that a light beam can pass through the cell. A pin hole at the top of the cell enabled the electrolyte solution to be filled with a syringe, and also, to insert the reference electrode. Optical measurements were performed in transmission mode during the EC switching. The spin-coated PB thin films on ITO worked as WE, and ITO substrate was used as CE. The area of the window letting the light through was about 0.79 cm^2, and the volume of the

electrolyte solution around 0.4 mL (40 mM KCl aqueous solution). A platinum wire was used as reference electrode.

4.2.4.1 Electrochromic switching of a 1 layer PB thin film

To define the trigger potential for switching the electrochromic smart window, the cyclic voltammetry (CV) measurement was carried out with the described electrochemical and photospectroscopic cell. As seen in Figure 4.24(a), a reversible redox reaction was observed from the spin-coated PB thin film deposited on ITO substrate. The anodic peak at –0.065 V contributed to the oxidation of Fe^{2+} to Fe^{3+}, and reciprocally the cathodic peak at –0.290 V for the reduction.

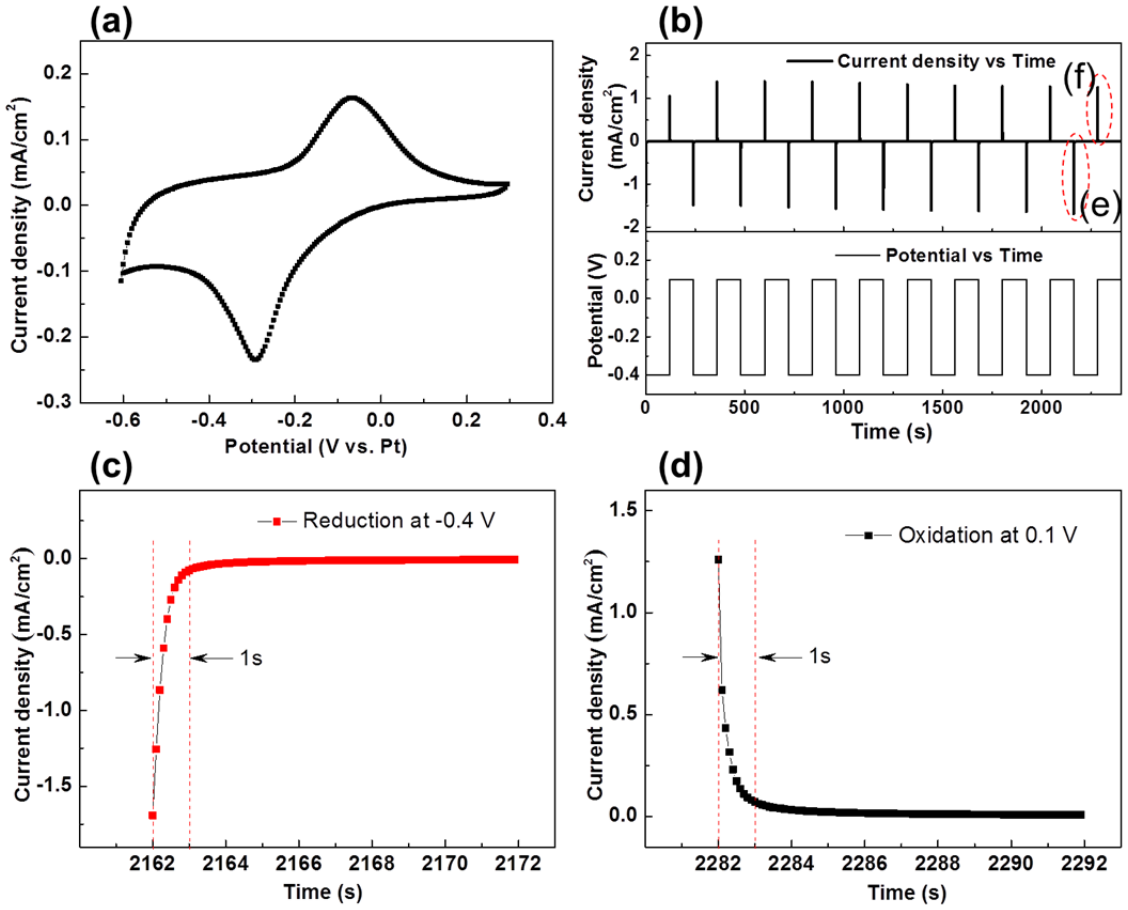

Figure 4.24 (a) CV of the spin-coated 1 layer PB thin film deposited on ITO substrate at the scan rate of 100 mV/s; (b) the waveform of the used PAD technique at the applied potential of E_{ox}= +0.1 V and E_{re}= –0.4 V (downside) and the corresponding current density (upside) for the reversible electrochromic switching; (c-d) the zoomed-in area in (b), corresponding to one segment of the PAD at the applied potential of E_{re}= –0.4 V (c) and E_{ox}= +0.1 V (d).

Figure 4.24(b) presents 10 cycles of reversible electrochromic switching of the spin-coated 1 layer PB thin film deposited on ITO substrate by employing the pulsed amperometric detection (PAD) method. A potential was applied to trigger the reversible switching ON and OFF of the electrochromic smart window in the same EC-system, and the current intensity was recorded during the switching. As presented in Figure 4.24(c-d), the time corresponding to complete color change (from blue to transparent, and inversely) of the smart window was around 5 seconds, with a switching time of roughly 1 second which corresponded to a rapid decrease of the current.

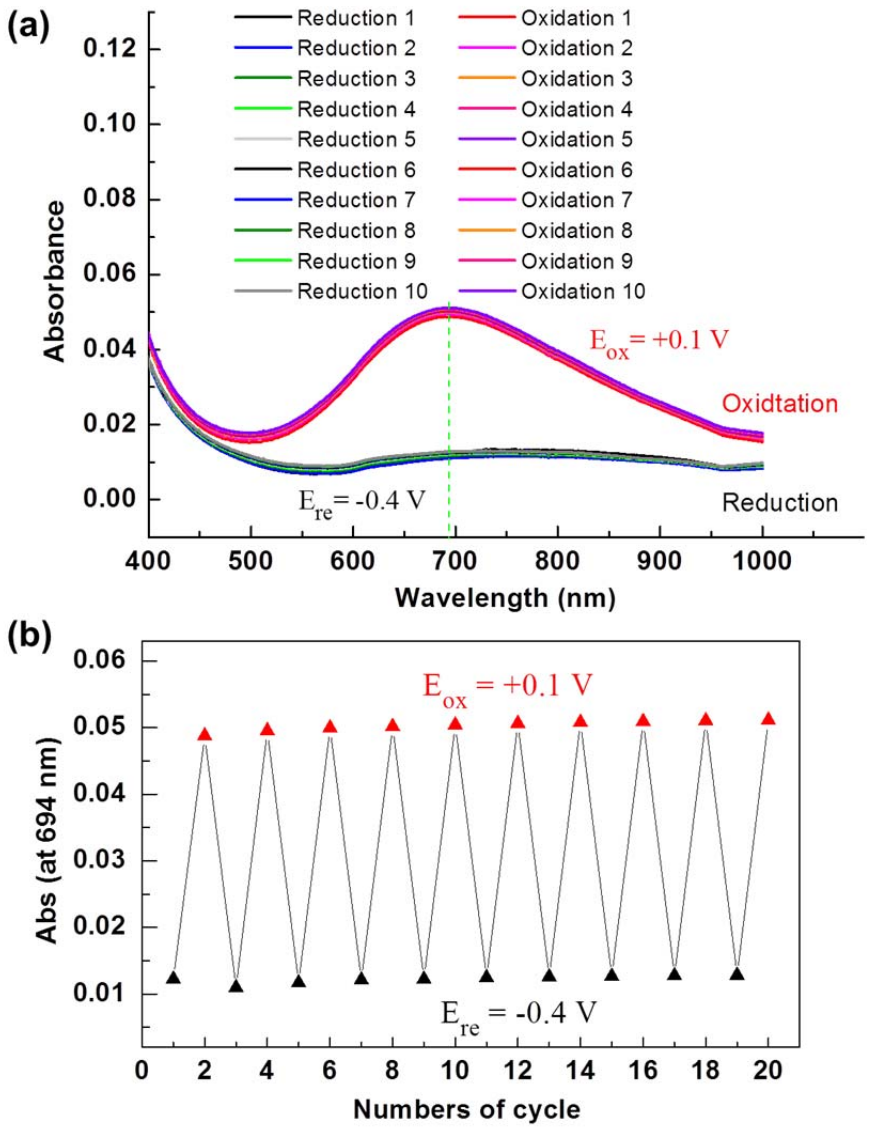

Figure 4.25 (a) UV-Vis spectra of the spin-coated 1 layer PB thin film for 10 cycles EC switching by PAD method at the applied potential E_{ox}= 0.1 V and E_{re}= –0.4 V; (b) UV-Vis absorbance (took from (a) at 694 nm) of the PB thin film in the oxidized and reduced states, showing a stable and reversible redox behavior.

As shown in Figure 4.25(a) on a spin-coated 1 layer PB thin film while applying a negative bias voltage (–0.4 V), the PB thin film was reduced to PW ($K_4Fe_4^{II}[Fe^{II}(CN)_6]_3$) and changed to a the transparent state, whereas with a positive bias voltage (0.1 V) the PB thin film was oxidized to a mixed-valence component PB which provided a strong and blue color to the thin film. The blue color of the oxidized state represents the mixed valence of Fe ions in $Fe_4^{III}[Fe^{II}(CN)_6]_3$ and is based on a metal-to-metal charge transfer transition from the C-coordinated Fe^{2+} ions across the C≡N organic ligand to N-coordinated Fe^{3+} ions.

The potentials were switched alternatively for cycling the electrochromic color change, while UV-Vis spectra were recorded in between and at interval with each potential switch. The cycling behavior of PB thin films during EC switching can be directly observed spectroscopically thanks to the in-situ EC-UV-Vis experimental set-up. Figure 4.25(b) presents the changes of the absorbance (at 694 nm) during cycling of EC switching. No fatigue effect of the optical or electrical properties were observed after 10 switching cycles with the applied potential. This shows the stability, reversibility and reproducibility of the PB thin film during EC switching.

4.2.4.2 Electrochromic switching of a 5 layers PB thin film

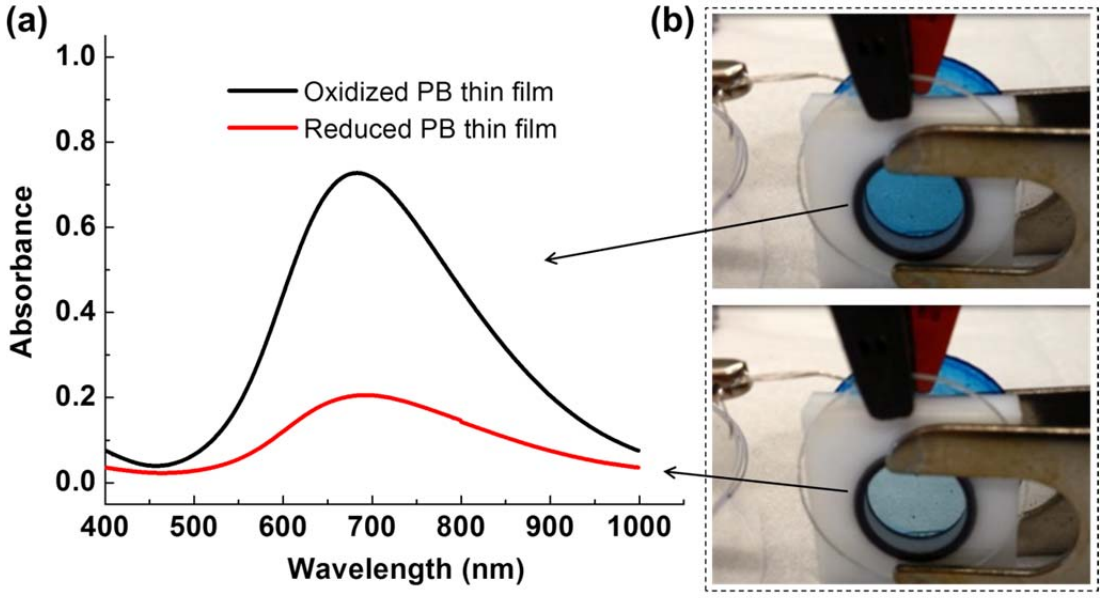

Figure 4.26 (a) UV-Vis spectra of the spin-coated 5 layers PB film after EC switching at the oxidized and reduced states; (b) picture of EC cell composed out of ITO-PB/KCl-Pt/ITO for the oxidized (upside) and reduced (downside) PB film.

To further study the electrochromic behavior, thicker film, the spin-coated 5 layers PB film (the thickness is around 250 nm as mentioned previously) was tested. Figure 4.26(a) shows the UV-Vis spectra of the 5 layer film after EC switching. A significant change in the optical absorption properties were observed between the oxidized and reduced states of the PB thin film. The optical images taken for both the oxidized and reduced PB thin film shows the obvious color change (Figure 4.26(b))

4.2.4.3 XRD analysis of the PB thin films after EC switching

The crystal structure of the oxidized and reduced states of PB thin film by EC switching was characterized by XRD. Prussian Blue crystallizes in the cubic space group #221 Pm3m.[202] The powder XRD data of PB is presented in Figure 4.21(a), and was used also for the refinement of the crystal structure. In order to solve a structure from the powder diffraction measurement, extracting as many (hkl)-peaks and intensity values as possible is necessary to have a precise analysis. The Pawley method is known to produce very precise lattice parameter,[203] and represents a procedure which is widely used for the refinement of the crystal structure crystal unit cell from a powder pattern. For this method, the knowledge of the crystal structure of the material is not required, and a list of indexed intensities is obtained at the end of the refinement. The lattice parameter a_o of 1.0221 ± 0.0003 nm was calculated by lattice cell refinement following the Pawley method. The obtained standard deviation can be viewed as a lower estimation (as discussed on many User-meetings dealing with the Rietveld method).

Comparing with the XRD patterns of PB powder in Figure 4.21, the deposited PB revealed the presence of a crystalline film oriented along the [00l] direction without showing any other (hkl)-peak, and the intensity of all the (00l) peaks was high enough for further analysis. By measuring the specific angular ranges of the (00l) peak-series (with l=2,4,6,8) of the PB thin film in detail, the coherent scattering domain size as well as stress/strain PB thin films were analyzed according to the Williamson-Hall method as described in previous section.[185] Most importantly, the Williamson-Hall method was also applied to analyze the changes of domain size and the stress/strain for both the oxidized and reduced states of PB thin films with the effect of EC switching.

The XRD patterns of the (002), (004) and (006) peaks of the oxidized and reduced PB film are presented in Figure 4.27(a-c), and were recorded after EC switching. It can be seen that the positions of the (00l) peak-series were shifted to a higher 2θ after reduction of the PB to be PW; this represents a contraction of the lattice structure. The reversible

oxido-reduction led to a reversible change in the XRD peak position. Figure 4.27(d) presents the Williamson-Hall plot analysis by considering all the refraction peaks at the oxidized and reduced states expect for the (006) peak of the reduced PB because of the weak intensity, so it is a rough evaluation. In the plot, FWHM at Y-axis represents *B-b* (where B is the integral breadth, *b* is the instrumental width), and the instrumental contribution to the line broadening was considered.

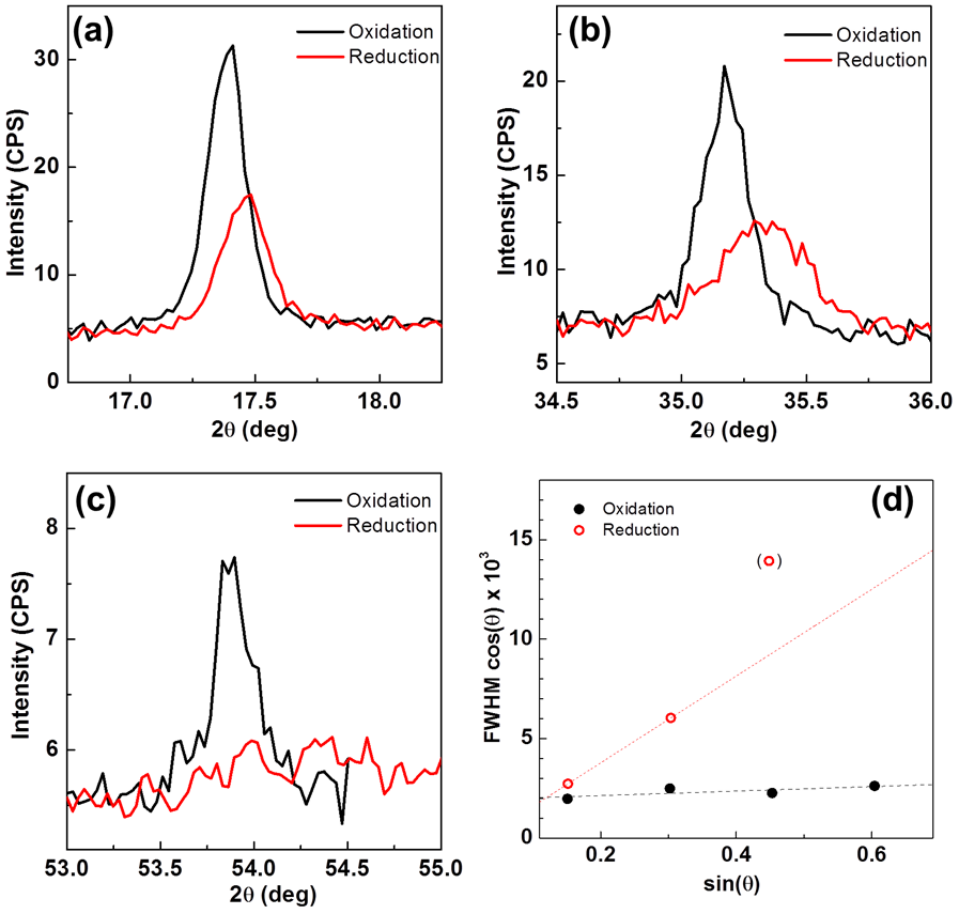

Figure 4.27 (a-c) XRD of the (002), (004) and (006) peaks of the oxidized (black) and reduced (red) Prussian Blue thin film deposited on ITO; (d) Williamson-Hall plots of the (00l) peak-series of oxidized (full symbol in black, l=2,4,6,8) and for the reduced sample (open symbol in red, l=2,4,6), the (006) peak of the reduced PB was not considered for the fitting because of the weak intensity.

Williamson-Hall plot showed that the coherent scattering domain size (L_{vol}) of the oxidized and reduced PB is 82 nm an 81 nm, respectively. And the unit cells (a_o) of these two states, oxidized PB (a_o = 1.0205 ± 0.0003 nm) and reduced PB (a_o = 1.0151 ± 0.0001

nm), show a difference of 0.0054 nm. This is equivalent to a 0.5% dynamic change of the unit cell parameters during the EC switching process. The stress/strain parameter ε_o (~ Δd/d, with d lattice space parameter) remained constant at 0.5% during EC switching. No significant change of the domain size (L_{vol}) and the stress/strain (ε_o) were observed after 30 to 40 redox cycles of the PB film by EC switching. This shows the dynamic, fully reversible, and flexible expansion and contraction of the unit cells (±0.0054 nm) between the PB (Fe^{II}–C≡N···Fe^{3+}) and PW (Fe^{II}–C≡N···Fe^{2+}) structures of the film.

4.2.4.4 IRRAS analysis of the PB thin film after EC switching

The PB films deposited on MHDA modified Au substrate was characterized by infrared after EC switching. The IRRA spectra of spin-coated 3 layers PB film is shown in Figure 4.28(a). The strongest band at around 2120 cm^{-1} corresponds to a C≡N group vibration from PB. When the PB is reduced, this band appears at around 2120 cm^{-1}. A shift of ≈14 cm^{-1} was observed between the oxidized and reduced states of the PB, which resulted from the change in the valence state in the Fe-ion to which the C≡N groups are bound.

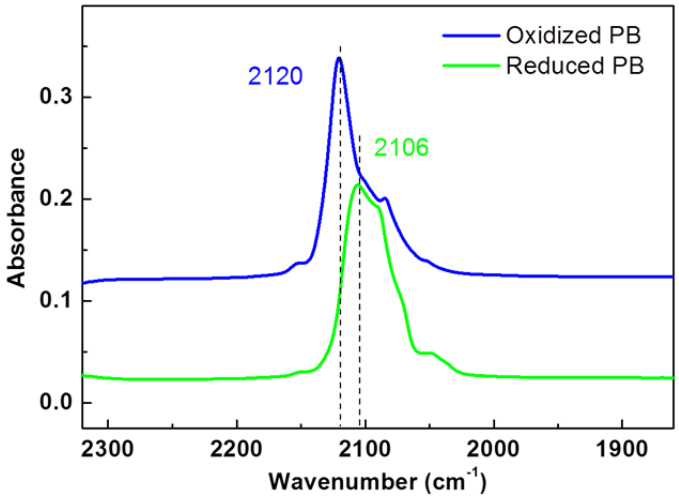

Figure 4.28 IRRAS of the oxidized and reduced states of spin-coated 3 layers PB thin film on MHDA modified Au substrate.

The observed red-shift in the IR spectra for the oxidized and reduced PB corresponds to changing the Fe^{II}–C≡N···Fe^{3+} bridge into Fe^{II}–C≡N···Fe^{2+} bridge. This significant red-shift to a longer wavelength can be explained with the reduction of trivalent Fe-ions to their reduced state decreasing the influence on the bonding.[204] The reduction of Fe^{3+} to be Fe^{2+} and the incorporation of K^+ ions in the lattice led to the contraction of the whole cubic-unit

cell (from PB to PW) of around 0.5 %, which was determined by XRD analysis. The vibrational spectroscopy as well as data from XRD measurements can be described in a coherent manner in regard to the change of PB into PW. So apart from IR, the Raman spectroscopy analysis was also performed on these films.

4.2.4.5 Raman spectra analysis of the PB thin film after EC switching

The PB films deposited on MHDA modified Au substrates were characterized through Raman measurements after EC switching. Raman spectra were recorded using a green laser at 532 nm for excitation. The integration time was 60 s with 3 co-additions.

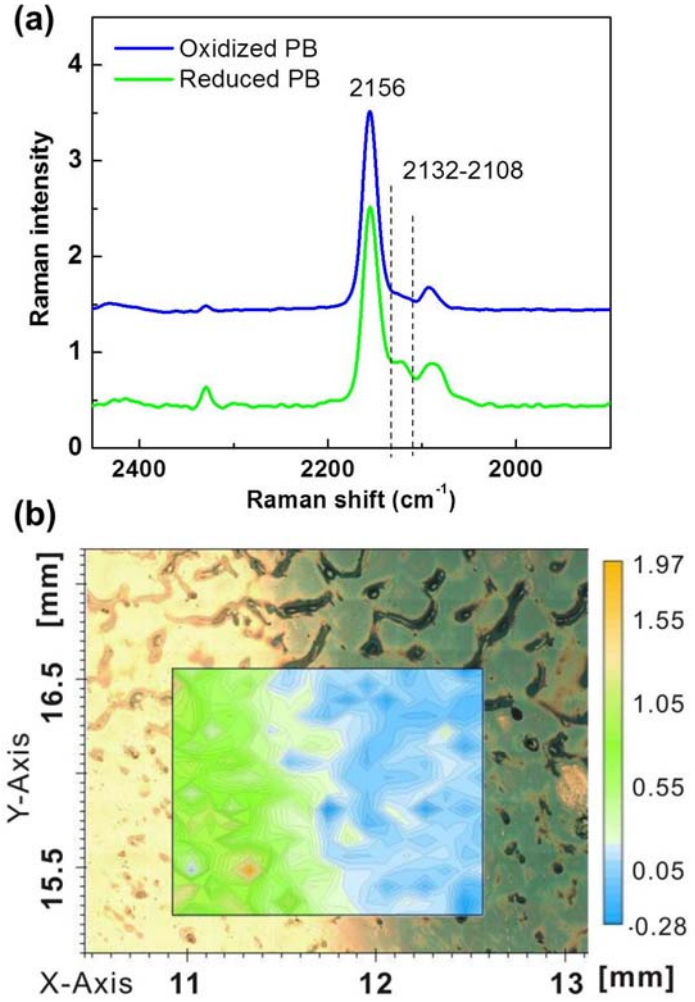

Figure 4.29 (a) Raman spectra of the oxidized and reduced states of spin-coated 3 layers PB thin film on MHDA modified Au substrate; (b) 2D Raman-Map of the half-oxidized and half-reduced PB thin film; the interface in the middle of the image shows the two states (oxidized and reduced) of the film, and the inner area shows the integration result of the C≡N band between 2132 and 2108 cm^{-1} as marked in (a).

Figure 4.29(a) presents the Raman spectra of the oxidized and reduced states of spin-coated 3 layer PB thin films. A typical band at 2156 cm^{-1} corresponding to the vibration of C≡N group was observed on the PB thin films, and this band had no shift through EC switching. However, a new band at 2123 cm^{-1} appeared after the reduction of the PB film. This change revealed the conversion of PB (Fe^{II}–C≡N···Fe^{3+}) to PW (Fe^{II}–C≡N···Fe^{2+}).[204, 205]

2D Raman-Map characterization gives specific band information with lateral resolved resolution, which enables the mapping of the specific band by integrating all the spectra at each point of a large area. To record Raman spectra for both the oxidized and reduced PB films, and to give the laterally resolved mapping, the two states of the film have to be integrated in one sample. This requirement was done by using an electrochemical cell, as presented in Figure 4.30, for full-oxidation and thereafter half-reduction.

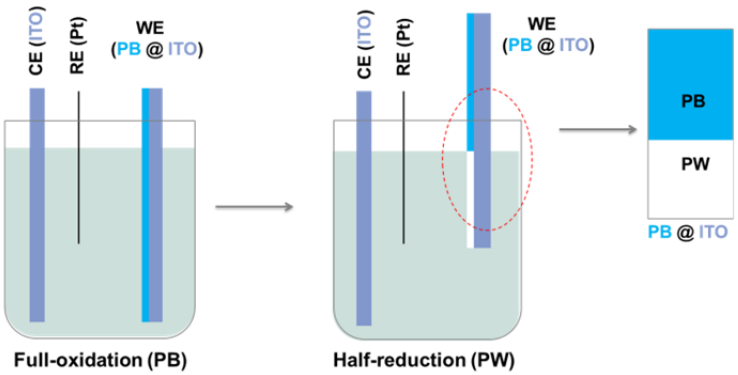

Figure 4.30 Schematic representation of the electrochemical cell for full-oxidation and thereafter half-reduction of the PB film to get an interface of the two states (oxidized and reduced states). The half-oxidized and half-reduced PB thin film is developed for 2D Raman-Map.

The 2D Raman mapping was recorded on 17 x 17 mm^2 spots, as shown in the highlighted area in Figure 4.29(b). The data analysis was done with the Bruker Spectrometer provided software (OPUS 7.2). Before integration on the assigned areas, the Raman spectra were normalized (min - max) for a band at 2156 cm^{-1}. The integration time was 60 seconds with 3 co-additions. A baseline correction was conducted (concave rubber band correction; numbers of iterations 24 and 64 baseline points).

By integrating the Raman spectra of the PB film between 2132 and 2108 cm^{-1} recorded from the inner area in Figure 4.30, the image of 2D Raman-map was produced (Figure

4.29(b)) with a clear difference between oxidized and reduced states of the PB film. The green color represents the reduced state whereas blue represents the oxidized state of PB thin film.

4.2.5 Conclusion

Crystalline and highly oriented thin films of Prussian Blue, a coordinative network compound, were produced on various substrates by layer-by-layer and spin-coating methods. The substrates used are made of either conductive ITO or Au, or semiconductor Si. The monolithic PB thin films prepared on transparent and conductive ITO substrate was used directly as electrodes to fabricate an electrochromic smart window device. By applying an electrical potential, the PB film was switched between a strong blue and a transparent state. The oxidized and reduced states, PB (Fe^{II}–C≡N···Fe^{3+}) and PW (Fe^{II}–C≡N···Fe^{2+}), of the film were characterized by XRD, IR and Raman measurements. The monolithic PB thin films were shown to be robust and stable during the EC switching for multiple times, and demonstrated a reversible electrochromic behavior. The research showed a simple way to fabricate optoelectronic and display devices.

Part of the results in this section has been published in Opt. Express by Jianxi Liu et al.(2015) as ref.[206]

5 Conclusion and Outlook

1. A series of HKUST-1 SURMOFs with different thickness were successfully produced on a CMMT SAM template along their [111] crystallographic orientation. Then, the guest molecules, ferrocene, were loaded within the nanometer size pores. IRRAS and out-of-plane XRD were used and confirmed the guest loading. To explore and reveal the transport properties of SURMOFs, notably their charge transport mechanism, HKUST-1 SURMOF films of different thicknesses were reproducibly incorporated in Hg-based tunneling junction set-up. The extremely shallow dependence of the current density on the film thickness, as indicated by a low value of the attenuation factor ($\beta \approx 0.006$ Å^{-1}), were understood in terms of a linear, ohmic increase of resistance with length in the incoherent charge hopping regime. The decrease in overall resistance and its weaker increase with film thickness, measured after incorporation of ferrocene inside the pores of HKUST-1 SURMOFs, indicated a reduction in the charge injection barrier and an improved electronic coupling between metal nodes.

Assembling of SURMOF films in tunneling junctions showed to be effective and permitted the investigation of their transport properties. It also offered the possibility to gain insights into the effect of small electroactive molecules. Further studies using SURMOFs of different chemical composition or crystallographic orientation, as well as different guest molecules, is also interesting and important and would be conveniently realized by using such tunneling junctions. This would provide fundamental results on electric transport properties within MOFs and paves the way for their future integration in electronic devices.

2. SURMOFs with different orientation were produced on CMMT and TPMTA modified gold electrodes. The electric properties of these porous and crystalline SURMOF coatings deposited on gold working electrode were characterized using cyclic voltammetry experiments by using an ionic liquid as inert supporting electrolyte and ferrocene as redox active probe. The pristine HKUST-1 SURMOFs demonstrated an insulating behavior, and a high quality compact films structures. An extremely low density of defects or pin-holes was then concluded also in relation with the AFM scratching experiment. Furthermore, electroactive ferrocene molecules were used as guests in HKUST-1 SURMOFs for enhancing its electrical conductivity, as this was proven by CV experiments.

Following the present strategy, the relevant electrochemical characterization of other SURMOFs is to be studied. Especially, the relation between electrochemical behavior of SURMOFs and their crystalline orientation, pore sizes, or the immobilized electroactive guests within could be bridged.

3. Crystalline and porous porphyrin-based SURMOFs were prepared on transparent and conductive FTO substrates by the LPE spraying method. The photocurrent generation properties of the highly oriented and ordered porphyrin-based SURMOF thin films as electrodes were investigated using a photoelectrochemical cell. Comparing to free base porphyrin Zn-SURMOF 2, the enhancement of the photocurrent efficiency was observed on Pd porphyrin Zn-SURMOF 2.

The strategy for stacking of the high ordered photoelectroactive molecules offers a great opportunity towards developing solar cell conversion and artificial photocatalysis applications. Since the crystalline lattices fabricated here were highly porous, these SURMOFs are likely to achieve higher performances by loading further the pores with charge-donating or charge-accepting molecules.

4. Multilayered hybrid materials, obtained by the combination of a LPE spraying process, yielding high quality SURMOFs (HKUST-1), with an ITO sputtering process, were fabricated on a Si substrate with a high quality for optical application on a centimeter scale. By modifying the individual layer thicknesses of porous SURMOF (low RI layer) and conductive ITO (high RI layer) alternatively, the resulting SURMOF-based hybrid PBG materials were produced with color tunable over the whole visible range. The monolithic Bragg stacks were characterized and displayed an outstanding optical quality with low scattering losses as manifested by a reflectance of around 80% at the maximum PBG wavelength. The SURMOF-based hybrid PBG materials presented here also provided a tunable platform with regard to developing chemo-responsive optical sensing devices. Pronounced changes of the optical properties of the PBG materials were measured by simply loading and unloading specific guest molecules within the nanopores of the framework in the hybrid PBG systems.

Due to their high optical quality, the SURMOF-based PBG device could be further extended to other (water stable, faster response, as well as with variable color options) monolithic systems. SURMOFs produced by LPE process are suitable for large scales industrial device applications. The possible realization of wider systems would provide the development of robust SURMOF-based, photonic color-coded chemical sensors and

nano-photonic devices with broad perspectives.

5. Thin films of the porous coordination network compounds (CNC), Prussian blue (PB), were produced on various substrates (Au, ITO and Si) by means of a layer-by-layer or LPE, as well as through spin-coating process. The monolithic PB thin films, coated on transparent and conductive ITO substrates, were then used directly without any further modification in an electrochemical cell as electrodes to constitute an electrochromic device. By applying a potential in electrochemistry cell, the PB thin film were switched between two states, referred to the blue colored PB (Fe^{II}–C≡N···Fe^{3+}) and transparent PW (Fe^{II}–C≡N···Fe^{2+}); these states were fully characterized by XRD, IR and Raman measurements.

The highly oriented, crystalline and monolithic CNC thin films were shown to be robust, stable, and could be switched multiple times. This demonstrates a simple way to produce cost-efficiently optoelectronic and display devices or smart window materials. Further monolithic CNC materials with improved properties to eventually yield materials with “tunable porosity” and “tunable potential barriers” are in progress.

List of Abbreviations

1D	One-dimensional
2D	Two-dimensional
3D	Three-dimensional
AFM	Atomic force microscopy
BS	Bragg stacks
BTC	1,3,5-benzenetricarboxylic acid
[BMIM] [NTf_2]	1-butyl-3-methylimidazolinium bis(trifluoronethylsulfonyl)imide
CE	Counter electrode
CMMT	9-carboxy-10-(mercaptomethyl) triptycene
CNC	Coordination network compound
CV	Cyclic voltammetry
DC	Direct current
DFT	Density functional theory
EC	Electrochromic
EtOH	Ethanol
FC	Ferrocene
FIB	Focused ion beam
FTIR	Fourier transform infrared
FTO	Fluorine doped tin oxide
FWHM	Full width at half maximum
HD	Hexadecane
HDT	Hexadecanethiol

HR-SEM	High-resolution scanning electron microscope
HKUST-1	Hong-Kong University structure 1
HOMO	Highest occupied molecular orbital
IL	Ionic liquid
IR	Infrared
IRRAS	Infrared reflection absorption spectroscopy
ITO	Indium tin oxide
I-V	Current-voltage
LED	Light-emitting diode
LPE	Liquid-phase epitaxy
LUMO	Lowest unoccupied molecular orbital
MCT	Mercury cadmium telluride
MHDA	16-mecaptohexa-decanoic acid
MOF	Metal-organic frameworks
NIR	Near infrared
OLEDs	Organic light emitting diodes
PAD	Pulsed amperometric detection
PB	Prussian Blue
PBG	Photonic band-gap
PCP	Porous coordination polymer
PW	Prussian white
QCM	Quartz crystal microbalance
RE	Reference electrode
RI	Refractive index
RMS	Root mean square

SAM	Self-assembled monolayer
SE	Spectroscopic ellipsometry
SEM	Scanning electron microscopy
SFM	Scanning force microscopy
Si	Silicon
SPM	Scanning probe microscopy
SURMOF	Surface-anchored metal-organic frameworks
SURMOF 2	2 dimensional surface-anchored metal-organic framework
TCO	Transparent conductive oxides
TCNQ	Tetracyano-quinodimethane
TDM	Transition dipole moment
TEM	Transmission electron microscopy
TPMTA	4'-carboxyterphenyl-4-methanethiol
ToF-SIMS	Time-of-flight secondary ion mass spectrometry
UV-Vis	Ultraviolet-visible
WE	Working electrode
XRD	X-ray diffraction

References

[1] Zhu, Q. L.; Xu, Q. Metal-Organic Framework Composites. *Chem. Soc. Rev.* **2014,** *43*, 5468-5512.

[2] Furukawa, H.; Cordova, K. E.; O'Keeffe, M.; Yaghi, O. M. The Chemistry and Applications of Metal-Organic Frameworks. *Science* **2013,** *341*, 974.

[3] Férey, G. Hybrid Porous Solids: Past, Present, Future. *Chem. Soc. Rev.* **2008,** *37*, 191-214.

[4] Kitagawa, S.; Kitaura, R.; Noro, S. Functional Porous Coordination Polymers. *Angew. Chem., Int. Ed.* **2004,** *43*, 2334-2375.

[5] Yaghi, O. M.; O'Keeffe, M.; Ockwig, N. W.; Chae, H. K.; Eddaoudi, M.; Kim, J. Reticular Synthesis and the Design of New Materials. *Nature* **2003,** *423*, 705-714.

[6] Kinoshita, Y.; Matsubara, I.; Higuchi, T.; Saito, Y. The Crystal Structure of Bis(Adiponitrilo)Copper(I) Nitrate. *Bull. Chem. Soc. Jpn.* **1959,** *32*, 1221-1226.

[7] Hoskins, B. F.; Robson, R. Design and Construction of a New Class of Scaffolding-Like Materials Comprising Infinite Polymeric Frameworks of 3-D-Linked Molecular Rods - a Reappraisal of the $Zn(CN)_2$ and $Cd(CN)_2$ Structures and the Synthesis and Structure of the Diamond-Related Frameworks $[N(CH_3)_4][Cu^{I}Zn^{II}(CN)_4]$ and Cu^{I}[4,4',4'',4'''-Tetracyanotetraphenylmethane]$BF_4.XC_6H_5NO_2$. *J. Am. Chem. Soc.* **1990,** *112*, 1546-1554.

[8] Deng, H. X.; Grunder, S.; Cordova, K. E.; Valente, C.; Furukawa, H.; Hmadeh, M.; Gandara, F.; Whalley, A. C.; Liu, Z.; Asahina, S.; Kazumori, H.; O'Keeffe, M.; Terasaki, O.; Stoddart, J. F.; Yaghi, O. M. Large-Pore Apertures in a Series of Metal-Organic Frameworks. *Science* **2012,** *336*, 1018-1023.

[9] He, Y. B.; Zhou, W.; Qian, G. D.; Chen, B. L. Methane Storage in Metal-Organic Frameworks. *Chem. Soc. Rev.* **2014,** *43*, 5657-5678.

[10] Suh, M. P.; Park, H. J.; Prasad, T. K.; Lim, D. W. Hydrogen Storage in Metal-Organic Frameworks. *Chem. Rev.* **2012,** *112*, 782-835.

[11] Peng, Y.; Li, Y. S.; Ban, Y. J.; Jin, H.; Jiao, W. M.; Liu, X. L.; Yang, W. S. Metal-Organic Framework Nanosheets as Building Blocks for Molecular Sieving Membranes. *Science* **2014,** *346*, 1356-1359.

[12] Gu, Z. Y.; Yang, C. X.; Chang, N.; Yan, X. P. Metal-Organic Frameworks for Analytical Chemistry: From Sample Collection to Chromatographic Separation. *Acc. Chem. Res.* **2012,** *45*, 734-745.

[13] Yoon, M.; Srirambalaji, R.; Kim, K. Homochiral Metal-Organic Frameworks for Asymmetric Heterogeneous Catalysis. *Chem. Rev.* **2012,** *112*, 1196-1231.

[14] Lee, J.; Farha, O. K.; Roberts, J.; Scheidt, K. A.; Nguyen, S. T.; Hupp, J. T. Metal-Organic Framework Materials as Catalysts. *Chem. Soc. Rev.* **2009,** *38*, 1450-1459.

[15] Kreno, L. E.; Leong, K.; Farha, O. K.; Allendorf, M.; Van Duyne, R. P.; Hupp, J. T. Metal-Organic Framework Materials as Chemical Sensors. *Chem. Rev.* **2012,** *112*, 1105-1125.

[16] Horcajada, P.; Gref, R.; Baati, T.; Allan, P. K.; Maurin, G.; Couvreur, P.; Férey, G.; Morris, R. E.; Serre, C. Metal-Organic Frameworks in Biomedicine. *Chem. Rev.* **2012,** *112*, 1232-1268.

[17] Shi, D. B.; Ren, Y. W.; Jiang, H. F.; Cai, B. W.; Lu, J. X. Synthesis, Structures, and Properties of Two Three-Dimensional Metal-Organic Frameworks, Based on Concurrent Ligand Extension. *Inorg. Chem.* **2012,** *51*, 6498-6506.

[18] Phan, A.; Doonan, C. J.; Uribe-Romo, F. J.; Knobler, C. B.; O'Keeffe, M.; Yaghi, O. M. Synthesis, Structure, and Carbon Dioxide Capture Properties of Zeolitic Imidazolate Frameworks. *Acc. Chem. Res.* **2010,** *43*, 58-67.

[19] Tranchemontagne, D. J.; Hunt, J. R.; Yaghi, O. M. Room Temperature Synthesis of Metal-Organic Frameworks: MOF-5, MOF-74, MOF-177, MOF-199, and IRMOF-0. *Tetrahedron* **2008,** *64*, 8553-8557.

[20] Son, W. J.; Kim, J.; Kim, J.; Ahn, W. S. Sonochemical Synthesis of MOF-5. *Chem. Commun.* **2008**, 6336-6338.

[21] Klinowski, J.; Paz, F. A. A.; Silva, P.; Rocha, J. Microwave-Assisted Synthesis of Metal-Organic Frameworks. *Dalton Trans.* **2011,** *40*, 321-330.

[22] Li, M. Y.; Dincă, M. Reductive Electrosynthesis of Crystalline Metal-Organic Frameworks. *J. Am. Chem. Soc.* **2011,** *133*, 12926-12929.

[23] Yan, D. P.; Gao, R.; Wei, M.; Li, S. D.; Lu, J.; Evans, D. G.; Duan, X. Mechanochemical Synthesis of a Fluorenone-Based Metal Organic Framework with Polarized Fluorescence: An Experimental and Computational Study. *J. Mater. Chem. C* **2013,** *1*, 997-1004.

[24] Khan, N. A.; Jhung, S. H. Synthesis of Metal-Organic Frameworks (MOFs) with Microwave or Ultrasound: Rapid Reaction, Phase-Selectivity, and Size Reduction. *Coord. Chem. Rev.* **2015,** *285*, 11-23.

[25] Stock, N.; Biswas, S. Synthesis of Metal-Organic Frameworks (MOFs): Routes to Various MOF Topologies, Morphologies, and Composites. *Chem. Rev.* **2012,** *112*, 933-969.

[26] Tranchemontagne, D. J.; Mendoza-Cortes, J. L.; O'Keeffe, M.; Yaghi, O. M. Secondary Building Units, Nets and Bonding in the Chemistry of Metal-Organic Frameworks. *Chem. Soc. Rev.* **2009,** *38*, 1257-1283.

[27] Lu, W. G.; Wei, Z. W.; Gu, Z. Y.; Liu, T. F.; Park, J.; Park, J.; Tian, J.; Zhang, M. W.; Zhang, Q.; Gentle, T.; Bosch, M.; Zhou, H. C. Tuning the Structure and Function of Metal-Organic Frameworks via Linker Design. *Chem. Soc. Rev.* **2014,** *43*, 5561-5593.

[28] Tanabe, K. K.; Cohen, S. M. Postsynthetic Modification of Metal-Organic Frameworks-A Progress Report. *Chem. Soc. Rev.* **2011,** *40*, 498-519.

[29] Wang, Z. Q.; Cohen, S. M. Postsynthetic Modification of Metal-Organic Frameworks. *Chem. Soc. Rev.* **2009,** *38*, 1315-1329.

[30] Brozek, C. K.; Dincă, M. Lattice-Imposed Geometry in Metal-Organic Frameworks: Lacunary Zn_4O Clusters in MOF-5 Serve as Tripodal Chelating Ligands for Ni^{2+}. *Chem. Sci.* **2012,** *3*, 2110-2113.

[31] Tanabe, K. K.; Wang, Z. Q.; Cohen, S. M. Systematic Functionalization of a Metal-Organic Framework Via a Postsynthetic Modification Approach. *J. Am. Chem. Soc.* **2008,** *130*, 8508-8517.

[32] Wang, Z. B.; Liu, J. X.; Arslan, H. K.; Grosjean, S.; Hagendorn, T.; Gliemann, H.; Bräse, S.; Wöll, C. Post-Synthetic Modification of Metal-Organic Framework Thin Films Using Click Chemistry: The Importance of Strained C-C Triple Bonds. *Langmuir* **2013,** *29*, 15958-15964.

[33] Bradshaw, D.; Garai, A.; Huo, J. Metal-Organic Framework Growth at Functional Interfaces: Thin Films and Composites for Diverse Applications. *Chem. Soc. Rev.* **2012,** *41*, 2344-2381.

[34] Uemura, T.; Yanai, N.; Kitagawa, S. Polymerization Reactions in Porous Coordination Polymers. *Chem. Soc. Rev.* **2009,** *38*, 1228-1236.

[35] Eddaoudi, M.; Kim, J.; Rosi, N.; Vodak, D.; Wachter, J.; O'Keeffe, M.; Yaghi, O. M. Systematic Design of Pore Size and Functionality in Isoreticular MOFs and Their Application in Methane Storage. *Science* **2002,** *295*, 469-472.

[36] Chui, S. S. Y.; Lo, S. M. F.; Charmant, J. P. H.; Orpen, A. G.; Williams, I. D. A Chemically Functionalizable Nanoporous Material $[Cu_3(TMA)_2(H_2O)_3]_n$. *Science* **1999,** *283*, 1148-1150.

[37] Banerjee, R.; Phan, A.; Wang, B.; Knobler, C.; Furukawa, H.; O'Keeffe, M.; Yaghi, O. M. High-Throughput Synthesis of Zeolitic Imidazolate Frameworks and Application to CO_2 Capture. *Science* **2008,** *319*, 939-943.

[38] Farha, O. K.; Eryazici, I.; Jeong, N. C.; Hauser, B. G.; Wilmer, C. E.; Sarjeant, A.

A.; Snurr, R. Q.; Nguyen, S. T.; Yazaydin, A. O.; Hupp, J. T. Metal-Organic Framework Materials with Ultrahigh Surface Areas: Is the Sky the Limit? *J. Am. Chem. Soc.* **2012,** *134*, 15016-15021.

[39] Li, H.; Eddaoudi, M.; O'Keeffe, M.; Yaghi, O. M. Design and Synthesis of an Exceptionally Stable and Highly Porous Metal-Organic Framework. *Nature* **1999,** *402*, 276-279.

[40] Férey, G.; Mellot-Draznieks, C.; Serre, C.; Millange, F.; Dutour, J.; Surble, S.; Margiolaki, I. A Chromium Terephthalate-Based Solid with Unusually Large Pore Volumes and Surface Area. *Science* **2005,** *309*, 2040-2042.

[41] Horcajada, P.; Serre, C.; Maurin, G.; Ramsahye, N. A.; Balas, F.; Vallet-Regi, M.; Sebban, M.; Taulelle, F.; Férey, G. Flexible Porous Metal-Organic Frameworks for a Controlled Drug Delivery. *J. Am. Chem. Soc.* **2008,** *130*, 6774-6780.

[42] Kim, M.; Cohen, S. M. Discovery, Development, and Functionalization of Zr(IV)-Based Metal-Organic Frameworks. *CrystEngComm* **2012,** *14*, 4096-4104.

[43] Rowsell, J. L. C.; Yaghi, O. M. Effects of Functionalization, Catenation, and Variation of the Metal Oxide and Organic Linking Units on the Low-Pressure Hydrogen Adsorption Properties of Metal-Organic Frameworks. *J. Am. Chem. Soc.* **2006,** *128*, 1304-1315.

[44] Rowsell, J. L. C.; Yaghi, O. M. Strategies for Hydrogen Storage in Metal-Organic Frameworks. *Angew. Chem., Int. Ed.* **2005,** *44*, 4670-4679.

[45] Li, B.; Wen, H. M.; Wang, H. L.; Wu, H.; Tyagi, M.; Yildirim, T.; Zhou, W.; Chen, B. L. A Porous Metal-Organic Framework with Dynamic Pyrimidine Groups Exhibiting Record High Methane Storage Working Capacity. *J. Am. Chem. Soc.* **2014,** *136*, 6207-6210.

[46] Furukawa, H.; Ko, N.; Go, Y. B.; Aratani, N.; Choi, S. B.; Choi, E.; Yazaydin, A. O.; Snurr, R. Q.; O'Keeffe, M.; Kim, J.; Yaghi, O. M. Ultrahigh Porosity in Metal-Organic Frameworks. *Science* **2010,** *329*, 424-428.

[47] Deng, H. X.; Doonan, C. J.; Furukawa, H.; Ferreira, R. B.; Towne, J.; Knobler, C. B.; Wang, B.; Yaghi, O. M. Multiple Functional Groups of Varying Ratios in Metal-Organic Frameworks. *Science* **2010,** *327*, 846-850.

[48] Fujita, M.; Kwon, Y. J.; Washizu, S.; Ogura, K. Preparation, Clathration Ability, and Catalysis of a 2-Dimensional Square Network Material Composed of Cadmium(II) and 4,4'-Bipyridine. *J. Am. Chem. Soc.* **1994,** *116*, 1151-1152.

[49] Alaerts, L.; Seguin, E.; Poelman, H.; Thibault-Starzyk, F.; Jacobs, P. A.; De Vos, D. E. Probing the Lewis Acidity and Catalytic Activity of the Metal-Organic Framework $[Cu_3(BTC)_2]$ (BTC = Benzene-1,3,5-Tricarboxylate). *Chem. Eur. J.* **2006,** *12*, 7353-7363.

[50] Ma, L. Q.; Falkowski, J. M.; Abney, C.; Lin, W. B. A Series of Isoreticular Chiral Metal-Organic Frameworks as a Tunable Platform for Asymmetric Catalysis. *Nat. Chem.* **2010,** *2*, 838-846.

[51] Sabo, M.; Henschel, A.; Froede, H.; Klemm, E.; Kaskel, S. Solution Infiltration of Palladium into MOF-5: Synthesis, Physisorption and Catalytic Properties. *J. Mater. Chem.* **2007,** *17*, 3827-3832.

[52] Liu, D. M.; Lu, K. D.; Poon, C.; Lin, W. B. Metal-Organic Frameworks as Sensory Materials and Imaging Agents. *Inorg. Chem.* **2014,** *53*, 1916-1924.

[53] Hu, Z. C.; Deibert, B. J.; Li, J. Luminescent Metal-Organic Frameworks for Chemical Sensing and Explosive Detection. *Chem. Soc. Rev.* **2014,** *43*, 5815-5840.

[54] Lu, Z. Z.; Zhang, R.; Li, Y. Z.; Guo, Z. J.; Zheng, H. G. Solvatochromic Behavior of a Nanotubular Metal-Organic Framework for Sensing Small Molecules. *J. Am. Chem. Soc.* **2011,** *133*, 4172-4174.

[55] Huxford, R. C.; Della Rocca, J.; Lin, W. B. Metal-Organic Frameworks as Potential Drug Carriers. *Curr. Opin. Chem. Biol.* **2010,** *14*, 262-268.

[56] Horcajada, P.; Chalati, T.; Serre, C.; Gillet, B.; Sebrie, C.; Baati, T.; Eubank, J. F.; Heurtaux, D.; Clayette, P.; Kreuz, C.; Chang, J. S.; Hwang, Y. K.; Marsaud, V.; Bories, P. N.; Cynober, L.; Gil, S.; Férey, G.; Couvreur, P.; Gref, R. Porous Metal-Organic-Framework Nanoscale Carriers as a Potential Platform for Drug Delivery and Imaging. *Nat. Mater.* **2010,** *9*, 172-178.

[57] Chen, X. M.; Tong, M. L. Solvothermal in situ Metal/Ligand Reactions: A New Bridge between Coordination Chemistry and Organic Synthetic Chemistry. *Acc. Chem. Res.* **2007,** *40*, 162-170.

[58] Falcaro, P.; Ricco, R.; Doherty, C. M.; Liang, K.; Hill, A. J.; Styles, M. J. Mof Positioning Technology and Device Fabrication. *Chem. Soc. Rev.* **2014,** *43*, 5513-5560.

[59] Stavila, V.; Talin, A. A.; Allendorf, M. D. Mof-Based Electronic and Optoelectronic Devices. *Chem. Soc. Rev.* **2014,** *43*, 5994-6010.

[60] Hermes, S.; Schroder, F.; Chelmowski, R.; Wöll, C.; Fischer, R. A. Selective Nucleation and Growth of Metal-Organic Open Framework Thin Films on Patterned COOH/CF_3-Terminated Self-Assembled Monolayers on Au(111). *J. Am. Chem. Soc.* **2005,** *127*, 13744-13745.

[61] Biemmi, E.; Scherb, C.; Bein, T. Oriented Growth of the Metal Organic Framework $Cu_3(BTC)_2(H_2O)_3 \cdot XH_2O$ Tunable with Functionalized Self-Assembled Monolayers. *J. Am. Chem. Soc.* **2007,** *129*, 8054-8055.

[62] Gascon, J.; Aguado, S.; Kapteijn, F. Manufacture of Dense Coatings of $Cu_3(BTC)_2$

(HKUST-1) on Alpha-Alumina. *Microporous Mesoporous Mater.* **2008,** *113*, 132-138.

[63] Schoedel, A.; Scherb, C.; Bein, T. Oriented Nanoscale Films of Metal-Organic Frameworks by Room-Temperature Gel-Layer Synthesis. *Angew. Chem. Int. Ed.*. **2010,** *49*, 7225-7228.

[64] Mueller, U.; Schubert, M.; Teich, F.; Puetter, H.; Schierle-Arndt, K.; Pastré, J. Metal-Organic Frameworks-Prospective Industrial Applications. *J. Mater. Chem.* **2006,** *16*, 626-636.

[65] Makiura, R.; Motoyama, S.; Umemura, Y.; Yamanaka, H.; Sakata, O.; Kitagawa, H. Surface Nano-Architecture of a Metal-Organic Framework. *Nat. Mater.* **2010,** *9*, 565-571.

[66] Shekhah, O.; Wang, H.; Kowarik, S.; Schreiber, F.; Paulus, M.; Tolan, M.; Sternemann, C.; Evers, F.; Zacher, D.; Fischer, R. A.; Wöll, C. Step-by-Step Route for the Synthesis of Metal-Organic Frameworks. *J. Am. Chem. Soc.* **2007,** *129*, 15118-15119.

[67] Shekhah, O.; Liu, J.; Fischer, R. A.; Wöll, C. Mof Thin Films: Existing and Future Applications. *Chem. Soc. Rev.* **2011,** *40*, 1081-106.

[68] Wade, C. R.; Li, M. Y.; Dincă, M. Facile Deposition of Multicolored Electrochromic Metal-Organic Framework Thin Films. *Angew. Chem., Int. Ed.* **2013,** *52*, 13377-13381.

[69] Kung, C. W.; Wang, T. C.; Mondloch, J. E.; Fairen-Jimenez, D.; Gardner, D. M.; Bury, W.; Klingsporn, J. M.; Barnes, J. C.; Van Duyne, R.; Stoddart, J. F.; Wasielewski, M. R.; Farha, O. K.; Hupp, J. T. Metal-Organic Framework Thin Films Composed of Free-Standing Acicular Nanorods Exhibiting Reversible Electrochromism. *Chem. Mater.* **2013,** *25*, 5012-5017.

[70] Zacher, D.; Baunemann, A.; Hermes, S.; Fischer, R. A. Deposition of Microcrystalline $[Cu_3(BTC)_2]$ and $[Zn_2(BDC)_2(Dabco)]$ at Alumina and Silica Surfaces Modified with Patterned Self Assembled Organic Monolayers: Evidence of Surface Selective and Oriented Growth. *J. Mater. Chem.* **2007,** *17*, 2785-2792.

[71] Lu, G.; Hupp, J. T. Metal-Organic Frameworks as Sensors: A ZIF-8 Based Fabry-Perot Device as a Selective Sensor for Chemical Vapors and Gases. *J. Am. Chem. Soc.* **2010,** *132*, 7832-7833.

[72] Zhang, Y. L.; Gao, Q. M.; Lin, Z.; Zhang, T.; Xu, J. D.; Tan, Y. L.; Tian, W. Q.; Jiang, L. Constructing Free Standing Metal Organic Framework MIL-53 Membrane Based on Anodized Aluminum Oxide Precursor. *Scientific Reports* **2014,** *4*, 4947.

[73] Scherb, C.; Schodel, A.; Bein, T. Directing the Structure of Metal-Organic Frameworks by Oriented Surface Growth on an Organic Monolayer. *Angew. Chem., Int. Ed.* **2008,** *47*, 5777-5779.

[74] Hou, C. T.; Peng, J. Y.; Xu, Q.; Ji, Z. P.; Hu, X. Y. Elaborate Fabrication of MOF-5 Thin Films on a Glassy Carbon Electrode (GCE) for Photoelectrochemical Sensors. *RSC Advances* **2012,** *2*, 12696-12698.

[75] Hu, Z. H.; Tao, C. A.; Liu, H. P.; Zou, X. R.; Zhu, H.; Wang, J. F. Fabrication of an NH_2-MIL-88b Photonic Film for Naked-Eye Sensing of Organic Vapors. *J. Mater. Chem. A* **2014,** *2*, 14222-14227.

[76] Ameloot, R.; Stappers, L.; Fransaer, J.; Alaerts, L.; Sels, B. F.; De Vos, D. E. Patterned Growth of Metal-Organic Framework Coatings by Electrochemical Synthesis. *Chem. Mater.* **2009,** *21*, 2580-2582.

[77] Li, M. Y.; Dincă, M. Selective Formation of Biphasic Thin Films of Metal-Organic Frameworks by Potential-Controlled Cathodic Electrodeposition. *Chem. Sci.* **2014,** *5*, 107-111.

[78] Hod, I.; Bury, W.; Karlin, D. M.; Deria, P.; Kung, C. W.; Katz, M. J.; So, M.; Klahr, B.; Jin, D. N.; Chung, Y. W.; Odom, T. W.; Farha, O. K.; Hupp, J. T. Directed Growth of Electroactive Metal-Organic Framework Thin Films Using Electrophoretic Deposition. *Adv. Mater.* **2014,** *26*, 6295-6300.

[79] Mondloch, J. E.; Bury, W.; Fairen-Jimenez, D.; Kwon, S.; DeMarco, E. J.; Weston, M. H.; Sarjeant, A. A.; Nguyen, S. T.; Stair, P. C.; Snurr, R. Q.; Farha, O. K.; Hupp, J. T. Vapor-Phase Metalation by Atomic Layer Deposition in a Metal-Organic Framework. *J. Am. Chem. Soc.* **2013,** *135*, 10294-10297.

[80] Katz, M. J.; Brown, Z. J.; Colon, Y. J.; Siu, P. W.; Scheidt, K. A.; Snurr, R. Q.; Hupp, J. T.; Farha, O. K. A Facile Synthesis of UiO-66, UiO-67 and Their Derivatives. *Chem. Commun.* **2013,** *49*, 9449-9451.

[81] Loiseau, T.; Serre, C.; Huguenard, C.; Fink, G.; Taulelle, F.; Henry, M.; Bataille, T.; Férey, G. A Rationale for the Large Breathing of the Porous Aluminum Terephthalate (MIL-53) Upon Hydration. *Chem. Eur. J.* **2004,** *10*, 1373-1382.

[82] Betard, A.; Fischer, R. A. Metal-Organic Framework Thin Films: From Fundamentals to Applications. *Chem. Rev.* **2012,** *112*, 1055-1083.

[83] Shekhah, O. Layer-by-Layer Method for the Synthesis and Growth of Surface Mounted Metal-Organic Frameworks (SURMOFs). *Materials* **2010,** *3*, 1302-1315.

[84] Allendorf, M. D.; Houk, R. J. T.; Andruszkiewicz, L.; Talin, A. A.; Pikarsky, J.; Choudhury, A.; Gall, K. A.; Hesketh, P. J. Stress-Induced Chemical Detection Using Flexible Metal-Organic Frameworks. *J. Am. Chem. Soc.* **2008,** *130*, 14404-14405.

[85] Heinke, L.; Cakici, M.; Dommaschk, M.; Grosjean, S.; Herges, R.; Bräse, S.; Wöll, C. Photoswitching in Two-Component Surface-Mounted Metal-Organic Frameworks: Optically Triggered Release from a Molecular Container. *ACS Nano* **2014,** *8*, 1463-1467.

[86] Arslan, H. K.; Shekhah, O.; Wohlgemuth, J.; Franzreb, M.; Fischer, R. A.; Wöll, C. High-Throughput Fabrication of Uniform and Homogenous MOF Coatings. *Adv. Funct. Mater.* **2011,** *21*, 4228-4231.

[87] Arslan, H. K.; Shekhah, O.; Wieland, D. C.; Paulus, M.; Sternemann, C.; Schroer, M. A.; Tiemeyer, S.; Tolan, M.; Fischer, R. A.; Wöll, C. Intercalation in Layered Metal-Organic Frameworks: Reversible Inclusion of an Extended pi-System. *J. Am. Chem. Soc.* **2011,** *133*, 8158-8161.

[88] Munuera, C.; Shekhah, O.; Wang, H.; Wöll, C.; Ocal, C. The Controlled Growth of Oriented Metal-Organic Frameworks on Functionalized Surfaces as Followed by Scanning Force Microscopy. *Phys. Chem. Chem. Phys.* **2008,** *10*, 7257-7261.

[89] Stavila, V.; Volponi, J.; Katzenmeyer, A. M.; Dixon, M. C.; Allendorf, M. D. Kinetics and Mechanism of Metal-Organic Framework Thin Film Growth: Systematic Investigation of HKUST-1 Deposition on QCM Electrodes. *Chem. Sci.* **2012,** *3*, 1531-1540.

[90] Gu, Z.-G.; Pfriem, A.; Hamsch, S.; Breitwieser, H.; Wohlgemuth, J.; Heinke, L.; Gliemann, H.; Wöll, C. Transparent Films of Metal-Organic Frameworks for Optical Applications. *Microporous Mesoporous Mater.* **2015,** *211*, 82-87.

[91] Sauerbrey, G. Verwendung von Schwingquarzen zur Wägung dünner Schichten und zur Mikrowägung. *Zeitschrift Fur Physik* **1959,** *155*, 206-222.

[92] Allendorf, M. D.; Schwartzberg, A.; Stavila, V.; Talin, A. A. A Roadmap to Implementing Metal-Organic Frameworks in Electronic Devices: Challenges and Critical Directions. *Chem. Eur. J.* **2011,** *17*, 11372-11388.

[93] D'Alessandro, D. M.; Kanga, J. R. R.; Caddy, J. S. Towards Conducting Metal-Organic Frameworks. *Aust. J. Chem.* **2011,** *64*, 718-722.

[94] Morozan, A.; Jaouen, F. Metal Organic Frameworks for Electrochemical Applications. *Energy Environ. Sci.* **2012,** *5*, 9269-9290.

[95] Wu, D. F.; Guo, Z. Y.; Yin, X. B.; Pang, Q. Q.; Tu, B. B.; Zhang, L. J.; Wang, Y. G.; Li, Q. W. Metal-Organic Frameworks as Cathode Materials for Li-O_2 Batteries. *Adv. Mater.* **2014,** *26*, 3258-3262.

[96] Zhang, Z. Y.; Yoshikawa, H.; Awaga, K. Monitoring the Solid-State Electrochemistry of Cu(2,7-AQDC) (AQDC = Anthraquinone Dicarboxylate) in a Lithium Battery: Coexistence of Metal and Ligand Redox Activities in a Metal-Organic Framework. *J. Am. Chem. Soc.* **2014,** *136*, 16112-16115.

[97] Sadakiyo, M.; Yamada, T.; Kitagawa, H. Rational Designs for Highly Proton-Conductive Metal-Organic Frameworks. *J. Am. Chem. Soc.* **2009,** *131*, 9906-9907.

[98] Liu, B.; Shioyama, H.; Jiang, H. L.; Zhang, X. B.; Xu, Q. Metal-Organic Framework (MOF) as a Template for Syntheses of Nanoporous Carbons as Electrode Materials for Supercapacitor. *Carbon* **2010,** *48*, 456-463.

[99] Querebillo, C. J.; Terfort, A.; Allara, D. L.; Zharnikov, M. Static Conductance of Nitrile-Substituted Oligophenylene and Oligo(Phenylene Ethynylene) Self-Assembled Monolayers Studied by the Mercury-Drop Method. *J. Phys. Chem. C* **2013,** *117*, 25556-25561.

[100] Tuccitto, N.; Ferri, V.; Cavazzini, M.; Quici, S.; Zhavnerko, G.; Licciardello, A.; Rampi, M. A. Highly Conductive Similar to 40-nm-Long Molecular Wires Assembled by Stepwise Incorporation of Metal Centres. *Nat. Mater.* **2009,** *8*, 41-46.

[101] Dragasser, A.; Shekhah, O.; Zybaylo, O.; Shen, C.; Buck, M.; Wöll, C.; Schlettwein, D. Redox Mediation Enabled by Immobilised Centres in the Pores of a Metal-Organic Framework Grown by Liquid Phase Epitaxy. *Chem. Commun.* **2012,** *48*, 663-665.

[102] Talin, A. A.; Centrone, A.; Ford, A. C.; Foster, M. E.; Stavila, V.; Haney, P.; Kinney, R. A.; Szalai, V.; El Gabaly, F.; Yoon, H. P.; Leonard, F.; Allendorf, M. D. Tunable Electrical Conductivity in Metal-Organic Framework Thin-Film Devices. *Science* **2014,** *343*, 66-69.

[103] Kobayashi, Y.; Jacobs, B.; Allendorf, M. D.; Long, J. R. Conductivity, Doping, and Redox Chemistry of a Microporous Dithiolene-Based Metal-Organic Framework. *Chem. Mater.* **2010,** *22*, 4120-4122.

[104] Narayan, T. C.; Miyakai, T.; Seki, S.; Dincă, M. High Charge Mobility in a Tetrathiafulvalene-Based Microporous Metal-Organic Framework. *J. Am. Chem. Soc.* **2012,** *134*, 12932-12935.

[105] Leong, C. F.; Chan, B.; Faust, T. B.; D'Alessandro, D. M. Controlling Charge Separation in a Novel Donor-Acceptor Metal-Organic Framework via Redox Modulation. *Chem. Sci.* **2014,** *5*, 4724-4728.

[106] Mitzi, D. B. Thin-Film Deposition of Organic-Inorganic Hybrid Materials. *Chem. Mater.* **2001,** *13*, 3283-3298.

[107] Mitzi, D. B.; Prikas, M. T.; Chondroudis, K. Thin Film Deposition of Organic-Inorganic Hybrid Materials Using a Single Source Thermal Ablation Technique. *Chem. Mater.* **1999,** *11*, 542-544.

[108] Dinnebier, R. E.; Friese, K. Modern XRD Methods in Mineralogy. *Max-Planck-Institute for Solid State Research*, Stuttgart. FRG.

[109] Klug, H. P.; Alexander, L. E. X-Ray Diffraction Procedures for Polycrystalline and Amorphous Materials. *John Wiley & Sons* **1954**, New York.

[110] Tilley, R. J. D. Crystals and Crystal Structures. *John Wiley & Sons* **2006**, England.

[111] Introduction to Powder X-Ray Diffraction. **2001**, Bruker AXS.

[112] Weidenthaler, C. Pitfalls in the Characterization of Nanoporous and Nanosized Materials. *Nanoscale* **2011,** *3*, 792-810.

[113] Inaba, K. X-Ray Thin-Film Measurement Techniques. *The rigaku Journal* **2010,** *24*, 10-15.

[114] Kobayashi, S. X-Ray Thin-Film Measurement Techniques. *The rigaku Journal* **2010,** *26*, 3-9.

[115] Skoog, D. A.; Holler, F. J.; Crouch, S. R. Principles of Instrumental Analysis. *Thomson Brooks/Cole* **2007**, Belmont.

[116] Rouessac, F.; Rouessac, A. Chemical Analysis: Modern Instrumentation Methods and Techniques, 2nd Edition. *John Wiley & Sons* **2007**, Chichester.

[117] Nassau, K. The Physics and Chemistry of Color, 2nd Ed. *John Wiley & Sons* **2001**, New York.

[118] Gorel'skii, S. I.; Kim, T. G.; Klimova, T. P.; Kotov, V. Y.; Lokshin, B. V.; Perfil'ev, Y. D.; Sherbak, T. I.; Tsirlina, G. A. Outer-Sphere Anion-Anion Charge Transfer in a Solid Hexacyanoferrate. *Mendeleev Commun.* **2000**, 86-87.

[119] Faust, B. Modern Chemical Techniques: Background Reading for Chemistry Teachers. *Unilever* **2010**, 92-95.

[120] Griffith, P. R.; de Haseth, J. A. Fourier Transform Infrared Spectrometry, 2nd Ed. *John Wiley & Sons* **2007**, New Jersey.

[121] Infrared Spectroscopy: Theory. University of Colorado. *Department of Chemistry and Biochemistry*. Http://orgchem.colorado.edu/Spectroscopy/irtutor/tutorial.html. Link is taken at 10/05/2015.

[122] Kattner, J.; Homann, H. External Reflection Spectroscopy of Thin Films on Dielectric Substrates, in Handbook of Vibrational Spectroscopy. *John Wiley & Sons* **2002**, Chichester.

[123] Hoffmann, F. M. Infrared Reflection-Absorption Spectroscopy of Adsorbed Molecules. *Surf. Sci. Rep* **1983,** *3*, 107-192.

[124] Sheppard, N. The Historical Development of Experimental Techniques in Vibrational Spectroscopy, in Handbook of Vibrational Spectroscopy. *John Wiley & Sons* **2002**, Chichester.

[125] Gardiner, D. J.; Graves, P. R. Practical Raman Spectroscopy. *Springer* **1989**,

Heidelberg.

[126] Fujiwara, H. Spectroscopic Ellipsometry: Principles and Applications. *John Wiley & Sons* **2007**, Tokyo.

[127] Surface and Interface Physics, School of Physics, Trinity College Dublin. Https://www.Tcd.Ie/Physics/Surfaces/Ellipsometry2.Php. Link is taken at 10/05/2015.

[128] Ellipsometry Solutions. *J. A. Woollam, Co.*

Http://www.jawoollam.com/tutorial_1.html. Link is taken at 10/05/2015

[129] Goldstein, J. I.; Newbury, D. E.; Joy, D. C.; Lyman, C. E.; Echlin, P.; Lifshin, E.; Sawyer, L.; Michael, J. R. Scanning Electron Microscopy and X-Ray Microanalysis. *Springer* **2003**, New York.

[130] SEM. Http://En.Wikipedia.Org/Wiki/Scanning_Electron_Microscope. Link is taken at 10/05/2015.

[131] Binnig, G.; Quate, C. F.; Gerber, C. Atomic Force Microscope. *Phys. Rev. Lett.* **1986,** *56*, 930-933.

[132] Casero, E.; Vazquez, L.; Parra-Alfambra, A. M.; Lorenzo, E. AFM, SECM and QCM as Useful Analytical Tools in the Characterization of Enzyme-Based Bioanalytical Platforms. *Analyst* **2010,** *135*, 1878-1903.

[133] Vickerman, J. C.; Briggs, D. Tof-Sims: Surface Analysis by Mass Spectrometry, 2nd Ed. *SurfaceSpectra, Manchester and IM Publications* **2013**, Chichester.

[134] Belu, A. M.; Graham, D. J.; Castner, D. G. Time-of-Flight Secondary Ion Mass Spectrometry: Techniques and Applications for the Characterization of Biomaterial Surfaces. *Biomaterials* **2003,** *24*, 3635-3653.

[135] ION-TOF GmbH. Https://www.iontof.com/. Link is taken at 10/05/2015.

[136] Rampi, M. A.; Schueller, O. J. A.; Whitesides, G. M. Alkanethiol Self-Assembled Monolayers as the Dielectric of Capacitors with Nanoscale Thickness. *Appl. Phys. Lett.* **1998,** *72*, 1781-1783.

[137] Haag, R.; Rampi, M. A.; Holmlin, R. E.; Whitesides, G. M. Electrical Breakdown of Aliphatic and Aromatic Self-Assembled Monolayers Used as Nanometer-Thick Organic Dielectrics. *J. Am. Chem. Soc.* **1999,** *121*, 7895-7906.

[138] Holmlin, R. E.; Haag, R.; Chabinyc, M. L.; Ismagilov, R. F.; Cohen, A. E.; Terfort, A.; Rampi, M. A.; Whitesides, G. M. Electron Transport through Thin Organic Films in Metal-Insulator-Metal Junctions Based on Self-Assembled Monolayers. *J. Am. Chem. Soc.* **2001,** *123*, 5075-5085.

[139] Rampi, M. A.; Whitesides, G. M. A Versatile Experimental Approach for

Understanding Electron Transport through Organic Materials. *Chem. Phys.* **2002,** *281*, 373-391.

[140] Tran, E.; Rampi, M. A.; Whitesides, G. M. Electron Transfer in a Hg-SAM//SAM-Hg Junction Mediated by Redox Centers. *Angew. Chem., Int. Ed.* **2004,** *43*, 3835-3839.

[141] Bard, A. J.; Faulkner, L. R. Electrochemical Methods: Fundamentals and Applications, 2nd Ed. *John Wiley & Sons* **2001**, New York.

[142] Turbomole 6.5, Turbomole Gmbh Karlsruhe, http://www.turbomole.com. Turbomole Is a Development of the University of Karlsruhe and Forschungszentrum Karlsruhe 1989-2007, Turbomole Gmbh since 2007.

[143] Schafer, A.; Huber, C.; Ahlrichs, R. Fully Optimized Contracted Gaussian-Basis Sets of Triple Zeta Valence Quality for Atoms Li to Kr. *J. Chem. Phys.* **1994,** *100*, 5829-5835.

[144] Grimme, S.; Antony, J.; Ehrlich, S.; Krieg, H. A Consistent and Accurate ab initio Parametrization of Density Functional Dispersion Correction (DFT-D) for the 94 Elements H-Pu. *J. Chem. Phys.* **2010,** *132*, 154104.

[145] St Petkov, P.; Vayssilov, G. N.; Liu, J. X.; Shekhah, O.; Wang, Y. M.; Wöll, C.; Heine, T. Defects in MOFs: A Thorough Characterization. *ChemPhysChem* **2012,** *13*, 2025-2029.

[146] Damato, J. L.; Pastawski, H. M. Conductance of a Disordered Linear-Chain Including Inelastic-Scattering Events. *Phys. Rev. B* **1990,** *41*, 7411-7420.

[147] Lee, D. Y.; Shinde, D. V.; Yoon, S. J.; Cho, K. N.; Lee, W.; Shrestha, N. K.; Han, S. H. Cu-Based Metal-Organic Frameworks for Photovoltaic Application. *J. Phys. Chem. C* **2014,** *118*, 16328-16334.

[148] Patterson, A. L. The Scherrer Formula for X-Ray Particle Size Determination. *Phys. Rev.* **1939,** *56*, 978-982.

[149] Grave, C.; Tran, E.; Samori, P.; Whitesides, G. M.; Rampi, M. A. Correlating Electrical Properties and Molecular Structure of Sams Organized between Two Metal Surfaces. *Synth. Met.* **2004,** *147*, 11-18.

[150] Holmlin, R. E.; Ismagilov, R. F.; Haag, R.; Mujica, V.; Ratner, M. A.; Rampi, M. A.; Whitesides, G. M. Correlating Electron Transport and Molecular Structure in Organic Thin Films. *Angew. Chem., Int. Ed.* **2001,** *40*, 2316-2320.

[151] Chabinyc, M. L.; Chen, X. X.; Holmlin, R. E.; Jacobs, H.; Skulason, H.; Frisbie, C. D.; Mujica, V.; Ratner, M. A.; Rampi, M. A.; Whitesides, G. M. Molecular Rectification in a Metal-Insulator-Metal Junction Based on Self-Assembled Monolayers. *J. Am. Chem.*

Soc. **2002,** *124*, 11730-11736.

[152] Bundschuh, S.; Kraft, O.; Arslan, H. K.; Gliemann, H.; Weidler, P. G.; Wöll, C. Mechanical Properties of Metal-Organic Frameworks: An Indentation Study on Epitaxial Thin Films. *Appl. Phys. Lett.* **2012,** *101*,101910.

[153] Untiedt, C.; Yanson, A. I.; Grande, R.; Rubio-Bollinger, G.; Agrait, N.; Vieira, S.; van Ruitenbeek, J. M. Calibration of the Length of a Chain of Single Gold Atoms. *Phys. Rev. B* **2002,** *66*, 085418.

[154] Liu, J.; Wachter, T.; Irmler, A.; Weidler, P. G.; Gliemann, H.; Pauly, F.; Mugnaini, V.; Zharnikov, M.; Wöll, C. Electric Transport Properties of Surface-Anchored Metal-Organic Frameworks and the Effect of Ferrocene Loading. *ACS Appl. Mat. Interfaces* **2015,** *7*, 9824-9830.

[155] Mayor, M.; Weber, H. B.; Reichert, J.; Elbing, M.; von Hanisch, C.; Beckmann, D.; Fischer, M. Electric Current through a Molecular Rod - Relevance of the Position of the Anchor Groups. *Angew. Chem., Int. Ed.* **2003,** *42*, 5834-5838.

[156] Aradhya, S. V.; Meisner, J. S.; Krikorian, M.; Ahn, S.; Parameswaran, R.; Steigerwald, M. L.; Nuckolls, C.; Venkataraman, L. Dissecting Contact Mechanics from Quantum Interference in Single-Molecule Junctions of Stilbene Derivatives. *Nano Lett.* **2012,** *12*, 1643-1647.

[157] Arroyo, C. R.; Frisenda, R.; Moth-Poulsen, K.; Seldenthuis, J. S.; Bjornholm, T.; van der Zant, H. S. J. Quantum Interference Effects at Room Temperature in OPV-Based Single-Molecule Junctions. *Nanoscale Res. Lett.* **2013,** *8*, 1-6.

[158] Feigelman, M.; Pokrovsky, V. Long-Range Order and Diffraction of X-Ray Waves on Multilayered Crystalline Films. *J. Phys.* **1981,** *42*, 125-131.

[159] Shekhah, O.; Wang, H.; Paradinas, M.; Ocal, C.; Schupbach, B.; Terfort, A.; Zacher, D.; Fischer, R. A.; Wöll, C. Controlling Interpenetration in Metal-Organic Frameworks by Liquid-Phase Epitaxy. *Nat. Mater.* **2009,** *8*, 481-484.

[160] Liu, J. X.; Shekhah, O.; Stammer, X.; Arslan, H. K.; Liu, B.; Schupbach, B.; Terfort, A.; Wöll, C. Deposition of Metal-Organic Frameworks by Liquid-Phase Epitaxy: The Influence of Substrate Functional Group Density on Film Orientation. *Materials* **2012,** *5*, 1581-1592.

[161] Horcas, I.; Fernandez, R.; Gomez-Rodriguez, J. M.; Colchero, J.; Gomez-Herrero, J.; Baro, A. M. WSXM: A Software for Scanning Probe Microscopy and a Tool for Nanotechnology. *Rev. Sci. Instrum.* **2007,** *78*, 013705.

[162] Rogers, R. D.; Seddon, K. R. Ionic Liquids--Solvents of the Future? *Science* **2003,** *302*, 792-793.

[163] Le, A. D.; Yu, L. Irreversible Redox Reactions of Ferrocene/Ferrocenium on Self-Assembled Monolayer Modified Gold Electrode in Ionic Liquid $BMIMBF_4$. *J. Electrochem. Soc.* **2011,** *158*, F10-F14.

[164] Miller, C.; Cuendet, P.; Gratzel, M. Adsorbed .omega.-Hydroxy Thiol Monolayers on Gold Electrodes: Evidence for Electron Tunneling to Redox Species in Solution. *J. Phys. Chem.* **1991,** *95*, 877-886.

[165] Finklea, H. O.; Snider, D. A.; Fedyk, J.; Sabatani, E.; Gafni, Y.; Rubinstein, I. Characterization of Octadecanethiol-Coated Gold Electrodes as Microarray Electrodes by Cyclic Voltammetry and AC-Impedance Spectroscopy. *Langmuir* **1993,** *9*, 3660-3667.

[166] Mugnaini, V.; Tsotsalas, M.; Bebensee, F.; Grosjean, S.; Shahnas, A.; Bräse, S.; Lahann, J.; Buck, M.; Wöll, C. Electrochemical Investigation of Covalently Post-Synthetic Modified Surgel Coatings. *Chem. Commun.* **2014,** *50*, 11129-11131.

[167] Guo, W.; Liu, J. X.; Weidler, P. G.; Liu, J. X.; Neumann, T.; Danilov, D.; Wenzel, W.; Feldmann, C.; Wöll, C. Loading of Ionic Compounds into Metal-Organic Frameworks: A Joint Theoretical and Experimental Study for the Case of La^{3+}. *Phys. Chem. Chem. Phys.* **2014,** *16*, 17918-17923.

[168] Sun, L.; Miyakai, T.; Seki, S.; Dincă, M. Mn_2(2,5-Disulfhydrylbenzene-1,4-Dicarboxylate): A Microporous Metal-Organic Framework with Infinite (-Mn-S-)(Infinity) Chains and High Intrinsic Charge Mobility. *J. Am. Chem. Soc.* **2013,** *135*, 8185-8188.

[169] Dou, L. T.; You, J. B.; Hong, Z. R.; Xu, Z.; Li, G.; Street, R. A.; Yang, Y. 25th Anniversary Article: A Decade of Organic/Polymeric Photovoltaic Research. *Adv. Mater.* **2013,** *25*, 6642-6671.

[170] Seo, D. K.; Hoffmann, R. Direct and Indirect Band Gap Types in One-Dimensional Conjugated or Stacked Organic Materials. *Theor. Chem. Acc.* **1999,** *102*, 23-32.

[171] Liu, J. X.; Lukose, B.; Shekhah, O.; Arslan, H. K.; Weidler, P.; Gliemann, H.; Bräse, S.; Grosjean, S.; Godt, A.; Feng, X. L.; Mullen, K.; Magdau, I. B.; Heine, T.; Wöll, C. A Novel Series of Isoreticular Metal Organic Frameworks: Realizing Metastable Structures by Liquid Phase Epitaxy. *Scientific Reports* **2012,** *2*, 921.

[172] Higashino, T.; Imahori, H. Porphyrins as Excellent Dyes for Dye-Sensitized Solar Cells: Recent Developments and Insights. *Dalton Trans.* **2015,** *44*, 448-463.

[173] Martin, K. E.; Wang, Z. C.; Busani, T.; Garcia, R. M.; Chen, Z.; Jiang, Y. B.; Song, Y. J.; Jacobsen, J. L.; Vu, T. T.; Schore, N. E.; Swartzentruber, B. S.; Medforth, C. J.; Shelnutt, J. A. Donor-Acceptor Biomorphs from the Ionic Self-Assembly of Porphyrins. *J. Am. Chem. Soc.* **2010,** *132*, 8194-8201.

[174] Ng, K. K.; Lovell, J. F.; Vedadi, A.; Hajian, T.; Zheng, G. Self-Assembled

Porphyrin Nanodiscs with Structure-Dependent Activation for Phototherapy and Photodiagnostic Applications. *ACS Nano* **2013,** *7*, 3484-3490.

[175] Zhou, H.; Li, X. F.; Fan, T. X.; Osterloh, F. E.; Ding, J.; Sabio, E. M.; Zhang, D.; Guo, Q. X. Artificial Inorganic Leafs for Efficient Photochemical Hydrogen Production Inspired by Natural Photosynthesis. *Adv. Mater.* **2010,** *22*, 951-956.

[176] Liu, J.; Zhou, W.; Liu, J.; Howard, I.; Kilibarda, G.; Schlabach, S.; Coupry, D.; Addicoat, M.; Yoneda, S.; Tsutsui, Y.; Sakurai, T.; Seki, S.; Wang, Z.; Lindemann, P.; Redel, E.; Heine, T.; Wöll, C. Photoinduced Charge-Carrier Generation in Epitaxial MOF Thin Films: High Efficiency as a Result of an Indirect Electronic Band Gap? *Angew. Chem., Int. Ed.* **2015**, *54*, 7441-7445.

[177] Williams, M. J.; Cho, S. M.; He, S. S.; Lucovsky, G. Hydrogenated Amorphous Silicon-Nitrogen Alloys, a-Si,N:H: A Candidate Alloy for the Wide-Band Gap Photo-Active Material in Tandem Photovoltaic (PV) Devices. *J. Non-Cryst. Solids* **1993,** *166*, 67-70.

[178] Rai, M.; Singh, S. K.; Mishra, K.; Shankar, R.; Srivastava, R. K.; Rai, S. B. Eu^{3+}-Activated $CaGa_2O_4$ Wide Band Gap (WBG) Material for Solar Blind UV Conversion: Fluorescence and Photo-Conductivity Performance. *J. Mater. Chem. C* **2014,** *2*, 7918-7926.

[179] Choi, S. Y.; Mamak, M.; von Freymann, G.; Chopra, N.; Ozin, G. A. Mesoporous Bragg Stack Color Tunable Sensors. *Nano Lett.* **2006,** *6*, 2456-2461.

[180] Wang, Z. H.; Zhang, J. H.; Xie, J.; Wang, Z. Y.; Yin, Y. S.; Li, J. X.; Li, Y. F.; Liang, S.; Zhang, L.; Cui, L. Y.; Zhang, H.; Yang, B. Polymer Bragg Stack as Color Tunable Photonic Paper. *J. Mater. Chem.* **2012,** *22*, 7887-7893.

[181] Kemling, J. W.; Qayi, A. J.; Bailey, R. C.; Suslick, K. S. Nanostructured Substrates for Optical Sensing. *J. Phys. Chem. Lett.* **2011,** *2*, 2934-2944.

[182] Redel, E.; Wang, Z. B.; Walheim, S.; Liu, J. X.; Gliemann, H.; Wöll, C. On the Dielectric and Optical Properties of Surface-Anchored Metal-Organic Frameworks: A Study on Epitaxially Grown Thin Films. *Appl. Phys. Lett.* **2013,** *103*, 091903.

[183] Hinterholzinger, F. M.; Ranft, A.; Feckl, J. M.; Ruhle, B.; Bein, T.; Lotsch, B. V. One-Dimensional Metal-Organic Framework Photonic Crystals Used as Platforms for Vapor Sorption. *J. Mater. Chem.* **2012,** *22*, 10356-10362.

[184] Terzini, E.; Thilakan, P.; Minarini, C. Properties of ITO Thin Films Deposited by RF Magnetron Sputtering at Elevated Substrate Temperature. *Mater. Sci. Eng. B* **2000,** *77*, 110-114.

[185] Williamson, G. K.; Hall, W. H. X-Ray Line Broadening from Filed Aluminium and Wolfram. *Acta Metallurgica* **1953,** *1*, 22-31.

[186] Fischei-Cripps, A. C. The Sharpness of a Berkovich Indenter. *J. Mater. Res.* **2010,** *25*, 927-934.

[187] Zagorodniy, K.; Seifert, G.; Hermann, H. Metal-Organic Frameworks as Promising Candidates for Future Ultralow-K Dielectrics. *Appl. Phys. Lett.* **2010,** *97*, 251905.

[188] Eslava, S.; Zhang, L. P.; Esconjauregui, S.; Yang, J. W.; Vanstreels, K.; Baklanov, M. R.; Saiz, E. Metal-Organic Framework ZIF-8 Films as Low-Kappa Dielectrics in Microelectronics. *Chem. Mater.* **2013,** *25*, 27-33.

[189] Schoenecker, P. M.; Carson, C. G.; Jasuja, H.; Flemming, C. J. J.; Walton, K. S. Effect of Water Adsorption on Retention of Structure and Surface Area of Metal-Organic Frameworks. *Ind. Eng. Chem. Res.* **2012,** *51*, 6513-6519.

[190] Rezk, A.; Al-Dadah, R.; Mahmoud, S.; Elsayed, A. Characterisation of Metal Organic Frameworks for Adsorption Cooling. *Int. J. Heat Mass Transfer* **2012,** *55*, 7366-7374.

[191] Walheim, S.; Boltau, M.; Mlynek, J.; Krausch, G.; Steiner, U. Structure Formation via Polymer Demixing in Spin-Cast Films. *Macromolecules* **1997,** *30*, 4995-5003.

[192] Liu, J.; Redel, E.; Walheim, S.; Wang, Z.; Oberst, V.; Liu, J.; Heissler, S.; Welle, A.; Moosmann, M.; Scherer, T.; Bruns, M.; Gliemann, H.; Wöll, C. Monolithic High Performance Surface Anchored Metal−Organic Framework Bragg Reflector for Optical Sensing. *Chem. Mater.* **2015,** *27*, 1991-1996.

[193] Zhang, X.; Zhang, Z. Y.; Zhao, H. H.; Mao, J. G.; Dunbar, K. R. A Cadmium Tcnq-Based Semiconductor with Versatile Binding Modes and Non-Integer Redox States. *Chem. Commun.* **2014,** *50*, 1429-1431.

[194] Fernandez, C. A.; Martin, P. C.; Schaef, T.; Bowden, M. E.; Thallapally, P. K.; Dang, L.; Xu, W.; Chen, X. L.; McGrail, B. P. An Electrically Switchable Metal-Organic Framework. *Scientific Reports* **2014,** *4*, 6114.

[195] Xia, L.; McCreery, R. L. Structure and Function of Ferricyanide in the Formation of Chromate Conversion Coatings on Aluminum Aircraft Alloy. *J. Electrochem. Soc.* **1999,** *146*, 3696-3701.

[196] Brunschwig, B. S.; Creutz, C.; Sutin, N. Optical Transitions of Symmetrical Mixed-Valence Systems in the Class II-III Transition Regime. *Chem. Soc. Rev.* **2002,** *31*, 168-184.

[197] Wang, J. M.; Sun, X. W.; Jiao, Z. H. Application of Nanostructures in Electrochromic Materials and Devices: Recent Progress. *Materials* **2010,** *3*, 5029-5053.

[198] Itaya, K.; Uchida, I. Nature of Intervalence Charge-Transfer Bands in Prussian Blues. *Inorg. Chem.* **1986,** *25*, 389-392.

[199] Robin, M. B. Color and Electronic Configurations of Prussian Blue. *Inorg. Chem.* **1962,** *1*, 337-342.

[200] Pintado, S.; Goberna-Ferron, S.; Escudero-Adan, E. C.; Galan-Mascaros, J. R. Fast and Persistent Electrocatalytic Water Oxidation by Co-Fe Prussian Blue Coordination Polymers. *J. Am. Chem. Soc.* **2013,** *135*, 13270-13273.

[201] Nakanishi, S.; Lu, G. T.; Kothari, H. M.; Bohannan, E. W.; Switzer, J. A. Epitaxial Electrodeposition of Prussian Blue Thin Films on Single-Crystal Au(110). *J. Am. Chem. Soc.* **2003,** *125*, 14998-14999.

[202] Buser, H. J.; Schwarzenbach, D.; Petter, W.; Ludi, A. Crystal-Structure of Prussian Blue - $Fe_4[Fe(CN)_6]_3.XH_2O$. *Inorg. Chem.* **1977,** *16*, 2704-2710.

[203] Pawley, G. S. Unit-Cell Refinement from Powder Diffraction Scans. *J. Appl. Crystallogr.* **1981,** *14*, 357-361.

[204] Khorami, H. A.; Botero-Cadavid, J. F.; Wild, P.; Djilali, N. Spectroscopic Detection of Hydrogen Peroxide with an Optical Fiber Probe Using Chemically Deposited Prussian Blue. *Electrochim. Acta* **2014,** *115*, 416-424.

[205] Pitarch, A.; Alvarez-Perez, A.; Castro, K.; Madariaga, J. M.; Queralt, I. Raman Analysis Assessed by Fourier-Transformed Infrared and X-Ray Fluorescence Spectroscopies: A Multi-Analytical Approach of Ancient Chromolithographs from the 19th Century. *J. Raman Spectrosc.* **2012,** *43*, 411-418.

[206] Liu, J.; Zhou, W.; Walheim, S.; Wang, Z.; Lindemann, P.; Heissler, S.; Liu, J.; Weidler, P. G.; Schimmel, T.; Wöll, C.; Redel, E. Electrochromic Switching of Monolithic Prussian Blue Thin Film Devices. *Opt. Express* **2015,** *23*, 13725.

Publications

[1] **Liu, J.**; Wachter, T.; Irmler, A.; Weidler, P. G.; Gliemann, H.; Pauly, F.; Mugnaini, V.; Zharnikov, M.; Wöll, C. Electric Transport Properties of Surface-Anchored Metal-Organic Frameworks and the Effect of Ferrocene Loading. *ACS Appl. Mat. Interfaces* **2015,** *7*, 9824-9830.

[2] **Liu, J.**; Redel, E.; Walheim, S.; Wang, Z.; Oberst, V.; Liu, J.; Heissler, S.; Welle, A.; Moosmann, M.; Scherer, T.; Bruns, M.; Gliemann, H.; Wöll, C. Monolithic High Performance Surface Anchored Metal−Organic Framework Bragg Reflector for Optical Sensing. *Chem. Mater.* **2015,** *27*, 1991-1996.

[3] **Liu, J.**; Zhou, W.; Walheim, S.; Wang, Z.; Lindemann, P.; Heissler, S.; Liu, J.; Weidler, P. G.; Schimmel, T.; Wöll, C.; Redel, E. Electrochromic Switching of Monolithic Prussian Blue Thin Film Devices. *Opt. Express* **2015,** *23*, 13725-13733.

[4] Liu, J.; Zhou, W.; **Liu, J.**; Howard, I.; Kilibarda, G.; Schlabach, S.; Coupry, D.; Addicoat, M.; Yoneda, S.; Tsutsui, Y.; Sakurai, T.; Seki, S.; Wang, Z.; Lindemann, P.; Redel, E.; Heine, T.; Wöll, C. Photoinduced Charge-Carrier Generation in Epitaxial MOF Thin Films: High Efficiency as a Result of an Indirect Electronic Band Gap? *Angew. Chem., Int. Ed.* **2015**, *54*, 7441-7445.

[5] Guo, W.; Liu, J.; Weidler, P. G.; **Liu, J.**; Neumann, T.; Danilov, D.; Wenzel, W.; Feldmann, C.; Wöll, C. Loading of Ionic Compounds into Metal-Organic Frameworks: A Joint Theoretical and Experimental Study for The Case of La^{3+}. *Phys. Chem. Chem. Phys.* **2014,** *16*, 17918-17923.

[6] Best, J. P.; Michler, J.; **Liu, J.**; Wang, Z.; Tsotsalas M.; Maeder X.; Röse S.; Oberst, V.; Liu, J.; Walheim, S.; Gliemann, H.; Weidler, P. G.; Redel, E.; Wöll, C. Nanomechanical investigation of thin-film electroceramic/metal-organic-framework multilayers. **Submitted**.

[7] Wang, Z.; Nminibapiel, D.; Shrestha, P.; **Liu, J.**; Guo, W.; Weidler, P. G.; Baumgart, H.; Wöll, C.; Redel, E. Nanomechanical investigation of thin-film electroceramic/metal-organic-framework multilayers. **Submitted**.

[8] **Liu, J.**; Paradinas, M.; Heinke, L.; Buck, M.; Ocal, C.; Mugnaini, V.; Wöll, C. Film quality and electronic properties of surface anchored metal-organic frameworks as revealed by cyclic voltammetry. **To be submitted**.

[9] **Liu, J.**; Wachter, T.; Weidler, P. G.; Gliemann, H.; Mugnaini, V.; Zharnikov, M.; Wöll, C. Guest Molecules Modulated Electrical Conductivity of Surface-Anchored Metal-Organic Frameworks: the Effect of TCNQ Loading. **In preparation**.

Acknowledgements

Firstly, I would like to express my deepest sense of gratitude to my supervisor, Prof. Dr. Christof Wöll, who offered me not only the opportunity to study and work at the KIT, but also his support and encouragement during my Ph.D study. Without his supervision and kind help, I could not have finished this thesis.

I would also like to thank Prof. Dr. Stefan Bräse for accepting to be the co-referee of my thesis. I really appreciate the time and effort he dedicated to my thesis.

Many thanks also go to Dr. Hartmut Gliemann, Dr. Peter G. Weidler, Stefan Heissler and Dr. Alexander Welle for kindly providing me a lot of help, valuable suggestions, and constructive discussions during my time at the IFG. Your training and teaching have greatly enriched my knowledge and will benefit me in my future career.

I am especially grateful to Dr. Veronica Mugnaini, Dr. Engelbert Redel and Dr. Jinxuan Liu for their assistance and support during my Ph.D study, as well as for their contributions to my publications. The collaboration with you has extended my expertise in different research areas. I am also very grateful to Dr. Pierre Tremouilhac for helping with the proofreading and the correction of my thesis.

I would also like to thank my other colleagues, Peter Lindemann, Wencai Zhou, Wei Guo, Peter Krolla-Sidenstein, Dr. Zhengbang Wang, Dr. Lars Heinke, Chengwu Yang, Dr. Zhigang Gu, Dr. Manuel Tsotsalas, Sophia Schmitt, Silvana Röse, Weiwei Qin, Dr. Carlos Azucena, Jonas Wohlgemuth, Stefanie Sellheim-Ret, Astrid Biedermann, for their help and valuable discussion. I have really enjoyed the moments shared with you during my time working and living in Germany.

I greatly appreciate the external collaborations with, Dr. Stefan Walheim, Markus Moosmann, Torsten Scherer from the Institute of Nanotechnology (INT), Vanessa Oberst and Dr. Michael Bruns from the Institute of Applied Materials (IAM), Tobias Wächter, Chia-I Hung and Prof. Michael Zharnikov from the University of Heidelberg, Andreas Irmler and Prof. Fabian Pauly from the University of Konstanz, Prof. Manfred Buck from the University of St Andrews, as well as Markos Paradinas and Prof. Carmen Ocal from the Autonomous University of Barcelona, for their supports.

I give my heartfelt thanks to my family for their endless love and support throughout my

entire life, in particular to my beloved wife, Huidan, for believing in me and being by my side even though we have been separated by such a long distance for many years. Without you I would not have been able to accomplish so much. I am overjoyed to be together with you to pursue our happiness. Many thanks also to my friends for supporting me. The hope and encouragement from all of you make up all of my momentum.

Finally, I gratefully acknowledge the financial support provided by the China Scholarship Council (CSC), as well as the priority program SPP 1362 of the German Research Foundation (DFG).